



HAL
open science

Nanocarbon from food waste: dispersions and applications

Aikaterini Kampioti

► **To cite this version:**

Aikaterini Kampioti. Nanocarbon from food waste: dispersions and applications. Chemical Physics [physics.chem-ph]. Université de Bordeaux, 2016. English. NNT: 2016BORD0364 . tel-01536074

HAL Id: tel-01536074

<https://theses.hal.science/tel-01536074>

Submitted on 10 Jun 2017

HAL is a multi-disciplinary open access archive for the deposit and dissemination of scientific research documents, whether they are published or not. The documents may come from teaching and research institutions in France or abroad, or from public or private research centers.

L'archive ouverte pluridisciplinaire **HAL**, est destinée au dépôt et à la diffusion de documents scientifiques de niveau recherche, publiés ou non, émanant des établissements d'enseignement et de recherche français ou étrangers, des laboratoires publics ou privés.

THÈSE PRÉSENTÉE
POUR OBTENIR LE GRADE DE

DOCTEUR DE
L'UNIVERSITÉ DE BORDEAUX

ÉCOLE DOCTORALE DE SCIENCES CHIMIQUES
SPÉCIALITÉ: CHIMIE-PHYSIQUE

Par Katerina KAMPIOTI

**NANOCARBON FROM FOOD WASTE:
DISPERSIONS AND APPLICATIONS**

Sous la direction de : Alain PÉNICAUD
co-encadrante : Christèle JAILLET

Soutenue le 9 décembre 2016

Membres du jury :

Mme VASQUEZ, Ester
M. DUVAIL, Jean-Luc
M. GALIOTIS, Costas
M. CHAPEL, Jean-Paul
M. WILTSHIRE, Andy
Mme JAILLET, Christèle
M. PÉNICAUD, Alain

Professeure, Université de Castilla la Mancha
Professeur, Université de Nantes
Professeur, Université de Patras
Directeur de Recherche, CNRS
Co-directeur de la société GAP, Gateshead
Maître de conférences, Université de Bordeaux
Directeur de Recherche, CNRS

Rapporteur
Rapporteur
Examineur
Examineur
Examineur
Encadrante de thèse
Directeur de thèse

To my family...

To my loved ones...

Acknowledgements

Due to several parameters, such as the different country/culture, daily routine, working environment and interaction with people from all over the world, the last three years were a unique experience for me! That's why I feel the need to express my gratitude to all of those who participated physically and spiritually at this phase of my life.

Initially, I'd like to thank my supervisors, Dr. Alain Pénicaud and Dr. Christèle Jaillet-Bartholome for giving me the opportunity to be a part of NanoTubes and Graphene (NTG) group. Thanks to our discussions and our disagreements, their precious advices and questions, they are the main actors of my scientific evolution. Dr. A. Pénicaud, as my main supervisor, gave me the opportunity to attend conferences, to interact and collaborate with scientists of field as well as scientists from different fields, and to present our work throughout many events, from NTG meetings, national and/or international congresses with industrial partners. I would like to emphasize as well that both Alain and Christèle did their best in the way they approached me, given the fact that my personality is influenced from a totally different background. For all of these reasons I am sincerely thankful!

I am very grateful to the jury members: Prof. Ester Vasquez, Prof. Jean-Luc Duvail, Prof. Costas Galiotis, Dr. Jean-Paul Chapel and Mr. Andy Wiltshire, for giving their precious time to read my thesis and for providing me with constructive conversations, with their comments and suggestions. I'd also like to thank Dr. Alain Derré, Dr. Kai Huang, Dr. George Bepete and Dr. Ferdinand Hof for our fruitful discussions and the working environment during my PhD thesis. A sincere "thank you" to Dr. Deniz Pekin for her constant assistance! I am also very grateful to Dr. Carolina F. Matos and Prof. Aldo J.G. Zarbin for our excellent collaboration.

I would like to thank all the members of the NTG group from the present to the past, who, with one way or another, contributed to the present work and for the positive working environment: Dr. Yu Wang, Dr. Eduardo G. Cividini Neiva, Mr. Guillaume Pino, Mr. Arthur Werner, Dr. Jonathan Idier, Dr. Fabienne Dragin, Dr. Julia Messner, Mr. Marco Alfonso, Mrs. Marie Follmer, Dr. Cintia Mateo, Dr. Franco Tardani, Dr. Fernando Torres Canas, Dr. Brigitte Delord, Dr. Wilfrid Neri, Dr. Jinkai Yuan, Dr. Jean-Paul Salvetat, Dr. Philippe Poulin and Dr. Cécile Zakri. The collaboration in this group has even led to the creation of friendships and for this, I am extremely grateful.

My appreciation is extended to all the partners of the Plascarb team with whom I developed a great collaboration. I would especially like to thank Mr. Andy Wiltshire

(GAP), Mrs. Krisztina Toth (Geonardo), Mr. Daniel Frohnmaier (Geonardo), Mrs. Valentina Zuri (Geonardo), Mr. Rune Wendelbo (Abalonyx), Mr. Neville Slack (CPI), Mr. Nigel Okey (CPI), Mrs. Joanna Waterton (CPI), Mr. Anand Pogul (CPI), Mr. Peter Brandstetter (Fraunhofer), Mrs. Catharina Paukner (cnanos), Mrs. Anna Mieczakowski (cnanos), Mr. Jerome Joaug (cnanos), Mr. Aaron Clayton (cnanos-gasplas) and Mr. Robert St John Cooper (cnanos-gasplas).

I would also like to acknowledge Mrs. Isabelle Ly for her lectures and knowledge on the SEM and TEM characterizations. I would like to acknowledge again Dr. Kai Huang and Dr. Hassan Saadaoui for the AFM analyses. I would like to thank Dr. Christine Labrugère for XPS experiments and for training me for the XPS characterization. Sincere thanks as well to Mr. Eric Lebraud for performing XRD measurements and to Dr. Frédéric Louerat and Mr. Xavier Brilland for their help in many different scientific aspects and their supply of chemical products. I also would like to express my sincere gratitude to Mr. Ahmed Bentaleb and Mr. Eric Laurichesse for our constructive discussions. I am definitely grateful to Mr. Stéphane Bechemin and Mr. Lionel Chevalier for their patience when my working hours were exceeding the limits of the accepted timetable, several times. I would like to thank the people in the reception, Mrs. Béatrice Huynh-Tan and Mrs. Nathalie Touzé and the mechanical workshop, Mr. Philippe Barboteau and Mr. Emmanuel Texier for their essential help whenever I needed it!

I wish to express my gratitude to Mrs. Corinne Amengual, Mrs. Béatrice Dupin, Mrs. Elisabeth Hortolland and Mrs. Evangéline Lounissie for their administrative support. I would also like to thank the informatics group: Mrs. Anne Facq, Mr. Jean-Luc Laborde, Ms. Sandrine Maillet and Mr. Philippe Hortolland for their IT support.

I would also like to acknowledge the people from the documentation service: Mrs. Nadine Laffargue, the people from the chemistry service: Mrs. Stéphanie Exiga and Mr. Mbolotiana Rajaoarivelo and from instrumentation: Mr. Lionel Buisson and Mr. Pascal Merzeau.

Huge thanks to all my friends in CRPP, both “foreigners” and “French”, for the moments we spent together, not only in the working environment but also in our leisure time! Amazing experiences that I hope will continue to take place! Unfortunately, it is not possible to name each and every one separately, since luckily the nice people are many, but I would like to thank my office mates: Mrs. Margot Stasse and Mr. Antoine Robert, the people who do or did sports with me like volleyball and dancing and the lunch and lab groups. I am also extremely grateful to my friends outside CRPP, from France, Greece and other countries who stood by me as brothers and sisters to all the different phases

of my life and mainly my Greek brother and sisters Mrs. Maria Mousoura, Mr. Nikos Stathopoulos, Mr. Evangelos Vekios, Mrs. Polina Theofanopoulou, Mrs. Rozalia Papadhmhtirou, Mrs. Nantia Sarri and Mr. Periklhs Tsoukalas and our Spanish “family”! Last but not least, I would like to express a profound gratitude to my family, Mrs. Marietta Mylona, Mr. Anastasios Kampiotis, Mrs. Maria Kampiote, Mr. Dimitrios Kampiotis, Mr. Enni Amaefule and my love Nneka - Marietta Amaefule for their encouragements, moral support and for making my life beautiful, happier and less stressful. An honest “thank you” for being always here for me and for your infinite love, I feel so lucky!

Introduction générale - Résumé

Une caractéristique intéressante du carbone est sa capacité à former beaucoup d'allotropes grâce à sa valence. Parmi ces allotropes on peut compter les fullerènes, les nanotubes de carbone (CNT), le graphite (et le graphène). Après l'exfoliation du graphite en graphène par Geim et al. en 2004, les nanomatériaux à base de graphène ont suscité un immense intérêt pour la recherche et l'applications industrielles; en attendant, des études exploitent des voies de synthèse et précurseurs de carbone pour produire des matériaux à base de nanocarbone à la fois respectueux de l'environnement et rentable. La dégradation du biogaz en carbone et en hydrogène en utilisant le procédé plasma hyperfréquence est une technique prometteuse pour produire des grandes quantités de nanomatériaux de graphite durables.

Le Parlement Européen considère que les déchets alimentaires ne peuvent être recyclés ni exploités comme source matérielle. Cependant, les déchets alimentaires peuvent être transformés en produits nanocarbone graphitiques de grande valeur et l'hydrogène renouvelable par la transformation du méthane résultant de la décomposition des déchets alimentaires.^{1,2} Dans le cadre du projet européen "PlasCarb", le mélange méthane / dioxyde de carbone a été séparé en nanocarbone et en hydrogène via le processus de plasma hyperfréquence. À cet égard, le nanocarbone graphitique traité, pourrait être présenté comme un candidat valable pour remplacer le carbone provenant du pétrole (noir de carbone).

Cette thèse se concentre sur la caractérisation et la dispersion de ce nanocarbone graphite ainsi que ses applications, telles que la formation de charges dans des composites de caoutchouc naturel ou l'utilisation de nano-graphites comme des centres de photoluminescence. En outre, les dispersions développées dans cette étude ont été utilisés dans notre groupe pour préparer des encres conductrices et des supercondensateurs. En raison de sa forme, le matériau nanocarboné est appelé Nanopalets de Carbone (NPC ou CNP en Anglais) (voir chapitre 2).

La structure de ce manuscrit est la suivante:

Le chapitre 1 est consacré à la bibliographie du carbone. Les états d'hybridation et le contexte historique du carbone sont décrits ainsi que la structure et les propriétés du graphène. Ensuite, les processus de production et les applications d'une forme de carbone industriel, à savoir le noir de carbone sont décrits. Finalement, les CNP sont présentés en tant que matériau intermédiaire entre l'allotrope de carbone le plus

prometteur: graphène, et la forme de carbone avec une utilisation industrielle répandue : le noir de carbone, suivie d'une brève description du projet PlasCarb.

Le chapitre 2 est consacré à la caractérisation des CNP. Des CNP de différentes qualités ont été fournis par le projet PlasCarb et la société Cambridge Nanosystems. Leur caractérisation détaillée a été systématiquement réalisée en utilisant plusieurs techniques telles que la spectroscopie Raman, l'analyse thermogravimétrique (TGA), la diffraction de rayons X (XRD) et la spectroscopie photoélectronique de rayons X (XPS).

Le chapitre 3 décrit le processus d'obtention des dispersions aqueuses de CNP bien définies et fortement concentrées. Tout d'abord, différents protocoles d'exfoliation sont présentés. Ensuite, dans la section expérimentale, la purification de CNP, est initialement introduite. Différents paramètres sont décrits pour obtenir une solution aqueuse optimisée. Les dispersions sont calibrées en taille en utilisant un surfactant. Le chapitre 3 se termine par la caractérisation de ces dispersions.

Le chapitre 4 décrit deux ensembles de composites CNP avec du caoutchouc naturel (NR) qui diffèrent en tensioactif et le précurseur de CNP. Au départ, le contexte du caoutchouc naturel et des composites est donné. Puis, dans la section expérimentale, les dispersions de CNP utilisés, la procédure de préparation des composites CNP / NR et leur techniques de caractérisation sont décrites. Ensuite, la caractérisation des deux ensembles de composites est rapportée en utilisant une variété de techniques telles que la spectroscopie Raman, la microscopie électronique en transmission (TEM) et la microscopie de force atomique (AFM). Finalement, l'accent est mis sur leur propriétés thermiques, mécaniques, électriques et piézorésistives.

Le chapitre 5 présente la photoluminescence des CNP qui ont été dispersés et dissous dans des milieux liquides avec quatre procédures de préparation différentes. Ces procédures impliquent la dissolution de CNP dans un solvant organique par l'intermédiaire d'un composé d'intercalation de graphite (GIC) et ses dispersions dans l'eau via GIC et son transfert ultérieur dans de l'eau dégazée et par des traitements oxydants. Dans un premier temps, un rapport de la documentation de photoluminescence des nanomatériaux de carbone est présenté. La partie expérimentale implique les processus synthétiques des CNP et leur caractérisation préliminaire. Finalement, les spectres d'émission de la dissolution et des dispersions de CNP sont présentés.

*Two roads diverged in a yellow wood,
And sorry I could not travel both
And be one traveler, long I stood
And looked down one as far as I could
To where it bent in the undergrowth;*

*Then took the other, as just as fair,
And having perhaps the better claim,
Because it was grassy and wanted wear;
Though as for that the passing there
Had worn them really about the same,*

*And both that morning equally lay
In leaves no step had trodden black.
Oh, I kept the first for another day!
Yet knowing how way leads on to way,
I doubted if I should ever come back.*

*I shall be telling this with a sigh
Somewhere ages and ages hence:
Two roads diverged in a wood, and I—
I took the one less traveled by,
And that has made all the difference.*

by Robert Frost

Table of contents

General Introduction	15
Chapter 1.....	19
Carbon	19
Introduction.....	21
1. Carbon introduction	22
2. Graphene.....	26
a. Structure.....	26
b. Properties	29
c. Synthesis.....	35
3. Carbon black.....	36
a. Atomic structure and morphology	37
b. Parameters influencing properties	38
c. Production	40
d. Industrial designations	42
e. Applications.....	42
4. Carbon nanopucks.....	43
5. Plascarb project.....	44
Conclusion	47
References.....	49
Chapter 2.....	55
Characterization of carbon nanopucks	55
Introduction.....	57
1. Experimental section.....	58
a. Carbon nanopucks synthesis.....	58
b. Carbon nanopucks purification	58
c. Characterization of carbon nanopucks	58
d. Formulation of the dispersion.....	60
2. Results	61
a. Characterization of carbon nanopucks	61
b. Dispersion of the purified carbon nanopucks	74
3. Discussion	83
Conclusion	85
References.....	86

Chapter 3.....	89
Carbon nanopuck dispersions	89
Introduction.....	91
1. Liquid phase exfoliation	92
a. Graphite intercalation compounds	92
b. Dispersion of graphene oxide and reduced graphene oxide	93
c. Dispersion of graphene from pristine graphite.....	94
2. Experimental section.....	100
a. Carbon nanopucks purification	100
b. Characterization techniques	100
c. Formulation of the dispersion.....	100
3. Results and discussion.....	101
a. Characterization of unpurified CNP	101
b. Characterization of purified CNP.....	102
c. Carbon nanopuck dispersion conditions.....	104
d. Characterization of carbon nanopuck dispersions.....	114
Conclusion	118
References.....	119
Chapter 4.....	125
Natural rubber/carbon nanopuck composites	125
Introduction.....	127
1. Natural rubber and composites background	128
a. Natural rubber.....	128
b. Composites.....	129
2. Experimental section.....	130
a. CNP dispersions.....	130
b. CNP/NR composites preparation procedure	131
c. CNP/NR composites characterization	133
3. Results and discussion.....	137
a. CNP ₅ /NR composites	137
b. CNP _{HT2} /NR composites	145
Conclusion	162
References.....	163
Chapter 5.....	167
Carbon nanopuck photoluminescence.....	167

Introduction.....	169
1. State of the art	170
2. Experimental section.....	173
a. Solution/dispersion preparation procedures.....	173
b. Characterization techniques	178
3. Results and discussion.....	178
a. CNPa	178
b. CNPb.....	182
c. CNPc	185
d. CNPd.....	188
Conclusion	192
References.....	193
General conclusion	197
Acronyms	201

General Introduction

An interesting feature of carbon is its ability to form many allotropes due to its valence. Fullerenes, carbon nanotubes (CNTs), graphite and graphene are few of them. Especially after the simple and feasible exfoliation of graphite into graphene by Geim *et al.* in 2004, graphene-based nanomaterials have generated tremendous interest in research and industrial area; meanwhile, studies exploit alternative synthetic routes and carbon precursors to produce nanocarbon materials both environmentally friendly and cost-effectively. Splitting of biogas to carbon and hydrogen by using microwave plasma process is a promising technique to produce large quantities of sustainable graphitic nanomaterials.

The European Parliament considers that food waste could not be recycled or harnessed as a material source. However, food waste can be transformed into high value graphitic nanocarbon and renewable hydrogen through the transformation of methane resulting from decomposition of food waste.^{1,2} Within the framework of the European project “PlasCarb”, methane/carbon dioxide mix is split into nanocarbon and hydrogen via microwave plasma process. In this respect, graphitic nanocarbon after being processed, could be introduced as a valid candidate to substitute petroleum-based carbon materials.

This PhD thesis is focused on the characterization and dispersion of this graphitic nanocarbon and its applications. The uses developed in this study are as fillers in natural rubber composites and as photoluminescence centers. Moreover, the dispersions developed in this study have been used to prepare conductive inks and supercapacitors in our group. Due to its shape, the nanocarbon material is referred to as carbon nanopucks (CNPs) (cf chapter 2). The structure of the manuscript is as follows:

Chapter 1 is dedicated to the bibliographic background of carbon. At first, the hybridization states and historical background of carbon are presented. Afterwards, the structure and properties of graphene are given. Then, the production processes and applications of an industrial carbon form, namely carbon black are described. Ultimately, CNPs, as an intermediate material between the most promising carbon allotrope, graphene, and the carbon form with widespread industrial usage, carbon black is presented followed by a brief description of the PlasCarb project.

Chapter 2 is devoted to the characterization of CNPs. Different CNPs grades have been provided from the PlasCarb project and Cambridge Nanosystems company. Their detailed characterization has been systematically carried out by using several

techniques such as Raman spectroscopy, thermogravimetric analysis (TGA), X-ray diffraction (XRD) and X-ray photoelectron spectroscopy (XPS).

Chapter 3 reports the route that has been followed in order to obtain well-defined, high concentrated aqueous CNP dispersions. Firstly, different liquid exfoliation processes are presented. Afterwards, in the experimental section, the CNP purification is initially introduced. Then, different parameters are determined to obtain optimized aqueous dispersions calibrated in size with the use of surfactant. Chapter 3 ends with the characterization of these dispersions.

Chapter 4 describes two sets of CNP composites with natural rubber (NR) which differ in the surfactant and CNP precursor. Initially, the background of natural rubber and composites is given. Then, in the experimental section, the CNP dispersions that have been used, the CNP/NR composites preparation procedure and their characterization techniques are described. Afterwards, the characterization of the two sets of composites is reported using a variety of techniques such as Raman spectroscopy, transmission electron microscopy (TEM) and atomic force spectroscopy (AFM). Eventually, emphasis is given to their thermal, mechanical, electrical and piezoresistive properties.

Chapter 5 presents the photoluminescence of CNPs that have been dispersed and dissolved in liquid media with four different preparation procedures. These procedures involve the CNP dissolution in organic solvent through graphite intercalation compound (GIC) and its dispersions in water via GIC and subsequent transfer to degassed water, and via oxidative treatments. Initially, a report of relevant literature of the photoluminescence of carbon nanomaterials is given. Afterwards, the experimental part involves the synthetic processes of CNPs and their preliminary characterization. Ultimately, the emission spectra of CNP dissolution and dispersions are presented.

Chapter 1

Carbon

Table of contents

Chapter 1	19
Carbon	19
Introduction.....	21
1. Carbon introduction	22
2. Graphene.....	26
a. Structure.....	26
b. Properties	29
c. Synthesis.....	35
3. Carbon black.....	36
a. Atomic structure and morphology	37
b. Parameters influencing properties	38
c. Production	40
d. Industrial designations	42
e. Applications.....	42
4. Carbon nanopucks.....	43
5. Plascarb project.....	44
Conclusion	47
References.....	49

Introduction

This chapter comprises the bibliographic background of carbon which is essential to comprehend the study described in this manuscript. In part 1, a very first contact with carbon chemistry is achieved through the presentation of its hybridization states and historical background. Part 2 emphasizes the carbon allotrope with superior properties, graphene. Its structure, mechanical, electronic, optical, thermal and chemical properties are presented while a brief report of its synthesis is also given. Part 3 describes a specific carbon form, known as carbon black (CB). Initially, its proper definition is given. Then, different production paths are presented which leads to different CB, their commercial designations as well as their applications. Part 4 introduces the carbon material that was utilized in this study, referred to as carbon nanopuck (CNP) due to its shape. Its experimental characterization will be provided in details in the following chapter. Eventually, a summary of what is presented with useful remarks will conclude the background section.

1. Carbon introduction

The terrestrial occurrence of carbon renders it the seventeenth most abundant element on earth.³ Carbon with an atomic number of 6, has an electron configuration of $1s^2$, $2s^2$, and $2p^2$ atomic orbitals and is able to exist in three hybridization states, sp^3 , sp^2 and sp^1 as they are shown in **fig. 1.1**.

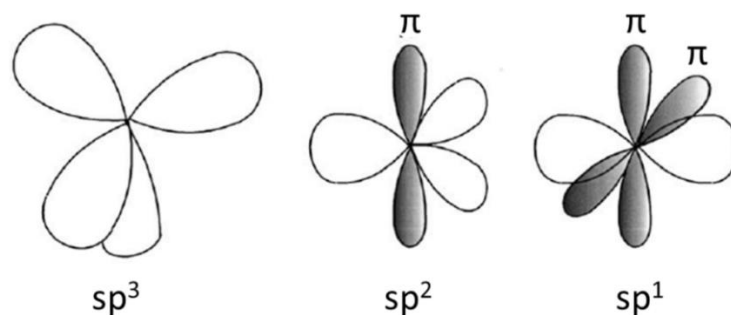


Figure 1.1: Hybridization states of carbon. Image reproduced from reference ⁴.

In sp^3 configuration, carbon atoms are hybridized as in diamond. Diamond is an isotropic, cubic insulator.⁵ Its sp^3 carbon atoms in tetrahedral geometry form strong σ bonds which explain the remarkable hardness and insulating properties.³ Except for its hardness which is designated as 10 on the Mohs scale (it is the hardest material known), diamond also exhibits extraordinary strength (130–140 GPa)⁶ and high density (3.514 g.cm^{-3}).⁵

In the sp^2 conformation, as in graphite, each hybridized carbon atom is covalently bonded to three adjacent carbon atoms located at the edges of a triangle in plane with the central atom, forming σ bonds. The two sp^2 unhybridized p orbitals perpendicular to the plane, with a p_z -electron cloud over and under the graphite plane in each sp^2 carbon atom, overlap with each other to form a π bond (weaker than σ bond). In the graphitic phase, the structure is highly anisotropic, since poor electrical conductivity occurs along the c-axis (perpendicular to the carbon sheets) while exceptional electrical properties along its sheets are evident due to the p electrons' delocalization in the plane.^{5,7} Other basic characteristics of graphite are its semi-metallic behavior in the basal plane, low hardness (1-2 on the Mohs scale) and low density ($2.09\text{--}2.23 \text{ g.cm}^{-3}$).⁵ 3D structures of diamond and graphite are depicted in **fig. 1.2**.

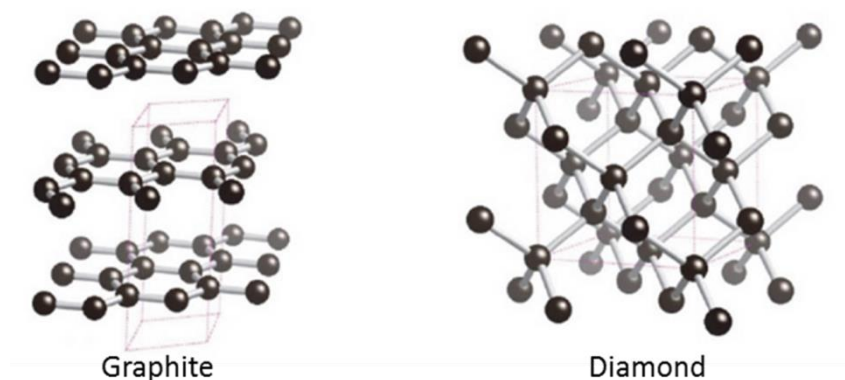


Figure 1.2: Naturally occurring carbon allotropes. Image reproduced from references ^{8,9}.

In the sp hybridization state, two sp hybridized electrons form one σ bond and the two unhybridized p electrons in each atom form two π bonds. Due to the aforementioned hybridized states, a huge variety of carbon materials occur (e.g. carbon black and carbon reduced graphene oxide), with often perplexing definitions.^{10,11}

Although carbon was first classified as an element by the French chemist A. Lavoisier in his “*Traité Élémentaire de Chimie*” in the 18th century,¹² it has long been revered for its outstanding properties. Its study has been initially reported in 3750 BC where it was used to reduce copper, zinc and tin ores in the manufacture of bronze. Over the centuries, carbon utilization and study has been continued and documented all over the world. Charcoal was used in medicine in 1500 BC according to Egyptian papyri and during 400 BC from Hippocrates and Pliny.¹³ Moreover, at the same period, Phoenician and Hindu cultures were harnessing charcoal as water filter. Further evidence of the scientific exploitation of carbon has been obstructed for over 1000 years due to the command of the Roman Emperor Diocletian of the total destruction of scientific books within the Roman empire during his persecution of other religions about 300 AD.¹³

As for the allotropes of carbon, they had a similar historical route with two different kinds of terrestrial pure carbon: the diamond and the graphite both known in the ancient and the Middle Ages.³ Particularly, the definition of graphite was not used until 1789 and this allotrope was known under different names such as “blacklead” and “plumbago”. The word graphite derives from the Greek word “γράφειν” which means “to write” and it was given from the German mineralogist and geologist A. G. Werner in an article in the “*Bergmännisches*” Journal.^{14,15}

In 1985, Kroto *et al.* synthesized the third allotrope. It is a close icosahedral cage molecule called C_{60} fullerene. It was synthesized in Rice university by vaporizing the

graphite by laser irradiation.¹⁶ Subsequently, Curl, Kroto and Smalley received the Nobel prize of chemistry in 1996 for their discovery.^{16,17} The representation of C₆₀ fullerene in shape of a soccer ball was, however, first mentioned by Leonardo da Vinci in 1498 (*De Divina Proportione*, Luca Pacioli), then later in 1970 by Osawa as a chemically stable, hypothetical molecule.^{5,18–20} The C₆₀ molecule, also called Buckminsterfullerene, consists of fused pentagons and hexagons. It could be considered as a 0D carbon allotrope placed between graphite and diamond owing to its bond hybridization due to their spherical shape.⁵

In less than a decade after the pioneer preparation of C₆₀ fullerenes for researchers discovered the fourth in a row carbon allotrope with a cylindrical structure also known as carbon nanotubes (CNTs). In particular, multi-walled CNTs (MWCNTs) were synthesized in 1991 by Iijima using an arc discharge evaporation method.²¹ The first transmission electron microscope (TEM) evidence though of this carbon tubular shape had long been reported from Radushkevich and Lukyanovich in the *Journal of Physical Chemistry of Russia* in 1952.²²

MWCNTs preparation followed by the synthesis of single-walled carbon nanotubes (SWCNTs) in 1993 from two groups which were working independently and published their discoveries in the same issue of *Nature*. Iijima and Ichihashi demonstrated the iron catalyzed formation of SWCNTs in a carbon arc chamber under methane and argon. Bethune *et al.* from the IBM group synthesized SWCNTs using a cobalt catalyst under helium.^{23,24} CNTs have 1D periodic structure and they are of high interest due to their excellent mechanical properties and the dependence of the electronic structure on chirality and diameter.⁵

On the trail of the continuous progress in the nano-world of carbon, the isolation of individual graphite layers, known as graphene, in 2004, is considered the apex of nanocarbon research.²⁵ Graphene, the basal plane of graphite, could be defined as one-atom thick layer of sp² carbon atoms arranged in a honeycomb 2D crystal lattice. It can be rolled to form 1D nanotubes, or wrapped up to create 0D fullerene, as shown in **fig. 1.3**.

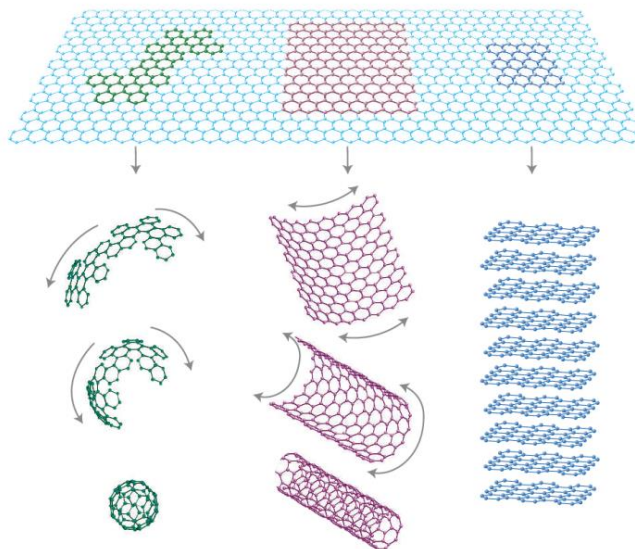


Figure 1.3: An 0D C60 fullerene molecule (leftmost, green), a carbon nanotube (middle, purple) and 3D graphite (far right, blue). 2D graphene (single layer of graphite) is the building block of all these carbon structures. Image reproduced from reference ²⁶.

However, graphene studies had started as early as the 1940s with Wallace's theoretical analysis. He suggested that the electrical conductivity of graphite is 100 times higher parallel than across to graphene planes.²⁷ But for many years this graphite monolayer was considered as only a concept since it was thought that it could not exist outside the 3D crystal lattice (the carbon sheets would restack to form graphite since it is thermodynamically the most stable). Nevertheless, the efforts to achieve the "impossible" were not discouraged. Early attempts were conducted by inserting small-molecule species in between the carbon sheets to reduce the interlayer interactions and increase their distance. In 1859, Brodie attempted to study the atomic weight of graphite by using strong acids and oxidants, (sulfuric and nitric acids and potassium chlorate as an oxidant).²⁸ He succeeded not only to form intercalation compounds but also to oxidize the surface which constitutes a fundamental step in the preparation of graphite oxide. In 1962, Boehm *et al.* used graphite oxide as precursor, to study the surface properties of thin graphite lamellae. They produced ultrathin carbon films by heating or reduction of graphite oxide in alkaline suspension.^{29,30} A thickness of 0.4–2 nm as indication of the exfoliation of graphene or few layers graphite was verified with TEM images. Even though only the microscopic observation of the defected and oxygen groups graphite is not enough to determine the number of layers, this study significantly has contributed to the research of the chemical preparation of graphene. Almost 20 years later, a precise definition of the term "graphene" was provided by Boehm *et al.*³¹

The term “graphite” comprises the 3D crystal lattice therefore it is not suitable to describe individual layers. Furthermore, the ending -ene is used for fused polycyclic aromatic hydrocarbons, such as naphthalene and anthracene. It is characteristically referred in the terminology provided from Boehm that “*a single carbon layer of the graphitic structure would be the final member of infinite size of this series. The term graphene layer should be used for such a single carbon layer*”.^{31,32} The actual exfoliation of graphene though, was accomplished not before 2004. The pioneering work of Andre Geim and Konstantin Novoselov from the University of Manchester who successfully produced unfolded graphene by mechanical exfoliation, constitutes a revolution in the research of graphene.²⁵ For their “ground-breaking experiments regarding the two-dimensional material graphene”, in 2010 they were rewarded with the Nobel Prize in Physics.³³ Their experiment consists of a repeated cleavage of highly oriented pyrolytic graphite (HOPG) with a scotch tape, which eventually produced few layers of graphite and ultimately graphene. This exfoliation path could be considered analogous to writing with a pencil. In this process the delamination of graphite flakes occurs due to the mechanical friction between the paper and the graphite, leaving graphite traces on the paper. Noteworthy that the same year, in 2004, Berger *et al.* by growing carbon films on the surface of SiC, produced carbon sheets with the electronic properties of graphene.³⁴ The production of unfolded graphene followed a vast number of studies which demonstrate its exceptional electronic, thermal and mechanical properties.^{26,30}

2. Graphene

a. Structure

The 2D honeycomb lattice of carbon could be seen as two inequivalent triangular sublattices which have a mirror relation. Each sublattice contains one carbon atom (designated as A and B respectively) that forms a triangular sp^2 network with three neighboring atoms as already mentioned in the previous subchapter on the hybridization states of carbon (**fig. 1.4 i**).^{35,36} Subsequently, the unit cell of graphene consists of the corresponding carbon atoms A and B with lattice vectors a_1 and a_2 and a carbon atom’s bond length a_0 of 0.142 nm. This bond length is the average of the single (C–C) and double (C=C) covalent bonds, as in the case of benzene with a 120° angle between bonds. The unit cell in reciprocal space is shown in **fig. 1.4 ii**).³⁷ The reciprocal lattice of graphene with vectors b_1 and b_2 is also a honeycomb, but rotated by 90°

relative to the real-space lattice. The first Brillouin zone has corners which are denoted as K and K' points. These points are inequivalent since no lattice vector connects them. All the other corners of the Brillouin zone can be mapped to either K or K' points.

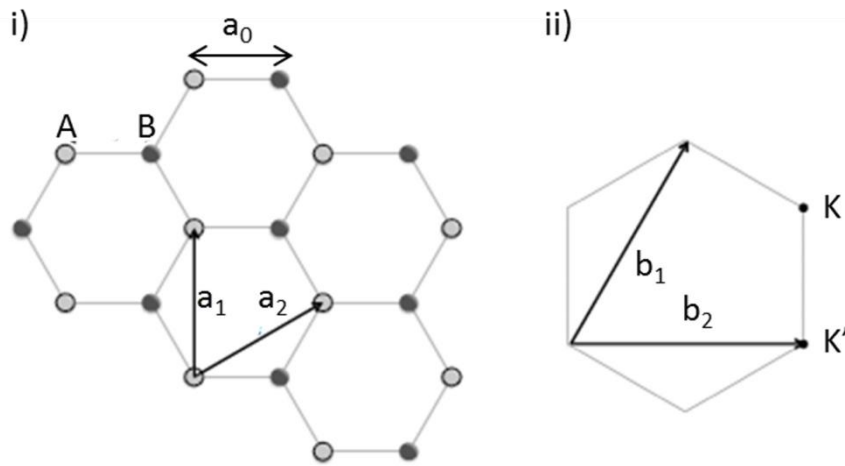


Figure 1.4: Graphene i) real and ii) reciprocal lattice.

Graphene, one-atom thick material, attracts the interest of the scientific community due to its unique structure.³⁸ Its name, as aforementioned, comprises its graphitic nature (graph) and the C-C double bonds (-ene).³¹ Three years ago, in 2013, it was identified by Bianco *et al.* as “a single-atom-thick sheet of hexagonally arranged, sp^2 -bonded carbon atoms that is not an integral part of a carbon material, but is freely suspended or adhered on a foreign substrate”.⁴⁰

The structure of graphene is affected by several parameters and characteristics, such as edge state, surface state, and in the case of more than one graphene layers, the stacking order plays a critical role.

This 2D material of around 0.34 nm thickness, it is not a perfect plane. In contrary, Meyer *et al.* by analyzing the electron diffraction patterns of suspended graphene sheets on a microfabricated scaffold, verified that its surface is not flat and exhibits microscopic roughness, as depicted in **fig. 1.5**.⁴¹

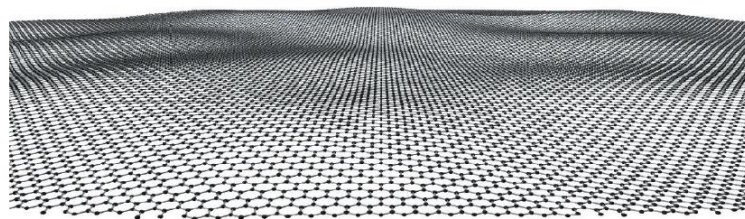


Figure 1.5: Schematic representation of the graphene surface. Adapted from reference ⁴¹.

The graphene structure also varies based on the edge states. The possible edge configurations are zigzag, armchair (**fig. 1.6**) or a mix of them. These different conformations influence the overall electronic properties of graphene.⁴²

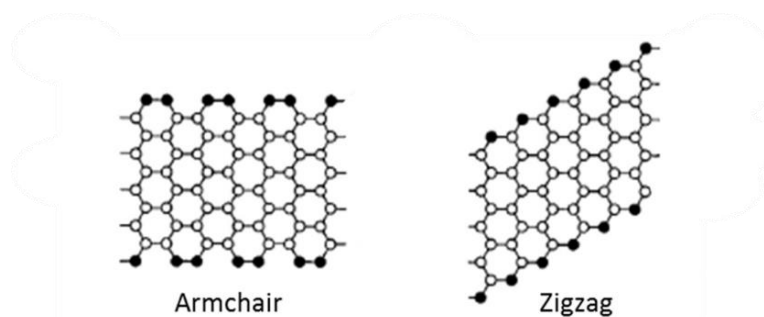


Figure 1.6: Edge states of graphene surface. Adapted from reference ⁴².

An interesting study on the stability and dynamics of graphene edges was performed by Girit *et al.*⁴³ They recorded movies of the movement of carbon atoms at the edge of a hole in a suspended graphene by using a high-energy electron beam in real time. They demonstrated the long-term stability of the zigzag edges in graphene through a time-average observation and modeling analysis. Graphene, as abovementioned, is the basal plane of graphite. Apart from single layer materials, bilayer or few layers graphite may occur. The different stacking order of the layers affects the properties of these materials. The most common stacking is the AB stacking, also known as Bernal arrangement, since the AA stacking is not thermodynamically favored (**fig. 1.7 b**) and **1.7 a**).³⁷ In AB stacking, above the corner atoms in a hexagon layer are the vacant centers of the second layer. The in-plane lattice constant of AB graphite is about 0.246 nm and that for the c-axis is 0.67 nm. Rhombohedral graphite with ABC stacking, also exists (**fig. 1.7 c**).⁴⁴ Unlike these perfectly stacked structures, the layers could be also arranged with no specific symmetry but with a rotational disorder. This atomic structure is known as turbostratic stacking with an interlayer spacing (>0.342 nm) larger than that for

crystalline graphite (0.335 nm) (**fig. 1.7 d**).^{37,44} A technique to distinguish the different structures is the Raman spectroscopy where there are differences like in I_{2D}/I_G ratio (intensity of 2D band over intensity of G band) and the shape of 2D band.³⁷

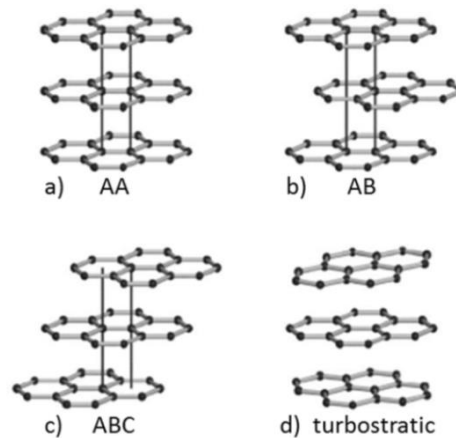


Figure 1.7: Stacking order of few layers of graphene. Adapted from reference ⁴⁵.

From all the aforementioned, it is clear that a variety of different materials can exist; graphene with different edge states, bilayer or few layers graphene with different edge arrangement, stacking order and/or a combination of them and so on. Another substantial parameter which will be described in details in chapter 3 is the preparation procedure of graphene-like materials which significantly determines their characteristics and properties. Graphene, graphene quantum dots (GQDs) and graphene oxide (GO) are few of these materials. In order to avoid any confusion, proper definition is mandatory. An order to the chaos in the nomenclature of graphene family has been given in 2013.⁴⁰

b. Properties

Mechanical properties

The formation of strong σ bonds, deriving from this sp^2 orbitals overlapping results in the extraordinary mechanical properties of graphene. Lee *et al.* via nanoindentation by using an atomic force microscope (AFM) determined the intrinsic strength of graphene. Schematic representation is depicted in **fig. 1.8**.⁴⁶ For instance, a single-layer, defect-free graphene has a Young's modulus of 1 TPa (while steel has around 0.2 TPa) and an intrinsic fracture strength of 130 GPa, making it the material with the best mechanical

properties. Notably, bulk graphite doesn't exhibit the same mechanical performance due to the ease of shearing between layers.

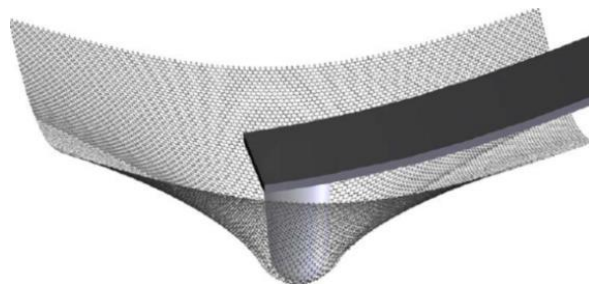


Figure 1.8: Schematic representation of nanoindentation on graphene layer.

In 2008, Chen *et al.* determined the elastic modulus and fracture strength of GO.⁴⁷ The significant decrease of both values (average elastic modulus 32 GPa and highest fracture strength obtained of 120 MPa) might be due to the presence of defects formed during the chemical reaction. After thermal annealing the elastic modulus and fracture strength values were increased. Reduced GO by hydrogen plasma treatment prepared by Gómez-Navarro *et al.*, exhibited a rather high Young's modulus of 0.25 TPa.⁴⁸

Electronic properties

As aforementioned, apart from the σ bonds, the carbon atoms have spatially delocalised π bonds owing to the overlap of the unhybridized p orbitals perpendicular to the plane on neighboring atoms. These π bonds form a band structure of π -band which is the valence band and π^* -band which is the conduction band as depicted in **fig. 1.9**. The unique electronic properties of graphene are the result of this particular band structure.⁴⁹ The valence and conduction bands intersect in two inequivalent points (K, K'), located at the corners of the first Brillouin zone of the reciprocal lattice, also known as Dirac points.

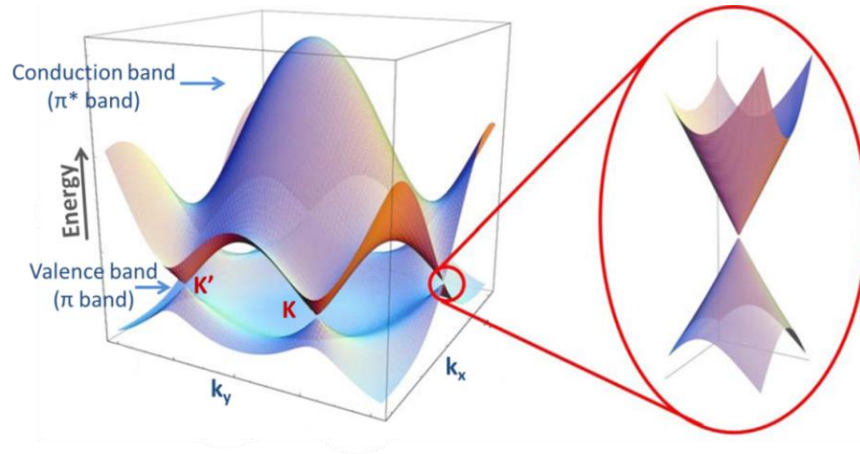


Figure 1.9: Band-structure of graphene describing the electronic dispersion. Right: zoom in of the energy bands close to the Dirac points. Adapted from reference ³⁵.

Introduced by Wallace, these crossing points are a consequence of the two triangular sublattices, reflected in the reciprocal lattice.²⁷ Near the Dirac points, there is a cone-formed linear electronic dispersion close to the Fermi level which is generally expressed as the **equation 1.1**:

$$E \cong \pm \hbar \cdot v_F \cdot |\mathbf{k} - \mathbf{K}| \quad [1.1]$$

where \hbar is the Planck constant, \mathbf{k} is the wave vector and Fermi velocity v_F is about 10^6 m.s⁻¹.

Based on the Dirac equation for massless fermion, the effective mass of charge carriers is zero since the energy at the Dirac point is zero and they behave like relativistic particles, as massless Dirac fermions.²⁵ As a direct consequence of the electronic structure and energy dispersion, graphene shows a pseudo spin, chirality and an anomalous Quantum Hall effect (first plateau of Hall conductivity is $2e^2/\hbar$ corresponding to the half integer N , where e is electron). Also, the charges in graphene exhibit a Klein paradox since the relative nature of Dirac fermions make them penetrate the barriers in a different way.³⁵ The Klein paradox refers to the unobstructed penetration of a relativistic quantum particle described by the Dirac equation through a sufficiently high potential barrier without exponential damping. Furthermore, owing to the electrons' behavior which acts more like photons rather than conventional massive particles (relativistic particles), it would be expected that they display high mobility. In fact, in 2008, Bolotin *et al.* reported the highest mobility in suspended and annealed graphene device. They performed transport measurements from which they verified the high mobility of charge carriers, in excess of 200000 cm².V⁻¹.s⁻¹. With this high value, the

charge transport could be considered as ballistic.⁵⁰ However, for graphene on a substrate, its mobility is largely limited due to scattering, and defects.^{26,51} The value of charge carriers mobility that was obtained for supported graphene films on multi-terminal devices can exceed $15000 \text{ cm}^2.\text{V}^{-1}.\text{s}^{-1}$. Moreover, the observed mobility is temperature independent between 10 and 100 K.²⁵

The carriers in graphene (electrons and holes) could also be continuously exchanged by providing the necessary gate bias. This ambipolar electric field effect was proved by Novoselov *et al.*^{25,52} Particularly, under a positive gate bias, the Fermi level was shifted above the Dirac point, resulting in high concentrations of electrons in the conduction band while under negative bias, the Fermi level is placed below the Dirac point, resulting in a large population of holes in the valence band.

Another characteristic of graphene's electronic behavior, is its high conductivity and optical transparency. In 2009 Kim *et al.* synthesized multilayer graphene films using chemical vapor deposition (CVD) on thin nickel layers, and then they transferred them to other substrates. The exhibited resistance is of $280 \text{ }\Omega.\text{sq}^{-1}$, with 80 % optical transparency.⁵³

Optical

The fine structure constant α is defined by the following **equation 1.2**:

$$\alpha = e^2/\hbar c \quad [1.2]$$

where e is the electron charge, \hbar is the Planck's constant and c is the speed of light. The equation describes coupling between light and relativistic electrons. The theoretical optical transmittance, T_{opt} , of a free standing graphene is expressed via α as follows (**equation 1.3**):

$$T_{\text{opt}} = (1 + \frac{\pi\alpha}{2})^{-2} \approx 1 - \pi\alpha \approx 0.977 \quad [1.3]$$

As a result the absorbance is of 0.023 or 2.3 %.⁵⁴ In 2008, Nair *et al.* experimentally determined the transmittance of large graphene crystals on oxidized Si wafer.⁵⁵ They revealed that graphene reflectance has a negligible value ($< 0.1\%$) of incident light in the visible region. Also, the transmittance is 97.7 % with an opacity to be 2.3 % and it increases linearly with the number of layers as demonstrated in **fig. 1.10**.⁵⁵

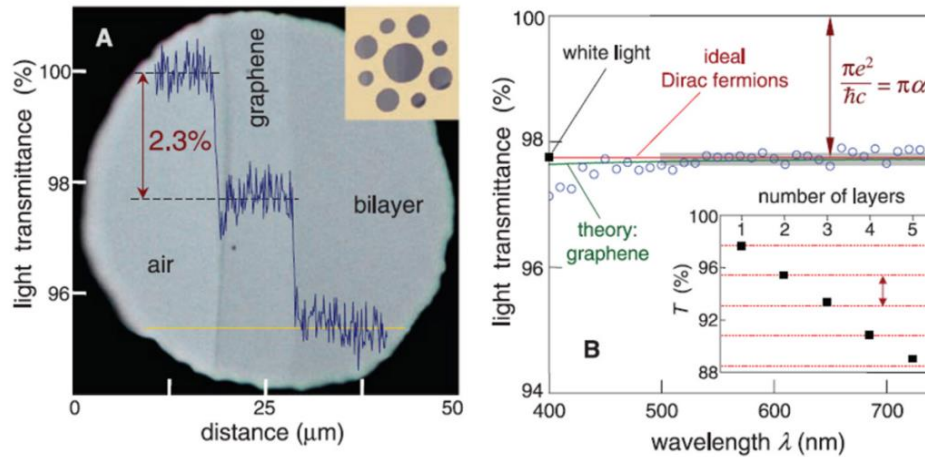


Figure 1.10: Optical properties of graphene. A) Optical image of a 50 μm aperture partially covered by monolayer and bilayer graphene sheets.⁵⁵ B) Transmittance spectrum of single-layer graphene (open circles). (Inset) Transmittance of white light as a function of number of graphene layers (squares).⁵⁵

The study of Nair *et al.* was confirmed by Bae *et al.* in 2010. They produced high quality graphene films via CVD that exhibit optical transmittance of 97.4 % which was decreased by 2.2–2.3 % for an additional layer (fig. 1.11 left).⁵⁶ Hence, the successful determination of the thickness of graphene layers (<10) was achieved by Ni *et al.* by using reflection, contrast and Raman spectroscopies (fig. 1.11 right).⁵⁷

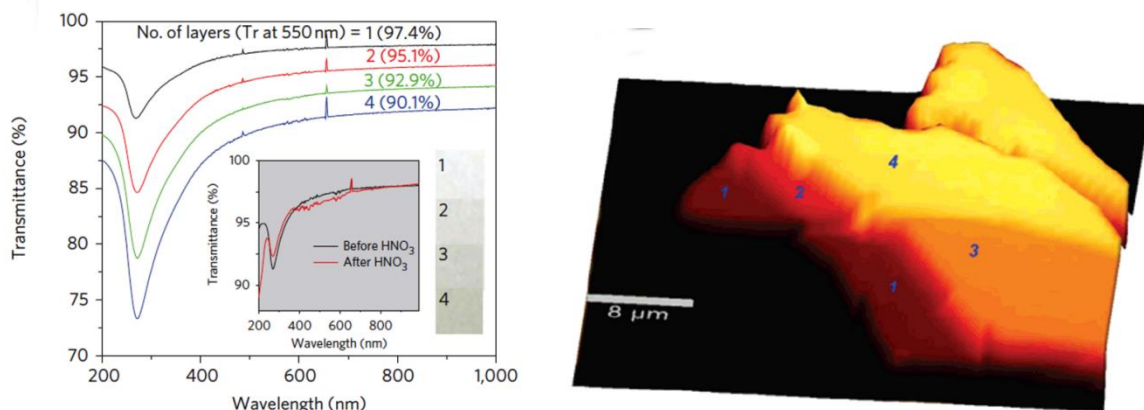


Figure 1.11: Left: UV-Vis spectra of graphene films on quartz substrates.⁵⁶ Right: optical image of graphene with one, two, three, and four layers.⁵⁷

Thermal

Graphene demonstrates high values of thermal conductivity.⁵⁸ Transport properties of phonons (vibrations of the atoms of the lattice) in graphene as energy dispersion and scattering rates, differ significantly from the 3D bulk crystals.⁵⁹ Since graphene exhibits

relatively low carrier density, thermal conductivity mainly derives from phonons based on the Wiedemann–Franz law which correlates electrical and thermal conductivity.^{58,60} There are two phonon categories: acoustic (phonons in which the atoms in each unit cell move in phase) and optical phonons (phonons in which the atoms in the unit cell move out of phase). Acoustic phonons are the main heat carriers in graphene near room temperature, while optical phonons are involved in the Raman scattering process, harnessed in counting the number of atomic planes in samples with few graphene layers.⁵⁹

In 2008, Balandin *et al.* measured the thermal conductivity of a suspended graphene sheet based on the dependence of the shift of the G band of the Raman spectrum on the power of the excitation laser.⁵⁸ As it is illustrated in **fig. 1.12**, a laser light was focused on a suspended graphene sheet which is on the top of a trench of 3 μm length connected with graphitic species acting as heat sinks. The thermal conductivity at room temperature for graphene was calculated in the ranged of 5000 $\text{W}\cdot\text{mK}^{-1}$ which is much higher than the thermal conductivity of the best bulk crystalline thermal conductor, diamond (1000–2200 $\text{W}\cdot\text{mK}^{-1}$) or from an individual SWCNT ($\approx 3500 \text{ W}\cdot\text{mK}^{-1}$).

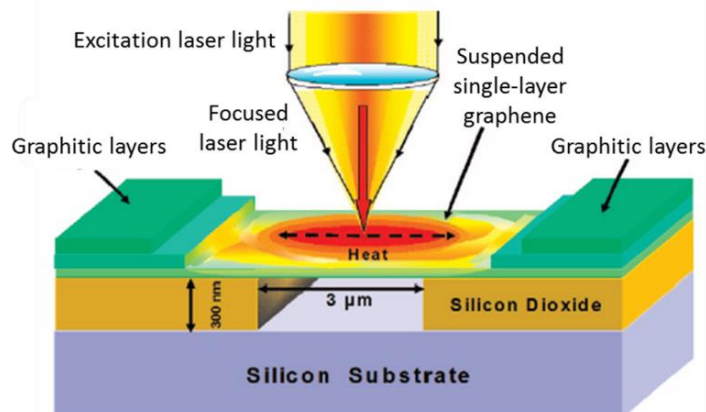


Figure 1.12: Schematic of the experiment showing the laser light focused on the graphene sheet suspended on a trench.⁵⁸

Chemical

Graphene can adsorb atoms or molecules which act as donors or acceptors, monitored by Raman spectroscopy.⁶¹ It can be functionalized by chemical groups, such as -OH, or -F while edges exhibit higher reactivity than surface.⁶² Graphene's theoretical surface area is 2600 $\text{m}^2\cdot\text{g}^{-1}$ while for multilayer materials the value is significantly lower, in the range

of 270 to 1550 m².g⁻¹.⁶¹ This high value of surface area could be exploited for hydrogen storage through its adsorption on graphene either by physisorption (van der Waals interaction), or by chemisorption (formation of a chemical bond with the carbon atoms).⁶³ Furthermore, graphene could be decorated with a range of nanoparticles such as Au, Pt, and Pd. This feature is useful for application in areas of energy conversion devices, catalysis and for optoelectronic devices.

c. Synthesis

Due to the exceptional properties of graphene, its use in a variety of applications such as flexible, transparent electronic devices and high performance electronic devices continuously increases. Therefore, the need to optimize the quality of graphene as well as to reach large scale production is an emerging issue. In this section, the major procedures for the synthesis of graphene are briefly presented. The liquid phase exfoliation, such as using intercalation compounds, graphene oxide or dispersive agents will be described in details in chapter 3 where carbon dispersions will be the main focus. As aforementioned, one of the initial exfoliation efforts of graphite into graphene was via graphite intercalation compounds (GICs).⁶⁴ Graphite oxide was introduced by Brodie, while Boehm produced ultrathin films from GO.²⁸⁻³⁰ However, the first successful exfoliation of graphene was accomplished by Geim and Novoselov in 2004.²⁵ Their method is known as mechanical exfoliation and by using a scotch tape they were removing layers of graphite from HOPG while peeling. This procedure was repeated several times until the final exfoliation of graphene of lateral size up to 20 μm. Their procedure is not the first to report a HOPG cleavage since in 1999 Lu *et al.* developed a controlled way to cleave HOPG and produce few layers samples, but it is the first to exfoliate high quality graphene.⁶⁵ As mentioned previously, their graphene on bulk graphite surface exhibits charge carriers mobility that can exceed 15000 cm².V⁻¹.s⁻¹, which is temperature independent between 10 and 100 K.²⁵ Even though the graphene obtained via mechanical exfoliation is of high quality, it suffers from limitations in mass production, a critical feature for industrial applications. Nevertheless, this synthesis procedure is one of the most widely used methods in fundamental studies. Other cleaving attempts used electrostatic forces (ionic conductivity) to bond bulk graphite onto an insulating substrate with subsequent cleavage⁶⁶ or laser assisted photo-exfoliation.⁶⁷

As a result to the limitations of mechanical exfoliation, alternative synthesis procedures appeared. Chemical vapor deposition uses a metal substrate in the presence of hydrogen and carbon precursor. The metal substrate is heated in the presence of hydrogen, and the carbon precursor (such as gas methane or solid precursor) decomposes (dehydrogenates) on the substrate after coming in contact. Then, during cooling, nucleation of carbon on the substrate occurs. By adjusting temperature and gas pressure, the nuclei density can alter, therefore optimizing CVD procedure. Graphene via CVD has been produced by using different metal substrates such as Pt, Ni and Ir, but the most commonly used substrate is Cu substrate.⁶⁸⁻⁷¹ An interesting study of CVD growth was performed by Bae *et al.* in 2010. 30-inch (ca. 76 cm) graphene films have grown by CVD onto flexible Cu substrate by low pressure and then transferred on (polyethylene terephthalate) PET flexible substrate. They exhibited a mobility of around $7000 \text{ cm}^2 \cdot \text{V}^{-1} \cdot \text{s}^{-1}$.⁵⁶ For graphene to be useful for applications, its transfer onto arbitrary wafers deems necessary.

Another synthesis route of graphene is the thermal decomposition of SiC over $1000 \text{ }^\circ\text{C}$. This epitaxial growth of graphene films depends on the specific polar SiC crystal surface.⁷² Graphene grows faster on the C-face than on the Si-face and has higher mobility. An advantage of this technique is that there is no necessity of transferring to another substrate. The graphene is of high quality but the cost of SiC substrate is high and this technique is not applicable in large scale.

Furthermore, graphene production can be achieved by a chemical synthesis from polycyclic aromatic hydrocarbons (PAHs).⁷³ In 2015, Salvatierra *et al.* produced an insoluble film of graphene at the liquid interface of benzene/water by starting from benzene.⁷⁴

3. Carbon black

Ahead of any attempt to describe CB, due to the plethora of carbon materials with similar characteristics, it is necessary to properly identify it. The first description of CB through X-ray diffraction (XRD) studies were performed in 1934 and 1942 by Warren and Biscoe.^{75,76} They characterized it as a heterogeneous mixture of particles consisting of single graphene layers and graphite crystals made up of several stacked graphene layers. However, CB is not a finely divided graphite because their studies indicated the existence of clusters a few hundred Ångstrom in size.

In 1995, Fitzer *et al.* in IUPAC recommendations defined CB as “*an industrially manufactured colloidal carbon material (a particulate carbon with particle sizes below ca. 1000 nm in at least one dimension) in the form of spheres and of their fused aggregates with sizes below 1000 nm*”.¹⁰ They also note that CB is a commercial material that has a well-defined morphology deriving from thermal decomposition (detonation or by incomplete combustion of carbon hydrogen compounds) while contains the lowest amount of tars or other byproducts. On the other hand, soot is defined as “*a randomly formed particulate carbon material and may be coarse, fine, and/or colloidal in proportions dependent on its origin. It consists of variable quantities of carbonaceous and inorganic solids together with absorbed and occluded tars and resins*”. However, it is common to see the misleading use of CB as a form of soot. Their major differences are the manufacture conditions (carbon black is controlled while soot is randomly formed) and their content of tar, ash and impurities.

a. Atomic structure and morphology

The arrangement of carbon atoms in the CB structure, has been estimated by XRD methods.⁷⁵⁻⁷⁷ As aforementioned, CB is a heterogeneous mixture of particles of graphene up to graphite crystals of turbostratically packed sheets. The inter-plane distance is higher compared to that of graphite (0.335 nm).⁷⁷ It was calculated in the range of 0.350 to 0.365 nm.⁷⁸ Also, from XRD analysis, L_a , which is the average in plane diameter, and L_c , which is the average crystallite thickness, were found to be 1.7 and 1.5 nm respectively which corresponds to a fundamental particle of three to four hexagonal layers.^{77,78} Moreover, the specific gravities of commercial carbon blacks (ratio of the density of a substance to the density of water) have lower values compare to graphite that has 2.26. Particularly, they range between 1.76 to 1.90 based on the grade.⁷⁷

CB building block is a primarily spherical particle. These particles quickly fuse/covalently bonded together in clusters, known as aggregates which can be formed by a few to hundreds of particles depending of the preparation procedure, as depicted in **fig. 1.13**.⁷⁸

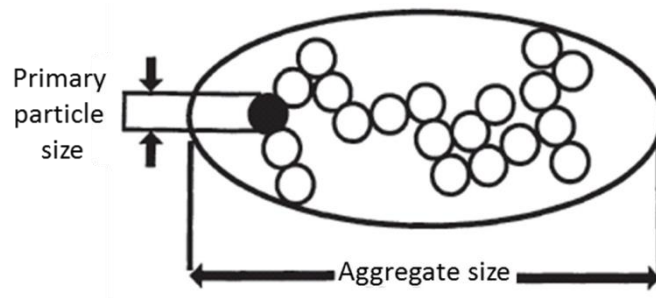


Figure 1.13: CB particle and aggregate size. Adapted from reference ⁷⁸.

A proposed definition for a CB particle and aggregate are: “CB particle is a small spheroidally shaped, paracrystalline (having short and medium range ordering in their lattice but lacking long-range ordering at least in one direction), non-discrete component of an aggregate. It is separable from the aggregate only by fracturing”.⁷⁹ “CB aggregate is a discrete, rigid colloidal entity that is the smallest dispersible unit; it is composed of extensively coalesced particles”.⁷⁹

Sometimes, the term agglomerate is used instead of aggregate. An agglomerate consists of many aggregates that are physically held together while an aggregate composed of fused spherical particles with continuous graphitic structure.⁷⁹ CB performance is strongly affected by the characteristics of both the particles and the aggregates.⁷⁸

b. Parameters influencing properties

The size of the primary particles is defined as its diameter and implies the thickness of the chain.⁸⁰ Typical furnace blacks (the most widely produced type of CB) are composed of spherical particles ranging in diameter from 10 to 100 nm and in surface area from 25 to 1500 m².g⁻¹. Since the unit of surface area is square meters per unit weight, the smaller the particles are, the larger the surface area is. Other parameters that affect the surface area are structure and porosity. Surface area influences the UV absorption, conductivity and jetness (intensity of the black color) of CB.⁷⁸ When the surface area is higher, the jetness and UV resistance are increased, since there is more available surface for the absorption of visible and UV light. Another important property of CB, except from its particle size and surface area, is its structure. CB structure can be defined from the amount of particles per aggregate as well as aggregate’s size and shape. For instance, CB that is composed of few primary particles forming a compact unit is considered as of a low structure while CB which has particles that form aggregates with significant branching and chaining is considered as high a structure CB.⁷⁸

Furthermore, the properties of CB are highly governed by its surface chemistry. Apart from the carbon element, there are more elements that can be found in CB. For instance, since CB is manufactured from hydrocarbons, hydrogen saturates the dangling bonds at the edges of the carbon sheets. Elements other than hydrogen exist also in CB. Sulfur and nitrogen derive from the oil precursor. However, the most important element that could also come from CB formation or storage is oxygen.⁸¹ All CB have a level of chemisorbed oxygen complexes on their surface such as carboxylic, quinonic (double carbonyl), phenolic (with hydrogen group) or lactonic groups as illustrated in **fig. 1.14**.⁸¹ The oxygen is chemisorbed on heating CB in air.

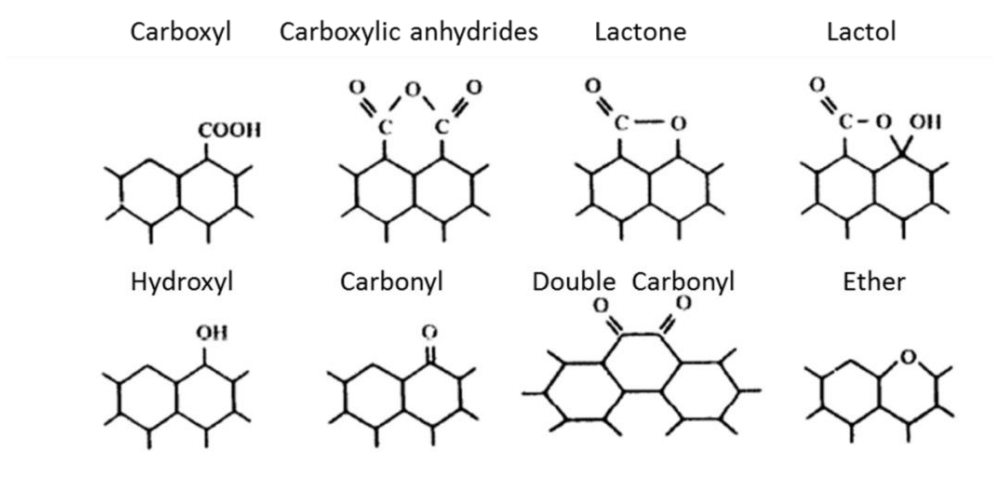


Figure 1.14: Oxygen complexes on the CB surface. Adapted from reference ⁸¹.

The surface oxides have a noticeable effect on the surface properties of CB. For instance, the oxygen presence on CB surface is responsible for the pH values. As the volatile content increases, the pH decreases. This feature is exploited for specific applications. CB could increase the volatile content by oxidation. As the volatile content increases, the aggregates become more and more insulated resulting in an increased difficulty of electron transfer, crucial for applications that require dielectric properties.⁷⁸ Furthermore, a reaction with free organic radicals can be used for the grafting of functional molecules or polymers onto the surface.⁸¹ Eventually, in order to choose a CB with specific properties, apart from its surface area, particle size, structure and surface chemistry, its content in ash and byproducts is equally determinant. CB grades with small amounts of ash and other impurities known as “grit” are available for plastics application. This CB with low levels of byproducts is easier to disperse and gives superior mechanical properties.⁷⁸

c. Production

CB can be manufactured via incomplete combustion or thermal decomposition of hydrocarbons based on the presence or absence of oxygen.⁷⁹ Incomplete combustion, also known as thermal-oxidative decomposition, plays the major role regarding the CB production in terms of quantity. The thermal-oxidative decomposition could be divided in two types: decomposition in a turbulent flow or via diffusion flames. Turbulent flow is a closed system process while diffusion flames procedure is an open system. Closed system process is superior since the components can be introduced in a controlled way and CB loss is minimized avoiding unwelcome pollution to the surroundings. The production processes are further divided into categories as presented in **table 1.1**. Moreover, the feedstock for each production method is different resulting in a plethora of CB grades (**table 1.1**).

Table 1.1: Classification of production processes and feedstocks.⁷⁹

	Production process	Feedstock
Thermal-oxidative decomposition		
Closed system (turbulent flow)	Furnace black process	Aromatic oils based on coal tar or crude oil, natural gas
Closed system (turbulent flow)	Lampblack process	Aromatic oils based on coal tar or crude oil
Open system (diffusion flames)	Channel black process	Natural gas
Thermal decomposition		
	Thermal black process	Natural gas
	Acetylene black	Acetylene
Future technology		
External electric energy supply	Plasma process	Biogas

From all the aforementioned, the most common procedure belongs to the thermal-oxidative decomposition process and it is the furnace black process and more specifically the furnace process that uses aromatic oils as feedstock, through which over 98 % of CB is produced. Via this process, the control of CB chemical and physical properties, such as particle size or structure is feasible. The oil furnace method produces CB in fluffy or low-density powder form. Therefore, the conversion to pellets for easier manipulation is often performed.⁷⁸ Moreover, it is the most commonly used method for the production of CB for various applications from rubber reinforcement to coloring.

Regarding the other production processes, the oldest process is lampblack. In this method, CB of particle size of 100 to 200 nm, is produced by collecting soot from fumes of burning oils or pinewood. It is not used for mass production but due to the precise color of the resulting CB, it is proper for ink sticks.^{82,83} Channel black is another process that belongs to thermal –oxidative decomposition. In this procedure, CB is obtained by contacting, partially combusted natural gas with channel steel (H-shaped steel). Due to the low yield and the environmental issues that arise from this process, it is not suitable for mass production. Nevertheless, some painting applications harness this CB due to the functional groups on its surface result of this process. As for the CB that is produced via thermal decomposition, it consists of thermal black and acetylene processes, as presented in **table 1.1**. In the thermal black process, CB is obtained from the oxygen-free decomposition of natural gas. The resulting material is of large particle size up to 500 nm and low surface area.⁸² In acetylene black process, CB is produced by thermal decomposition of acetylene gas. It is similar to lampblack but more advanced regarding purity, liquid-absorption capacity and electrical conductivity.⁸² Therefore, it is used in applications such as fillers in rubbers, plastics, and for electric conductive agents.

The research that currently evolves regarding alternative synthetic routes in order to produce CB is noteworthy. Since furnace process provides poor carbon yields and is characterized by high levels of atmospheric emission, there is plenty of space for alternative preparation procedures which will eliminate those drawbacks. Plasma technology is a possible future solution (**table 1.1**). The innovation of this process is based on the total replacement of thermal oxidative decomposition, also known as incomplete combustion from splitting the hydrocarbon into CB and hydrogen by utilizing an external electric energy supply.⁸⁴ This process has many advantages: total conversion of the precursor, pure hydrogen as a byproduct as well as new CB grades

since specific enthalpies and temperatures can be reached which with the conventional procedure were not feasible.

d. Industrial designations

Over the years different commercial designations were used to distinguish the CB grades. The dominating designation system is developed by the American Society for Testing and Materials (ASTM). This system, originally adopted in 1966, is primarily for rubber-grade CB. It consists of a letter followed by a three numbers. Therefore, the letter N signifies normal cure of a rubber compound. The first number stands for the CB group which is defined based on the average primary particle size as measured by electron microscopy.⁸⁵ The particle range size of CB is arbitrarily divided into 10 groups. The third and fourth characters are assigned arbitrarily.⁸⁵ For example, high-abrasion furnace black has ASTM number N330. In rubber industry more than 40 grades of carbon black are currently used. Moreover, CB grades are used in the paint, plastics, ink and other industries.

e. Applications

Carbon black (CB) is considered a vital economical filler in rubber market as a reinforcing agent.^{77,79} By introducing CB in a matrix several features are optimized: tensile strength, resistance against abrasion and corrosion are some of them. Since 20-40 % of rubber composite is CB, the global use of CB is mostly in the rubber industry.

Special CB grades with specific characteristics are used in other areas apart from the rubber industry such as in plastics, printing inks or in papers. These CB grades are usually more expensive than those used in the rubber market, since certain requirements are needed.⁷⁷

These requirements could be color, protection from UV radiation, mechanical reinforcement and conductivity. For instance, CB has lower electrical resistance than plastics. CB structure and the size of its particles and aggregates affect its conductivity. Highly structured CB, with many primary particles and significant branching and chaining could create more potential electron paths when it is incorporated into a matrix. Moreover, small sized particles and aggregates mean that more aggregates exist per unit of weight in the volume of the composite. As a consequence, the electron transfer is easier since the aggregates are closer. By oxidizing the surface, the resistance increases, therefore for applications where the conductivity is important, low volatile

levels are required. Conductive CB can be used in applications like in electronic packaging, hospital equipment that require anti-static properties, semi-conductive shielding for power cable, electromagnetic interference (EMI) shielding where maximum conductivity is important or as sensors.⁷⁸ The loading level of CB is also noteworthy. Usually, as the CB amount is higher in a composite, higher conductivity values are reached. Furthermore, CB is used in a variety of other materials such as in tubes, wires, belts, coated fabrics, gloves, footwear, tape and toys.⁸⁶

4. Carbon nanopucks

Before graphene, fullerenes and carbon nanotubes have been discovered. However, fullerenes have found barely any practical applications and even though carbon nanotubes had better course, their production is still costly and difficult to be controlled. On the other hand, graphene is the thinnest, strongest and stiffest material known. The number of publications for research on graphene and investments to commercialize it continuously increases.⁸⁷ Moreover, carbon black is a commercial material that has a well-defined morphology. In this study, the graphitic material that is used could be considered intermediate between the most promising carbon allotrope, graphene, and the carbon form with similar morphology, carbon black.

For this graphitic material, due to its disk shape (aspect ratio ~17), the nomenclature that was chosen in order to be disclosed the size, shape and nature of the material is carbon nanopuck (CNP), owing to its resemblance with an ice hockey puck, as illustrated in **fig. 1.15**. A detailed characterization of CNP will be presented in the following chapter.

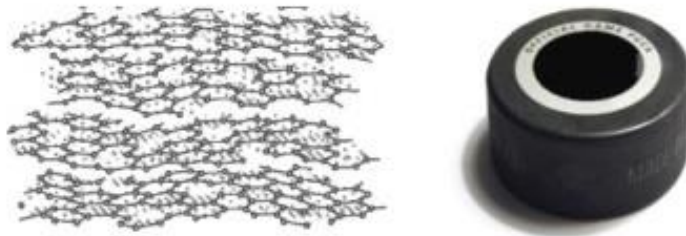


Figure 1.15: Shape resemblance of CNP (left) and a hockey puck (right).

CNP was provided within the framework of the European program PlasCarb,¹ which aims to transform biogas that derives from food waste into renewable hydrogen and high value graphitic carbon. In the manuscript, this carbon is referred as CNP, however, its PlasCarb name is Renewable PlasCarbon (RPC).

The split of the biogas (methane/carbon dioxide mix) is achieved by using an innovative low energy microwave plasma process. This process comprises microwave induced plasma to cleave methane into CNP and hydrogen with limited carbon dioxide emissions.¹ It is used 'cold' plasma (plasma which is not in a thermodynamic equilibrium) induced by microwave energy from magnetrons (electron tubes that produces coherent microwave radiation). Energy is transferred directly into the electron bonds in gas molecules by the aid of microwaves. The 'cold' plasma is not as sensitive as thermal plasma to thermal processes and its temperature because ionization and chemical processes are directly determined by electron temperatures. Therefore, milder process conditions, reduced process complexity and energy efficiency can be acquired. The novelty of this process is the generation of large, homogeneous 'cold' plasma zones for methane cracking at atmospheric pressure. The methane/carbon dioxide mix used as feedstock, had varied contents of carbon dioxide. As a reference case, pure methane was used. As it will be demonstrated in chapter 2, the concentration of carbon dioxide in the gas mixture has a direct impact on the quality and yield of the resulting CNP.

5. Plascarb project

PlasCarb, a three year collaborative project under the Seventh Framework Program (FP7) of the EU, transforms food-waste, from a catchment area of 35 miles, into biogas and upgrades it to bio-methane. From this, an innovative low-energy microwave plasma reactor generates renewable PlasCarbon (RPC) and renewable hydrogen (RH₂). The entire process flow is encompassed by life cycle analysis (LCA) which analyses that the approach is sustainable and taken beyond Best Available Technology. The quality and economic value of the RPC and RH₂ are currently being optimized using high quality research and industrial process engineering.

PlasCarb has the potential to generate RH₂, even though at low mass flow rate and currently at long payback. The ability to sustainably produce this element has added economic value, as nearly 96% of hydrogen is produced from fossil fuels. Predicted global demand in 2020 is 324 million m³ worth 125 billion €. Hydrogen is used in

significant quantities by industry, applications ranging from ammonia production to petroleum refining and electronics. Hydrogen is increasingly recognized as a potential future transport fuel for a low carbon economy, including use in the emerging fuel cell technology.

Renewable PlasCarbon (RPC) is a product generated by the PlasCarb technology which has been proved to be highly promising for industrial applications and as a sustainable alternative to market-available carbon products from fossil origin.^{2,88} The world graphite market is forecasted to grow at a Compound Annual Growth Rate (CAGR) of 3.7% from 2014 till 2020. PlasCarb offers a sustainable contribution to this growing demand by producing RPC from food waste. Potential applications include but are not limited to:

- Conductive inks for 2D and 3D printing, printable electronics
- Composites in rubber, plastic, etc.
- Electrodes, batteries, supercapacitors
- Photoluminescence, as a catalyst
- Opportunities within Fuel cells.

The corresponding Plascarb flow chart is presented in **fig. 1.16**.

PLASCARB

THE PROCESS

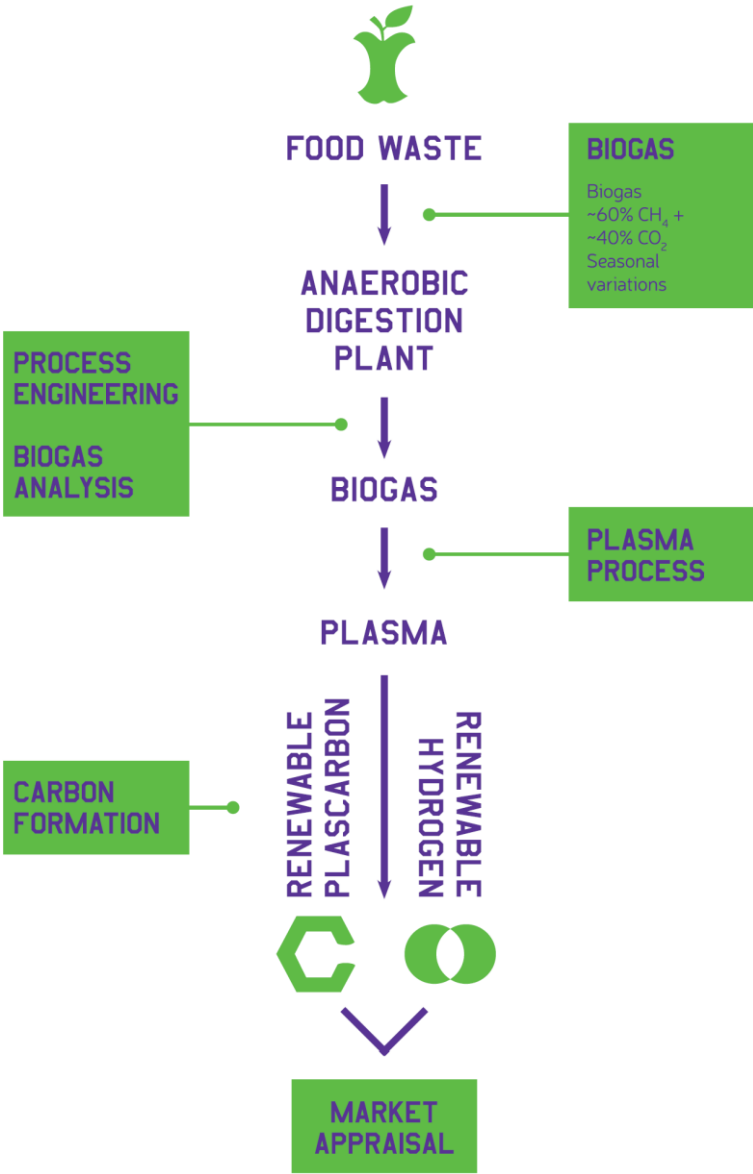


Figure 1.16: The PlasCarb flow chart.

Our participation (along with Dr Kai Huang and Dr Ferdinand Hof) under the supervision of Dr Alain Pénicaud, in this project, is the optimization, characterization and use of this carbon in a variety of applications.

Carbon output from the microwave plasma process (RPC or CNP) is analyzed systematically by the CRPP group using a full range of analytical techniques, e.g. thermogravimetric analysis (TGA), scanning and transmission electron microscopy (SEM and TEM) and Raman spectroscopy in order to assess the carbon content, form, sizes and shapes and respective yields. Furthermore, its dispersion and dissolution in liquid media is performed as well as its use in a variety of applications.



Figure 1.17: PlasCarb team.

Conclusion

In this chapter the background of carbon was presented. Graphene and carbon black (CB) were the two carbon materials that were further elucidated. Graphene's structure, properties and synthesis routes were described. CB definition, production paths, commercial designations and applications were given. Eventually, the carbon material that was actually utilized in this study, CNP and its preparation procedure are introduced. Graphene attracts the interest of the scientific and industrial community owing to its unique structure and mechanical, electrical, thermal and optical properties.²⁵ On the other side, CB is a colloidal carbon in the form of particles and aggregates. CB is a low density, heterogeneous mixture of particles of graphene up to graphite crystals of turbostratically packed sheets with an average fundamental particle of three to four hexagonal layers.^{77,78} It is an industrial product, more commonly produced via incomplete combustion of crude oil (petroleum). Both of these carbon forms have certain drawbacks. Regarding graphene, it still has limitations concerning its large scale production while its cost remains relatively high. In contrast, CB is cost-

Chapter 1 – Carbon

effective and is already an industrial product. However, its synthetic processes are not environmentally friendly while CB cannot compete the high quality, performance and properties of graphene. Therefore, the necessity of a material that will be the right balance between graphene and CB is required. As it will be demonstrated in this manuscript, CNP could be a promising solution.

References

1. PlasCarb. Available at: <http://www.plascarb.eu/>.
2. Hof, F. *et al.* Conductive inks of graphitic nanoparticles from a sustainable carbon feedstock. *Carbon N. Y.* **111**, 142–149 (2017).
3. Greenwood, N. & Earnshaw, A. *Chemistry of the elements*. (Butterworth-Heinemann, 1997).
4. Robertson, J. Diamond-like amorphous carbon. *Mater. Sci. Eng. R Reports* **37**, 129–281 (2002).
5. Dresselhaus, M. S., Dresselhaus G. & Eklund P.C. *Science of Fullerenes and Carbon Nanotubes: Their Properties and Applications - M. S. Dresselhaus, G. Dresselhaus, P. C. Eklund*, Elsevier Science, USA (1996).
6. Eremets, M. I. *et al.* The strength of diamond. *Appl. Phys. Lett.* **87**, 141902 (2005).
7. Chambers, C. & Hollyday, A. . *Modern inorganic chemistry | Chambers C., Hollyday A.K.* (1975).
8. Oganov, A. R., Hemley, R. J., Hazen, R. M. & Jones, A. P. Structure, Bonding, and Mineralogy of Carbon at Extreme Conditions. *Rev. Mineral. Geochemistry* **75**, 47–77 (2013).
9. Liang, D., Stolt, M. J. & Jin, S. Metastable skyrmions: Beat the heat. *Nat. Phys.* **12**, 25–26 (2016).
10. Fitzer, E., Kochling, K.-H., Boehm, H. P. & Marsh, H. Recommended terminology for the description of carbon as a solid (IUPAC Recommendations 1995). *Pure Appl. Chem.* **67**, 473–506 (1995).
11. Wick, P. *et al.* Classification Framework for Graphene-Based Materials. *Angew. Chemie Int. Ed.* **53**, 7714–7718 (2014).
12. A. L. Lavoisier. *Oeuvres: Traité élémentaire de chimie*. (Imprimerie impériale, 1864).
13. *Porosity in Carbons: Characterization and Applications*. Patrick, J. W., Arnold E. Wiley (1995).
14. Evans, J. W. V.- The meanings and synonyms of plumbago. *Trans. Philol. Soc.* **26**, 133–179 (1908).
15. Dreyer, D. R., Ruoff, R. S. & Bielawski, C. W. From Conception to Realization: An Historical Account of Graphene and Some Perspectives for Its Future. *Angew. Chemie Int. Ed.* **49**, 9336–9344 (2010).
16. Kroto, H. W., Heath, J. R., O'Brien, S. C., Curl, R. F. & Smalley, R. E. C60: Buckminsterfullerene. *Nature* **318**, 162–163 (1985).
17. David, W. I. F. *et al.* Crystal structure and bonding of ordered C60. *Nature* **353**, 147–149 (1991).
18. Osawa, E., Kagaku. Superaromaticity. **25**, 854–863 (1970).
19. Osawa, E., Kroto, H. W., Fowler, P. W. & Wasserman, E. The Evolution of the Football Structure for the CFormula Molecule: A Retrospective [and Discussion].

- Philos. Trans. R. Soc. A Math. Phys. Eng. Sci.* **343**, 1–8 (1993).
20. Boyd, D. B. & Slanina, Z. Introduction and foreword to the special issue commemorating the thirtieth anniversary of Eiji Osawa's C60 paper. *Journal of Molecular Graphics and Modelling* **19**, 181–184 (2001).
 21. Iijima, S. Helical microtubules of graphitic carbon. *Nature* **354**, 56–58 (1991).
 22. Monthieux, M. & Kuznetsov, V. L. Who should be given the credit for the discovery of carbon nanotubes? *Carbon* **44**, 1621–1623 (2006).
 23. Iijima, S. & Ichihashi, T. Single-shell carbon nanotubes of 1-nm diameter. *Nature* **363**, 603–605 (1993).
 24. Bethune, D. S. *et al.* Cobalt-catalysed growth of carbon nanotubes with single-atomic-layer walls. *Nature* **363**, 605–607 (1993).
 25. Novoselov, K. S. *et al.* Two-dimensional gas of massless Dirac fermions in graphene. *Nature* **438**, 197–200 (2005).
 26. Geim, A. K. & Novoselov, K. S. The rise of graphene. *Nat. Mater.* **6**, 183–191 (2007).
 27. Wallace, P. R. The Band Theory of Graphite. *Phys. Rev.* **71**, 622–634 (1947).
 28. Brodie, B. C. On the Atomic Weight of Graphite : Brodie, B. C. *Philos. Trans. R. Soc. London* **149**, 12 (1859).
 29. Mrozowski, S., Studebaker, M. L. & Walker, P. L. *Proceedings of the Fifth Conference on Carbon - S. Mrozowski - Google Books.* (1962).
 30. Liu, Z. (Chemist) & Zhou, X. *Graphene : energy storage and conversion applications.* Zhang, J., Canada (2014).
 31. Boehm, H. P., Setton, R. & Stumpp, E. Nomenclature and terminology of graphite intercalation compounds. *Carbon N. Y.* **24**, 241–245 (1986).
 32. Boehm, H. P., Setton, R. & Stumpp, E. Nomenclature and terminology of graphite intercalation compounds (IUPAC Recommendations 1994). *Pure Appl. Chem.* **66**, 1893–1901 (1994).
 33. Warner, J. H., Schaffel, F., Rummeli, M. & Bachmatiuk, A. *Graphene: Fundamentals and emergent applications.* Elsevier, UK, (2013).
 34. Claire Berger, † *et al.* Ultrathin Epitaxial Graphite: 2D Electron Gas Properties and a Route toward Graphene-based Nanoelectronics. *J. Phys. Chem.* **108**, 19912–19916 (2004).
 35. Castro Neto, A. H., Guinea, F., Peres, N. M. R., Novoselov, K. S. & Geim, A. K. The electronic properties of graphene. *Rev. Mod. Phys.* **81**, 109–162 (2009).
 36. Das Sarma, S., Adam, S., Hwang, E. H. & Rossi, E. Electronic transport in two-dimensional graphene. *Rev. Mod. Phys.* **83**, 407–470 (2011).
 37. Malard, L. M., Pimenta, M. A., Dresselhaus, G. & Dresselhaus, M. S. Raman spectroscopy in graphene. *Phys. Rep.* **473**, 51–87 (2009).
 38. Novoselov, K. S. *et al.* Electric field effect in atomically thin carbon films. *Science* **306**, 666–9 (2004).
 39. IUPAC, 2006. *IUPAC goldbook.* (2006).
 40. Bianco, A. *et al.* All in the graphene family – A recommended nomenclature for

- two-dimensional carbon materials. *Carbon* **65**, 1–6 (2013).
41. Meyer, J. C. *et al.* The structure of suspended graphene sheets. *Nature* **446**, 60–63 (2007).
 42. Nakada, K., Fujita, M., Dresselhaus, G. & Dresselhaus, M. S. Edge state in graphene ribbons: Nanometer size effect and edge shape dependence. *Phys. Rev. B* **54**, 17954–17961 (1996).
 43. Girit, C. O. *et al.* Graphene at the edge: stability and dynamics. *Science* **323**, 1705–8 (2009).
 44. Latil, S. & Henrard, L. Charge Carriers in Few-Layer Graphene Films. *Phys. Rev. Lett.* **97**, 36803 (2006).
 45. Kolmogorov, A. N. & Crespi, V. H. Registry-dependent interlayer potential for graphitic systems. *Phys. Rev. B* **71**, 235415 (2005).
 46. Lee, C., Wei, X., Kysar, J. W. & Hone, J. Measurement of the elastic properties and intrinsic strength of monolayer graphene. *Science* **321**, 385–8 (2008).
 47. Chen, H., Müller, M. B., Gilmore, K. J., Wallace, G. G. & Li, D. Mechanically Strong, Electrically Conductive, and Biocompatible Graphene Paper. *Adv. Mater.* **20**, 3557–3561 (2008).
 48. Gómez-Navarro, C., Burghard, M. & Kern, K. Elastic Properties of Chemically Derived Single Graphene Sheets. *Nano Lett.* **8**, 2045–2049 (2008).
 49. Katsnelson, M. I. *Graphene: Carbon in Two Dimensions*. Cambridge University Press, (2012).
 50. Bolotin, K. I. *et al.* Ultrahigh electron mobility in suspended graphene. *Solid State Communications* **146**, (2008).
 51. Geim, A. K. Graphene: status and prospects. *Science* **324**, 1530–4 (2009).
 52. Novoselov, K. S. *et al.* Two-dimensional atomic crystals. *Proc. Natl. Acad. Sci.* **102**, 10451–10453 (2005).
 53. Kim, K. S. *et al.* Large-scale pattern growth of graphene films for stretchable transparent electrodes. *Nature* **457**, 706–710 (2009).
 54. Kuzmenko, A. B., van Heumen, E., Carbone, F. & van der Marel, D. Universal Optical Conductance of Graphite. *Phys. Rev. Lett.* **100**, 117401 (2008).
 55. Nair, R. R. *et al.* Fine structure constant defines visual transparency of graphene. *Science* **320**, 1308 (2008).
 56. Bae, S. *et al.* Roll-to-roll production of 30-inch graphene films for transparent electrodes. *Nat. Nanotechnol.* **5**, 574–578 (2010).
 57. Ni, Z. H. *et al.* Graphene Thickness Determination Using Reflection and Contrast Spectroscopy. *Nano Lett.* **7**, 2758–2763 (2007).
 58. Balandin, A. A. *et al.* Superior Thermal Conductivity of Single-Layer Graphene. *Nano Lett.* **8**, 902–907 (2008).
 59. Nika, D. L. *et al.* Two-dimensional phonon transport in graphene. *J. Phys. Condens. Matter* **24**, 233203 (2012).
 60. Vlasiouk, I. *et al.* Electrical and thermal conductivity of low temperature CVD

- graphene: the effect of disorder. *Nanotechnology* **22**, 275716 (2011).
61. Rao, C. N. R., Sood, A. K., Voggu, R. & Subrahmanyam, K. S. Some Novel Attributes of Graphene. *J. Phys. Chem. Lett.* **1**, 572–580 (2010).
 62. Wu, Q. *et al.* Selective surface functionalization at regions of high local curvature in graphene. *Chem. Commun.* **49**, 677–679 (2013).
 63. Tozzini, V. & Pellegrini, V. Prospects for hydrogen storage in graphene. (2012).
 64. Schafhaeutl, C. *LXXXVI. On the combinations of carbon with silicon and iron, and other metals, forming the different species of cast iron, steel, and malleable iron.* *Philos. Mag. Ser. 3* **16**, 570–590 (1840).
 65. Lu, X. *et al.* Tailoring graphite with the goal of achieving single sheets. *Nanotechnology* **10**, 269–272 (1999).
 66. Shukla, A., Kumar, R., Mazher, J. & Balan, A. Graphene made easy: high quality, large-area samples. **149**, 718–721 (2009).
 67. Lenner, M., Kaplan, A., Huchon, C. & Palmer, R. E. Ultrafast laser ablation of graphite. *Phys. Rev. B* **79**, 184105 (2009).
 68. Rutter, G. M. *et al.* Imaging the interface of epitaxial graphene with silicon carbide via scanning tunneling microscopy. *Phys. Rev. B* **76**, 235416 (2007).
 69. N'Diaye, A. T. *et al.* Structure of epitaxial graphene on Ir(111). *New J. Phys.* **10**, 43033 (2008).
 70. Li, X. *et al.* Large-area synthesis of high-quality and uniform graphene films on copper foils. *Science* **324**, 1312–4 (2009).
 71. Lahiri, J. *et al.* Graphene growth and stability at nickel surfaces. *New J. Phys.* **13**, 25001 (2011).
 72. de Heer, W. A. *et al.* Large area and structured epitaxial graphene produced by confinement controlled sublimation of silicon carbide. *Proc. Natl. Acad. Sci.* **108**, 16900–16905 (2011).
 73. Dössel, L., Gherghel, L., Feng, X. & Müllen, K. Graphene Nanoribbons by Chemists: Nanometer-Sized, Soluble, and Defect-Free. *Angew. Chemie Int. Ed.* **50**, 2540–2543 (2011).
 74. Salvatierra, R. V., Souza, V. H. R., Matos, C. F., Oliveira, M. M. & Zarbin, A. J. G. Graphene chemically synthesized from benzene at liquid–liquid interfaces. *Carbon N. Y.* **93**, 924–932 (2015).
 75. Warren, B. E. X-Ray Diffraction Study of Carbon Black. *J. Chem. Phys.* **2**, 551 (1934).
 76. Biscoe, J. & Warren, B. E. An X-Ray Study of Carbon Black. *J. Appl. Phys.* **13**, 364 (1942).
 77. Kirk-Othmer. *Encyclopedia of Chemical Technology.* (2004).
 78. Accorsi, J. & Yu, M. *Carbon Black.* 153–161, Springer Netherlands, (1998).
 79. Donnet, J.-B., Bansal, R. C. & Wang, M.-J. *Carbon black: science and technology.* (Dekker, 1993).
 80. Papirer, E., Lacroix, R., Donnet, J.-B., Nanse, G. & Fioux, P. XPS Study of the halogenation of carbon black-part 1. Bromination. *Carbon* **32**, 1341–1358 (1994).

81. Boehm, H. P. Some aspects of the surface chemistry of carbon blacks and other carbons. *Carbon* **32**, 759–769 (1994).
82. Pierson, H. O. *Handbook of carbon, graphite, diamond, and fullerenes: properties, processing, and applications*. (Noyes Publications, 1993).
83. Mitsubishi Chemical. Manufacturing Process of Carbon Black. (2006). Available at: <http://www.carbonblack.jp/en/cb/seizou.html>.
84. Fulcheri, L. *et al.* Plasma processing: a step towards the production of new grades of carbon black. *Carbon* **40**, 169–176 (2002).
85. ASTM International. *Standard Classification System for Carbon Blacks Used in Rubber Products*. (American Society for Testing and Materials., 2005).
86. Auchter, J. *Chemical Economics Handbook: Carbon Black*. (Menlo Park, CA, SRI Consulting, 2005).
87. Van Noorden, R. Chemistry: The trials of new carbon. *Nature* **469**, 14–16 (2011).
88. Oguz Tezel, A., Fotedar, S., Kampioti, K., Wendelbo Tezel, R. & -, W. *Test Report: Application of Renewable PlasCarbon in Batteries*. (2016).

Chapter 2

Characterization of carbon nanopucks

Table of contents

Chapter 2	55
Characterization of carbon nanopucks	55
Introduction.....	57
1. Experimental section.....	58
a. Carbon nanopucks synthesis	58
b. Carbon nanopucks purification	58
c. Characterization of carbon nanopucks	58
d. Formulation of the dispersion.....	60
2. Results	61
a. Characterization of carbon nanopucks	61
Thermogravimetric analysis and purification	61
X-ray diffraction.....	62
Raman spectroscopy	65
X-ray photoelectron spectroscopy	68
Infrared spectroscopy	72
BET.....	73
b. Dispersion of the purified carbon nanopucks.....	74
UV/Vis absorption spectroscopy	74
Atomic force microscopy.....	75
Scanning tunneling microscopy	80
Transmission electron microscopy.....	81
3. Discussion.....	83
Conclusion	85
References.....	86

Introduction

Graphene and carbon black (CB) are two carbon forms presented in the previous such that carbon nanopucks (CNPs) can be considered intermediate between them. The interest in graphene has grown in the last years, after its successful exfoliation and the report of its interesting properties.¹⁻⁴ However, graphene's large-scale production is still a costly process. In contrast, CB is a crucial industrial product. Distinct CB grades have specific characteristics for different requirements and applications.⁵⁻⁸ Its drawbacks, though, are the feedstock (petroleum) and synthesis route which are not environmentally friendly. Another disadvantage is CB inhomogeneity, not only in the sp^2 to sp^3 ratio but also concerning the heteroatom content.⁹⁻¹¹ Therefore, the research of alternative preparation procedures and substitution of petroleum precursors has led to plasma technology as a possible solution.¹²⁻¹⁵

CNP is the material which this study was built on. It is principally generated by mixture of methane/carbon dioxide (CO_2) split into hydrogen and graphitic nanocarbon via 'cold' microwave plasma process. The ultimate step of this project is the substitution of the feed gas by biogas actually deriving from food waste.¹⁶ The content of CO_2 in the feedstock in CO_2 significantly influences the quality and yield of the final product. Hence, its detailed characterization was systematically carried out and is presented in this chapter. Several techniques were utilized, e.g. Raman spectroscopy, thermogravimetric analysis (TGA), X-ray diffraction (XRD) and X-ray photoelectron spectroscopy (XPS).

1. Experimental section

a. Carbon nanopucks synthesis

CNP samples have been produced via microwave plasma process using a mixture of methane/carbon dioxide as precursor by FGV Cambridge Nanosystems, United Kingdom.¹⁷ In this process the power supply and the flux of the feedstock in the plasma reactor were kept constant, 6 kW and 21.4 L.min⁻¹ respectively. After reaction time of 30 min the carbon powders were collected. The amount of CO₂ (from 0.0 vol % to 7.4 vol%) in the feed gas and the yield of five carbon solid products are illustrated in **table 2.1**.

Table 2.1: Production parameters of five carbon samples generated from the cleave of methane/CO₂. The content of CO₂ in the feed gas mixture varies the final product yield and results in different carbon samples.

Unpurified CNP Conditions	CNP ₀	CNP ₁	CNP ₂	CNP ₃	CNP ₄
CO ₂ (vol %)	0.0	0.4	1.7	4.9	7.4
Yield of carbon (g)	120	40.8	33.9	22.1	8.9

b. Carbon nanopucks purification

The purification of CNP was achieved by heat treatment in a Nabertherm oven. The parameters were adjusted based on the data provided from thermogravimetric analysis (TGA). Particularly, the carbon samples were heated with a heating slope of 5 °C.min⁻¹ until 500 °C. After 6h plateau at 500 °C, the temperature was decreased with the same slope (5 °C.min⁻¹) until 30 °C. For simplicity, when the samples are not purified, they will be referred as CNP_x and the heat treated corresponding samples with the designations CNP_{HTX} (where x is from 0 to 4 respectively).

c. Characterization of carbon nanopucks

The structural characterization of CNPs and the description of the properties of CNPs were accomplished with a series of techniques described below.

Raman analysis was carried out by Dr Ferdinand Hof to assess the samples' structure. It was performed in a Horiba JobinYvonXplora microscope equipped with a cooled Andor CCD detector.

The parameters of the present analysis are an Olympus objective 50x LWD, ~1 μm laser spot size with excitation wavelength 532 nm, grating 1200 lines per mm and SiO_2 calibration. As regards the Raman mappings, a motorized x-y μm scanning table was utilized and around 2000 individual spectra per sample were taken.

X-ray diffractograms (XRD) were acquired with a PANalytical X'pert MPD-PRO Bragg-Brentano θ - θ geometry diffractometer equipped with a secondary monochromator over an angular range of $2\theta = 8$ - 80° at room temperature. The Cu-K α radiation ($\lambda = 0.15418$ nm) was generated at 45 KV and 40 mA. The samples were placed on a silicon wafer ("zero background") sample holder and flattened with a piece of glass. Each acquisition lasted for 2 h and 5 min.

Thermogravimetric analysis (TGA) was performed to evaluate the thermal properties of CNPs before purification treatment. The measurements were conducted on a Setaram instrument equipped with a 2 balance setup for equilibration under air atmosphere. Samples of around 10 mg were placed on a Pt-crucible.

Atomic force microscope (AFM) imaging was carried out by Dr Kai Huang. It was performed in ambient conditions using a Nanoscope III microscope in tapping mode using 8 nm radius tips MPP-111000.

Scanning tunneling microscopy (STM) images were recorded by Dr Kai Huang. The characterization was performed in ambient atmosphere using a Nanoscope III microscope operated in STM mode using platinum (Pt)/iridium (Ir) wire that was freshly cut (Pt 80% and Ir 20%, 0.25mm wire-tip diameter).

For AFM and STM imaging the samples were placed onto surfaces by drop-casting of the dispersions. For AFM the substrate that was used is freshly cleaved mica and for STM is HOPG. Mica substrate was used because it has a flat surface and HOPG for STM characterization since conductive substrate is required. In detail, 20 μL of CNP dispersions were deposited on a substrate area of 1 cm^2 . Both the surfaces with carbon dispersions, were dried under vacuum at room temperature and washed with deionized water. Then, the coated mica substrate was dried at 100 $^\circ\text{C}$ and the coated HOPG substrate was dried at 50 $^\circ\text{C}$ under vacuum overnight. In the case of the HOPG substrate, high temperatures were not used in order to avoid any influence in the HOPG – CNP interaction.

X-ray photoelectron spectroscopy (XPS) measurements were made with a ThermoFisher Scientific K-ALPHA spectrometer with a monochromatized Al-K α excitation source ($h\nu = 1486.6$ eV) and a 200 microns spot size. The pressure in the

analysis chamber was maintained at 10^{-7} Pa (in vacuum) during data acquisition. The full spectra (0-1150 eV) were acquired with constant pass energy of 200 eV and high resolution spectra at constant pass energy of 40 eV. Charge neutralization was applied for all samples. AVANTAGE software provided by ThermoFisher Scientific and the Scofield sensitivity factors available from the internal database were used to fit and quantify high resolution spectra.

Infrared (IR) spectra were obtained in transmittance on a Thermo Fischer Nicolet 6700 spectrometer. Samples were prepared using the potassium bromide pellet method (grinding 200 mg potassium bromide (KBr) with 1 mg CNP and compressing using standard equipment to a 13 mm platelet).

Absorption spectra were recorded using Unicam **UV/Vis spectrometer** UV4 (filter = 325 nm). All the CNP dispersions after tip sonication treatment and centrifugation times 2 min/4000 rpm (2486 x g) and 20 min/4000 rpm (2486 x g), prior to the absorption measurements, they were diluted. Particularly, all the samples were diluted with a dilution factor (DF) 2000 except of CNP₄ which was diluted with a DF 500.

Static Light Scattering (SLS) analysis was carried out using a Mastersizer 2000 - Malvern Instrument. The CNP dispersion was diluted about 5 %. In SLS analysis, the scattered light in different angles is recorded and the final CNP particle size is calculated from the software using the Mie theory.

Transmission electron microscopy (TEM) images were acquired using a TEM-FEG HR (JEOL 2200FS) microscope. 20 μ L of diluted (DF: 2000) CNP dispersions were drop casted on CF400-CU TEM grids (Electron microscopy science).

Scanning electron microscopy (SEM) measurements were performed on FEI QUANTA 200 scanning electron microscope. The solid samples were place onto an aluminium (Al) holder and attached with a carbon double side rubber.

d. Formulation of the dispersion

To fully characterize the different CNP samples, aqueous dispersions were formulated. The procedure that was followed to achieve the present optimized dispersions is fully described in chapter 3. Concisely, CNP_{HT} samples were dispersed in aqueous media using surfactant, tip sonication and centrifugation treatment. Typically, 320 mg of CNP_{HT}, 50 mg of bile salt and 9.63 mL of H₂O were mixed and tip sonicated for 30 min using a Branson Digital Sonifier tip sonicator. The sonication was performed in interval mode (pulse on: 0.5 sec, pulse off: 0.2 sec) with a total applied energy of 14.4 kJ.

Subsequently, the CNP_{HT} dispersions were centrifuged for 2 and 20 min at 4000 rpm (2486 x g) with a Fisher Bioblock Scientific centrifuge. The final concentration of CNP_{HT} is about 17 mg.mL⁻¹ (1.7 wt%) with 5 mg.mL⁻¹ (0.5 wt%) bile salt verified after weighing the freeze dried powder (yield ~53 %). The dispersions were used for AFM, STM characterization, optical measurements and to prepare conductive films.

2. Results

The CNP raw powders were produced by splitting the mixture of methane and carbon dioxide into carbon and hydrogen using ‘cold’ microwave plasma process. The amount of added CO₂ within the precursor varies from 0.0 vol% to 7.4 vol% of added CO₂ as depicted in **table 2.1**. As it is also illustrated in **table 2.1**, by increasing the carbon dioxide content in the feedstock, the CNP yield drops from 120 to 26.9 g.h⁻¹ for CNP₄.

a. Characterization of carbon nanopucks

Thermogravimetric analysis and purification

TGA analysis was performed to evaluate the mass loss of the CNP powders before heat treatment for temperatures from 20 to 750 °C under air as illustrated in **fig. 2.1**.

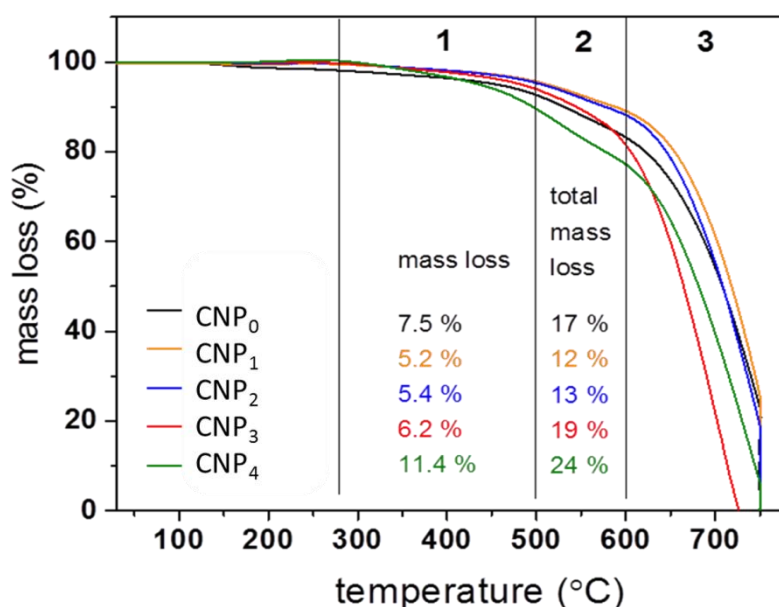


Figure 2.1: TGA measurements under air to follow the combustion rate between 20 °C - 750 °C. Three different regions can be attributed that exhibit different mass losses.

The resulting thermograms could be distinguished in four temperature ranges depending on the mass loss variations: from 20 °C to 280 °C, from 280 °C to 500 °C, from 500 °C to 600 °C and from 600 °C to 750 °C. In the first T region no mass losses are detectable. Then, from 280 °C to 500 °C mass losses between 5 to 11 % are observed with the sample CNP₄ to exhibit the highest mass loss and CNP₁ the lowest. Beyond 500 °C a more drastic mass loss occurs. Particularly, from 500 to 600 °C the mass losses have almost double values from the corresponding ones in the previous T region (280 to 500 °C). Above approximately 600 °C the CNP materials are totally burned resulting into an almost 100 wt% mass loss. Interestingly all the samples show the same thermograms' trends. Furthermore, the ash contents were calculated and were found generally low, less than 0.5 wt%, as presented in **table 2.2**.

Table 2.2: Ash content of CNP samples before heat treatment. m_b : the mass of the sample holder before thermal annealing under air. m_a : the mass after thermal annealing. The ash content was calculated from the $m_b - m_a$ difference.

	CNP₁	CNP₂	CNP₃	CNP₄
m_b (g) (before)	9.542	10.016	9.724	9.589
m_a (g) (after)	9.542	9.944	9.714	9.569
$m_b - m_a$	0.00	0.072	0.01	0.02
<u>ash content (%)</u>	<u>0.0</u>	<u>0.71</u>	<u>0.1</u>	<u>0.2</u>

Based on the TGA results, **purification treatment** was designed for CNP samples. Approximately 2 g of each sample was **heat treated at 500 °C for 6 h**. The weight losses of the purified materials are between 12 to 24 % which are in total agreement with TGA results.

X-ray diffraction

The crystalline structure of all the five CNP samples before and after purification treatment has been determined via XRD analysis. The corresponding spectra are illustrated in **fig. 2.2** and **2.3**.

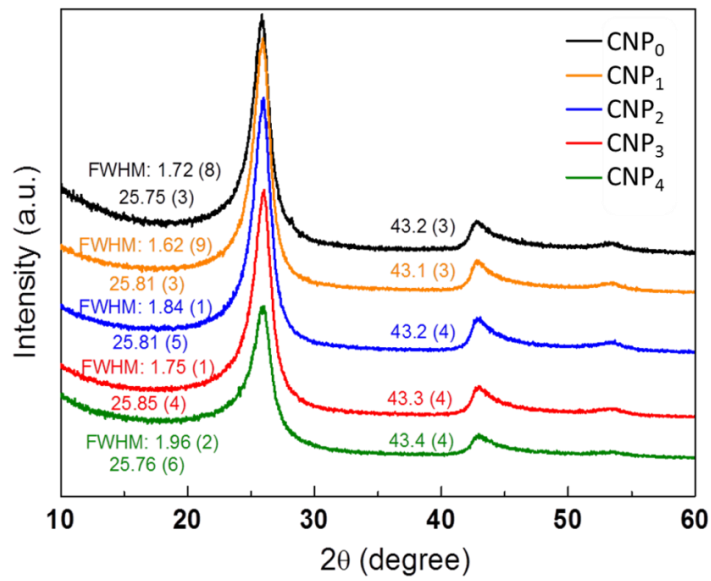


Figure 2.2: XRD data of the five CNP samples before purification treatment. Cu-K α radiation of $\lambda = 0.15418$ nm. The digits in brackets represent the error.

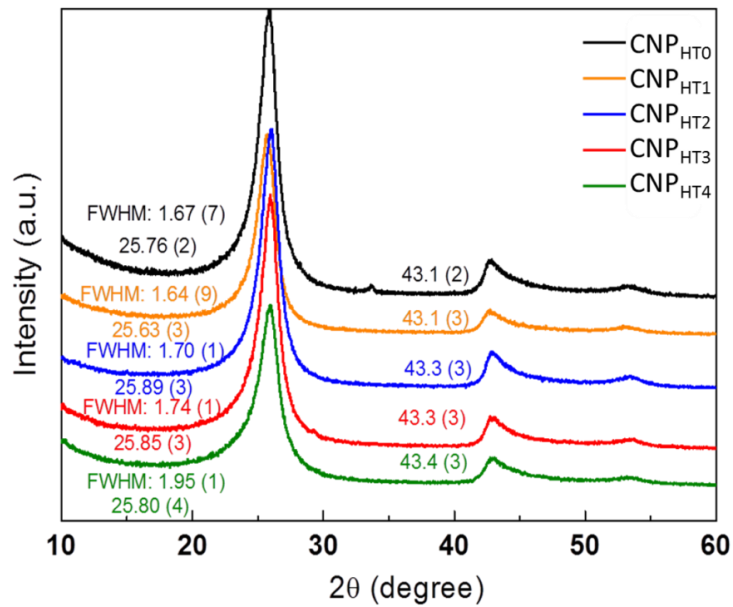


Figure 2.3: XRD data of the five CNP samples after heat treatment (at 500 °C for 6 h): Will be referred as CNP_{HT} samples. Cu-K α radiation of $\lambda = 0.15418$ nm. The digits in brackets represent the error.

All the diffractograms show three distinct peaks: at 25.8°, 43° and 52° 2 θ degrees. The samples before and after heat treatment (at 500 °C for 6 h) are virtually identical therefore, XRD analysis is described only for the CNP materials after thermal annealing while all the resulting data are presented in **table 2.3**.

The peak at ca 25.8° corresponds to the (002) peak of graphite. Its full width at the half maximum (FWHM) is rather broad, more than 1.6° and is typical for nanographitic carbons.¹⁸ Furthermore, by applying the Scherrer equation, the mean crystalline size was calculated which varies from 8 to 6 nm as depicted in **table 2.3**.

Table 2.3: Crystalline domains from the samples CNP₀-CNP₄ extracted from XRD data.

Samples	Mean size of the ordered (crystalline) domains (nm)	Plane distance (nm)	Number of planes	Mean size of the ordered (crystalline) domains (nm)	Plane distance (nm)
	2 θ ~ 26 degrees	2 θ ~ 26 degrees	2 θ ~ 26 degrees	2 θ ~ 43 degrees	2 θ ~ 43 degrees
CNP ₀	9.7	0.346	28	8.1	0.209
CNP _{HT0}	10.0	0.346	29	10	0.210
CNP ₁	10.2	0.345	30	10.2	0.209
CNP _{HT1}	10.2	0.348	29	8.7	0.210
CNP ₂	9.1	0.345	26	11.1	0.209
CNP _{HT2}	9.8	0.344	28	10.8	0.209
CNP ₃	9.5	0.345	28	8.3	0.209
CNP _{HT3}	9.6	0.345	28	8.7	0.209
CNP ₄	8.5	0.346	25	7.0	0.209
CNP _{HT4}	8.6	0.345	25	7.0	0.208

The interplane distance was found by using Bragg's law and has a value of about 0.345 nm, which is characteristic for turbostratic graphite.¹⁹ From the mean crystalline size and the plane distance of (002) plane, the number of carbon layers was also calculated (**table 2.3**). All in all, from the (002) peak, crystalline domains of mean size 8 to 10 nm were found which consist of 25 to 29 layers turbostratically packed layers of graphene. The 2θ peak at around 43° can be assigned to the (100) plane.^{18,20} From this peak, the corresponding mean domain size and plane distance was calculated and illustrated in **table 2.3**. Values between 7 to 11 nm of the mean size of crystalline domains were found.

Raman spectroscopy

Raman spectroscopy has emerged as the most powerful and convenient probe to characterize the graphene samples.^{21,22,23} D, G and 2D bands are the significant bands in a Raman spectrum of a carbon material.²⁴ The ratio of the area of D over G bands ($A_{D/G}$) can provide information about the amount of sp^3 carbon in graphitic materials. Moreover, the CNP samples that are studied in these manuscript are inhomogeneous, therefore mapping deemed necessary.^{25,26} 1681 individual Raman spectra (size for analyzed data: $200 * 200 \mu m^2$) were recorded for each carbon sample and the D and G bands for each spectra were fitted using Lorentzian function where the D, G and D' bands were fitted. The histograms of the $A_{D/G}$ of CNP_{HT} samples are depicted in **fig. 2.4**.

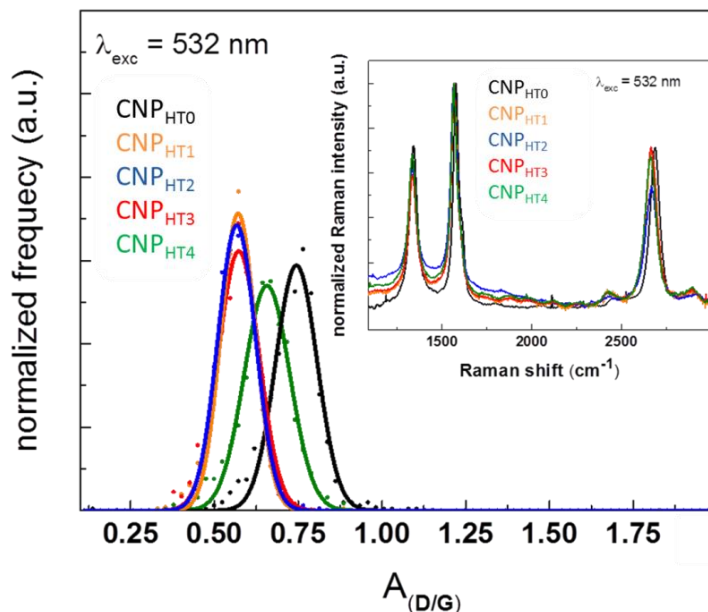


Figure 2.4: Histograms of $A_{(D/G)}$ values of the CNP_{HT} samples measured at 532 nm excitation wavelength. Inset: Representative Raman spectra of heat treated samples.

The $A_{(D/G)}$ values of all CNP samples show Gaussian statistics with values in the range of $0.5-0.7 \pm 0.1$ to $0.6-0.8 \pm 0.1$. The CNP_{HT2} sample exhibits the lowest $A_{(D/G)}$ value while the CNP_{HT0} the highest one. Similarly, G band width also exhibits Gaussian distributions from 39 cm^{-1} average value for CNP_{HT0} to 56 cm^{-1} for CNP_{HT2} as shown in **fig. 2.5**. $\Gamma_{(G)}$ values of 39 to 56 cm^{-1} correspond to mean crystalline domains of 5 to 20 nm based on the studies of Ferrari *et al.*^{27,28} and Cançado *et al.*²⁹

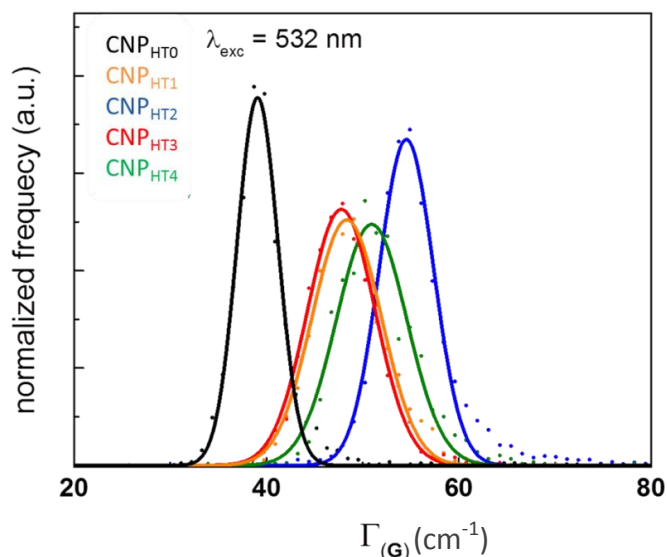


Figure 2.5: Width of the G-mode extracted on a statistical analysis of recorded Raman spectra of CNP_{HTX} samples at 532 nm excitation wavelength.

Likewise, additional Raman data (histograms of $A_{(D/G)}$ values and G mode width) for the pre-heated samples are illustrated in **fig. 2.6** and **2.7**.

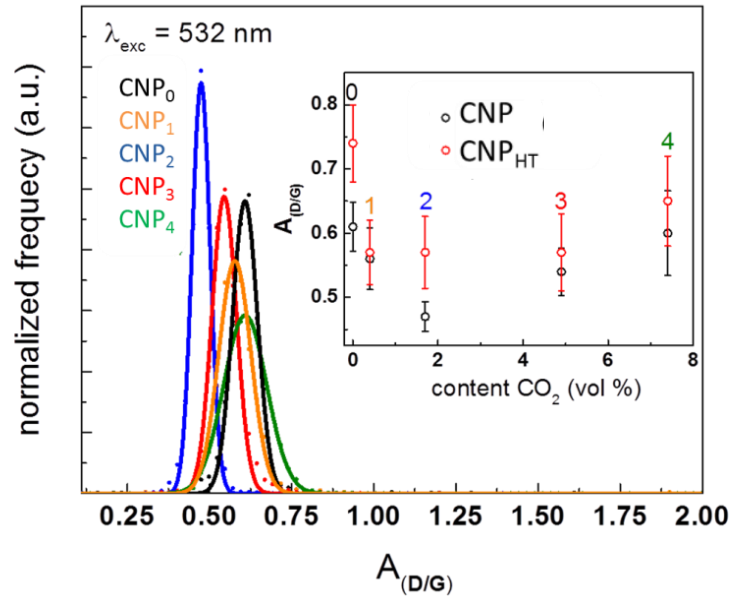


Figure 2.6: Histograms of $A_{(D/G)}$ values of the CNP samples measured at 532 nm excitation wavelength. Inset: $A_{(D/G)}$ values of the CNP and CNP_{HT} samples as a function of CO₂ concentration within the plasma process.

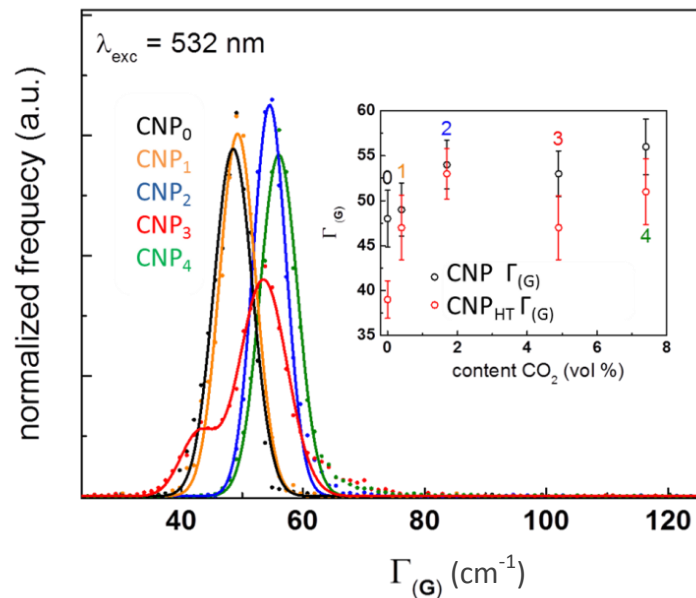


Figure 2.7: Width of the G mode extracted on a statistical analysis of recorded Raman spectra of CNP samples at 532 nm excitation wavelength. Inset: Width of the G mode of the CNP and CNP_{HT} samples as a function of CO₂ concentration within the plasma process.

Ferrari *et al.* studied the disordered graphitic materials and they classified these materials based on the amount of sp^3 carbon with stage I to correspond to the least disordered material and stage III to the most disordered one.^{27,28} All the CNP samples can be characterized as stage II due to their G mode position, line width, and $A_{(D/G)}$ values. In stage II the $A_{(D/G)}$ increases. Moreover, an increase of order in the carbon lattice has as a consequence a decrease of the intensity of D band which is not the case for less disordered materials.²⁹ G band width decreases with the increase of ordering. From the insets of **fig. 2.4** to **2.7** the following conclusions can be extracted: the 2D band which is influenced from the carbon quality, doping and strain/stress is high and very similar for all the samples. CO_2 presence is not beneficial to CNP quality since the most ordered material appeared to be the CNP_{HTO} . Also, between the samples of which the feed gasses contained CO_2 , there is no significant difference in terms of ordering indicating that the exact CO_2 concentration doesn't influence distinctively. Another valuable conclusion is that the heat treated samples are of higher crystallinity than the raw materials.

X-ray photoelectron spectroscopy

XPS analysis provides information about element concentrations and chemical binding environments as illustrated in **fig. 2.8** to **2.10**.

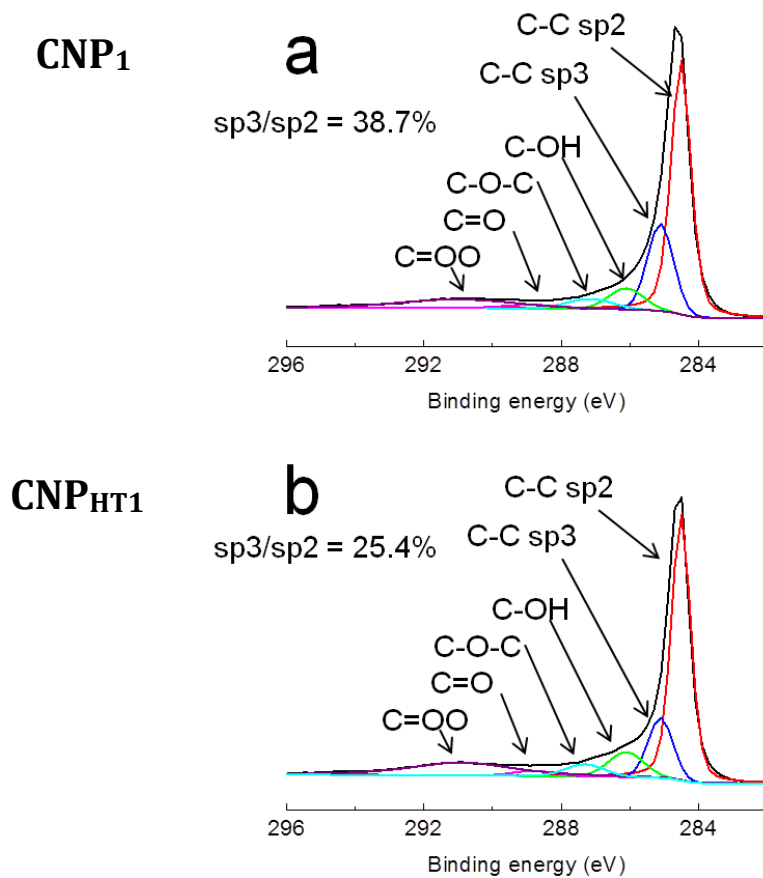


Figure 2.8: XPS spectra and fits of the respective carbon peak of a) CNP₁, b) CNP_{HT1}.

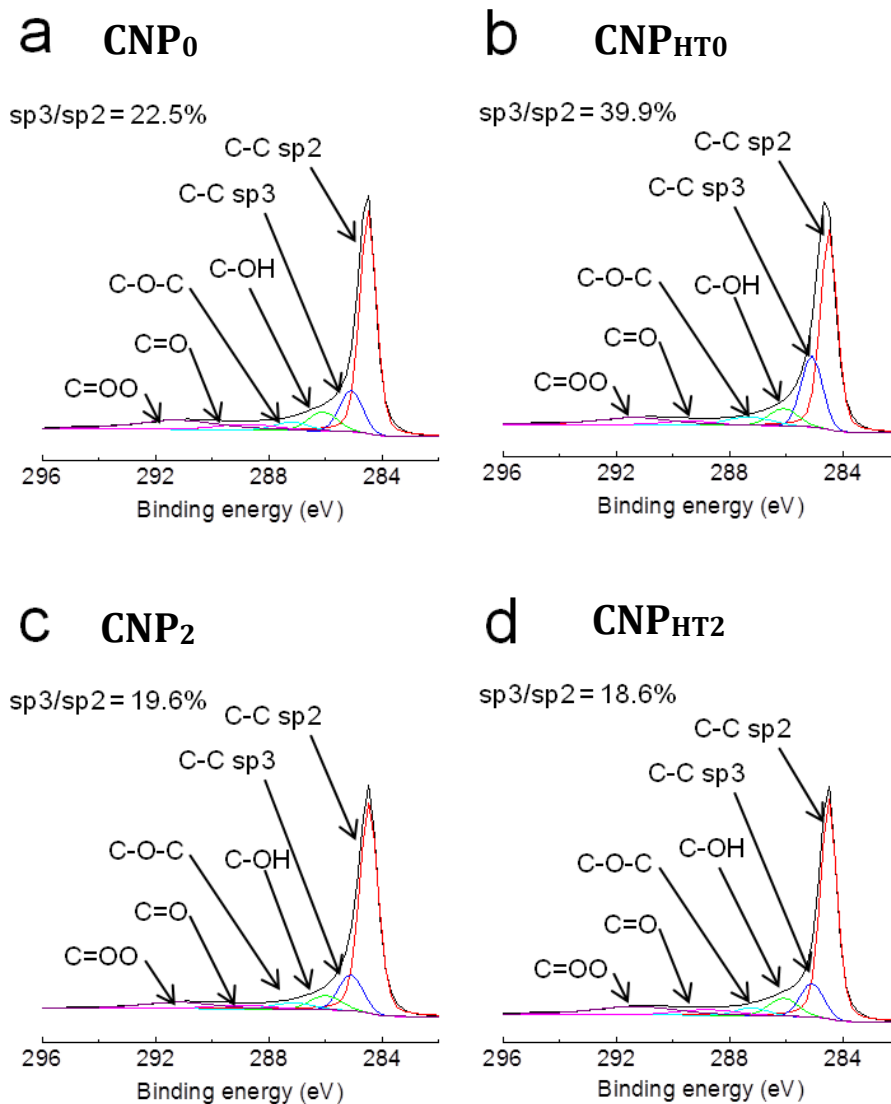


Figure 2.9: XPS spectra and fits of the respective carbon peak of a) CNP₀, b) CNP_{HT0}, c) CNP₂ and d) CNP_{HT2}.

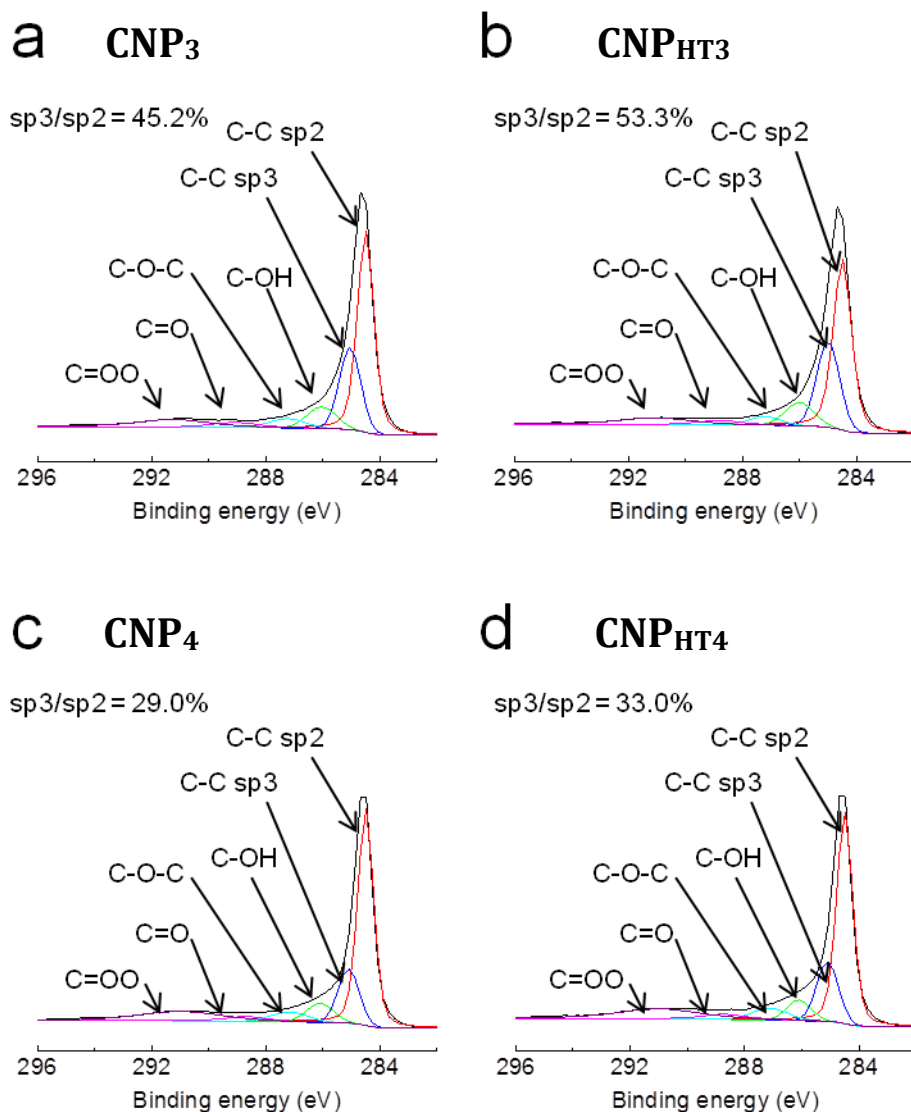


Figure 2.10: XPS spectra and fits of the respective carbon peak of a) CNP₃, b) CNP_{HT3}, c) CNP₄ and d) CNP_{HT4}.

Peaks which correspond to carbon and oxygen presence respectively are illustrated in XPS spectra. The carbon spectra show a broad carbon peak accompanied with a broad tail. After heat treatment a decrease of the width of the carbon peak is observed while the tail remains practically the same. The tail can be assigned to a variety of carbon oxygen bonds and groups. Furthermore, from the XPS analysis the carbon and oxygen contents of all the samples were calculated as described in **table 2.4**. The carbon atomic percentage is more than 97 % and an expected oxygen increase for samples after heat treatment was observed, except for CNP₄.

Table 2.4: Atomic percentage of carbon and oxygen all CNP samples based on XPS spectra analysis.

	CNP 0	CNP HT0	CNP 1	CNP _H T1	CNP 2	CNP _H T2	CNP 3	CNP _H T3	CNP 4	CNP _H T4
C (at. %)	98.95	98.21	98.54	98.49	98.53	98.37	98.14	98.41	97.70	97.83
O (at. %)	1.05	1.79	1.46	1.51	1.47	1.55	1.86	1.50	2.30	2.05

Infrared spectroscopy

From the IR spectra of the CNP samples, different functional groups can be determined (**fig. 2.11** and **2.12**). The most pronounced peaks are at 1574 cm^{-1} , 1368 cm^{-1} , 1062 cm^{-1} and about 3400 cm^{-1} . Vibrations of COH, CO and COC groups correspond to 3400 cm^{-1} , 1368 cm^{-1} , and 1062 cm^{-1} peaks respectively. Moreover, peaks with low intensities between 2960 cm^{-1} to 2840 cm^{-1} were found and can be assigned to alkylic C-H vibration. The most intense peak is at 1574 cm^{-1} and is attributed to the C=C vibration. Also, in **table 2.5** is shown the elemental analysis of all CNP samples before and after heat treatment which provides an additional evidence of the small concentration of hetero atoms. Further analysis should be performed to identify the elements that correspond to the remaining approximately 7 %.

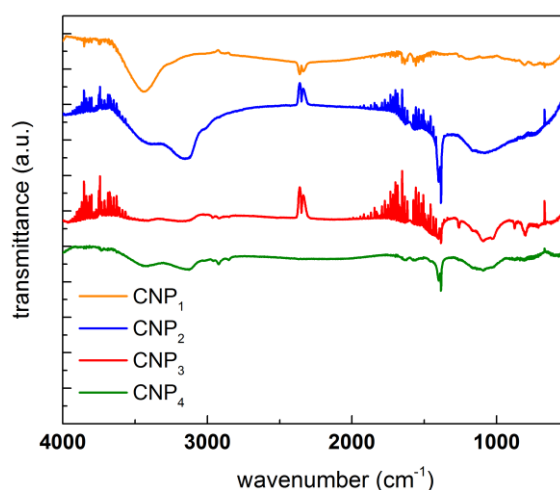


Figure 2.11: IR-spectra of the four CNP samples before heat treatment.

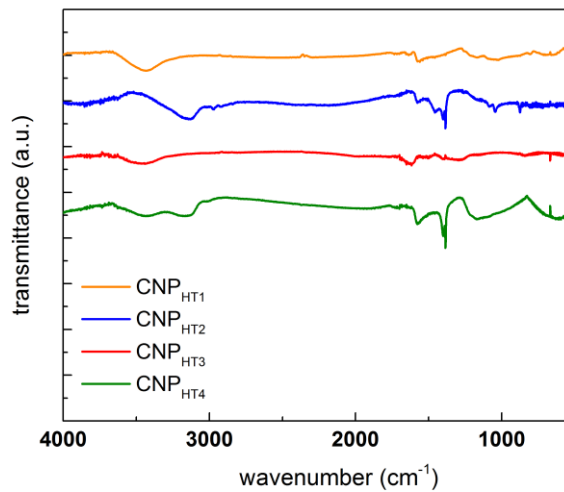


Figure 2.12: IR-spectra of the four CNP samples after (bottom) heat treatment.

Table 2.5: Elemental data of the four different CNP before (CNP) and after heat treatment (CNP_{HT}).

	C (%)	H (%)	N (%)	O (%)	S (%)
CNP ₁	92.5	1.00	< 0.05	0.60	< 0.05
CNP _{HT1}	92.2	0.74	< 0.05	1.26	< 0.05
CNP ₂	92.3	1.00	< 0.05	0.59	< 0.05
CNP _{HT2}	91.8	0.72	< 0.05	0.96	< 0.05
CNP ₃	91.9	1.08	< 0.05	0.77	< 0.05
CNP _{HT3}	91.2	0.72	< 0.05	1.46	< 0.05
CNP ₄	91.0	1.36	< 0.05	1.27	< 0.05
CNP _{HT4}	90.7	0.72	< 0.05	1.75	< 0.05

BET

The specific surface area (total surface area of a material per unit of mass) of CNP_x samples was acquired from BET measurements, performed by FGV Cambridge Nanosystems, United Kingdom (**table 2.6**) and has values between 141 m².g⁻¹ and 196 m².g⁻¹.¹⁷

Table 2.6: BET surface area of the different CNP_x .

	CNP_0	CNP_1	CNP_2	CNP_3	CNP_4
BET (N_2) $m^2.g^{-1}$		153	141	158	196

b. Dispersion of the purified carbon nanopucks

To further evaluate the properties of these nanographitic carbons the different purified carbon nanopuck samples were dispersed with the aid of surfactant (bile salt) in water. Adjusting literature procedures,^{30,31} optimized surfactant concentration of 0.5 wt% (5 $mg.mL^{-1}$) bile salt have been used. CNP concentration up to 32 $mg.mL^{-1}$ has been obtained. Moreover, both sonication and centrifugation parameters have been optimized in order to obtain different compositions of sample sizes. After tip sonication, centrifugation treatment was performed. Centrifugation of 2 min at 4000 rpm results into bidisperse populations; the majority (2/3) consists of 60 nm particle size and the other 1/3 of other particles around 0.5 μm lateral size. With further centrifugation treatment (20 min/4000 rpm), monodisperse population was successfully isolated at around 60 nm. Detailed analysis is presented in Chapter 3.

The final carbon nanopuck concentrations were verified by freeze drying of the CNP_{HTX} dispersions. Dispersions with two (2 min centrifugation) and one size populations (20 min centrifugation) have concentrations of 2.4 wt% and 1.7 wt% respectively (centrifugation loss was 21 % for the former and 47 % for the latter).

UV/Vis absorption spectroscopy

In order to characterize the aqueous dispersions, absorption spectra were taken in the UV/Vis region using a Unicam UV/Vis spectrometer UV4 (**fig. 2.13**).

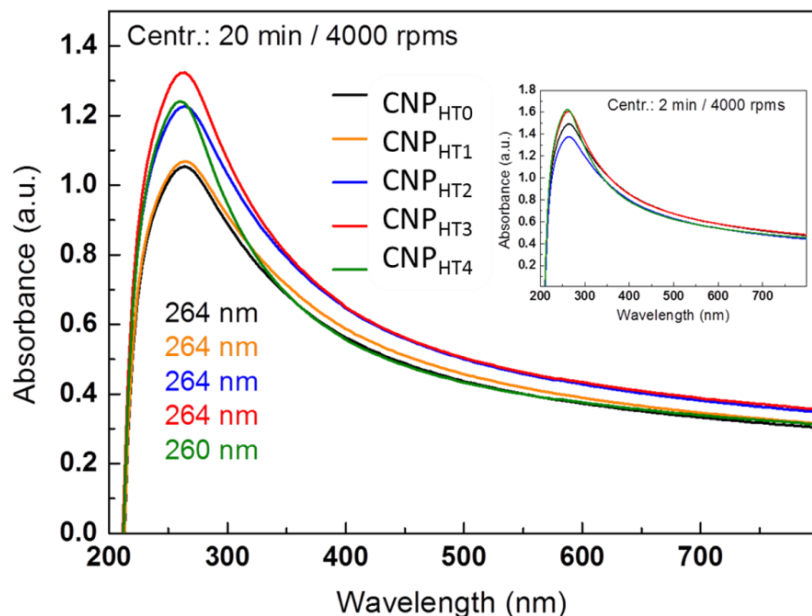


Figure 2.13: Absorption spectra in the UV/Vis region of the different CNP_{HTX} samples with centrifugation treatment 2 min/4000 rpm and 20 min/4000 rpm.

All absorption spectra exhibit a peak at 264 nm except of CNP_{HT4} for which a peak is found at 260 nm. The peak at 264 nm is due to the collective π - π^* electronic transition of the condensed aromatic rings in the graphene sheet.³² There is a tail in the absorption spectra because the graphenic materials absorb all energies.

Atomic force microscopy

The size and height of all different CNP_{HTX} particles in an aqueous dispersion were determined by means of AFM (**fig. 2.14** to **2.18**). 20 μ L of dispersions after 20 min/4000 rpm centrifugation were drop-casted on freshly cleaved mica substrates. The AFM topography images (**fig. 2.14 a** to **2.18 a**) of CNP_{HTX} samples exhibit essentially flat surfaces of homogenous nanocarbon particles characterized by a height range of 1 to 4 nm (see also insets with height from the cross sections). Individual objects are also noticeable. The statistical analysis reveals that the resulting height distribution (**fig. 2.14 b** to **2.18 b**) differs from one sample to the other with CNP_{HT2} dispersion to show the highest mean height of 3 nm for the carbon nanopucks. Moreover, statistical analysis of diameter distributions (**fig. 2.14 c** to **2.18 c**) shows a mean lateral size from 15 nm up to ca 40 nm with relatively broad distributions. Overall, homogeneity within the sample is observed. A useful material from robust dispersion procedure is obtained with monodisperse population of particles in water.

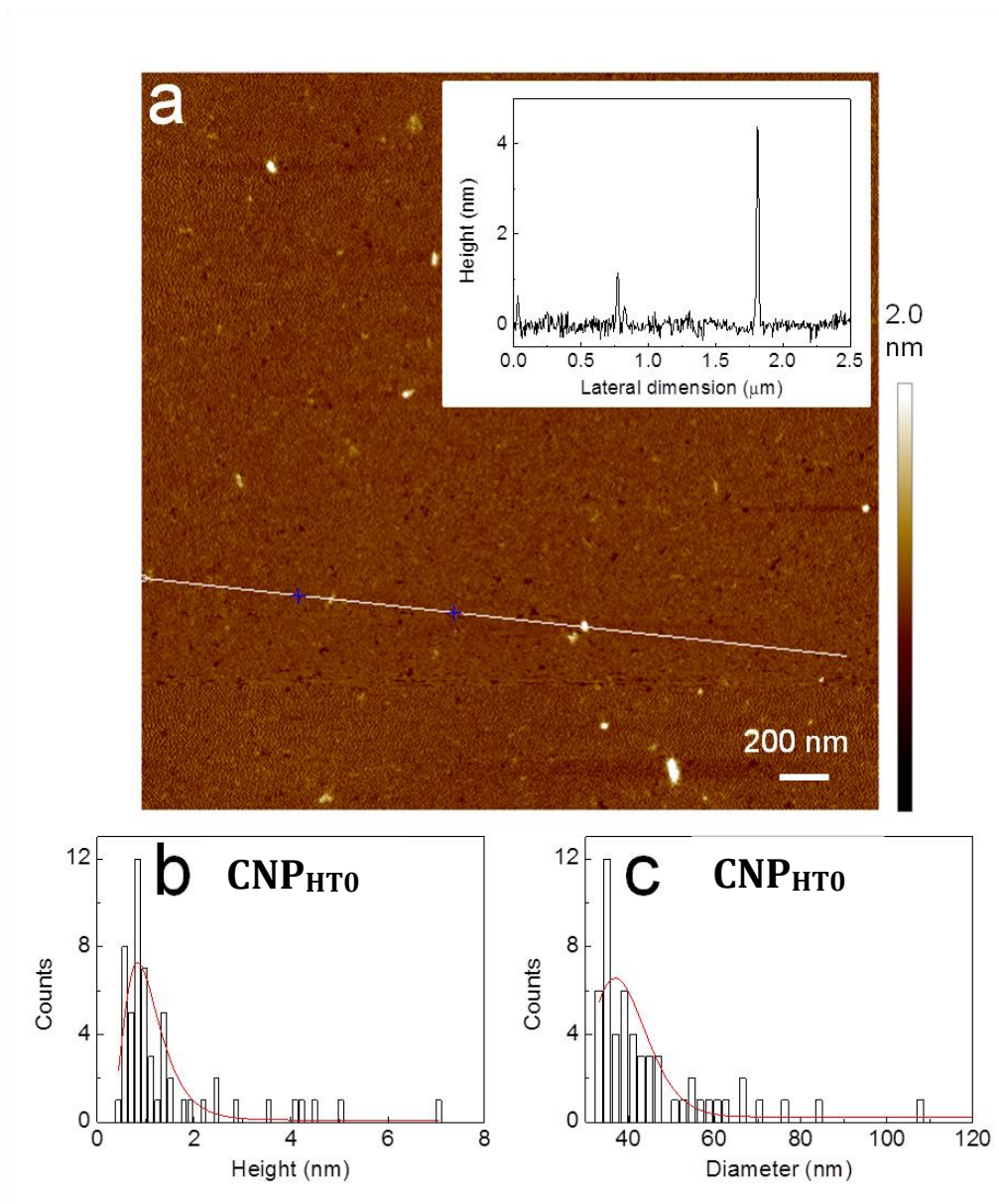


Figure 2.14: (a) AFM topography image of CNP_{HTO} dispersion deposited on mica surface. In the inset cross section along the white line of the topography image is plotted which show height of the carbon on the surface between 1 to 4 nm. (b) Height distribution of CNP_{HTO} with a mean height of 1 nm. (c) Lateral size distribution of CNP_{HTO} particles showing that their mean size is 40 nm.

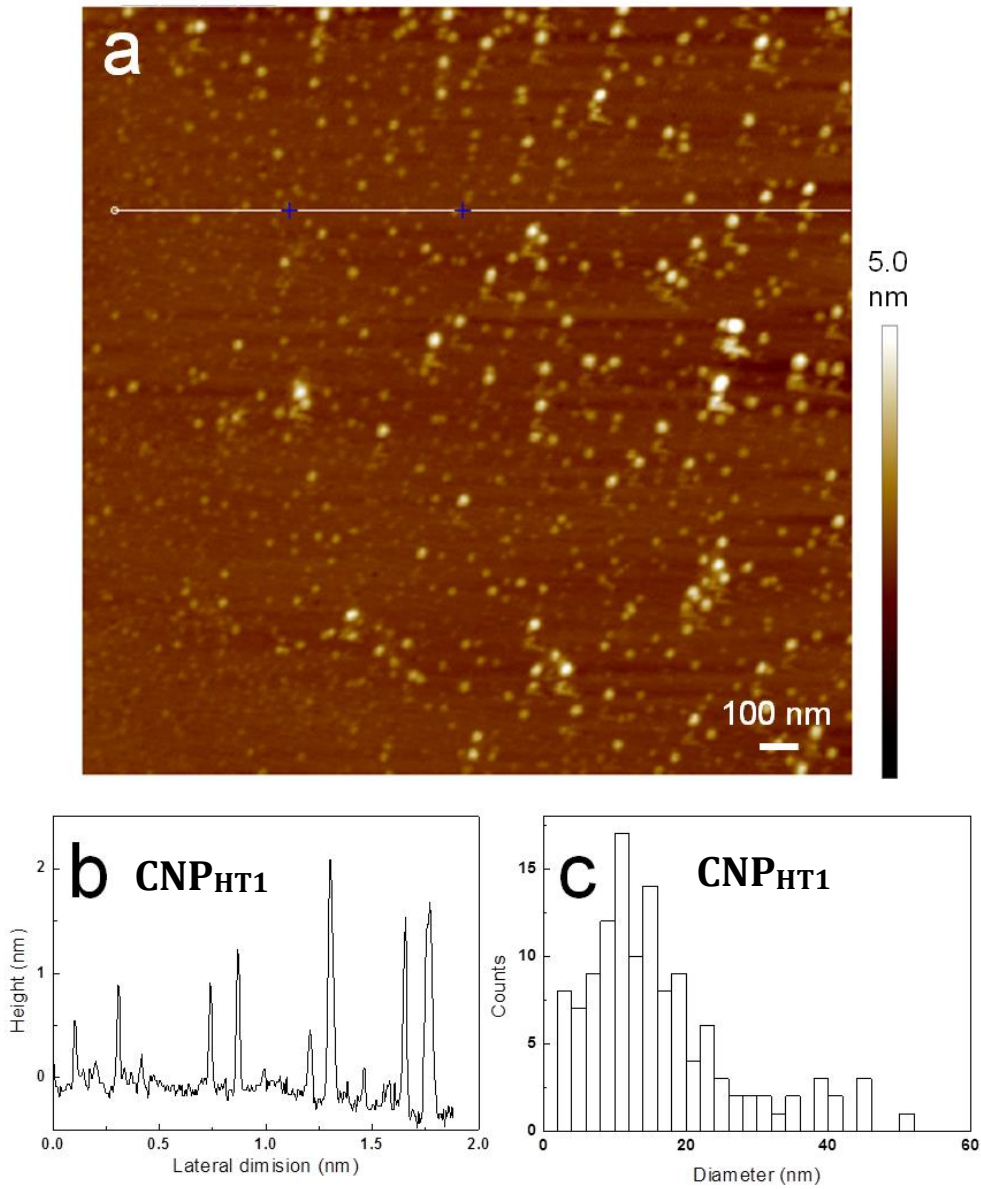


Figure 2.15: (a) AFM topography image of CNP_{HT1} dispersion deposited on mica surface. (b) Cross sections of the topography image taken along the white line are plotted, showing that the height of the CNP_{HT1} particles on the surface is 1-2 nm. (c) Lateral size distribution of CNP_{HT1} particles showing that their mean size is 15 nm.

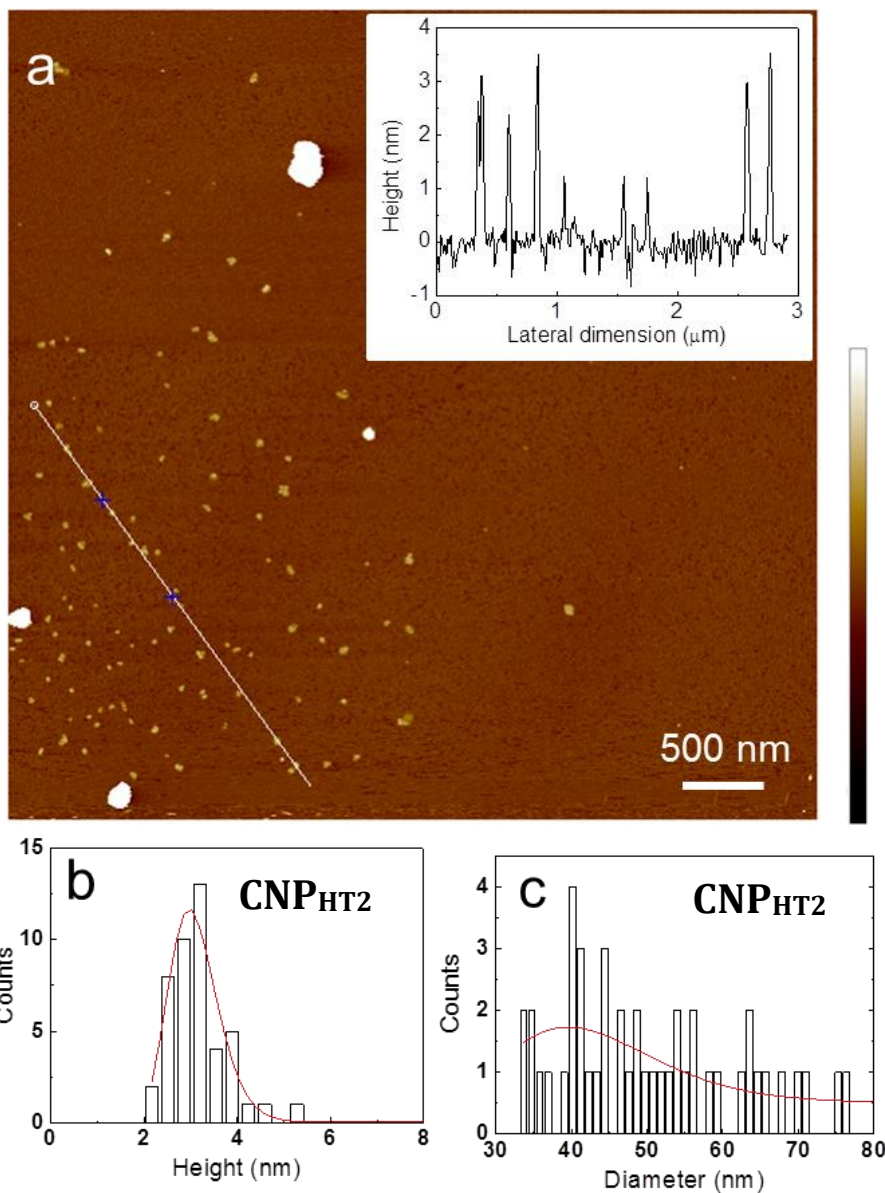


Figure 2.16: (a) AFM topography image of deposits of CNP_{HT2} dispersion on mica surface. Cross sections of the topography image taken along the white line are plotted in the inset. (b) Height distribution of the CNP_{HT2} particles showing that their mean height is 3 nm. (c) Lateral size distribution of CNP_{HT2} particles showing that their mean size is 40 nm.

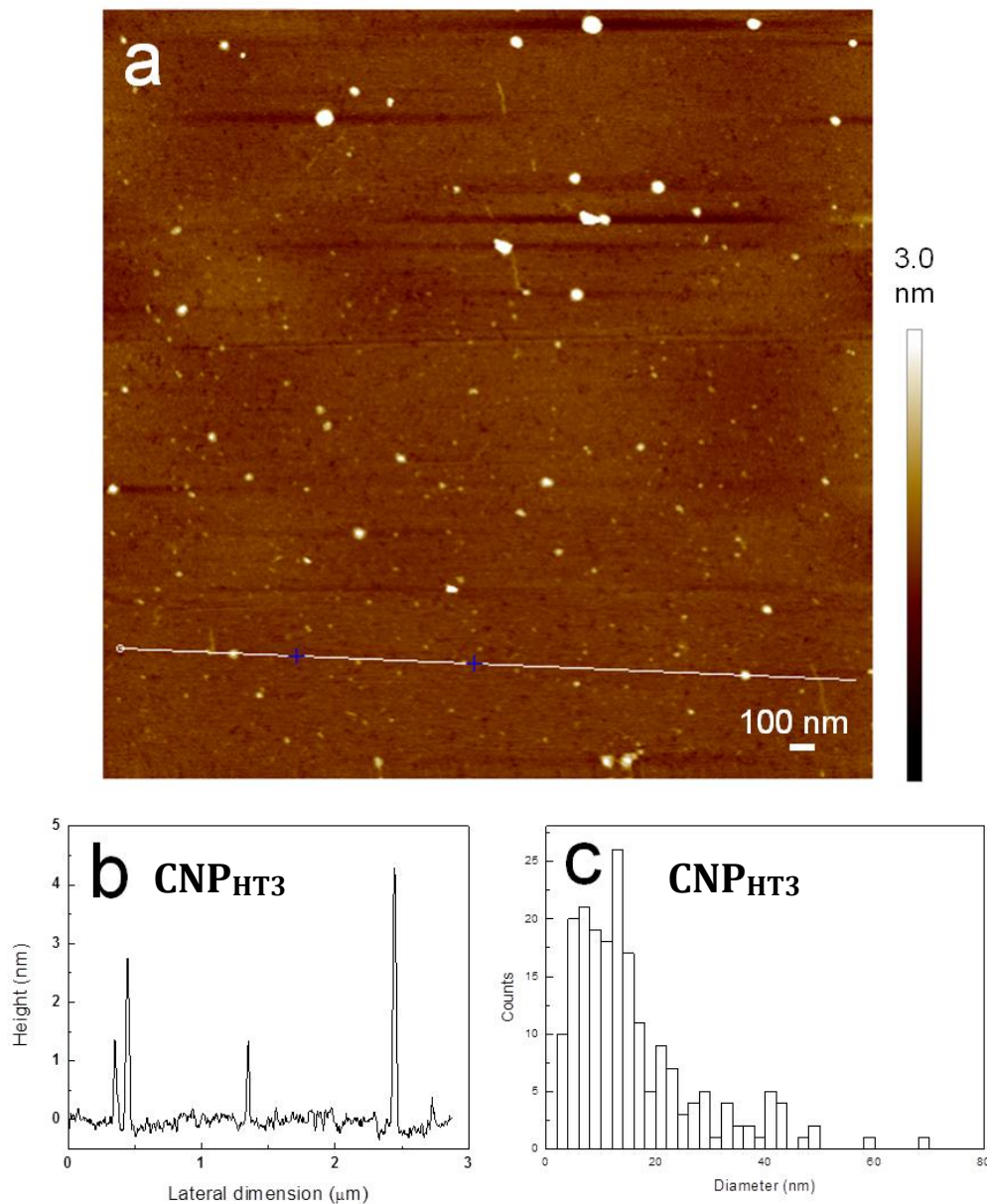


Figure 2.17: (a) AFM topography image of deposits of CNP_{HT3} dispersion on mica surface. (b) Cross sections of the topography image taken along the white line are plotted, showing that the height of the nano objects on the surface is 1-4 nm. (c) Lateral size distribution of CNP_{HT3} particles showing that their mean size is 15 nm.

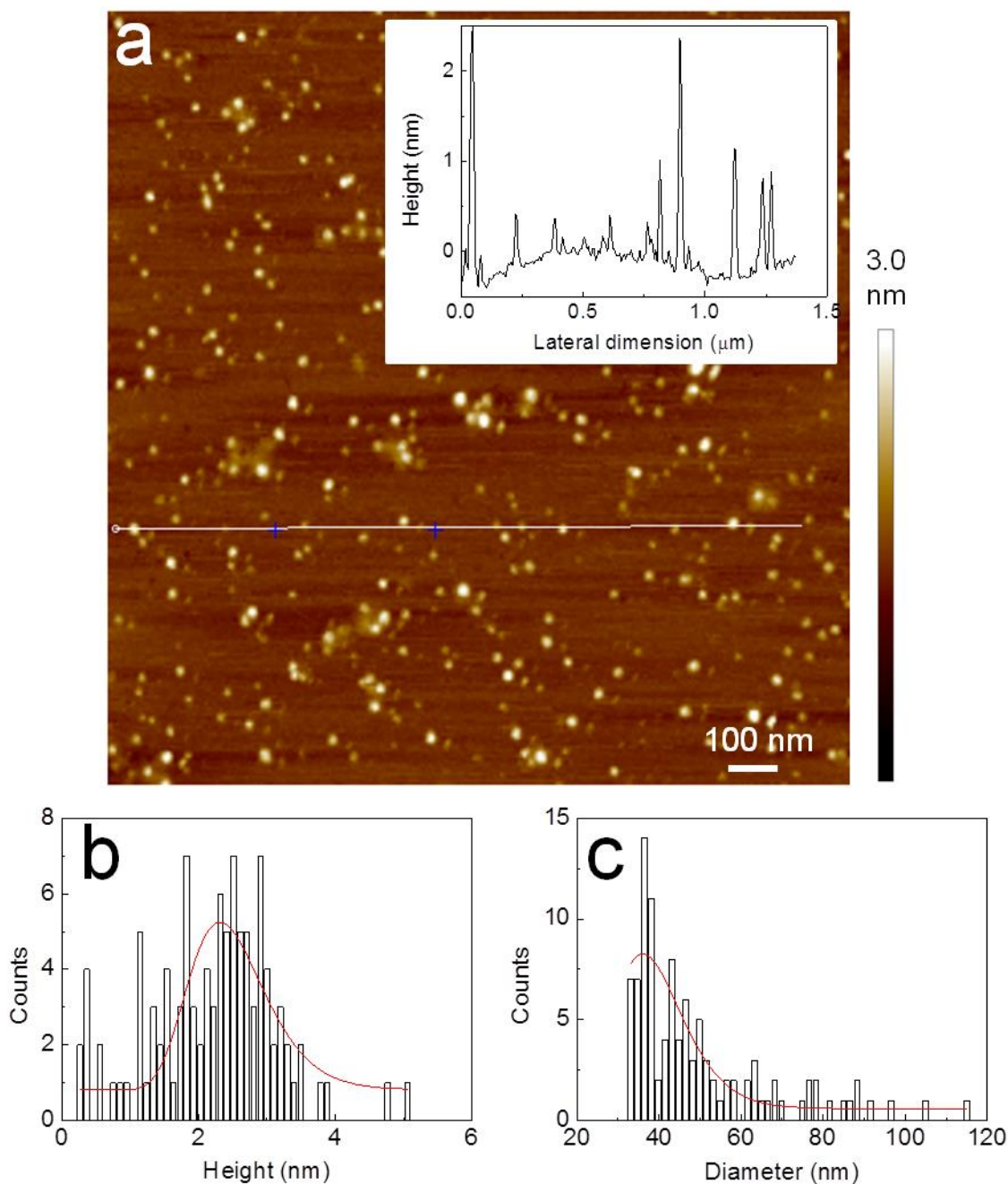


Figure 2.18: AFM topography image of deposits of CNP_{HT4} dispersion on mica surface (cross sections of the topography image taken along the white line are plotted in inserted figure, showing that the height of the nano object on the surface 1-3 nm. (b) Height distribution of the CNP_{HT4} particles showing that their mean height is 2.5 nm. (c) Lateral size distribution of CNP_{HT2} particles showing that their mean size is 40 nm.

Scanning tunneling microscopy

In **fig. 2.19 a** is represented an ambient STM image of CNP_{HT2} dispersion placed on HOPG. The image bears several nanocarbon objects and a small area of aggregates with

similar form and shape than the individual ones. In **fig. 2.19 b** and **2.19 c** the cross sections 1 and 2 are plotted providing information about the range of size and height of the particles which are 30 to 60 nm and 0.4 to 1.6 nm respectively.

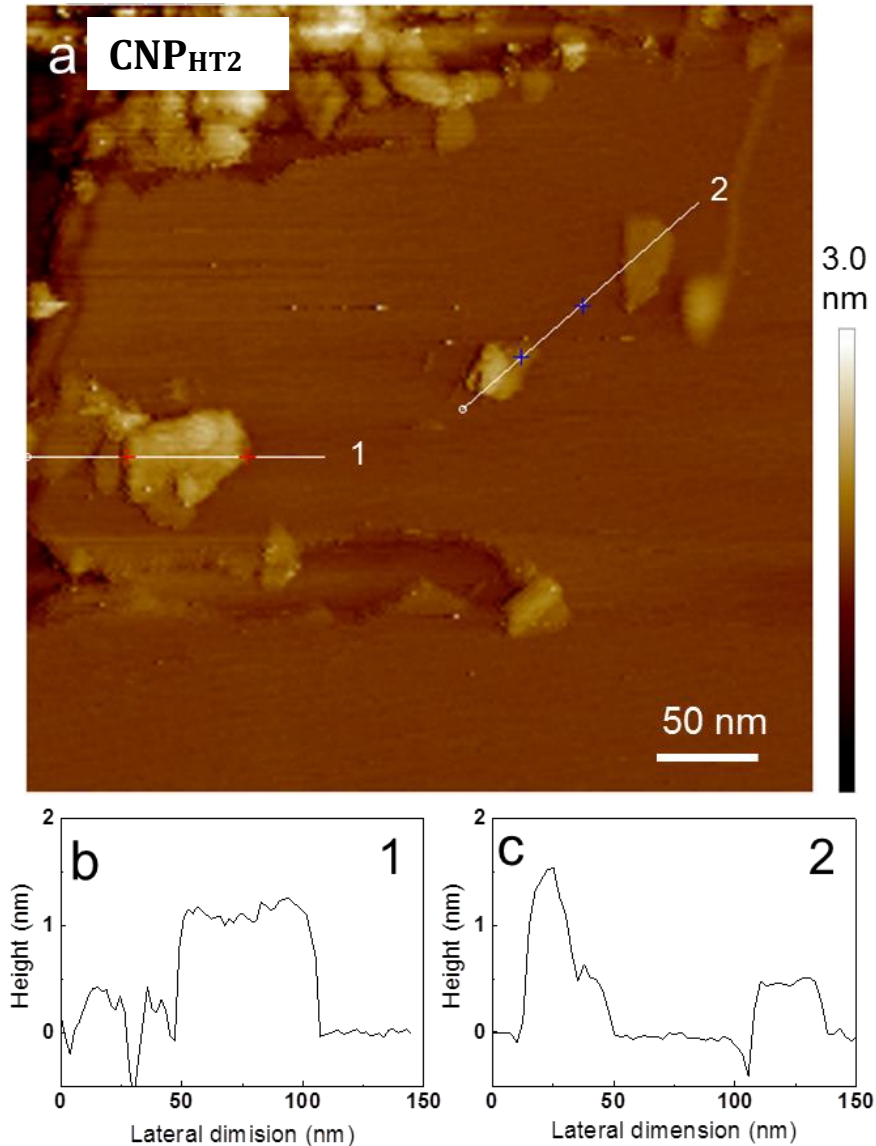


Figure 2.19: Ambient STM image of CNP_{HT2} deposits on freshly cleaved HOPG. (a) Several individual carbon particles and aggregates can be clearly observed. (b, c) Cross sections taken along the white lines 1 and 2.

Transmission electron microscopy

Transmission electron microscopy images were recorded for all the purified samples. **Fig. 2.20 a)** and **2.20 b)** show the aggregate morphology that the carbon nanopuck sample exhibits. In **fig. 2.20 c)** and **2.20 d)** representative high resolution images of CNP_{HT2} are showed. Similar images of the other four heat treated samples are depicted in **fig. 2.21**. In the former images, (**2.20 c)** and **2.20 d)**) graphitic domains within the

Chapter 2 – Characterization of carbon nanopucks

aggregates are clearly observed while the distance between layers of graphene can be estimated around 0.34 nm. The lateral size of the ordered regions exhibits values of ca. 10 nm.

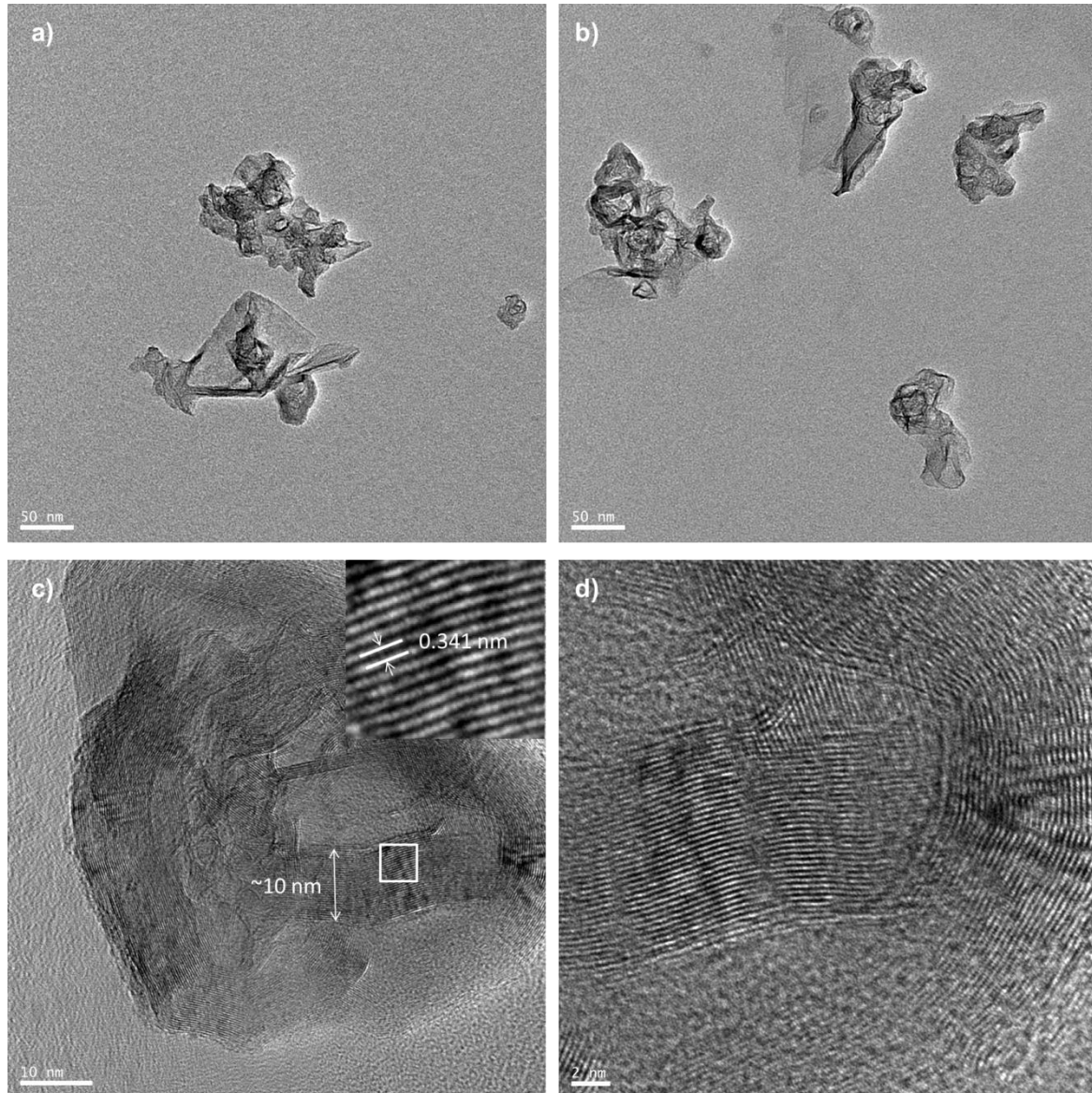


Figure 2.20: Representative HRTEM images of the sample CNP_{HRT2} . a), b) scale bar: 50 nm, c) scale bar 10 nm and d) scale bar 2 nm.

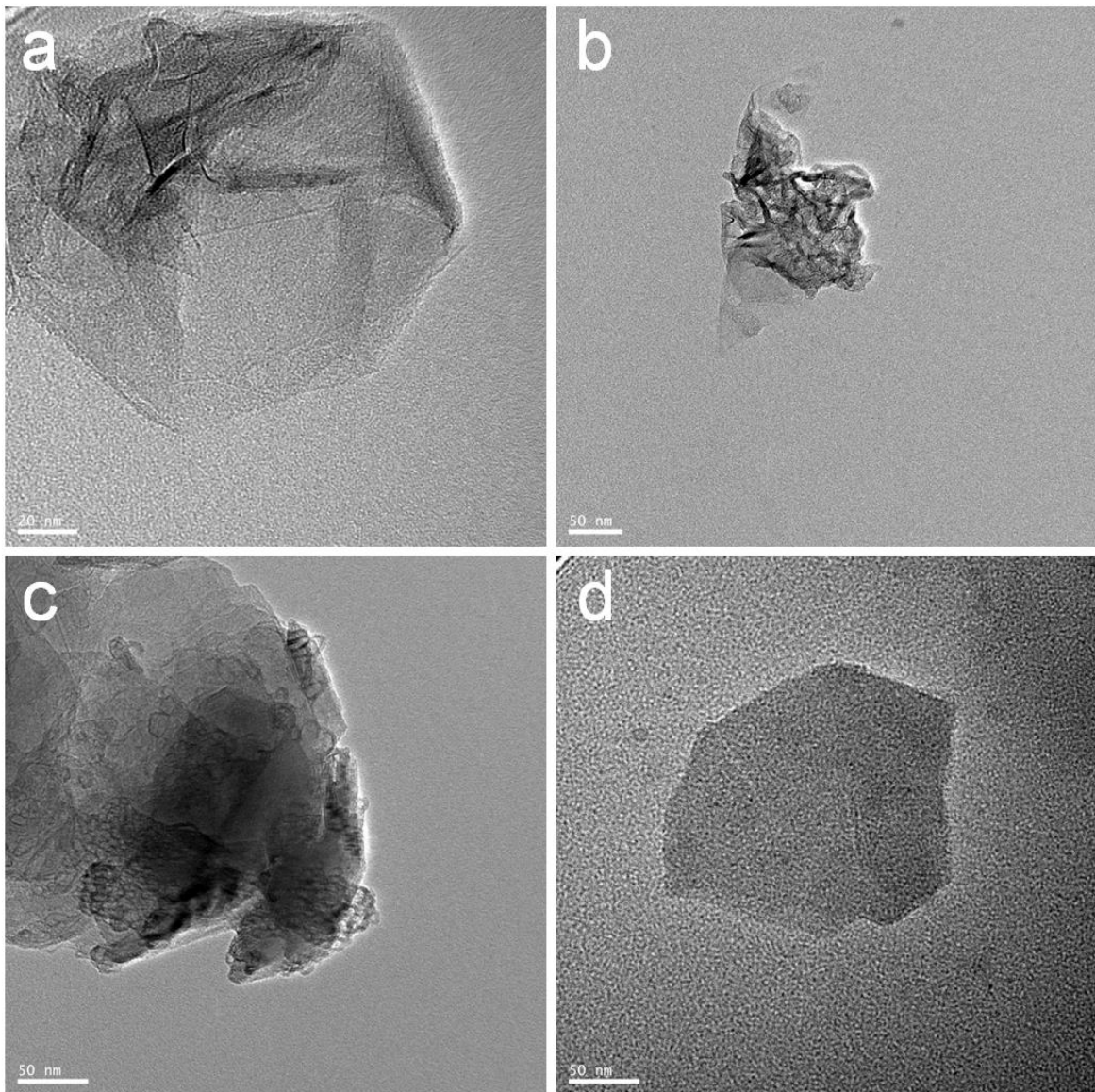


Figure 2.21: HR-TEM images of a) CNP_{HT0} , b) CNP_{HT1} , c) CNP_{HT3} and d) CNP_{HT4} .

3. Discussion

Different grades of sustainable carbon nanopucks are produced from the mixture of methane and carbon dioxide (CO_2) via microwave plasma process. The content of carbon dioxide to the feed gas affects the yield of the resulting CNP with the later to be inversely dependent on the CO_2 concentration. A series of techniques; from thermogravimetric analysis to UV/Vis absorption, has been applied in order to evaluate the quality of the produced carbon materials.

By means of **TGA** under air, a mass loss of 10 to 25 % is evident between 20 to 500 °C which could be attributed to the amorphous content of the samples. Moreover, the thermal stability of carbon lattice is determined; up to 600 °C the samples are stable and above this temperature their total burning occurs.

CNP lattice stability is further supported by XRD and **Raman analysis** which is assigned to the graphitic nature of these carbon products. The values of the area of the D mode over G mode ($A_{(D/G)}$) by statistical analysis in Raman spectra are increased after purification of the samples. This $A_{(D/G)}$ enhancement could be translated to the production of less defective material after heat treatment (500 °C for 6 h) (stage II compounds) which is contrary to the trend of $A_{(D/G)}$ for pristine graphite or graphene.²⁸ The mean widths of the G band is 40 to 55 cm^{-1} which corresponds to a mean size of graphitic domains of ca. 5 to 20 nm.

X-ray diffraction analysis indicates a mean size of crystalline domains along the c axis of about 10 nm which resembles to 30 layers of graphene in turbostratic packing extracted from the (002) peak of the diffractogram. The XRD signature of purified and not purified samples is almost the same, prove that the heat treatment has successfully removed the amorphous part of the material since the XRD analysis probes principally the graphitic parts of the carbon samples.

The amorphous carbon has been also detected through **X-ray photoelectron spectroscopy**. The peak of the carbon spectra show that the samples consist principally of sp^2 carbon. A 40% of sp^3 carbon is however present for the unpurified materials and decreases to 25% for the purified ones (500 °C for 6 h). The fact that the content of oxygen groups in the samples before and after heat treatment remains practically the same, implies that the purification removes amorphous material and do not introduce defects in the graphitic layers.

Static light scattering analysis and UV/Vis absorption were used to determine the size of carbon particles in the aqueous dispersions. Two size populations (yield 79%) and one size population (yield 53%) could be obtained. Further data from SLS, TEM, AFM and STM analysis provide values of lateral size of the dispersed particles of 30 to 60 nm and height of 0.4 to 3.0 nm.

As aforementioned, the graphitic domains have size about 5 to 20 nm and the domains along the c axis about 10 nm, thus their values are in the same order of magnitude with the dispersed carbon objects. Therefore, it could be suggested that the present plasma process with biogas as a feedstock (mixture of methane and carbon dioxide) provides

well defined, crystalline carbon nanopucks (CNP) that could be harnessed in application such as conductive films as it will be presented in the following chapter.^{33,34}

Conclusion

Crystalline carbon nanopucks (CNPs) of turbostratically packed layers of graphene can be produced via microwave plasma process from the splitting of the mixture of methane and carbon dioxide. The graphitic products can be further improved by purification. Amorphous carbon content as low as 12% (for the best sample) could be removed by heat treatment (500 °C for 6 h). Moreover, their dispersion in aqueous media is feasible by using surfactant, sonication and centrifugation process. Monodispersed samples of 50% yield have been produced in this way with size of ca. 30 to 80 nm and 3 nm in thickness. A variety of characterization techniques has verified the high quality of the graphitic nature of these materials. CNPs are comparable or even superior to commercially available carbon black grades since they derive from an environmentally friendly feedstock.

References

1. Novoselov, K. S. *et al.* Two-dimensional gas of massless Dirac fermions in graphene. *Nature* **438**, 197–200 (2005).
2. Blake, P. *et al.* Graphene-based liquid crystal device. *Nano Lett.* **8**, 1704–1708 (2008).
3. Novoselov, K. S. *et al.* A roadmap for graphene. *Nature* **490**, 192–200 (2012).
4. Ferrari, A. C. *et al.* Science and technology roadmap for graphene, related two-dimensional crystals, and hybrid systems. *Nanoscale* **7**, 4598–4810 (2014).
5. Alexander, E. & Sommer, C. Systematic analysis of carbon black structures. *J. Phys. Chem.* **60**, 1646–1649 (1955).
6. Donnet, J.-B. Fifty years of research and progress on carbon black. *Carbon N. Y.* **32**, 1305–1310 (1994).
7. Voll, M. & Kleinschmit, P. in *Ullmann's Encyclopedia of Industrial Chemistry* 23–44 (Wiley-VCH Verlag GmbH & Co. KGaA, 2010).
8. Donnet, J.-B., Bansal, R. C. & Wang, M.-J. *Carbon black: science and technology.* (Dekker, 1993).
9. Boehm, H. P. Some aspects of the surface chemistry of carbon blacks and other carbons. *Carbon N. Y.* **32**, 759–769 (1994).
10. Fulcheri, L. *et al.* Plasma processing: a step towards the production of new grades of carbon black. *Carbon N. Y.* **40**, 169–176 (2002).
11. Boehm, H. . Surface oxides on carbon and their analysis: a critical assessment. *Carbon N. Y.* **40**, 145–149 (2002).
12. Kang, J., Li, O. L. & Saito, N. Synthesis of structure-controlled carbon nano spheres by solution plasma process. *Carbon N. Y.* **60**, 292–298 (2013).
13. Juan, L. *et al.* A New Grade Carbon Black Produced by Thermal Plasma Process. *Plasma Sci. Technol.* **5**, 1815–1819 (2006).
14. Gonzalez-Aguilar, J., Moreno, M. & Fulcheri, L. Carbon nanostructures production by gas-phase plasma processes at atmospheric pressure. *J. Phys. D. Appl. Phys.* **40**, 2361–2374 (2007).
15. Shashurin, a & Keidar, M. Synthesis of 2D materials in arc plasmas. *J. Phys. D. Appl. Phys.* **48**, 314007 (2015).
16. PlasCarb. Available at: <http://www.plascarb.eu/>.
17. Hof, F. *et al.* Conductive inks of graphitic nanoparticles from a sustainable carbon feedstock. *Carbon N. Y.* **111**, 142–149 (2017).
18. Li, Z. Q., Lu, C. J., Xia, Z. P., Zhou, Y. & Luo, Z. X-ray diffraction patterns of graphite and turbostratic carbon. *Carbon N. Y.* **45**, 1686–1695 (2007).
19. Fujimoto, H. Theoretical X-ray scattering intensity of carbons with turbostratic stacking and AB stacking structures. *Carbon N. Y.* **41**, 1585–1592 (2003).
20. Walker, P. L. Measurement and Crystal Sizes of Interlayer Spacings Carbons " in Turbostratic. *Carbon N. Y.* **1**, 3–9 (1963).

21. Ferrari, A. C. & Basko, D. M. Raman spectroscopy as a versatile tool for studying the properties of graphene. *Nat. Nanotechnol.* **8**, 235–246 (2013).
22. Jorio, A. & Cançado, L. G. Perspectives on Raman spectroscopy of graphene-based systems: from the perfect two-dimensional surface to charcoal. *Phys. Chem. Chem. Phys.* **14**, 15246 (2012).
23. Beams, R., Gustavo Cançado, L. & Novotny, L. Raman characterization of defects and dopants in graphene. *J. Phys. Condens. Matter* **27**, 83002 (2015).
24. Pimenta, M. A. *et al.* Studying disorder in graphite-based systems by Raman spectroscopy. *Phys. Chem. Chem. Phys.* **9**, 1276 (2007).
25. Eigler, S. *et al.* Statistical Raman Microscopy and Atomic Force Microscopy on Heterogeneous Graphene Obtained after Reduction of Graphene Oxide. (2014).
26. Hof, F., Bosch, S., Englert, J. M., Hauke, F. & Hirsch, A. Statistical Raman Spectroscopy: A Method for the Characterization of Covalently Functionalized Single-Walled Carbon Nanotubes. *Angew. Chemie Int. Ed.* **51**, 11727–11730 (2012).
27. Ferrari, A. C. & Robertson, J. Raman spectroscopy of amorphous, nanostructured, diamond-like carbon, and nanodiamond. *Philos. Trans. A. Math. Phys. Eng. Sci.* **362**, 2477–2512 (2004).
28. Ferrari, A. & Robertson, J. Interpretation of Raman spectra of disordered and amorphous carbon. *Phys. Rev. B* **61**, 14095–14107 (2000).
29. Cançado, L. G., Jorio, A. & Pimenta, M. A. Measuring the absolute Raman cross section of nanographites as a function of laser energy and crystallite size. *Phys. Rev. B* **76**, 64304 (2007).
30. Guardia, L. *et al.* High-throughput production of pristine graphene in an aqueous dispersion assisted by non-ionic surfactants. *Carbon N. Y.* **49**, 1653–1662 (2011).
31. Lotya, M. *et al.* Liquid Phase Production of Graphene by Exfoliation of Graphite in Surfactant / Water Solutions Liquid Phase Production of Graphene by Exfoliation of Graphite in Surfactant / Water Solutions. 3611–3620 (2009).
32. Carotenuto, G., Longo, A., De Nicola, S., Camerlingo, C. & Nicolais, L. A simple mechanical technique to obtain carbon nanoscrolls from graphite nanoplatelets. *Nanoscale Res. Lett.* **8**, 403 (2013).
33. Marinho, B., Ghislandi, M., Tkalya, E., Koning, C. E. & With, G. De. Electrical conductivity of compacts of graphene , multi-wall carbon nanotubes , carbon black , and graphite powder. *Powder Technol.* **221**, 351–358 (2012).
34. Sánchez-González, J., Macías-García, A., Alexandre-Franco, M. F. & Gómez-Serrano, V. Electrical conductivity of carbon blacks under compression. *Carbon N. Y.* **43**, 741–747 (2005).

Chapter 3

Carbon nanopuck dispersions

Table of contents

Chapter 3.....	89
Carbon nanopuck dispersions	89
Introduction.....	91
1. Liquid phase exfoliation	92
a. Graphite intercalation compounds	92
b. Dispersion of graphene oxide and reduced graphene oxide	93
c. Dispersion of graphene from pristine graphite.....	94
2. Experimental section.....	100
a. Carbon nanopucks purification	100
b. Characterization techniques	100
c. Formulation of the dispersion.....	100
3. Results and discussion.....	101
a. Characterization of unpurified CNP	101
X-ray photoelectron spectroscopy	101
Thermogravimetric analysis	101
b. Characterization of purified CNP.....	102
Raman spectroscopy	102
X-ray diffraction.....	103
c. Carbon nanopuck dispersion conditions.....	104
Choice of surfactant	105
Choice of sonication time-energy and type	107
Choice of surfactant concentration	108
CNP _{HT5} concentration	109
Centrifugation	111
Conductivity measurements	114
d. Characterization of carbon nanopuck dispersions.....	114
Atomic force microscopy.....	114
High resolution transmission electron microscopy	115
Conductivity measurements and scanning electron microscopy	116
Conclusion	118
References.....	119

Introduction

Harnessing the properties of carbon nanopucks (CNPs) that derive from the “cold” plasma process requires its dispersion into liquid media. In this chapter, well-defined, high concentrated aqueous CNP dispersions calibrated in size are described. The CNP grade that is used for the dispersions is similar regarding its size and shape, but differs from the ones described in chapter 2 regarding its synthetic parameters and the amount of amorphous carbon. The procedure that has been followed to acquire optimized CNP dispersions has been adapted to disperse CNP_{HTX} materials (chapter 2). For simplicity reasons, the nanocarbon sample will be referred as CNP₅ and CNP_{HT5} (after purification treatment) to distinguish it from the other CNP grades that have the designations CNP₀ to CNP₄ and CNP_{HT1} to CNP_{HT4} for the heat treated samples respectively.

Firstly, liquid exfoliation background is given, initially discussing graphite intercalation compounds, dispersion of graphene oxide and reduced graphene oxide and finally dispersion of graphene from pristine graphite with and without stabilizers.

Afterwards, in part 2 the experimental section presents the carbon nanopucks purification, characterization techniques and formulation of CNP_{HT5} dispersions. In part 3, in “results and discussions” characterization of CNP₅ is initially presented. Then, the purification procedure and the characterization of CNP₅ before and after heat treatment are described. Following the characterization, several parameters are determined to obtain optimized aqueous CNP_{HT5} dispersions. Part 3 ends with the characterization of CNP_{HT5} dispersions.

1. Liquid phase exfoliation

As witnessed from its name, in liquid phase exfoliation, graphite precursors are dispersed and/or dissolved in liquid media. Typically, the exfoliation occurs with the assistance of external energy. Graphite exfoliation into graphene in liquid media could be further categorized into dissolution and dispersion of graphene. Dissolution occurs through graphite intercalation compounds (GICs) while dispersions of graphene could be divided into categories based on the precursor: dispersion of graphene from pristine graphite or dispersion of graphene oxide (or reduced graphene oxide).

a. Graphite intercalation compounds

GICs are synthesized by injection of intercalant atoms or molecules between graphite layers. They provide a means to dissolve graphite through the reaction of alkali metals with graphite. In these materials, the plane distance is greater and the precursor's properties are altered.³ Addition of electrons (reduction) to the graphene layers through GICs formation e.g. KC_8 , $K(THF)_x C_{24}$ and $KC_{48}(NH_3)_4$ without sonication treatment results to the dissolution of graphite in organic solvents and these negatively charged sheets form two dimensional polyelectrolytes.⁴⁻⁷ An interesting study by Catheline *et al.* reported that the counterions' entropic gain promotes the dissolution of graphene in solution; a spontaneous process without sonication assistance.⁸ Other intercalants like oleum have been used to form GICs; upon thermal shock, a violent graphite exfoliation occurred.⁹ Shih *et al.* claimed that a majority of bi- or trilayer graphene solutions can be produced from graphite using iodine chloride (ICl) or iodine bromide (IBr) as intercalants.¹⁰ A recent ground-breaking study of Bepete *et al.* demonstrates the exfoliation of single layer graphene in organic solvent via GICs with successful ensuing transfer in aqueous media.¹¹ Particularly, KC_8 was initially prepared in inert atmosphere. Then, the graphenide ions are oxidized to graphene due to the contact with air. After air exposure, the solutions were directly transferred to degassed water. Degassed water was chosen in order to avoid the adsorption of gases dissolved in water on the surface of graphene. Without the presence of gases, water ions are readily adsorbed on the surface resulting to the electrostatic repulsion of the layers of graphene.

b. Dispersion of graphene oxide and reduced graphene oxide

The most common liquid phase exfoliation technique involves the oxidation of graphite followed by exfoliation in water.^{12,13} One of the most exploited oxidative treatments was developed by Hummers.¹³ In his study, a mixture of sulphuric acid (H_2SO_4), sodium nitrate ($NaNO_3$) and potassium permanganate ($KMnO_4$) was used, the sp^2 structure of graphene was disrupted inserting oxygen groups on the graphene layers and resulting in the formation of graphene oxide (GO). GO could be defined as an oxidized graphene layer having its basal planes decorated mostly with epoxide and hydroxyl groups and at the edges carboxyl and hydroxyl groups (fig. 3.1).¹⁴

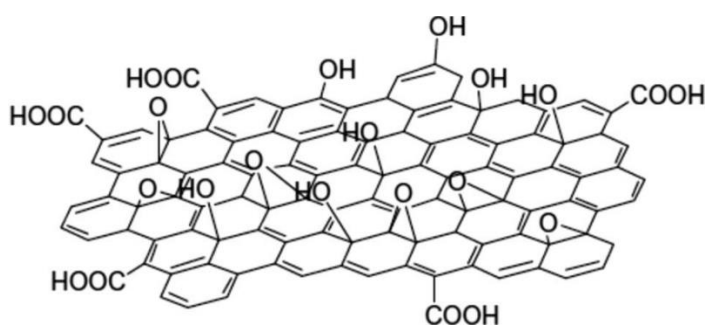


Figure 3.1: Proposed structure of graphene oxide (GO). Adapted from the reference ¹⁴.

The oxygen species allow the GO to be easier dispersed than graphite (make GO flakes hydrophilic) after sonication. The dispersion of GO can be achieved in a range of solvent as depicted in fig. 3.2 with better solubility to be achieved with dimethylformamide (DMF), N-Methyl-2-pyrrolidone (NMP), tetrahydrofuran (THF), ethylene glycol and water.¹⁵

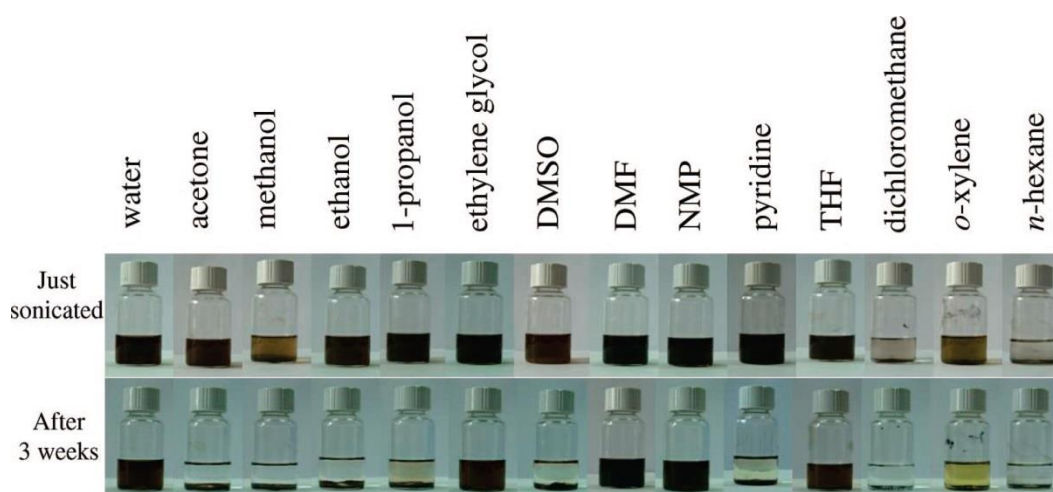


Figure 3.2: Digital pictures of GO dispersions in a variety of solvents immediately after sonication (top) and after settling 3 weeks (bottom). Adapted from the ref. ¹⁵.

However, GO is an insulating material (surface resistivity of $10^{12} \Omega \cdot \text{sq}^{-1}$ of a thin film from GO has been acquired)¹⁶, so in order to restore the graphene structure the GO is further reduced to yield reduced GO (rGO). There are several ways to reduce GO, e.g. chemical reduction, like hydrazine¹⁷ and hydride¹⁸ and thermal reduction.^{19,20} However, even after reduction treatment, the oxygen groups cannot be completely removed, thus the electronic and thermal properties are not as good as of pristine graphene. The results concerning the rGO dispersibility has been determined by Konios *et al.* as shown in **table 3.1**.²¹

Table 3.1: GO, rGO solubility values in a range of solvents. Reprinted (adapted) from Konios *et al.*²¹

Solvents	GO Solubility ($\mu\text{g/mL}$)	rGO Solubility ($\mu\text{g/mL}$)
Di water	6.6	4.74
Acetone	0.8	0.9
Methanol	0.16	0.52
Ethanol	0.25	0.91
2-propanol	1.82	1.2
Ethylene glycol	5.5	4.9
Tetrahydrofuran (THF)	2.15	1.44
N,N-dimethylformamide (DMF)	1.96	1.73
N-methyl-2-pyrrolidone (NMP)	8.7	9.4
n-Hexane	0.1	0.61
Dichloromethane (DCM)	0.21	1.16
Chloroform	1.3	4.6
Toluene	1.57	4.14
Chlorobenzene (CB)	1.62	3.4
<i>o</i> -Dichlorobenzene (<i>o</i> -DCB)	1.91	8.94
1-Chloronaphthalene (CN)	1.8	8.1
Acetylaceton	1.5	1.02
Diethyl ether	0.72	0.4

c. Dispersion of graphene from pristine graphite

Due to the defects that are present in rGO,¹⁷ several studies have focused to the dispersion of unfunctionalized graphene commonly with the help of ultrasonication.

i. Sonication

Conventional dispersion methods involve stirring. However, when the dispersed solid particles are of $10 \mu\text{m}$ size or smaller, then the rate of mixing and mass transfer reach a maximum value that cannot be overcome even if the speed is increased.²² By applying sonication, shear forces along with cavitations induce exfoliation of the graphite sheets.²² Cavitation is the phenomenon that occurs when high power ultrasound is

introduced in a liquid medium. At this process, the sound waves are transmitted in the liquid, creating alternating high-pressure (compression) and low-pressure (rarefaction) cycles. During the low-pressure cycle, high-intensity ultrasonic waves create small vacuum bubbles in the liquid. When the bubbles have a maximum volume above which they cannot absorb any more energy, they collapse violently during a high-pressure cycle. During the collapse, high temperature and pressure are reached locally.^{22,23} In the liquid, the particles vibrate due to cavitation process. These vibrations can break particles apart, and lead to their successful dispersion in a liquid media.²⁴ Sonicators can produce sound waves into a water bath (bath sonicator) where samples are placed, or can be probes that are put directly into the sample to be sonicated (tip sonicators).

ii. Dispersion of graphene from pristine graphite without stabilizer

Graphene or few layers of graphene can be dispersed in specific organic solvents without the use of surfactants.^{25,26} Carbon precursors are sonicated in organic solvents to yield graphene dispersions. Key parameter for a successful dispersion is the low interfacial tension between the graphite surface and the solvent in order to overcome the van der Waals forces between the graphene layers. If the value of interfacial tension is high, then the dispersion of the solid particles in the liquid medium is not efficient since poor association of the solid surface with the liquid occurs. For better exfoliation of graphene, solvents with surface tensions of ca. 40 mJ.m⁻² are preferable, e.g. NMP, DMF and ortho dichlorobenzene (*o*DCB).^{25,27} Hernandez *et al.* have shown that graphene sheets with a concentration of 0.01 mg.mL⁻¹ can be successfully dispersed in NMP.²⁵ Since then, many studies have followed so as to increase the graphene concentration by increasing the sonication time. Sonication time as high as 200 h would reach a concentration of 1.5 mg.mL⁻¹.²⁸ By applying ultrasound for extended time period, the flake size is reduced and the quality of graphene could be also affected while the process is considered high energy consuming. After sonication treatment, the presence of aggregates is removed by centrifugation. A drawback of stabilizer-free exfoliation is the use of toxic solvents with high boiling points which is not easy to remove.²⁹ Other studies to disperse graphene without stabilizer have been performed using ionic liquids (ILs), e.g. 1-hexyl-3-methyl-imidazolium hexafluorophosphate (HMIH), 1-alkyl-3-methylimidazolium and other imidazolium based ILs. The dispersion in ILs has been achieved via sonication, ball milling, shear milling, and electrochemical exfoliation techniques.³⁰⁻³³ ILs are semi-organic salts with melting point below 100 °C. They differ

from organic solvents in characteristics such as good thermal stability and non-flammability. ILs constitute efficient solvents for graphene dispersions because their surface tensions closely match with graphite.³¹ Furthermore, they are moderate conductors of electricity, thus electrochemical exfoliation could be performed. In **fig. 3.3** graphene sheets start to get dispersed in the ionic liquid from a piece of highly oriented pyrolytic graphite (HOPG) which is used as anode in an ionic liquid/water solution and placed parallel to the Pt wire (counter-electrode) after voltage application.³⁰

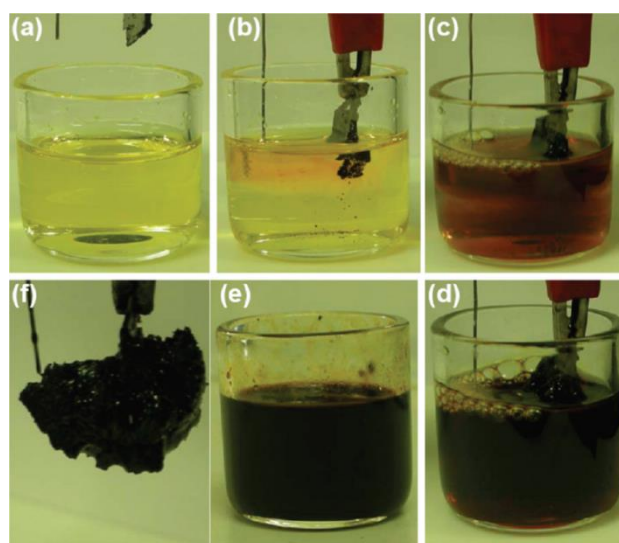


Figure 3.3: Electrochemical exfoliation of graphite into graphene in ionic liquid. Adapted from reference ³⁰.

Notable is also that graphene exfoliation progresses with time. However, the drawbacks of the use of ILs are that their removal from the dispersion is difficult while thick graphene flakes are produced (2 to 3 nm). Notable is also the use of superacids such as chlorosulfonic acid.³⁴ Superacids do not disperse graphene layers but rather dissolve them since they protonate the graphene surface. Behabtu *et al.* performed a successful exfoliation of graphene at concentration of ca. 2 mg.mL⁻¹.³⁴

iii. Dispersion of graphene from pristine graphite with stabilizer

Stabilizers such as surfactants, polymers and smaller aromatic molecules, e.g. pyrene derivatives have widely been used to aid the dispersion of graphene. The dispersion of graphene in water is particularly intriguing due to the hydrophobic nature of the graphene sheets. Graphite can be sonicated in water as an external mechanical energy that helps the particles to overcome the attractive van der Waals forces at contact in the presence of surfactant. Surfactants, and in general stabilizers, can modify the particles-

dispersing medium interface and prevent aggregation. They provide an extra repulsive force (electrostatic and/or steric) and lower the surface energy.³⁵ Due to cavitations created during sonication, the layers of graphene come apart. At this point, the hydrophobic part (tail) of the surfactant (surface active agent) non-covalently adsorbs on the graphene surface (through van der Waals interaction) leaving the hydrophilic part to interact with the aqueous environment keeping the graphene sheets stable in water. Hence, it does not unduly disturb the electronic properties of graphene and the use of toxic solvents is avoided as well as the aggregation of graphene sheets and the presence of oxygen on graphene surfaces. After sonication treatment, centrifugation follows in order to remove the large aggregates. Green *et al.* have dispersed graphene in aqueous medium in concentration of 0.09 mg.mL^{-1} using the surfactant sodium cholate (SC).³⁶ In particular, graphite flakes were mixed with SC in aqueous solution. After exfoliation of few layer graphene flakes by using horn sonicator, graphene flakes were encapsulated by SC micelles. In **fig. 3.4** is depicted the proposed mechanism for the surfactant stabilization of graphene in water. ³⁶



Figure 3.4: Schematic illustration of the graphite exfoliation into graphene. Adapted from ref. ³⁶.

Another study to exfoliate graphene in organic solvent, e.g. N,Ndimethylformamide (DMF) has been performed by Vadukumpully *et al.*³⁷ They used cationic cetyltrimethyl ammonium bromide (CTAB) as stabilizer to avoid agglomeration that commonly occurred in dispersions in organic solvents without stabilizer.²⁵ Several are the surfactants that have been used from research groups so as to exfoliate graphene in

aqueous or organic media, e.g. sodium dodecylsulfate (SDS), dodecyl benzene sulfonic acid (SDBS) and CTAB which could yield as high concentrations as 0.3 mg.mL⁻¹.³⁸⁻⁴⁰ Moreover, Guardia *et al.* by studying a variety of surfactants, have shown that based on the surfactant (ionic and non-ionic), the final concentration of the graphene in aqueous media could vary from <0.1 mg.mL⁻¹ for SDBS to >0.8 mg.mL⁻¹ with triblock copolymer poly(ethylene glycol)-poly(propylene glycol)-poly(ethylene glycol) (P123), as depicted in **fig. 3.5**.⁴¹

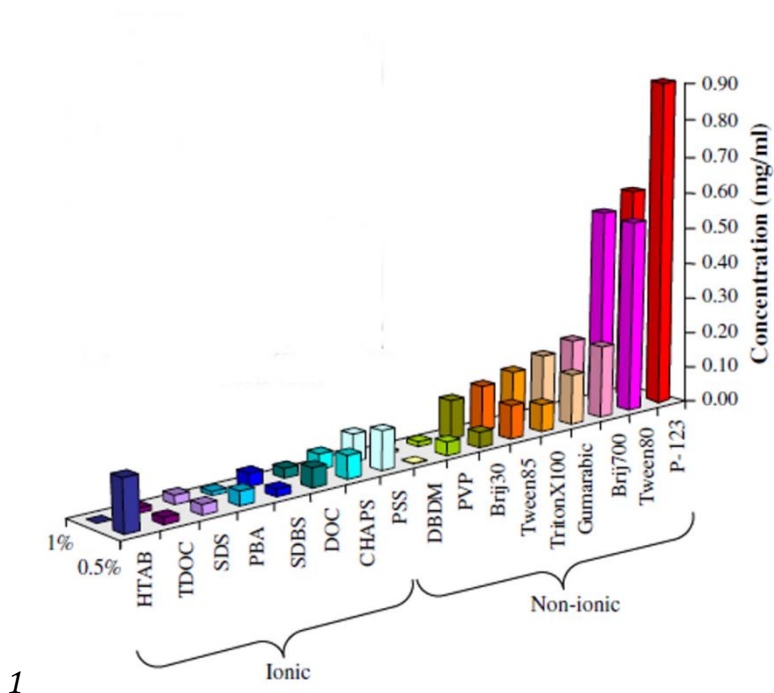


Figure 3.5: Concentration of graphene in aqueous media by the use of different surfactants. Adapted from the reference ⁴¹.

Furthermore, graphene sheets could be stabilized in water or organic solvents through polymer protection (steric stabilization) such as polyvinylpyrrolidone (PVP) and ethyl cellulose.^{42,43} **Fig. 3.6** illustrates a schematic representation of PVP stabilization of graphene.⁴²

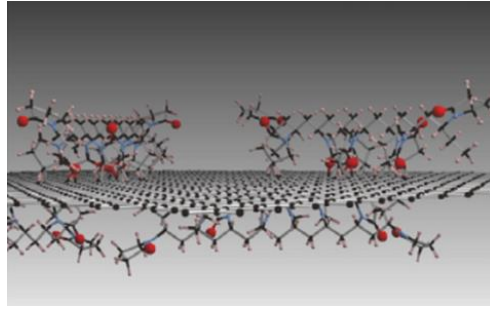


Figure 3.6: Schematic model of PVP-coated graphene. Adapted from ⁴².

Another category of stabilizers that have been used by various groups are polycyclic aromatic hydrocarbons (PAHs).^{44–47} Pyrene is a prominent example of PAHs. These molecules have a pyrene aromatic core with functional groups attached to the core. Adsorption of these stabilizers on the graphene surface occurs through π - π interactions between their planar surfaces and graphene (both aromatic planar surfaces share non-covalently the electrons of π -orbitals) reducing the surface free energy of the dispersion. Several are the solvents and stabilizers that have been used and they are currently used by research groups for a successful exfoliation of graphene with the best compromise between cost and quality of graphene. Novoselov *et al.* in their study have reviewed the different synthesis routes of graphene exfoliation based on the quality and the cost as depicted in **fig. 3.7**.⁴⁸

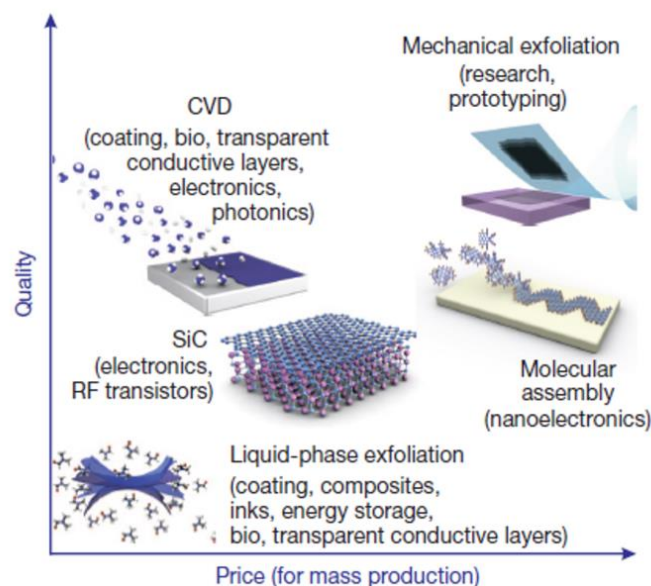


Figure 3.7: There are several methods of mass-production of graphene, which allow a wide choice in terms of size, quality and price for any particular application. Adapted from reference ⁴⁸.

2. Experimental section

a. Carbon nanopucks purification

The purification of CNP₅ was achieved by heat treatment in a home-made oven based on the data provided from thermogravimetric analysis (TGA). Particularly, CNP₅ was heated at 450 °C overnight.

b. Characterization techniques

Ahead of any endeavor to disperse carbon nanopucks (CNPs), their structure and nature had to be defined. Their characterization was performed using a series of techniques: X-ray photoelectron spectroscopy (XPS), thermogravimetric analysis (TGA), Raman spectroscopy, X-ray diffraction (XRD), atomic force microscopy (AFM), high resolution transmission electron microscopy (TEM) and scanning electron microscopy (SEM). Their parameters are described in chapter 2. Any modification will be highlighted where is needed.

X-ray diffraction (XRD) patterns were acquired with the same parameters as described in chapter 2. Each acquisition lasted for 7 hours.

Static light scattering (SLS) analysis was performed using a Mastersizer 2000 - Malvern Instruments. The dispersions have been diluted ca. 5 % and the scattered light in different angles was recorded. The particle size was taken directly from the software which used the Mie theory.

High resolution transmission electron microscopy (TEM) investigation was kindly performed by Luca Ortolani (CNR IMM – Bologna) using a Tecnai F20 microscope, operated at an accelerating voltage of 80 kV. The sample has been diluted in isopropanol (10 microliters in 1 ml) and then drop casted over a TEM grid.

Scanning electron microscopy (SEM) was performed on FEI QUANTA 200 scanning electron microscope.

c. Formulation of the dispersion

Dispersion of CNP_{HT5} after purification treatment has been obtained by using surfactant, tip sonication and centrifugation treatment. Several parameters, such as surfactant, sonication and centrifugation time have been optimized in order to acquire well-defined high concentrated CNP_{HT5} dispersions calibrated in size. Techniques such as static light scattering, atomic force microscopy and high resolution transmission electron microscopy have been used to characterize the dispersions. The parameters for

optimized CNP dispersions described in this chapter, have been used to disperse the CNP_x (where x is from 0 to 4 respectively) samples characterized in chapter 2.

3. Results and discussion

a. Characterization of unpurified CNP

X-ray photoelectron spectroscopy

Fig. 3.8 illustrates the XPS spectra of CNP_5 (before purification treatment).

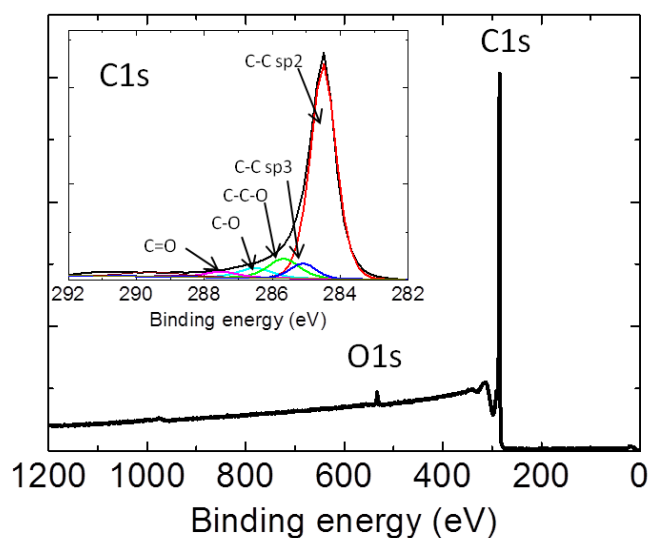


Figure 3.8: XPS spectra and fits of the respective carbon peak of CNP_5 .

Carbon and oxygen peaks at 285 eV and 533 eV respectively can be clearly observed. In the inset, the carbon spectrum shows a broad carbon peak accompanied with a broad tail. The tail represents a variety of carbon oxygen bonds and the presence of a small amount of sp^3 carbon. From XPS analysis, the atomic carbon and oxygen percentages have been calculated with carbon to be more than 98 % and oxygen 1.77 %.

Thermogravimetric analysis

TGA was performed in order to determine the mass loss as a function of temperature of CNP_5 under air atmosphere as depicted in **fig. 3.9**.

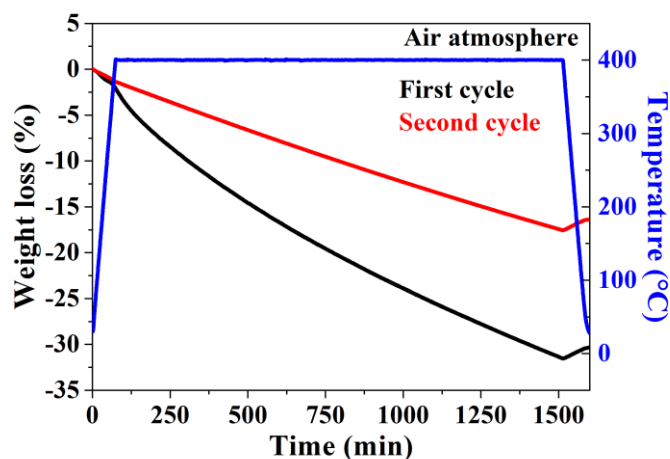


Figure 3.9: Thermogram of raw CNP under Air atmosphere.

In the first cycle, the carbon powder is burning as a function of increasing temperature in a relatively high speed until a weight loss of 10-15 wt% at 400 °C which indicates the presence of 10-15% amorphous carbon. Then, the decomposition continues with a lower speed due to the remaining well-organized material.

b. Characterization of purified CNP

After heat treatment at 400 °C in air, the amorphous material has been successfully removed from CNP₅. The purification parameters are described in chapter 2.

Raman spectroscopy

In a Raman spectrum of a carbonaceous material, the significant bands are D, G and 2D bands. ^{49-51,52} **Fig 3.10** shows the Raman spectra of carbon nanopucks before and after purification treatment at excitation wavelength 638 nm.

In the previous chapter the Raman characterization of CNP samples has been presented where it was used excitation wavelength at 532 nm (page 61). The intensity of the Raman signal is inversely proportional to the excitation wavelength. Starting the Raman analysis with this sample (CNP₅) by exciting at 638 nm, we decided to change excitation wavelength to 532 nm in order to increase the intensity and to compare more easily our results with the literature.

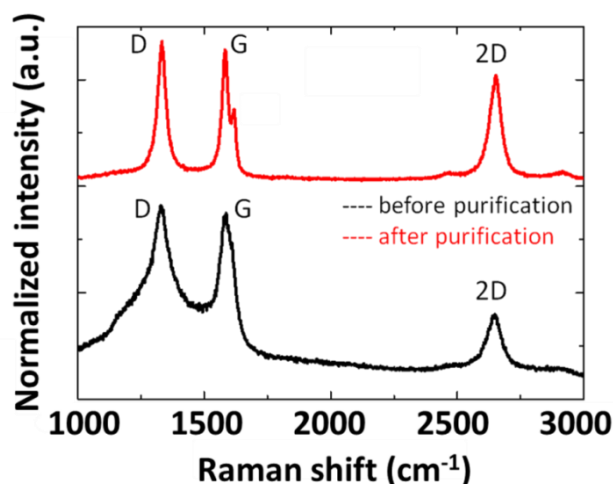


Figure 3.10: Raman shift versus the normalized intensity of the carbon nanopucks samples measured at 638 nm excitation wavelength before and after purification treatment.

A general comparison of the two spectra suggests that, from a structural point of view, the heat treated material is much more graphitized than before heat treatment since the amorphous background is eliminated after purification. The most prominent feature in the Raman spectra is the G band, an indication of sp² carbon network. The D band is related to the presence of structural defects and 2D band is a 2 phonon process and does not need a defect to be activated. Also it satisfies the Raman selection rule of zero momentum ($+q-q=0$, in a 2 phonon process with phonon of opposite signs). The 2D band, located at 2655 cm⁻¹ appears as broad and weak feature in the case of raw CNP₅, in comparison to the sharper and stronger after purification treatments which corresponds to a more crystalline sample. Likewise, the full width at the half maximum (FWHM) of 47 cm⁻¹ of the 2D band reflects the turbostratic order of the carbon samples.⁵³

X-ray diffraction

In **fig. 3.11** are depicted the XRD spectra of carbon nanopucks before and after thermal annealing.

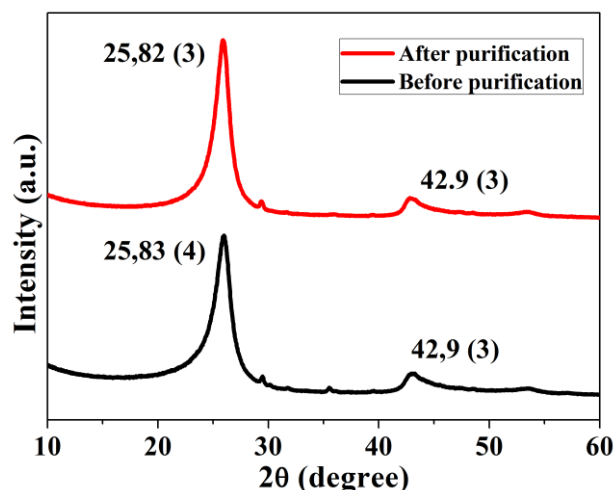


Figure 3.11: XRD data of carbon nanopuck samples before and after heat treatment. (Cu-K α radiation of $\lambda = 0.15418$ nm).

Both diffractograms show three distinct peaks at ca. 25.8°, 43° and ca. 53° 2 θ degrees. Samples before and after thermal annealing are identical. The peak at ca 25.8° corresponds to the (002) peak of graphite. Its FWHM is rather broad, more than 1.6°, typical for nanosized graphitic carbons.⁵⁴ Moreover, from Scherrer equation, the mean crystalline size was calculated from 8 to 10 nm which corresponds to 25-30 planes turbostratically packed since from Bragg's law, the d-spacing between layers was calculated 0.345 nm.

c. Carbon nanopuck dispersion conditions

For a useful CNP dispersion, essential criteria must be met: the carbon should be dispersed at an appropriate concentration, with an efficient dispersive agent and the consumption of a minimum viable energy. In this chapter the preparation of aqueous dispersions of CNP_{HT5} with the aid of surfactant is presented. The performances of CNP_{HT5} dispersions are compared with different surfactants-assisted dispersion in water, different types and time of sonication and time/rate of centrifugation. Well defined monodispersed or bidispersed CNP_{HT5} dispersions have been prepared. Concentrations, as high as 64 mg.mL⁻¹, can be attained with the use of ionic surfactant. The potential utility of these highly concentrated dispersions is demonstrated by using them as conductive inks or by preparing multifunctional polymer composites (chapter 4).

Choice of surfactant

The use of small organic molecules such as surfactants, promote the nanocarbon dispersions stabilizing the particles in water. A variety of stabilizers has been used from several research groups so as to disperse different forms of graphitic allotropes as abovementioned.^{25,36-48}

In this study, three main stabilizers were tested: poly(ethylene glycol)-block-poly(propylene glycol)-block-poly(ethylene glycol) or P123 (Pluronic P123) (**fig. 3.12 a**), polyethylene-block-poly(ethylene glycol) or PE-PEG (**fig. 3.12 (b)**), and bile Salt (**fig. 3.12 c**); purchased from Sigma Aldrich.

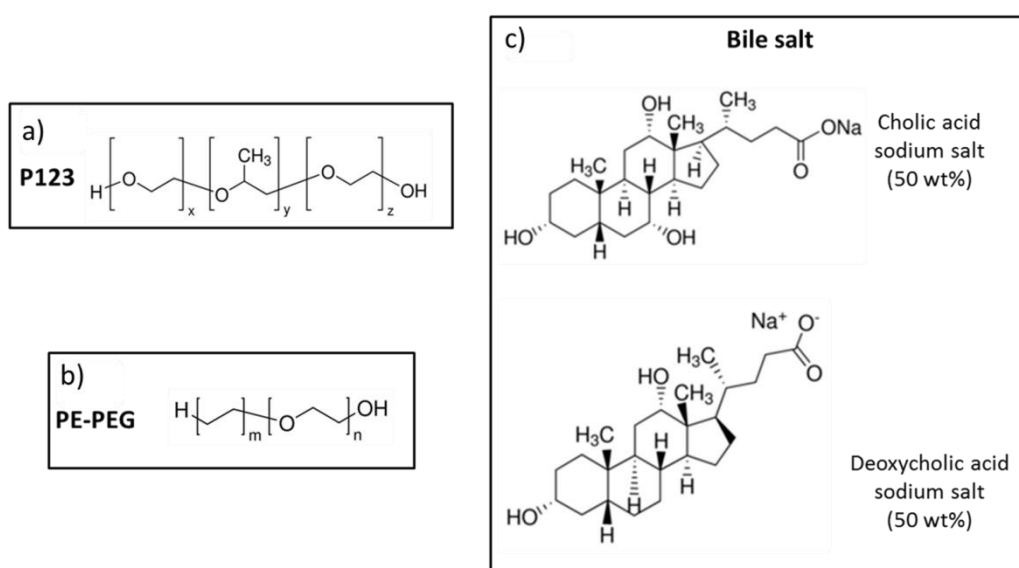


Figure 3.12: Surfactants: (a) P123, (b) PE-PEG and (c) bile salt.

The CNP_{HT5} dispersions have been tested for surfactant concentration of 0.3 wt%, typical tip sonication time of 1 h and at CNP concentration of 0.1 wt% in aqueous media. Optical spectroscopy was the technique of choice to estimate the dispersion ability of the surfactants. **Fig. 3.13** shows the optimum dispersion of each surfactant (with the minimum amount of aggregations).

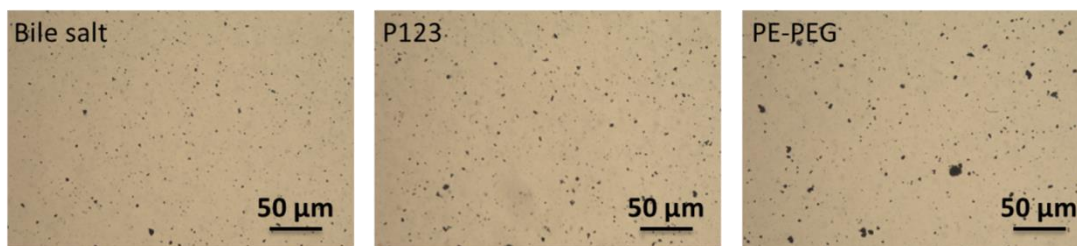


Figure 3.13: Optical microscopy images of CNP_{HT5} dispersions using left: bile salt, center: P123 and right: PE-PEG respectively.

Likewise, ahead of any optical observation, the samples have been left for 30 min for sedimentation of the largest aggregates to occur. After several trials, the less efficient surfactant appears to be PE-PEG with bile salt and P123 to show similar performances. Due to the fact that it is a biomaterial and easy to manipulate (powder form), **bile salt has been considered as the most suitable surfactant.**

Significant topic at this point to be elucidated is the arrangement of bile salts in the carbon dispersions. Due to their relatively bulky and rigid nature, bile salt surfactants differ from aliphatic surfactants. Owing to the arrangement of hydrophobic and hydrophilic groups, bile salts show a planar polarity (hence, they are facial amphiphiles), as illustrated in **fig. 3.14**.⁵⁵

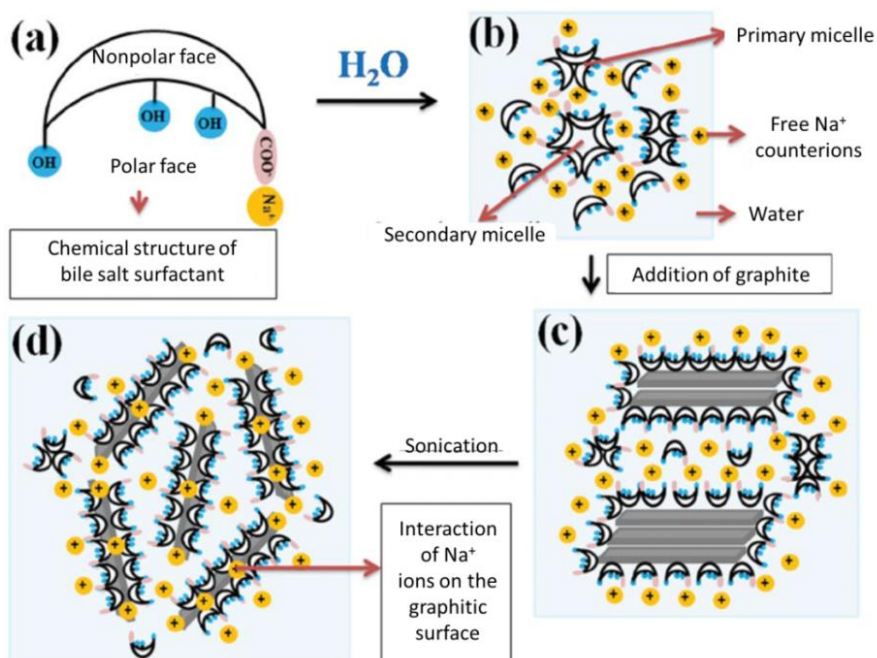


Figure 3.14: (a) Schematic structure of polar parts of bile salt molecules. (b) Micellization of surfactants. (c) Solubilization of graphite inside the micelles and (d) exfoliation of graphite into graphene and interaction of counterions with graphene/surfactant surfaces. Adapted from reference ⁵⁵.

Hydrophobic faces of surfactants with carbon aggregates interact forming primary micelles. Then, aggregation of primary micelles occurs due to the hydrogen bonding force among the hydrophilic faces resulting in formation of secondary micelles with rod-like or spherical shape (**fig. 3.14 b**) having both hydrophobic (van der Waals) and hydrophilic (H-bonding) interactions. Aqueous dispersion of graphitic particles occurs due to the hydrophobic interaction with the nonpolar face of bile salt molecules which form micelles around particles (**fig. 3.14 c**). Re-aggregation of surfactant-coated particles is hindered by electrostatic repulsive interactions between them. Also, when the concentration of surfactants in the dispersion is higher than their critical micelle concentration (CMC) values, the Na^+ counterions can interact with the graphene/micelle surfaces (**fig. 3.14 d**).⁵⁶

Choice of sonication time-energy and type

In 2008, Coleman's group has been successfully exfoliated sonicated-assisted few layers of graphene.²⁵ Since then, optimizations have been made regarding the time and energy of sonication in a combination with increased concentration and quality of graphitic dispersions.^{29,41,55} In this study, sonication type, time and energy have been investigated. Once the surfactant (bile salt) has been selected, the sonication type had to be assessed. Between bath and tip sonication (bath sonicator Elmasonic X-tra 100 H and tip sonicator Branson Digital Sonifier), keeping constant the other parameters such as CNP_{HT5} and bile salt concentration, **more efficient dispersion has been achieved via tip sonication** as depicted in **fig. 3.15**.

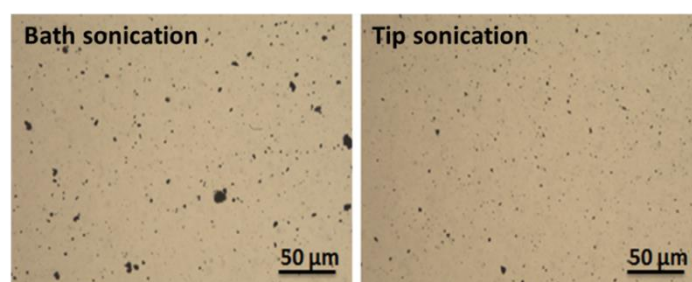


Figure 3.15: Optical microscopy images of the CNP_{HT5} dispersions using bath sonication (left) and tip sonication (right) (samples: 0.1 wt% CNP_{HT5} , 0.3 wt% bile salt in H_2O after 1h sonication).

With increasing sonication time (\approx energy), the size of graphitic flakes is severely reduced, being a critical parameter for several applications.²⁹ Moreover, long sonication times can also affect the quality of graphene, for example due to heating effect.

In our study, several sonication times up to 5 h (maximum energy 144 kJ)⁵⁷ have been tested with sonication times 30 min, 1h and 2h to exhibit the best performances as shown in **fig. 3.16**.

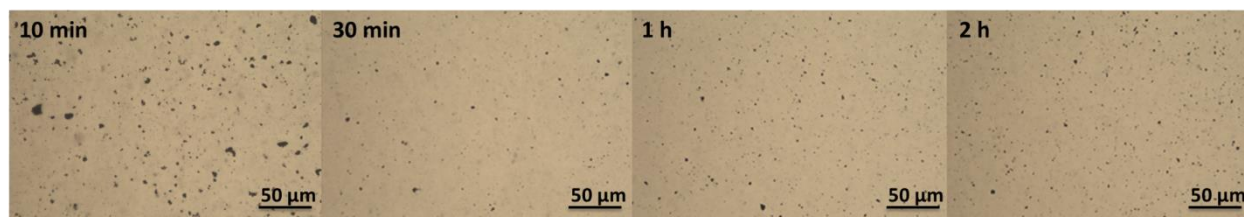


Figure 3.16: Optical microscopy images of the CNP dispersions using tip sonication times, from the left to the right, of: for 10min, 30 min, 1h and 2 h.

Thus, **sonication time of 30 min** (total applied energy of 14.4 kJ), as the less time consuming, has been chosen.

Choice of surfactant concentration

Dispersions with several bile salt concentrations have been prepared below and above the CMC in order to acquire the optimum concentration for a successful CNP_{HT5} dispersion.⁵⁸ Continuous increase of surfactant concentration starting from CNP_{HT5}/bile salt ratio 2, has ultimately led to a depletion effect as depicted in the optical image in **fig. 3.17 (a)** (with the results to be reproducible as shown in **fig. 3.17 (b)**).

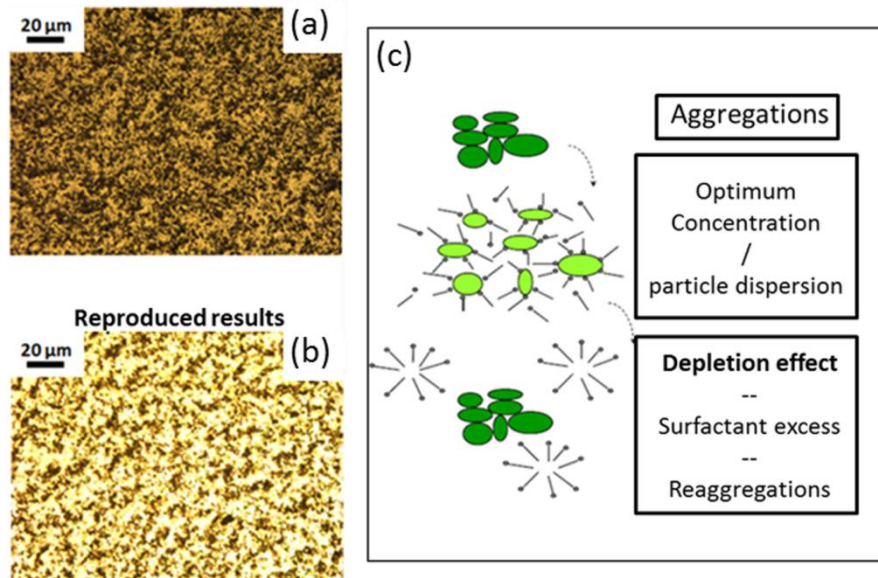


Figure 3.17: (a) and (b): Optical microscopy images of CNP_{HT5} dispersion with 4 wt% (40 mg.mL^{-1}) bile salt, 6.4 wt% (64 mg.mL^{-1}) CNP_{HT5} and tip sonication 30 min, showing the depletion effect. (c): Schematic representation of the depletion effect.

Depletion forces are often considered as entropic forces, based on Asakura-Oosawa model.⁵⁹ In this theory, the depletion force arises from an increase in osmotic pressure of the surrounding solution when colloidal particles get close enough such that the excluded depletants cannot fit in between them (**fig. 3.17 (c)**). For samples with lower surfactant concentration (30 mg.mL^{-1} or less) no surfactant depletion is observed. After extended investigation, a ratio 6 of CNP_{HT5} to bile salt concentration has been chosen for dispersion with the minimum amount of aggregates (**fig. 3.18**).

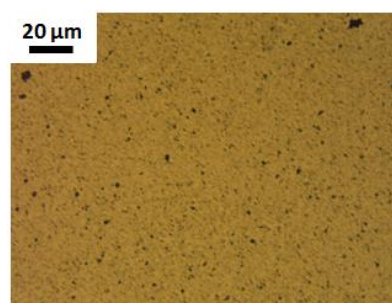


Figure 3.18: Optical microscopy image of aqueous dispersion with 1 wt% bile salt (10 mg.mL^{-1}), 6.4 wt% CNP_{HT5} (64 mg.mL^{-1}) and tip sonication: 30 min.

CNP_{HT5} concentration

Dispersions with various CNP_{HT5} concentrations have been prepared. Their optical images are presented in **fig. 3.19**.

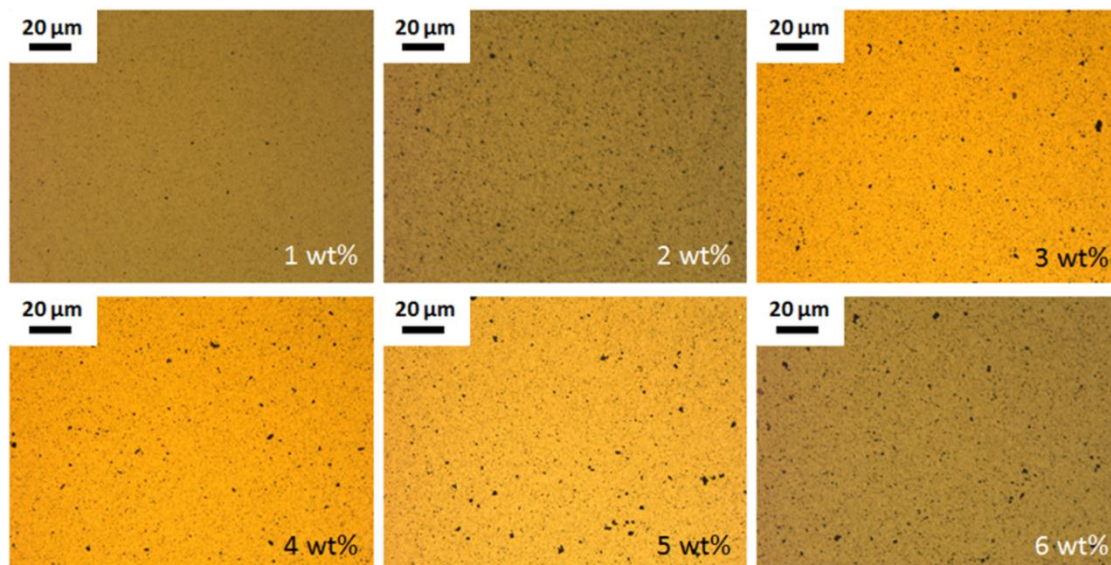


Figure 3.19: Optical microscopy images of aqueous dispersions with 1 wt% bile salt (10 mg.mL^{-1}) and 1-6 wt% CNP_{HT5} ($10\text{-}60 \text{ mg.mL}^{-1}$) in aqueous media after 10 min tip sonication.

After trials, a highly concentrated CNP_{HT5} dispersion of 6.4 wt% (64 mg.mL^{-1}) (other parameters: 1 wt% bile salt, 30 min tip sonication) has been acquired, as illustrated in **fig. 3.20**. Due to the great CNP_{HT5} content, observation by optical microscope with a conventional way (**fig. 3.20 up**) was not possible (the light couldn't be transmitted). Another solution to observe highly concentrated dispersions has been achieved by designing a narrow path between two glass slides for the dispersion to flow due to capillary forces. The path was created by placing carbon fiber of 7 μm thickness between two glass slides (**fig. 3.20 bottom**).

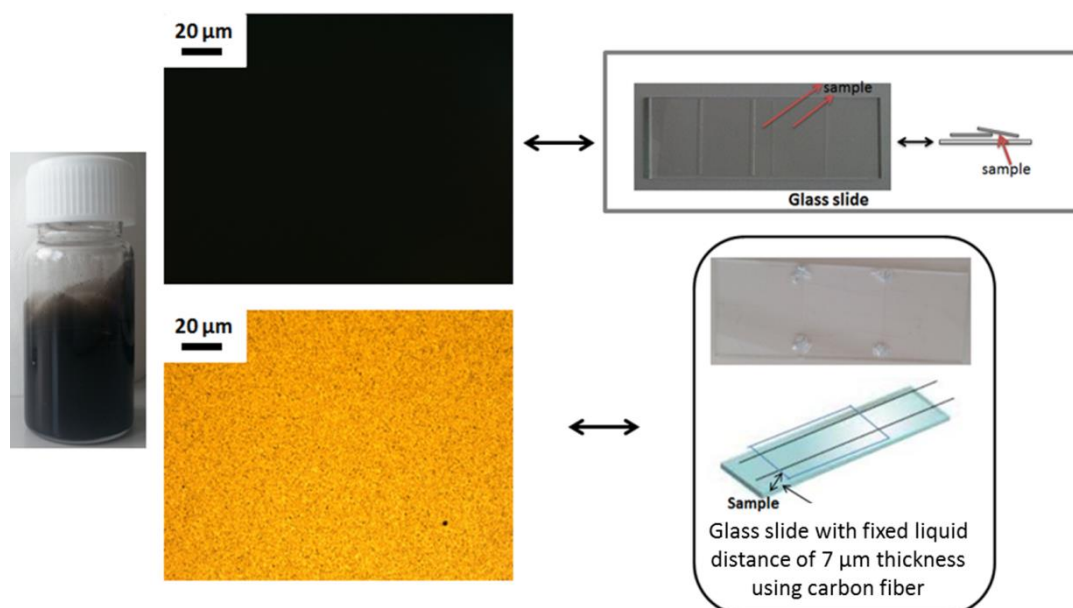


Figure 3.20: Left: Aqueous dispersion of 6.4 wt% CNP_{HT5}, 1 wt% bile salt and 30 min tip sonication after 2 min /4000 rpm centrifugation.

Optical microscopy images of the aqueous dispersion observed: up: by placing a drop between two glass slides. Bottom: by placing a drop between two glass slides of path thickness 7 μm .

Centrifugation

Once the dispersion had been sonicated, the samples were allowed to settle down for 30 min to sediment the large aggregates. Alternatively, the dispersion could be centrifuged for the minimum time (2 min) to remove the undispersed parts. Moreover, in order to separate the two size populations, the dispersions have been centrifuged at various times (up to 2 h) at 4000 rpm. The size analysis of the carbon particles dispersed in the aqueous media has been performed with the static light scattering (SLS, Malvern instrument, Mastersizer 2000) as a method of choice. In **fig. 3.21** optical images and SLS spectra of CNP dispersions with centrifugation times up to 40 min are presented.

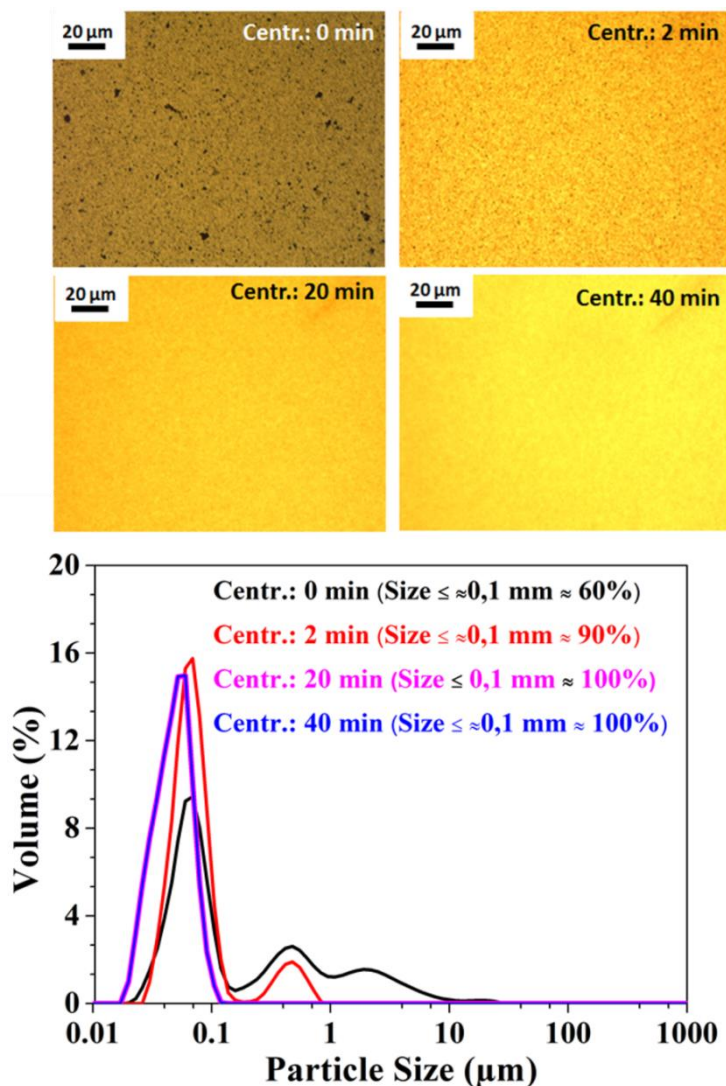


Figure 3.21: Dispersions of 6.4 wt% CNP, 1 wt% bile salt in water after tip sonication of 30 min and centrifugation times 0, 2, 20 and 40 min at 4000 rpm.

Up: their optical microscope images, bottom: their static light scattering analysis.

Monodisperse samples were obtained from 20 min centrifugation. With higher centrifugation times the final concentration is decreased. A successful elimination of the large aggregates has been acquired after 2 min (or more) centrifugation as it can be seen from the optical microscope images. From SLS analysis, CNP dispersions with no and after 2 min centrifugation treatments demonstrate particles with two size populations. For centrifugation 20 min and higher, a successful isolation of a narrow size distribution CNP particles of around 65 nm has been achieved. Aqueous CNP dispersions with centrifugation times 2 min and 20 min have been repeated several times. The results are reproducible as depicted in **fig. 3.22** and **fig. 3.23**.

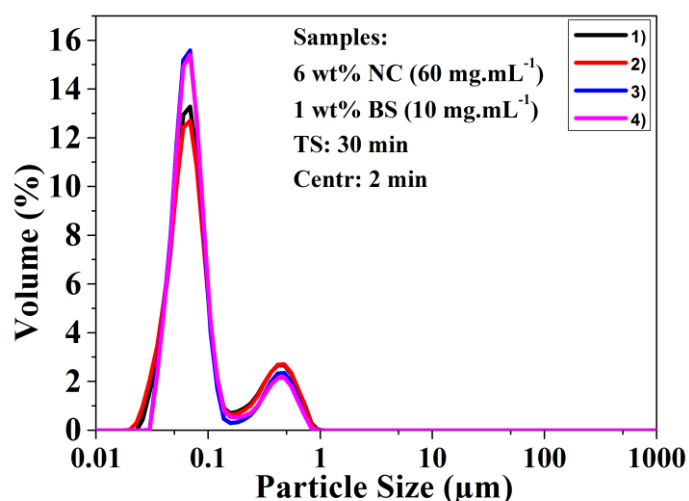


Figure 3.22: Static light scattering spectra of CNP dispersion with final concentration 6 wt% and particles of two size populations with reproducible results.

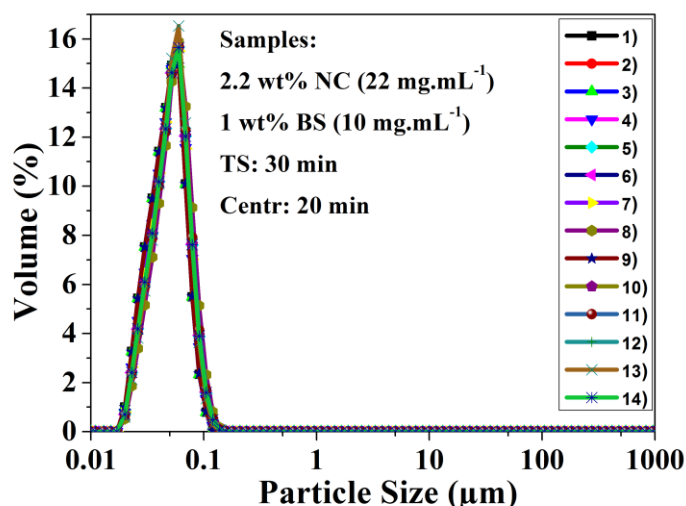


Figure 3.23: Static light scattering spectra of monodispersed CNP dispersions with final concentration 2.2 wt% with reproducible results.

The final concentrations of CNP dispersions have been verified after weighting the freeze dried powders. Dispersion with two size populations (centr.: 2 min) is about 6.0 wt% (60 mg.mL⁻¹) CNP with 1 wt% (10 mg.mL⁻¹) surfactant (yield ~94 %) and the final concentration of monodispersed CNP dispersion (centr.: 20 min) is about 2.2 wt% (22 mg.mL⁻¹) with (1 wt%) (10 mg.mL⁻¹) surfactant (yield ~34 %). The dispersions were used for AFM, HRTEM characterizations and to prepare conductive films.

Conductivity measurements

Based on the dispersion parameters defined in this chapter, successful dispersions of CNP_{HTX} have been formulated (as mentioned in chapter 2). Conductive films of CNP_{HTX} samples) were prepared by filtration of the CNP_{HTX} dispersions on a polyvinylidene fluoride (PVDF) hydrophilic membrane of 0.10 μm porosity. Dispersions of 0.25 mL, 0.5 mL and 1 mL of concentration 0.9 $\text{mg}\cdot\text{mL}^{-1}$ were diluted in 10 mL water (when more carbon was used, the film was thicker, which eventually gives the volume resistance). The films were then rinsed with Milli Q water to remove the surfactant and dried under vacuum as depicted in **fig. 3.24 a.** and **fig. 3.24 b.** Then the films were patterned by four gold contacts through a mask (**fig. 3.24 c.**) in order to measure the surface resistivity using a home-made four-point probe setup. Furthermore, the thickness of CNP_{HT} films was measured by SEM.

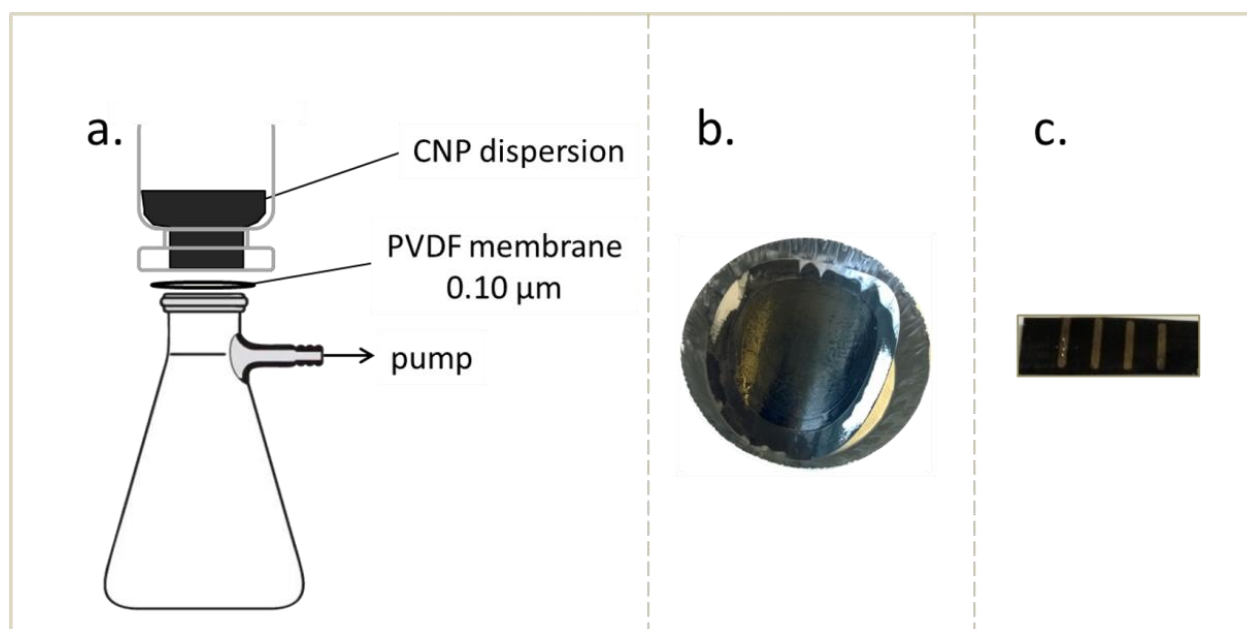


Figure 3.24: Scheme of filtration under vacuum used for the formulation of conductive films. b. Representative conductive film (diameter of 3.5 cm). c. Representative conductive film after cutting and deposition of the four gold contacts.

d. Characterization of carbon nanopuck dispersions

Atomic force microscopy

Since static light scattering take into consideration that the dispersed particles are spherical, a certain deviation from the absolute size value is expected. In order to assess SLS measurements, atomic force microscopy in tapping mode has been used to

determine the diameter and height of CNP particles in the monodispersed aqueous dispersion (**fig. 3.25**).

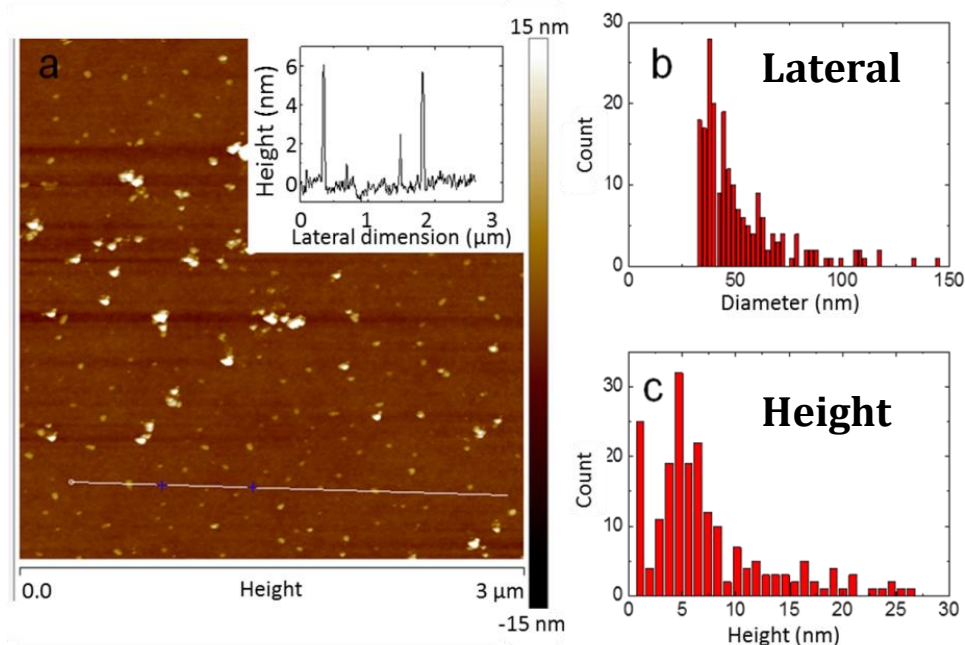


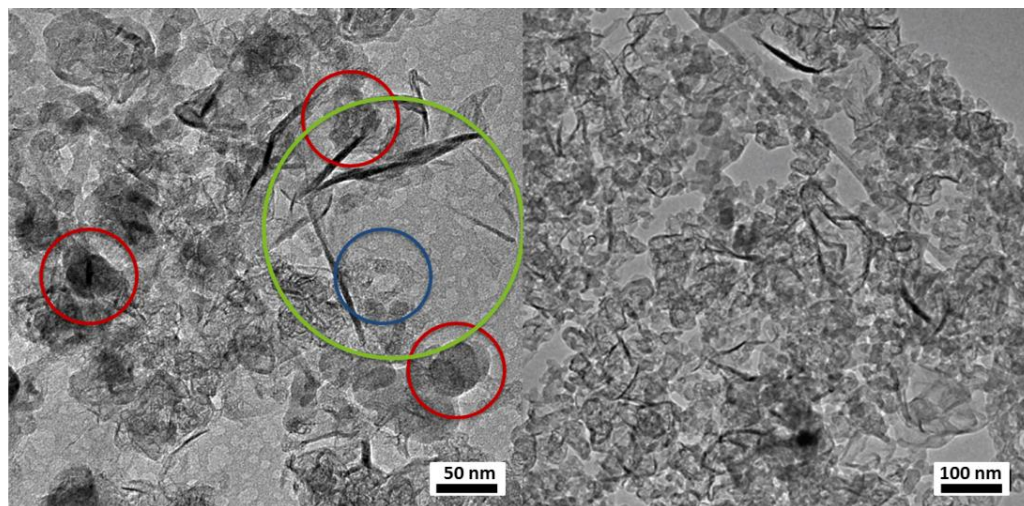
Figure 3.25: (a) AFM topography images of deposit of CNP dispersion on freshly cleaved mica surfaces. Cross section of the topography image taken along the white line is plotted in inserted figures showing that the height of the nano objects on the surface is ca. 6 nm. (b) Lateral size distribution of particles; the mean size is 40 nm. (c) Height distribution of particles; the mean height is 5 nm.

After 20 min/4000 rpm centrifugation, 20 μL of dispersion was drop-casted on freshly cleaved mica substrate. The AFM topography image exhibits basically flat surfaces of homogenous particles characterized by an average height of 6 nm. Individual objects can also be clearly observed. After statistical analysis, the resulting diameter distribution (**fig. 3.25 b and fig. 3.25 b c**) shows a mean size of 40 nm and mean height of 5 nm. AFM and SLS results are in the total agreement verifying the monodispersed, quite broad distribution character of CNP dispersions with size less than 100 nm.

High resolution transmission electron microscopy

A widely used characterization technique to identify carbon morphology and size is high resolution transmission electron microscopy (HRTEM) as depicted in **fig. 3.26**. HRTEM image of CNP dispersion with two size populations (**fig. 3.26 left**) shows the majority of particles to be of average size of 50 nm with the presence of larger aggregates.

Graphitized closed-shells, graphene petals/flakes and small graphitic fibers can be clearly observed. From the image of 2.2 wt% CNP dispersion (**fig. 3.26 right**) the monodispersibility is verified with individual nanoobjects of ca. 50 nm.



High concentrated dispersion of carbon nanopucks (6.4 wt%) with surfactant in H₂O with two size distributions.

Nanostructures zoology:

- Large graphitized closed-shells
- Graphene petals and flakes
- Small graphitic fibers

High concentrated dispersion of carbon nanopucks (2.2 wt%) with surfactant in H₂O with one size distribution.

Figure 3.26: HRTEM images of the CNP dispersion. Left: Dispersion 6.4 wt% CNP, 1 wt% bile salt (after tip sonication: 30 min). Right: Dispersion 2.2 wt% CNP, 1 wt% bile salt (after tip sonication: 30 min and centrifugation: 20 min).

Conductivity measurements and scanning electron microscopy

Sheet resistance (is defined as the resistance of thin films that are nominally uniform in thickness) of CNP_{HTX} films was measured using a four point probe technique. SEM was used to determine the thickness of the films (**fig. 3.27**) where uniform diameter is shown. Then by multiplying the sheet resistance by the thickness (in cm) the value of volume resistivity was obtained as depicted in **table 3.2**. The calculated volume resistivities are of 0.5 to 35 Ω.cm within the sample.

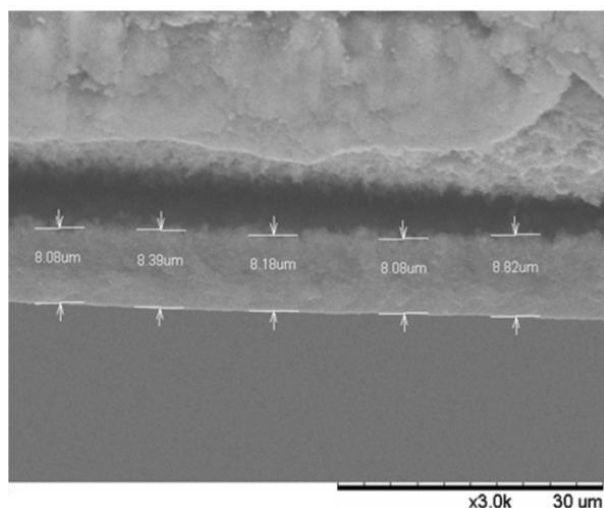


Figure 3.27: SEM picture of the 5 different membranes collected by vacuum filtration of carbon nanopuck (CNP_{HTX}) dispersion.

Table 3.2: Volume resistivity of carbon nanopucks (CNP_x) films.

Sample	Trial	Thickness (μm)	Sheet resistance ($\text{k}\Omega\cdot\text{sq}^{-1}$)	Volume resistivity ($\Omega\cdot\text{cm}$)	Average volume resistivity ($\Omega\cdot\text{cm}$)
CNP_{HT0}	1	19	0.90	1.7	2
	2	22	1.24	2.7	
	3	31	0.53	1.6	
CNP_{HT1}	1	8	1.00	0.8	0.88
	2	31	0.36	1.11	
	3	49	0.15	0.74	
CNP_{HT2}	1	15	0.21	0.32	0.39
	2	15	0.32	0.47	
	3	18	0.22	0.39	
CNP_{HT3}	1	10	1.65	2.1	1.48
	2	41	0.34	1.4	
	3	46	0.21	0.96	
CNP_{HT4}	1	12	42.0	50	34.4
	2	31	6.00	18.8	

It can be seen from the table 2 that the samples CNPHT₀ to CNPHT₃ exhibit similar volume resistivity of ca. 1.2 Ω .cm with only the CNPHT₅ to show an order of magnitude higher values. Overall, all the CNP samples could be considered as conductive films.

Conclusion

The present plasma process with biogas as a feedstock (mixture of methane and carbon dioxide) supplies well defined, crystalline carbon nanopucks (CNP). Their successful dispersion in aqueous media provides a mean to harness their properties. Well-defined high concentrated (6 wt% and 2.2 wt%) CNP dispersions of two and one size populations have been acquired. Bile salt has been used as the surfactant of choice, while mechanical energy has been introduced through sonication. Based on different times of centrifugation, dispersions with CNP particles sizes 50 nm and 0.45 μ m or with the narrow distribution of the smaller particles have been successfully prepared. The morphology and size of the dispersed particles could be clarified using characterization techniques such as optical microscopy, static light scattering, atomic force microscopy and high resolution transmission electron microscopy. A direct use of CNP dispersions is as conductive films (via vacuum filtration). In this study, the resistivity values of the dispersions of carbon nanopucks grades described in chapter 2 (CNP_{HTX}) have been measured and are of ca 1 Ω .cm which could be placed in the range of high quality CB grades (10^0 - 10^{-1} Ω .cm). Since a decrease in resistivity can be acquired by compression of the sample or with the increase of its thickness, resulting sheet resistance of 220 Ω .sq⁻¹ for CNPs films (less than 25 μ m thickness), suggests that these materials could be used in conductivity related applications including conductive coatings, electromagnetic shielding or as fillers for conductive composites.

References

1. PlasCarb. Available at: <http://www.plascarb.eu/>.
2. Hof, F. *et al.* Conductive inks of graphitic nanoparticles from a sustainable carbon feedstock. *Carbon N. Y.* **111**, 142–149 (2017).
3. Dresselhaus, M. S. & Dresselhaus, G. Intercalation compounds of graphite. *Adv. Phys.* **51**, 1–186 (2002).
4. Vallés, C. *et al.* Solutions of Negatively Charged Graphene Sheets and Ribbons. *J. Am. Chem. Soc.* **130**, 15802–15804 (2008).
5. Catheline, A. *et al.* Solutions of fully exfoliated individual graphene flakes in low boiling point solvents. *Soft Matter* **8**, 7882 (2012).
6. Milner, E. M. *et al.* Structure and Morphology of Charged Graphene Platelets in Solution by Small-Angle Neutron Scattering. *J. Am. Chem. Soc.* **134**, 8302–8305 (2012).
7. Pénicaud, A. & Drummond, C. Deconstructing graphite: Graphenide solutions. *Acc. Chem. Res.* **46**, 129–137 (2013).
8. Catheline, A. *et al.* Graphene solutions. *Chem. Commun.* **47**, 5470 (2011).
9. Li, X. *et al.* Highly conducting graphene sheets and Langmuir–Blodgett films. *Nat. Nanotechnol.* **3**, 538–542 (2008).
10. Shih, C.-J. *et al.* Bi- and trilayer graphene solutions. *Nat. Nanotechnol.* **6**, (2011).
11. Bepete, G. *et al.* Surfactant-Free Single Layer Graphene in Water. *Nat. Chem.* (2016).
12. Brodie, B. C. On the Atomic Weight of Graphite. *Phil. Trans. R. Soc. Lond.* **149**, 249–259 (1859).
13. Hummers, W. S. & Offeman, R. E. Preparation of Graphitic Oxide. *J. Am. Chem. Soc.* **80**, 1339–1339 (1958).
14. Nasrollahzadeh, M. *et al.* Synthesis, characterization, structural, optical properties and catalytic activity of reduced graphene oxide/copper nanocomposites. *RSC Adv.* **5**, 10782–10789 (2015).
15. Paredes, J. I., Villar-Rodil, S., Martínez-Alonso, A. & Tascón, J. M. D. Graphene Oxide Dispersions in Organic Solvents. *Langmuir* **24**, 10560–10564 (2008).
16. Becerril, H. A. *et al.* Evaluation of solution-processed reduced graphene oxide films as transparent conductors. *ACS Nano* **2**, 463–70 (2008).
17. Cristina Gómez-Navarro, † *et al.* Electronic Transport Properties of Individual Chemically Reduced Graphene Oxide Sheets. (2007). doi:10.1021/NL072090C
18. Si, Y. & Samulski, E. T. Synthesis of Water Soluble Graphene. *Nano Lett.* **8**, 1679–1682 (2008).
19. Robinson, J. T. *et al.* Wafer-scale Reduced Graphene Oxide Films for Nanomechanical Devices. *Nano Lett.* **8**, 3441–3445 (2008).
20. Trusovas, R. *et al.* Reduction of graphite oxide to graphene with laser irradiation. *Carbon N. Y.* **52**, 574–582 (2013).
21. Konios, D., Stylianakis, M. M., Stratakis, E. & Kymakis, E. *Dispersion behaviour of*

- graphene oxide and reduced graphene oxide. Journal of Colloid and Interface Science* **430**, (2014).
22. Mason, T. J. & Lorimer, J. P. *Applied sonochemistry : the uses of power ultrasound in chemistry and processing*. (Wiley-VCH, 2002).
 23. Suslick, K. *et al.* Acoustic cavitation and its chemical consequences. *Phil. Trans. R. Soc. Lond. A* **357**, 335–353 (1999).
 24. Lucas, A. *et al.* Kinetics of Nanotube and Microfiber Scission under Sonication. *J. Phys. Chem. C* **113**, 20599–20605 (2009).
 25. Hernandez, Y. *et al.* High-yield production of graphene by liquid-phase exfoliation of graphite. *Nat. Nanotechnol.* **3**, 563–568 (2008).
 26. Khan, U. *et al.* Solvent-Exfoliated Graphene at Extremely High Concentration. *Langmuir* **27**, 9077–9082 (2011).
 27. Hernandez, Y., Lotya, M., Rickard, D., Bergin, S. D. & Coleman, J. N. Measurement of Multicomponent Solubility Parameters for Graphene Facilitates Solvent Discovery. *Langmuir* **26**, 3208–3213 (2010).
 28. Khan, U., O'Neill, A., Lotya, M., De, S. & Coleman, J. N. High-Concentration Solvent Exfoliation of Graphene. *Small* **6**, 864–871 (2010).
 29. Ciesielski, A. & Samorì, P. Graphene via sonication assisted liquid-phase exfoliation. *Chem. Soc. Rev.* **43**, 381–98 (2014).
 30. Lu, J. *et al.* One-Pot Synthesis of Fluorescent Carbon Nanoribbons, Nanoparticles, and Graphene by the Exfoliation of Graphite in Ionic Liquids. *ACS Nano* **3**, 2367–2375 (2009).
 31. Wang, X. *et al.* Direct exfoliation of natural graphite into micrometre size few layers graphene sheets using ionic liquids. *Chem. Commun.* **46**, 4487 (2010).
 32. Nuvoli, D. *et al.* High concentration few-layer graphene sheets obtained by liquid phase exfoliation of graphite in ionic liquid. *J. Mater. Chem.* **21**, 3428–3431 (2011).
 33. Shang, N. G. *et al.* Controllable selective exfoliation of high-quality graphene nanosheets and nanodots by ionic liquid assisted grinding. *Chem. Commun.* **48**, 1877 (2012).
 34. Behabtu, N. *et al.* Spontaneous high-concentration dispersions and liquid crystals of graphene. *Nat. Nanotechnol.* **5**, 406–11 (2010).
 35. Bonard, J.-M. *et al.* Purification and size-selection of carbon nanotubes. *Adv. Mater.* **9**, 827–831 (1997).
 36. Green, A. A. & Hersam, M. C. Solution phase production of graphene with controlled thickness via density differentiation. *Nano Lett.* **9**, 4031–6 (2009).
 37. Vadukumpully, S., Paul, J. & Valiyaveetil, S. Cationic surfactant mediated exfoliation of graphite into graphene flakes. *Carbon N. Y.* **47**, 3288–3294 (2009).
 38. Hao, R., Qian, W., Zhang, L. & Hou, Y. Aqueous dispersions of TCNQ-anion-stabilized graphene sheets. *Chem. Commun.* **0**, 6576 (2008).
 39. Lotya, M., King, P. J., Khan, U., De, S. & Coleman, J. N. High-Concentration, Surfactant-Stabilized Graphene Dispersions. *ACS Nano* **4**, 3155–3162 (2010).

40. Smith, R. J. *et al.* The importance of repulsive potential barriers for the dispersion of graphene using surfactants. *New J. Phys.* **12**, 125008 (2010).
41. Guardia, L. *et al.* High-throughput production of pristine graphene in an aqueous dispersion assisted by non-ionic surfactants. *Carbon N. Y.* **49**, 1653–1662 (2011).
42. Bourlinos, A. B. *et al.* Aqueous-phase exfoliation of graphite in the presence of polyvinylpyrrolidone for the production of water-soluble graphenes. *Solid State Communications* **149**, (2009).
43. Liang, Y. T. & Hersam, M. C. Highly Concentrated Graphene Solutions via Polymer Enhanced Solvent Exfoliation and Iterative Solvent Exchange. *J. Am. Chem. Soc.* **132**, 17661–17663 (2010).
44. An, X. *et al.* Stable Aqueous Dispersions of Noncovalently Functionalized Graphene from Graphite and their Multifunctional High-Performance Applications. *Nano Lett.* **10**, 4295–4301 (2010).
45. Zhang, N. *et al.* Actuator materials based on graphene oxide/polyacrylamide composite hydrogels prepared by in situ polymerization. *Soft Matter* **7**, 7231 (2011).
46. Parviz, D. *et al.* Dispersions of Non-Covalently Functionalized Graphene with Minimal Stabilizer. *ACS Nano* **6**, 8857–8867 (2012).
47. Brinkhaus, L. *et al.* Tuning the Stability of Graphene Layers by Phthalocyanine-Based oPPV Oligomers Towards Photo- and Redoxactive Materials. *Small* **9**, 2348–2357 (2013).
48. Novoselov, K. S. *et al.* A roadmap for graphene. *Nature* **490**, 192–200 (2012).
49. Jorio, A. & Cançado, L. G. Perspectives on Raman spectroscopy of graphene-based systems: from the perfect two-dimensional surface to charcoal. *Phys. Chem. Chem. Phys.* **14**, 15246 (2012).
50. Ferrari, A. C. & Basko, D. M. Raman spectroscopy as a versatile tool for studying the properties of graphene. *Nat. Nanotechnol.* **8**, 235–246 (2013).
51. Beams, R., Gustavo Cançado, L. & Novotny, L. Raman characterization of defects and dopants in graphene. *J. Phys. Condens. Matter* **27**, 83002 (2015).
52. Pimenta, M. A. *et al.* Studying disorder in graphite-based systems by Raman spectroscopy. *Phys. Chem. Chem. Phys.* **9**, 1276 (2007).
53. Mafra, D. L. *et al.* Determination of LA and TO phonon dispersion relations of graphene near the Dirac point by double resonance Raman scattering. *Phys. Rev. B* **76**, 233407 (2007).
54. Li, Z. Q., Lu, C. J., Xia, Z. P., Zhou, Y. & Luo, Z. X-ray diffraction patterns of graphite and turbostratic carbon. *Carbon N. Y.* **45**, 1686–1695 (2007).
55. Ramalingam, P. *et al.* Role of deoxy group on the high concentration of graphene in surfactant/water media. *RSC Adv.* **3**, 2369 (2013).
56. Sugioka, H. & Moroi, Y. Micelle formation of sodium cholate and solubilization into the micelle. *Biochim. Biophys. Acta - Lipids Lipid Metab.* **1394**, 99–110 (1998).
57. Sun, Z., Masa, J., Liu, Z., Schuhmann, W. & Muhler, M. Highly Concentrated Aqueous

Chapter 3 – Carbon nanopuck dispersions

- Dispersions of Graphene Exfoliated by Sodium Taurodeoxycholate: Dispersion Behavior and Potential Application as a Catalyst Support for the Oxygen-Reduction Reaction. *Chem. - A Eur. J.* **18**, 6972–6978 (2012).
58. Blanch, A. J., Lenehan, C. E. & Quinton, J. S. Optimizing Surfactant Concentrations for Dispersion of Single-Walled Carbon Nanotubes in Aqueous Solution. *J. Phys. Chem. B* **114**, 9805–9811 (2010).
59. Asakura, S. & Oosawa, F. On Interaction between Two Bodies Immersed in a Solution of Macromolecules. *J. Chem. Phys.* **22**, 1255 (1954).

Chapter 4

Natural rubber/carbon nanopuck composites

Table of contents

Chapter 4.....	125
Natural rubber/carbon nanopuck composites	125
Introduction.....	127
1. Natural rubber and composites background	128
a. Natural rubber.....	128
b. Composites.....	129
2. Experimental section.....	130
a. CNP dispersions.....	130
b. CNP/NR composites preparation procedure	131
c. CNP/NR composites characterization	133
a. CNP ₅ /NR composites characterization.....	134
b. CNP _{HT2} /NR composites characterization.....	136
3. Results and discussion.....	137
a. CNP ₅ /NR composites	137
Scanning electron microscopy	137
Atomic force microscopy.....	138
Raman spectroscopy	140
X-ray diffraction.....	141
Thermal properties - Thermogravimetric analysis.....	141
Electrical properties - Impedance spectroscopy.....	143
Mechanical properties - Dynamic mechanical analysis	144
b. CNP _{HT2} /NR composites	145
Transmission electron microscopy.....	145
Peak atomic force microscopy	146
Raman spectroscopy	147
X-ray diffraction.....	148
Thermal properties - Thermogravimetric analysis.....	149
Electrical properties - Impedance spectroscopy.....	150
Mechanical properties – Tensile tests	152
Piezoresistive properties	157
Conclusion	162
References.....	163

Introduction

After purification, well defined, high concentration aqueous dispersions of carbon nanopucks (CNPs), calibrated in size were obtained and characterized, as described in detail in the previous chapter. Multifunctional nanocomposites with natural rubber latex, a biopolymer, were prepared by an environmentally friendly route that some of us have developed with carbon nanotubes and graphene species.^{3,4} The preparation of NR nanocomposites with CNPs aims to combine synergistically the properties of the two materials, thereby extending these application possibilities.

In this chapter two sets of composites with CNPs dispersions that differ in the surfactant and CNP precursor are presented. We report on these homogeneous nanocomposites and their thermal, mechanical, electrical and piezoresistive properties. The obtained multifunctional materials exhibit promising characteristics with potential for applications in a large number of systems.

In part 1, the first contact with natural rubber and composites is achieved. In part 2 the experimental section is provided presenting CNP dispersions, CNP/NR composites preparation procedure and CNP/NR composites characterization techniques. Afterwards, in part 3, the characterization of the composites is described using a variety of techniques while their properties are determined and discussed.

1. Natural rubber and composites background

a. Natural rubber

Rubber hydrocarbon is the main constituent of natural rubber (NR). NR is a biopolymer consisting of 97 % isoprene monomers in a *cis*-1,4 configuration (**fig. 4.1 left**). Its commercial source is the sap of the *Hevea brasiliensis* tree, also known as the rubber tree of the family Euphorbiaceae, which thrives in tropical climates (**fig. 4.1 right**).

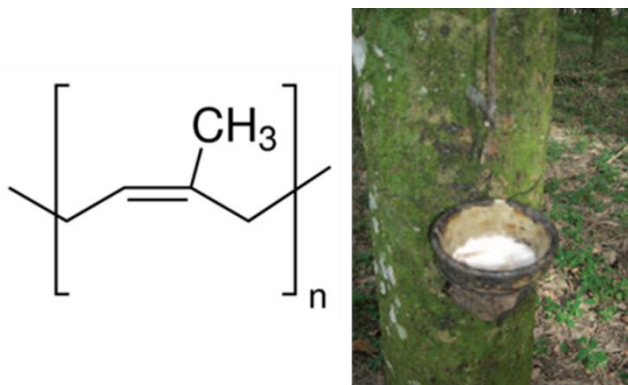


Figure 4.1: Left: The chemical structure of poly (*cis*-1,4-isoprene), the principle component of natural rubber. Right: Latex extracted from a rubber tree. Adapted from reference ⁵.

In 1600 B.C, Mesoamericans (the Olmecs), often referred to as the “rubber people”, were the first to discover NR.⁶ Its primary practical industrial application, however, was not until 1839, when Charles Goodyear combined sulfur and white lead with rubber under heat treatment occurring in resistance to oil solvents and temperature.⁷ This process was eventually refined to become what is known today as vulcanization, and includes the addition of sulfur, or other curatives, contributing to the superior properties of NR.

Latex, a stable colloidal dispersion in an aqueous medium, which is extracted from the rubber trees, consists of generally spherical isoprene particles, and in most plants is a white milky fluid, with some plants having a yellow, orange, or scarlet hue. Polyisoprene is then produced synthetically, usually by duplicating the naturally occurring material.

The chemical structure of NR was investigated for more than a century, but was fully clarified only after 1920. Latex consists of 35 % rubber hydrocarbon, 5 % non-rubber solids and 60 % water. The hydrocarbon is separated into 97 % *cis*-1,4 units, 1 % *trans*-1,4 units and 2 % 3,4 units in a head - tail structure. The polymer has an approximate average molecular weight of 38000 g mol⁻¹, which corresponds to ca. 560 isoprene units. The non-rubber solids are mainly protein, phospholipids and inorganic salts. Notably, the poly (*cis*-1,4-isoprene) particles in this complex colloidal suspension are stabilized by a charged protein/phospholipidic membrane.^{8,9}

NR is a thermoplastic (a polymer that becomes moldable after being heated, solidifies after being cooled, and can repeat this process, unlike thermosets) elastomer (a viscoelastic polymer with weak intermolecular forces) (fig. 4.2 a) and 4.2 b) respectively). After its vulcanization, it becomes a thermoset (a cured/vulcanizate polymer that changes permanently into an insoluble polymer network).

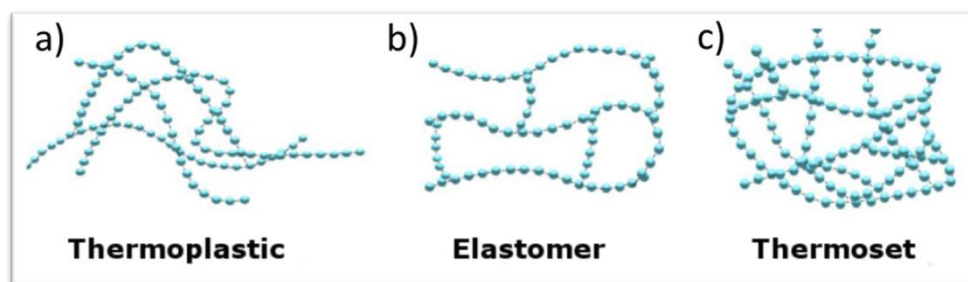


Figure 4.2: Classification of polymers.

Elastomers, such as NR, are used in high volume products like tires, pipes and belting.¹⁰ It is a strategic material that cannot be replaced by synthetic rubbers in a variety of applications, owing to its superior characteristics, such as outstanding elasticity, flexibility at low temperatures and resistance to abrasion.¹¹ It is also used in the manufacturing of a wide variety of products, ranging from medical devices to truck-tire treads.^{9,12}

b. Composites

The ultimate properties of NR composites depend not just on the polymer, but also on the fillers, such as nanocarbon, silica and others.¹⁰ Carbon black (CB) is one of the materials principally utilized to reinforce polymer properties.¹³⁻¹⁵ A lot of research has been performed in order to replace CB or to create hybrids. There are several academic studies that substitute CB by harnessing allotropes from the carbon family such as carbon nanotubes, graphene oxide, reduced graphene oxide and carbon nanoplatelets.^{3,4,14-20} However, in order to reinforce the properties of synthetic rubber and NR, the rubber industry still widely utilizes CB.¹⁰ Its cost-effectiveness combined with its intrinsic properties (such as mechanical response), makes CB the principle candidate to address rubber limitations. Therefore, a replacement candidate should be both economical and effective. In this chapter, homogeneous multifunctional composites of unvulcanized NR and carbon nanopucks (CNP) were produced. The preparation of CNP/NR composites aims to synergistically combine the properties of the two materials,

thereby extending their application possibilities, while maintaining low cost and high sustainability.

2. Experimental section

a. CNP dispersions

The incorporation of CNP into the polymer matrix was achieved by firstly dispersing the particles in an aqueous medium using a surfactant, then applying ultrasound energy.^{2,21-23} In this study, two CNP dispersions that they differ in terms of the carbon precursor and the surfactant have been used. Their features are summarized in **table 4.1** and a further, more detailed analysis are presented in chapter 3.

Table 4.1: Characteristics of CNP dispersions.

Dispersion s	CNP source	CNP structure	Surfactant	C of CNP (wt %)	C of surfactant (wt %)	Dimension s of particles (lateral size x thickness)
(x)	CNP ₅	Nano turbostratic multilayer of graphene with the presence of amorphous carbon (10-15 wt%)	Bile salt	2.2	1	40 nm x 5 nm
(y)	CNP _{HT2}	Nano turbostratic multilayer of graphene	Brij S 100	1.7	0.5	50 nm x 3 nm

Briefly, CNP precursors have been produced via the cracking of methane/carbon dioxide mixture by an innovative plasma process.² Dispersion (x) uses CNP₅ (chapter 3) and dispersion (y) uses CNP_{HT2} the characterization of which has been described in chapter 2. As mentioned in the previous chapters (chapter 2 and 3), CNP_{HT2} is carbon sample after purification treatment and consists of a highly organized graphitic structure with

practically no defects, while CNP₅ is accompanied by an amorphous background (**table 4.1**).

CNP dispersions in aqueous media were obtained using bile salt (anionic surfactant) and brij S 100 (nonionic surfactant) (used as received from Sigma Aldrich), with the application of ultrasound energy. Water was deionized using a Milli-Q system. In particular, well defined, high concentration aqueous dispersions of CNP were initially obtained based on the following protocol: 10 g of dispersion composed of 0.64 wt% of CNP, 0.1 wt% of surfactant in water was prepared with the help of tip sonication (Branson Digital Sonifier tip sonicator: 30 min, energy: 14.4 kJ in interval mode (pulse on: 0.5sec, pulse off: 0.2 sec)). The resulting dispersions were then centrifuged for 20 min at 4000 rpm (2486 x g) with a Fisher Bioblock Scientific centrifuge. The final concentrations of CNP were verified after weighing the freeze dried powder (yield ~50 %). The dispersions of particles were calibrated in size, and had a narrow distribution. The absolute values are disclosed in **table 4.1**.

The selection of the aforementioned carbon dispersions did not occur randomly. As an initial effort to prepare CNP/NR composites, dispersion (x) was used. Following their preparation and characterization, an attempt to further improve the composite properties was deemed necessary. CNP_{HT2} was the key to modifying their features, owing to its highly organized graphitic structure. However, a different interaction between CNP dispersions and natural rubber latex was observed by altering the carbon source. During the preparation procedure of the composites, and particularly during the mixing of the two components (CNP and NR) the liquid mixtures were sometimes solidified, preventing regularly the formation of the final materials. To overcome this, the bile salt was substituted with a non-ionic surfactant (dispersion (y)). Solidification has may occurred due to the electrostatic interaction between the ionic nature of the bile salt and the ionic environment of the natural rubber particles, which regularly prevented the formation of the final materials.

b. CNP/NR composites preparation procedure

Overall, two sets of CNP/NR composites were prepared and fully characterized. The samples will be referred to by the following designations: NR for natural rubber without filler (used as the control sample) along with CNP₅/NR and CNP_{HT2}/NR for the composites obtained by using CNP₅ and CNP_{HT2} respectively. The number that precedes the acronyms represent the percentage of filler, by weight (based on dry polymer),

added to the material, e.g. 10 wt% CNP_{HT2}/NR composite. Formulation of composites occurred via an environmental friendly procedure which has been developed with carbon nanotubes and graphene species, utilizing latex technology.^{3,4} For the preparation of composites, appropriate volumes of CNP aqueous dispersions were directly mixed with NR latex under 30 min magnetic stirring with often manual stirring. The mixtures were then sonicated for 10 min using a bath sonicator (Branson 5200) so as to remove the big bubbles created by the magnetic stirring. Afterwards, the slurries were placed onto molds and dried in an oven under vacuum at 70 °C for a suitable time (for 24 to 48 h), depending on the set of composites. For CNP_{HT2}/NR composites, a frequent manual stirring during the preparation was critical to avoid gel formation. **Fig. 4.3** shows pictures of the experimental procedure and conditions followed to obtain CNP/NR composites.

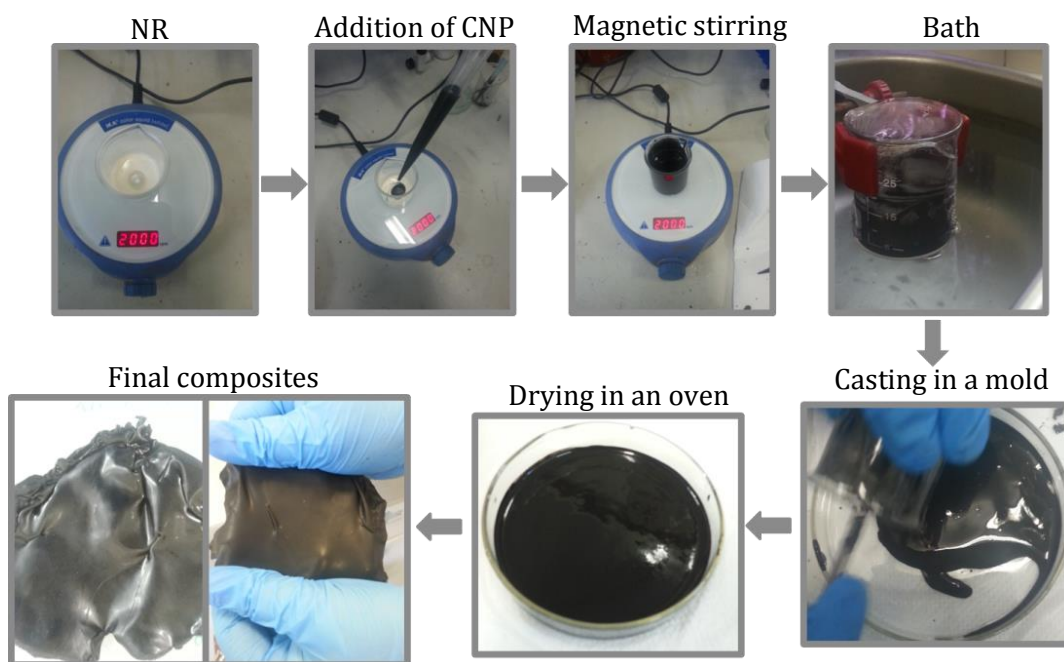


Figure 4.3: Preparation procedure of CNP/NR composites.

Samples with different filler concentrations have been prepared and are presented in **table 4.2**.

Table 4.2: CNP/NR composites with various CNP concentrations.

Sets of composites	
CNP ₅ /NR (wt%)	CNP _{HT2} /NR(wt%)
0	0
0.5	2
2	5
5	7.5
10	10

After the CNP₅/NR characterization, it was observed that the characteristics of 0.5 wt% composite were very similar to that of the NR, while an intermediate sample between 5 and 10 wt% carbon was needed to optimally monitor the progress of properties with carbon content.

c. CNP/NR composites characterization

The rubber composites have been characterized by a variety of techniques. An exhaustive report of all analytical techniques won't be presented in this manuscript. Instead, we will be aiming at comparing the different composites and highlighting their performances. The techniques that have been chosen for this characterization are listed in **table 4.3**.

Table 4.3: Characterization techniques.

CNP ₅ /NR	CNP _{HT2} /NR
SEM	TEM
AFM	Peak force AFM
Raman	Raman
XRD	XRD
TGA	TGA
DMA	Tensile test
AC σ	AC σ
-	Piezoresistivity test

a. CNP₅/NR composites characterization

Scanning electron microscopy (SEM) images of composite films in order to assess the state of dispersion of the filler particles within the elastomeric matrix were obtained on a MIRA 3 FEG- scanning electron microscope. The nanocomposites samples were fractured in liquid N₂. The films were arranged in copper double-sided tapes, pre-glued on the specimen holder. All nanocomposites and pure polymer were metalized with gold. The voltage source used was 15 kV.

The topography and phase contrast **atomic force microscopy (AFM)** images were obtained in non-contact mode, under air atmosphere and at room temperature, using SPM microscope Model 9700 of Shimadzu. The probe used Si (nanoworld) has spring constant of 45 N.m⁻¹ and a nominal resonance frequency of 333 kHz. Pure NR and nanocomposites freshly prepared were dripped on freshly cleaved mica and dried at 70 °C for 24 h were analyzed. The scans were performed at different areas at a speed of 1 Hz and digitized at 512 × 512 pixels.

The **Raman spectra** were recorded on a Renishaw Raman Imaging Microscope Equipment System 3000 in conjunction with an optical microscope and a He-Ne laser (emitting at 632.8 nm).

X-ray diffractograms (XRD) of bile salt, dry CNP₅ dispersion, NR and CNP₅/NR composites were acquired with a θ -2 θ geometry diffractometer equipped with a secondary monochromator. The Cu-K α radiation (λ : 1.5418 Å) was generated at 45 KV and 40 mA. The samples were placed on silicon wafer ("zero background") sample holder and flattened with a piece of glass when it was required. The spectra were obtained within a 2 θ range of 8 to 80° with acquisition time of 125 min.

Thermal properties of the NR and the CNP₅/NR composites were determined via **thermogravimetric analysis (TGA)** using a SDT Q600 (TA Instruments) under an atmosphere of synthetic air (White Martins, 100 mL/min) from room temperature to 1000 °C at a heating rate of 5 °C / min.

Dynamic mechanical analysis (DMA) was performed in a Mettler Toledo DMA, SDTA861 model with. specifications of the equipment: strength: 0.005 to 18 N resolution with 1 mN, frequency: 0.001 to 200 Hz, resolution 0.00001 Hz and displacement: -1.6 mm to 1.6 mm resolution 1 nm. Jaws voltage (clamp voltage) have been used. Scanning has been performed in increasing strain at room temperature and constant frequency (1 Hz) in order to determine the linear range of the material and to extract the elastic modulus. Then, the modulus has been determined on the load rate.

AC conductivity of the composites was measured as a function of frequency by Model M2 Materials Mates 7260 Impedance Analyser at room temperature (frequency range: 10 Hz–1 MHz). Prior to measurements, the samples of length, width and thickness of 10 mm * 10 mm * 0.5 mm respectively were gold metallized and then sandwiched between two electrodes in a cell. A parallel resistor-capacitor equivalent circuit was used to describe the samples which could be considered as plane capacitors. DC resistance was extrapolated from the measured AC resistance values. The conductivity was deduced from **equation (4.1)**,

$$\sigma = z' \cdot (z'^{-2} + z''^{-2}) d \cdot S^{-1} \quad (4.1)$$

where Z' and Z'' are the real and imaginary parts of the impedance respectively, S is the surface area (cross sectional area) and d is the distance between the two electrodes.

b. CNP_{HT2}/NR composites characterization

Internal structure and the state of dispersion of the filler particles within the elastomeric matrix were assessed via **transmission electron microscopy (TEM)** using a Hitachi 7650 operating at 80 kV. Ultrathin sections (70 nm x 70 nm) of the composites were microtomed using a cryo ultramicrotome Leica UC7 equipped with a cryo diamond knife Diatome at -120 °C and with a knife angle at 35°. The thin cuts were put on holey carbon grids.

Mechanical response and adhesion differences between the matrix and the additive were evaluated via **peak atomic force microscopy (peak AFM)** in ambient air in tapping mode. A peak force AFM on Icon microscopy was used. The tip was calibrated just before experiment. Ultrathin section was used, prepared as described above for SEM analysis. The cut was placed onto an aluminium substrate.

CNP_{HT2} and composites structure were evaluated via **Raman spectroscopy**. The characterization was carried out on a Horiba JobinYvonXplora microscope with a cooled Andor CCD detector and a laser spot size of ~1 µm. The spectra were recorded at an excitation wavelength 532 nm and calibrated with HOPG.

X-ray diffractograms (XRD) of brij s 100, dry CNP_{HT2} dispersion, NR and CNP_{HT2}/NR composites were acquired with a PANalyticalX'pertMPD-PRO Bragg-Brentano θ - θ geometry diffractometer (XRD) equipped with a secondary monochromator. The Cu-K α radiation (wavelength of λ : 1.5418 Å) was generated at 45 kV and 40 mA. The spectra were obtained within a range 2θ : 8-80° with acquisition time 2 hours and 5 min. The samples were placed on silicon wafer ("zero background") sample holder and flattened with a piece of glass when it was required.

The thermal properties of the NR and the composites were determined via **thermo gravimetric analysis (TGA)** using a Setaram instrument equipped with a 2 balance setup for equilibration under air. Samples of weights around 10 mg were collected on a Pt-holder and heated with a rate 5 °C / min.

The **AC conductivity** parameters are described above for the CNP₅/NR composite characterization.

The **mechanical response** of the neat NR and the composites was estimated from the stress-strain curves acquired using a ZwickRoell tensile machine at a strain rate 1

mm/min. Three to four specimens were tested for each sample and the showed values are representative results. The Young's modulus was extracted from the slope of the stress-strain plots in the Hooke's region (elastic part).

Moreover, the change on resistivity as a function of deformation (**piezoresistivity**) was determined after following the change in resistance (R) with a Keithley 6517A electrometer/high resistance meter during the elongation of the rubbers until break. The connection of the samples with the electrodes was achieved by using silver paint and copper wire. The gauge factor was determined from the slope of the elastic part of the curve $R-R_0 - \varepsilon$ (%) where ε is the strain. The resistivity (ρ) was calculated by taking into account the dimensions of the samples and considering the volume (V) constant (**equations (4.2) and (4.3)**)(safe assumption for high strains).

$$\rho = R.S.l^{-1} \quad (4.2)$$

$$V = S.l \quad (4.3)$$

From **equations (4.2) and (4.3)** we obtain the **equation (4.4)**:

$$\rho = R.V.l^{-2} \quad (4.4)$$

where l is the length.

Repeated experiments were performed were the deformation was filmed in actual time to verify the geometry effect (length increase and thickness decrease).

3. Results and discussion

Since the two sets of composites differ in two parameters (carbon precursor and type of surfactant), accurate conclusions of their comparison could not be extracted. Therefore, their characterization and properties will be presented independently.

a. CNP₅/NR composites

Scanning electron microscopy

Structure and state of dispersion of the carbon particles within the elastomeric matrix were assessed via scanning electron microscopy (SEM). **Fig. 4.4** shows SEM images of the pure polymer, a representative composite (with 0.5 wt% CNP₅), and 10 wt% CNP₅/NR.

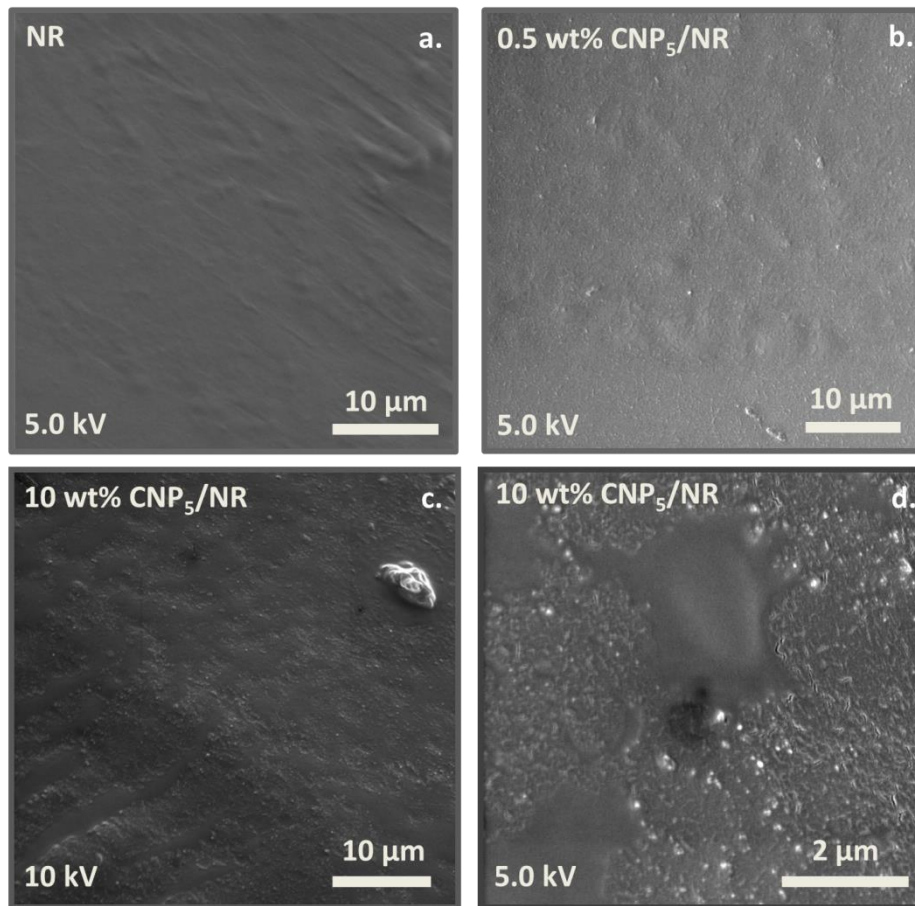


Figure 4.4: SEM images of of NR (a), 0.5 wt% CNP₅/NR (b) and 10 wt% CNP₅/NR (c and d, with d at higher magnification).

For the composite with 0.5 wt% CNP₅, the well distributed filler particles are seen. The composites up to 5 wt% CNP₅ have the same profile. Regarding the composite with 10 wt% carbon, two distinct environments are clear. Areas with large amounts of additive and areas with only the polymer matrix. This could be easier to notice in higher magnification SEM images, where the carbon particles surround natural rubber particles approximately 2 μm in diameter. Overall, all composites illustrate well distributed carbon particles throughout the polymer matrix. The sample with 10 wt% additive appears less homogeneous owing to the high amount of filler.

Atomic force microscopy

The composites were further characterized via atomic force microscopy (AFM). **Fig. 4.5** shows the phase AFM images of NR and CNP₅/NR composites.

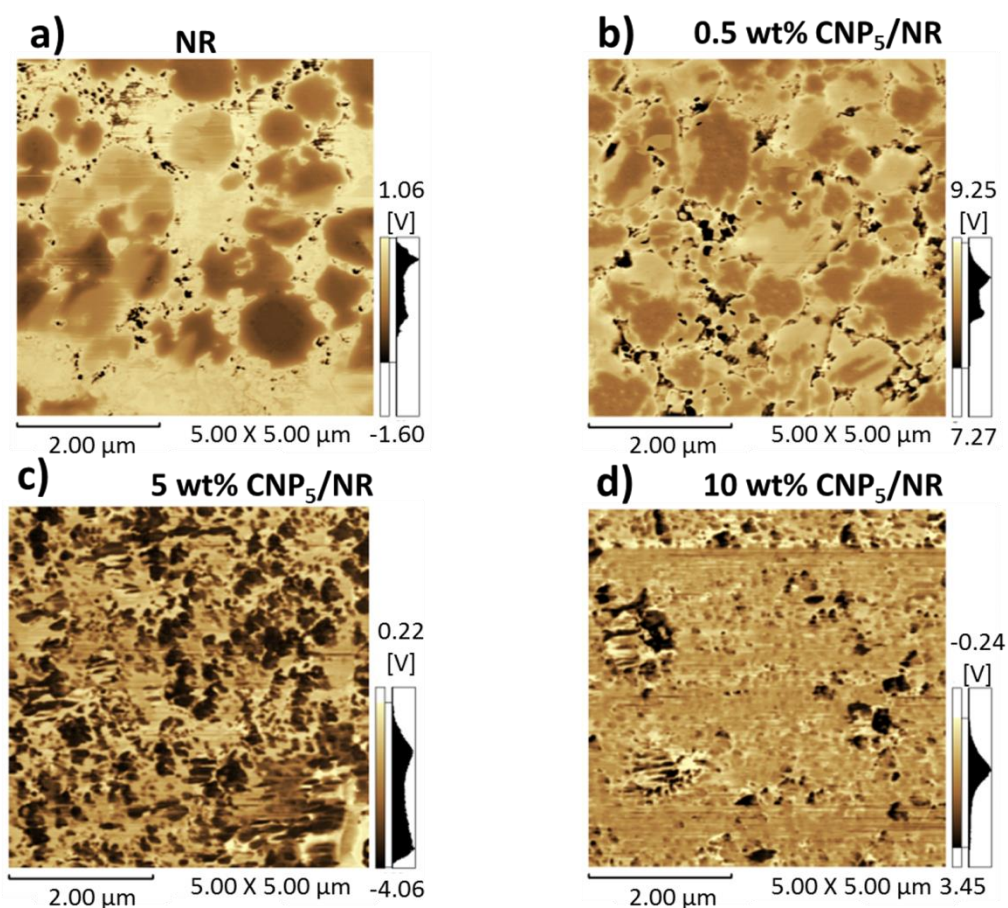


Figure 4.5: AFM phase images of NR and representative CNP_5/NR composites.

In the NR image (**fig. 4.5 a**)), due to the difference in the viscoelasticity, the darker areas correspond to the more elastic latex particles, and the lighter parts correspond to the latex serum which is more viscous.³ The dark spots that surround the NR particles could be attributed to harder particles, like $CaSO_4$, that are naturally present in natural rubber latex or even in AFM artifacts. With the addition of CNP_5 , an increase of dark spots (harder particles) is witnessed, which are more likely carbon particles (probably with a small amount of $CaSO_4$) (**fig. 4.5 b**)). The fillers surround the latex particles and are well dispersed throughout the composite surface. Furthermore, the NR particles initiate the coalescence process. The presence of CNP_5 initiates the coalescence of the latex particles because without fillers the coalescence is not observed. A similar profile is observed for the composite with 2 wt% CNP_5 . In the phase image of the 5 wt% CNP_5/NR sample, a higher amount of well distributed filler is evident (**fig. 4.5 c**)). No latex particles could be distinguished, only lighter areas of a continuous polymer could be seen, an indication that all of the NR particles have coalesced. It seems that the increase of carbon filler promotes the coalescence process of NR particles. In the case of 10 wt% CNP_5/NR , the

aggregates could act as weak points hindering the stress transfer between the two components (**fig. 4.5 d**).

Raman spectroscopy

CNP and composite structures were also evaluated via Raman spectroscopy. Four samples of each composite have been tested in order to evaluate their respective homogeneity.

In **fig. 4.6**, the Raman spectra of CNP₅ powder and its dried dispersion are shown, which contain the G and 2D bands corresponding to the graphitic structure, and the D band, which is used to indicate the presence of defects and/or amorphous carbon with the presence of amorphous carbon to be also verified from the broad background.

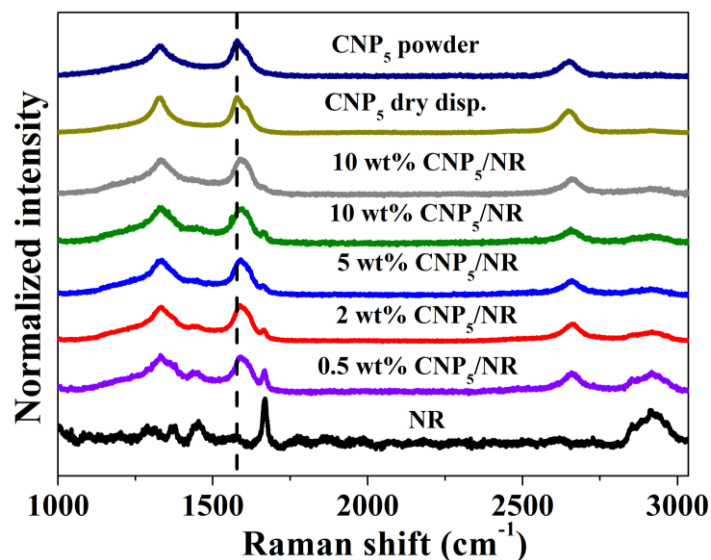


Figure 4.6: Raman spectra of CNP₅ powder, dried CNP₅ dispersion, NR and x CNP₅/NR composites (x = 0.5 to 10 wt%).

Fig. 4.6 also provides the Raman spectra of NR and CNP₅/NR composites with various loading levels of filler. The spectrum of the composite with the lowest amount of CNP₅ showed both of the characteristic bands of NR and CNP₅, thereby accounting for the presence of CNP₅. By increasing the additive concentration, the NR band is less and less observable, since the carbon signature dominates due to the higher sensitivity of carbon to Raman scattering. Overall, all the composites appear homogenous, except the one containing 10 wt% filler, where two different environments are present in the Raman spectra. Spectra with noticeable NR band and spectra without an apparent NR were

recorded in the 10 wt% CNP₅/NR composite, validating the information that has been extracted from the SEM and AFM images. Furthermore, by comparing the spectra of the CNP₅ with that of the composites, an up-shift in the G band of ~5 cm⁻¹ (from 1579 to 1583-1586 cm⁻¹) was observed owing to the possible interaction between the filler and the matrix.^{14,24}

X-ray diffraction

Additional evidence of the presence of NR and CNP in the composites was acquired by performing XRD analysis. **Fig. 4.7** shows the diffractograms of composites and raw carbon, the dry dispersion and the surfactant.

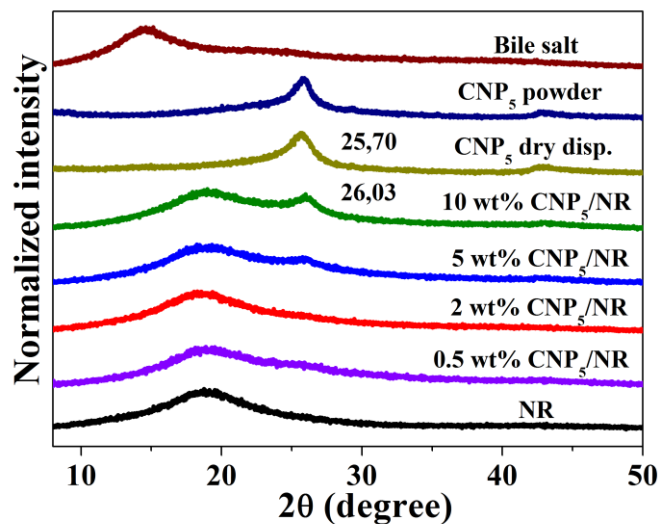


Figure 4.7: X-ray diffractograms of bile salt, CNP₅ powder, dried CNP₅ dispersion, NR and CNP₅/NR composites.

The NR shows a characteristic halo of amorphous materials. All the composites exhibit the same halo shaped spectrum. However, as the filler concentration increases, the peak derived from the CNP₅ is of higher intensity.

Thermal properties - Thermogravimetric analysis

A TGA analysis under air atmosphere was carried out in order to estimate the influence of the CNP additives on the thermal stability of the polymer. Three to four samples of each composite have been tested, so that reliable results could be obtained. **Fig. 4.8** shows the thermograms of NR and the composites.

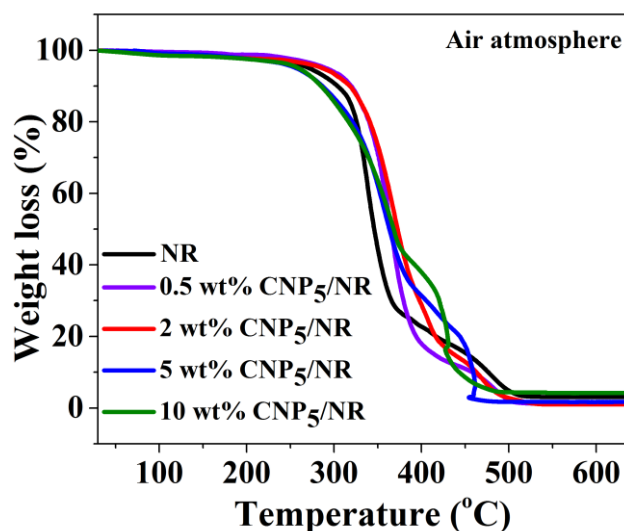


Figure 4.8: Thermograms of NR and CNP₅/NR composites.

The temperature at which the degradation process begins is chosen at a weight loss of 10 % (T_o = onset T) (indicated from the derivative) and the final combustion temperature (T_f) is reached when the decomposition is complete. The temperatures values of composites are listed in **table 4.4**.

Table 4.4: TGA data of NR and composites.

Set of composites	CNP ₅ /NR concentration wt%				
	0	0.5	2	5	10
T_o (°C)	303	319	319	287	287
T_f (°C)	510	510	510	510	510

Moreover, three degradation regions could be detected: the first degradation up to 250 °C, the degradation from 250°C to 360 °C and the degradation until a complete combustion occurs. The TGA profiles of all composites have similar characteristics to the pure NR. The onset temperature of all samples is comparable to that of the unfilled polymer. The T_o is 16 °C higher or lower relative to NR. The T_f is identical for the CNP₅/NR samples and pure NR. The profiles of the first two distinct weight loss regions (up to 250 °C and from 250 to 360 °C) are quite similar to the initial polymer. For the third temperature region, the composites display different degradation temperatures. The thermal stability of CNP₅/NR samples is confirmed by their similar T_o which is of high importance to applications where heat affects their performance. This could be

explained as follow: during heating, the CNP form a carbon film which hinders the mass and the heat transfer. Also, the interfacial adhesion between the matrix and the filler (strong links between CNP and NR by breaking the C = C bonds of NR and CNP with increasing temperature under air), possibly reduces the thermal motion of the polymer chains.²³

Electrical properties - Impedance spectroscopy

Rubbers have inherently low electrical conductivity. A way to overcome this limitation is the insertion of conductive additives into the polymer matrix, which leads to conductive materials. A number of studies with remarkable results have been performed using fillers from the carbon allotrope family. **Fig. 4.9** shows the AC conductivity as a function of frequency of NR and the composites.

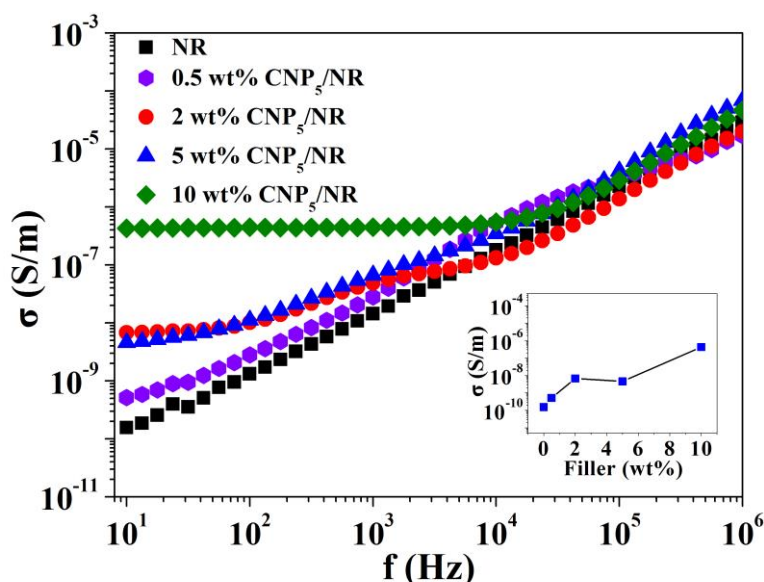


Figure 4.9: AC conductivity as a function of frequency for the pure NR and CNP₅/NR composites. Inset: AC conductivity as a function of the filler concentration at a frequency of 10 Hz.

The variation of AC conductivity with frequency is depicted in **fig. 4.9**. It is noted that the electrical response of the pure polymer is very low, approximately at 10^{-10} S.m⁻¹. As adding CNP₅ particles up to 5 wt%, the conductivity of polymer composites increases, but the values at low frequency are still inferior to 10^{-8} S.m⁻¹. Furthermore, the AC conductivities of pure nature rubber and their composites with low CNP₅ concentrations (<5 wt%) exhibit strong frequency dependence, showing a nearly linear increase with the frequency. At such low concentrations, owing to the absence of the conductive path, the conductivity is dominated by the polarization effects as well as the electron motion,

which highly depends on the frequency, consequently a frequency-dependent AC conductivity is exhibited.

The best electrical characteristics are detected for the sample with the highest amount of additive (10 wt%). A characteristic of direct conductivity is observed. The unchanged AC conductivity is revealed in a particular low frequency range. At this point, the particles are close enough to allow an electron transport through the composite, resulting in a three orders of magnitude increase to the electrical conductivity. In this case, CNP₅ percolating paths are formed through the polymer matrix, which induces the direct conductive characteristic of the nanocomposites in the low frequency range. The microcapacitors formed by the neighboring CNP₅ particles also contribute to the conductivity and become dominant after a critical frequency. More current passing through the capacitors with the increasing frequency results in the conductivity improvement.

These results indicate that CNP additive could enhance the electrical conductivity. However, since the particles are well dispersed into the rubber matrix, a sufficient network formation is prevented and consequently a further conductivity increase.

Mechanical properties - Dynamic mechanical analysis

The effect of the CNP fillers on the mechanical response was estimated by dynamic mechanical analysis. A preliminary investigation has been performed to estimate the storage modulus (E') of the samples (**fig. 4.10**).

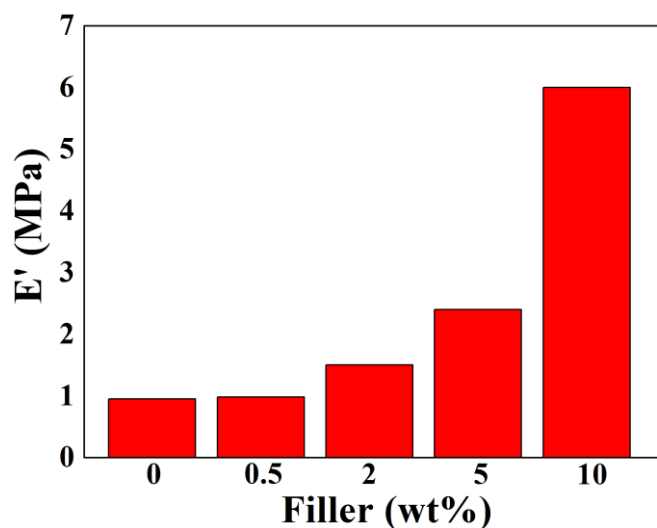


Figure 4.10: Preliminary results of the storage modulus as a function of filler concentration for CNP₅/NR composites.

The modulus of NR (zero carbon concentration) is 1 MPa and increases proportionally as CNP_5 is added. A large increase is noticeable for the composite with 10 wt% CNP_5 , where the E' is six times higher compared to the polymer. The addition of particles enhances the hardness of the polymer. This is due to a hydrodynamic effect arising from the inclusion of rigid particles into the soft rubber matrix. The materials with a CNP_5 additive are well distributed and dispersed into the polymer matrix resulting in great mechanical responses. A possible stress transfer between NR and CNP_5 samples is noticeable (also evident from Raman spectra).

b. $\text{CNP}_{\text{HT}2}$ /NR composites

Transmission electron microscopy

Internal structure of the composites was assessed via transmission electron microscopy (TEM). **Fig. 4.11** shows the images of the pure polymer, a representative composite (with 5 wt% $\text{CNP}_{\text{HT}2}$), the composite with the 10 wt% filler and a TEM image of 10 wt% $\text{CNP}_{\text{HT}2}$ at a higher magnification.

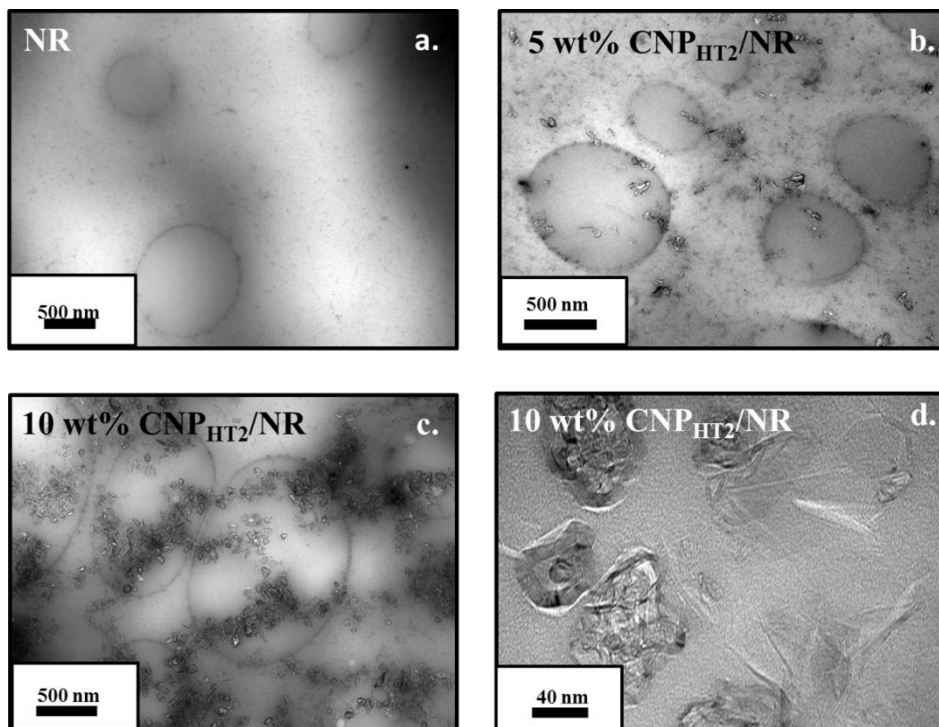


Figure 4.11: TEM images of NR, a representative composite (5 wt% $\text{CNP}_{\text{HT}2}$ /NR) and the composite with highest filler concentration.

The presence, or absence, of the carbon particles is obvious from the images of pure rubber and composites. The samples show a rather uniform distribution of the particles in the matrix. TEM images at higher resolution provide evidence of the presence of fully exfoliated graphene sheets in the matrix (**fig. 4.11 d.**). The difference in filler concentrations results in the construction of a network, most prominent for the 10 wt% CNP_{HT2}/NR composite. This morphological difference influences the properties of the composites, and will be discussed below. The composites show well distributed carbon particles all over the matrix with 10 wt% additive to appear less homogeneous owing to the high amount of additive creating a web-like formation.

Peak atomic force microscopy

Due to the network construction monitored in the SEM analysis, which is likely conductive, peak force AFM was deemed suitable for the characterization of the second set of composites. **Fig. 4.12** shows the images of the 10 wt% CNP_{HT2}/NR composite.

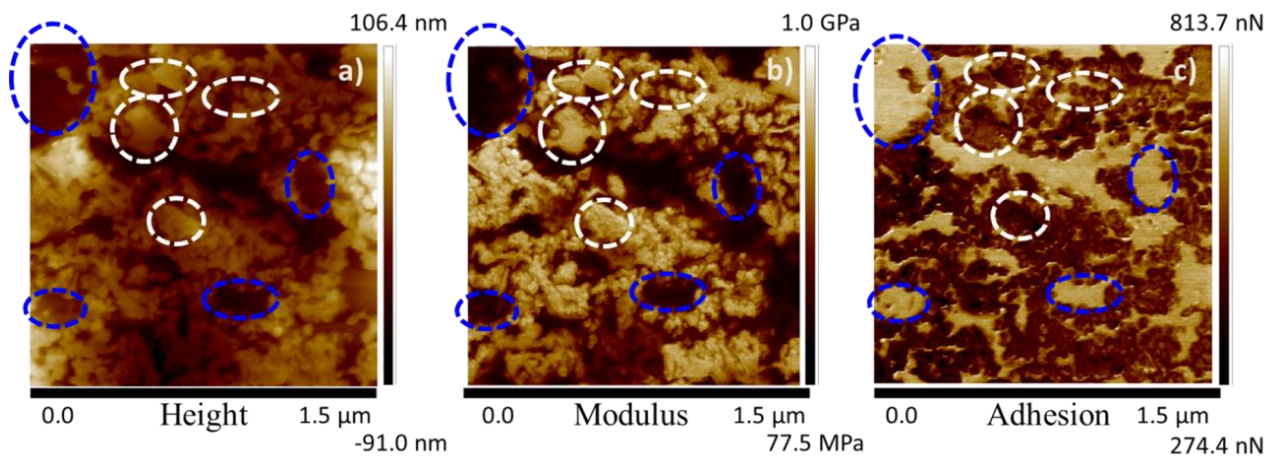


Figure 4.12: Peak force AFM images of 10 wt% CNP_{HT2}/NR composite.

From the AFM topography, the difference in height indicates the roughness of the material. **Fig. 4.12 b) and 4.12c)** show the difference in Young's modulus and adhesion between the softer (NR) and harder (carbon filler) materials. The lighter parts in **fig. 4.12 b)** represent materials with a higher mechanical response, while the darker parts are of lower modulus. In contrast, the lighter areas in **fig 4.12 c)** signify the part of the composite which demonstrates higher adhesion with the tip, and the darker areas illustrate the part where there is less tip-sample interaction. The AFM image (**fig 4.12 b)**), allowed the extraction of information about the mechanical response of the two

components. The rigid particles appear yellow and have a Young's modulus of around 500 MPa, while the matrix (dark areas) has modulus values of approximately two orders of magnitude lower. The occurrence of the CNP_{HT2} network is also evident throughout the matrix, with its presence being noticeable from the AFM image which demonstrates the adhesion of the sample with the tip (**fig. 12 c**). Herein, the harder material, which is the additive, does not interact with the tip; however, as the NR is a soft polymer, an adhesion with the tip is seen, as was expected. Furthermore, the AFM image shows a good matrix-additive adhesion, while a rough estimation of the size of the CNP_{HT2} particles is feasible with an average of 50 nm in diameter (in excellent agreement with the analysis results for the CNP_{HT2} dispersed in aqueous medium).

Raman spectroscopy

Raman spectra of four samples of each composite have been recorded in order to obtain reliable results. **Fig. 13** shows the Raman spectra of different components of the CNP_{HT2}/NR composites.

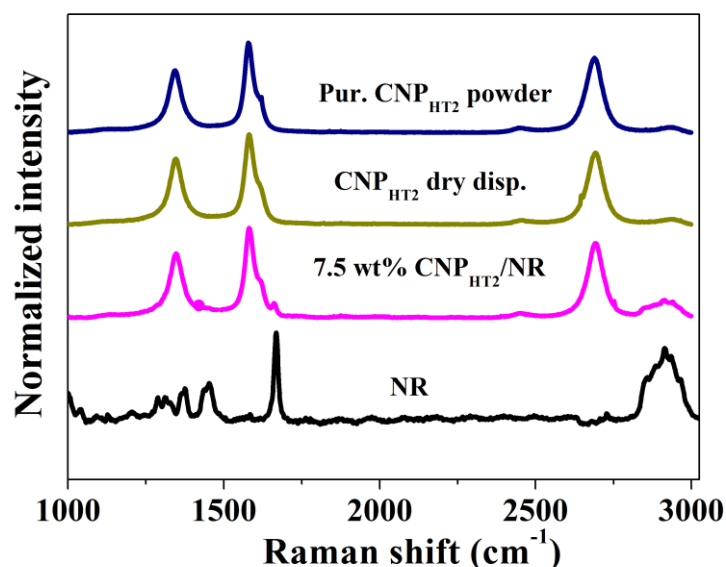


Figure 4.13: Raman spectra of purified CNP_{HT2} powder, dried CNP_{HT2} dispersion, NR and 7.5 wt% CNP_{HT2}/NR composite.

Particularly, the spectra of purified CNP_{HT2} powder, its dried dispersion, NR, and a representative composite are shown. As for the previous carbon source, purified CNP_{HT2} powder and its dried dispersion show well defined D, G and 2D bands. In contrast to CNP₅, there is no amorphous background. The Raman characterization of CNP_{HT2} has

been elucidated in chapter 2. In the spectrum of the dried $\text{CNP}_{\text{HT}2}$ dispersion, a slight shift 2-3 cm^{-1} in the D, G and 2D bands is revealed. This shift may occur due to the surfactant surrounding the particles. The Raman spectrum of the rubber composite shows both of the bands derived from $\text{CNP}_{\text{HT}2}$ and NR. Studies on carbon-polymer systems have shown that the G band appears at shifted frequencies in composites compared to fillers.¹⁴ This behavior has been attributed to the carbon-polymer stress transfer. In this system, no significant shift was observed. The interaction between $\text{CNP}_{\text{HT}2}$ and NR is mostly hydrodynamic, due to solely the inclusion of rigid particles in a soft matrix.

X-ray diffraction

Fig. 4.14 shows the diffractograms of brij S 100, the purified $\text{CNP}_{\text{HT}2}$ powder, the dried $\text{CNP}_{\text{HT}2}$ dispersion and the composites.

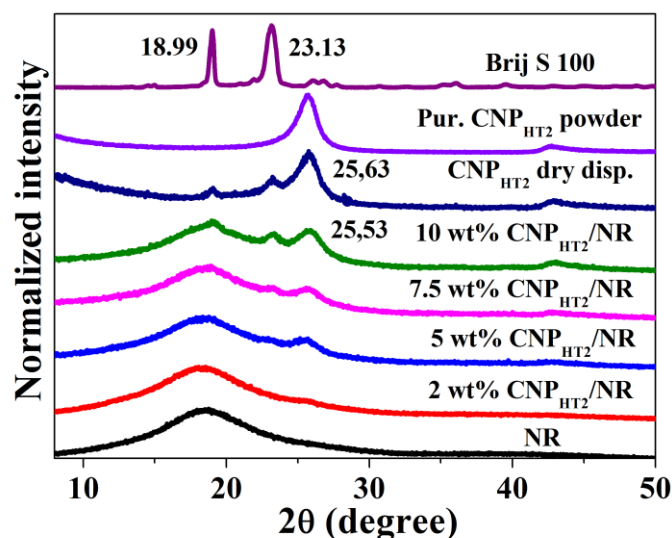


Figure 4.14: X-ray diffractograms of brij S 100 (surfactant), $\text{CNP}_{\text{HT}2}$ powder, dried $\text{CNP}_{\text{HT}2}$ dispersion, NR and $\text{CNP}_{\text{HT}2}$ /NR composites.

As has been shown above for the CNP_5/NR composite, NR exhibits the characteristic halo of amorphous materials. All the composites demonstrate the same halo shaped spectra. When the filler concentration increases, the peak derived from the $\text{CNP}_{\text{HT}2}$ is more intense.

Additionally, the presence of the surfactant peaks in the spectra of the composites with a higher carbon concentrations (7.5 and 10 wt%) is evident.

Thermal properties - Thermogravimetric analysis

Similarly to the CNP₅/NR composites, the thermal stability of the CNP_{HT2}/NR samples has been estimated via thermogravimetric analysis (TGA) under air atmosphere. Three to four samples of each composite have been measured. **Fig. 4.15** shows the thermograms of NR and CNP_{HT2}/NR composites.

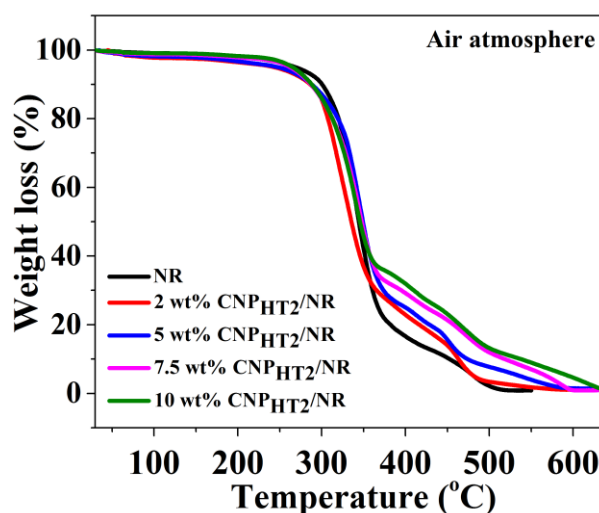


Figure 4.15: Thermograms of NR and CNP_{HT2}/NR composites.

To (onset T) is defined as the temperature at which degradation process starts and is chosen at weight loss 10 %. Tf represents the final combustion temperature when the degradation is completed. Their values are shown in **table 4.5**.

Table 4.5: TGA data of NR and composites.

Set of composites	CNP _{HT2} /NR concentration wt%				
	0	2	5	7.5	10
To (°C)	299	289	289	289	289
Tf (°C)	510	593	593	593	632

The thermograms could be divided in three temperatures regions: the first degradation up to 250 °C, the degradation from 250°C to 360 °C and the degradation until a complete burn occurs. NR and the composites exhibit similar TGA profiles. The composites demonstrate onset temperature of 10 °C lower relative to pure polymer. The Tf is

increased ca. 100 °C. Furthermore, the profiles of the first two weight loss regions (until 250 °C and from 250 to 360 °C) are similar to NR while for the third temperature region, the composites show different decomposition temperatures. Particularly, the combustion temperatures of the composites are shifted to higher values (up to 70°C increase). Overall, it could be deduced that the CNP_{HT2}/NR samples retain the thermal stability of NR. As it was mentioned above for the CNP₅/NR samples, this could be explained as follows: during heating, the CNP forms a carbon film which hinders the mass and the heat transfer. Also, the interfacial adhesion between matrix and filler reduces the thermal motion of the polymer chains.²³

Another outcome of the thermogravimetric analysis is that at the last thermal degradation region the CNP_{HT2}/NR samples combust at higher temperatures not only compared to NR but also to CNP₅/NR composites. A workable explanation has been given by Shtein *et al.*²⁵ They have studied, among other parameters, the influence of the amount of graphene nanoplatelet defects in the combustion temperatures of polymer matrices, and they saw that a decrease occurs when the defect density of the filler is increased, owing to the fact that the combustion process is initiated at the filler edges and defects.²⁵ To sum up, the stability of the thermal properties of NR is verified for both sets of composites, which is of high importance to applications where the temperature affects their performance.

Electrical properties - Impedance spectroscopy

Fig. 4.16 left shows the AC conductivity as a function of frequency of NR and the CNP_{HT2}/NR composites and right the AC conductivity as a function of filler concentration.

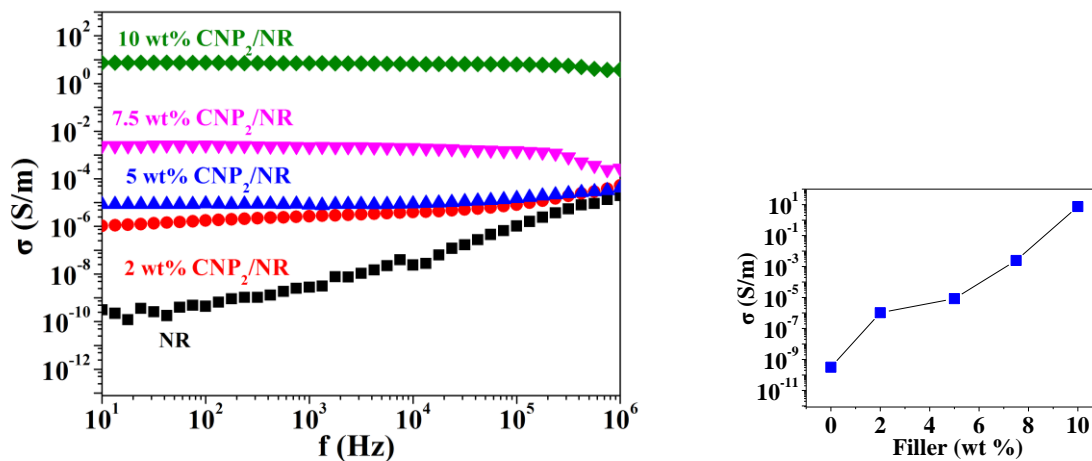


Figure 4.16: Left: AC conductivity as a function of frequency for the pure NR and CNP_{HT2}/NR composites. Right: AC conductivity as a function of the filler concentration at a frequency of 10 Hz.

As it has been mentioned before, the pure polymer has a conductivity of approximately 10^{-10} S.m⁻¹. The electrical response is enhanced when CNP_{HT2} fillers are inserted. By adding carbon particles, even for the samples with the lowest amount of additive, a conductive network was formed, which broke down the dielectric nature of the elastomer and induced an increase in conductivity via the contribution of free charges brought by the fillers. A higher value is evident with a higher filler loading. Above near 5 wt% filler, a further increase of four orders of magnitude is noticed. At this point, a sufficient amount of electron transport occurs through the composite, resulting in an abrupt change of electrical conductivity. A noteworthy 10 orders of magnitude increase was observed for the maximum conductivity value of the 10 wt% CNP_{HT2}/NR composite relative to the unfilled polymer. These results indicate that CNP additives could enhance the electrical conductivity of rubber. Moreover, the CNP_{HT2} fillers largely increase the electrical response by a lot, even for systems where commercial carbon black is used with the same filler loading.¹³⁻¹⁵ In **fig. 4.17** several studies are summarized for composite systems with carbon fillers and their conductivity values and the results of our study (in green color).

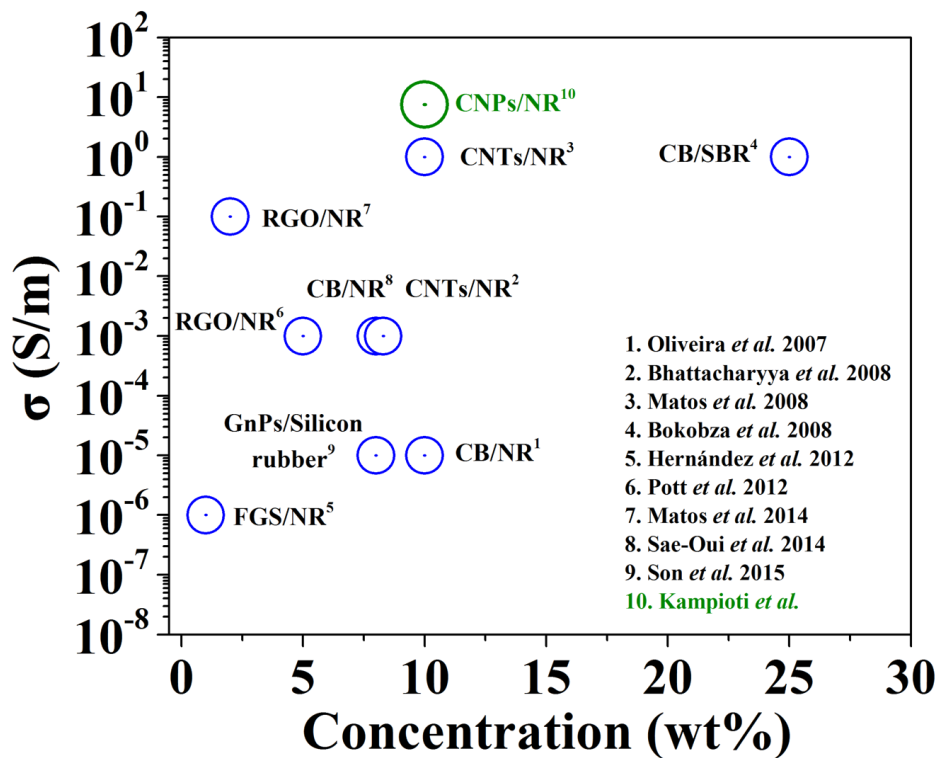


Figure 4.17: Conductivity values of polymer composite systems with carbon fillers reported in literature. With green colour is our conductivity result.

“CB” is carbon black, “SBR” is styrene-butadiene rubber, “RGO” is reduced graphene oxide, “GnPs” is graphene platelets, “CNTs” is carbon nanotubes and “FGS” is few layers graphene.

Independent studies from three different groups of Bokobza,¹⁴ Sae-Oui¹⁵ and Oliveira¹³ reported conductivity values in the range of 10^{-6} to 10^{-4} S.m⁻¹ for their composites with 8-10 wt% commercial carbon blacks; 4-6 orders lower than our result. Similar, or lower electrical enhancement was observed in CNTs-filled polymers as reported by Matos *et al.*,³ Sun *et al.*¹⁹ and others.¹⁴⁻¹⁶ Numerous studies were also made with other carbon fillers such as graphene nanoplatelets^{18,23} and reduced graphene oxide.^{4,17} Our significant electrical conductivity increase could be attributed to the good adhesion between the two components and to the formation of a sufficient conductive network.

Mechanical properties – Tensile tests

Tensile tests have been performed for the CNP_{HT2}/NR composites. **Fig. 4.18** shows representatives stress-strain curves of NR and the composites. The strain “ ϵ ” is defined as the difference of the length and the initial length over the initial length ($(l-l_0)/l_0$). The

inset graph shows the average values of the Young's modulus as a function of filler concentration (wt%).

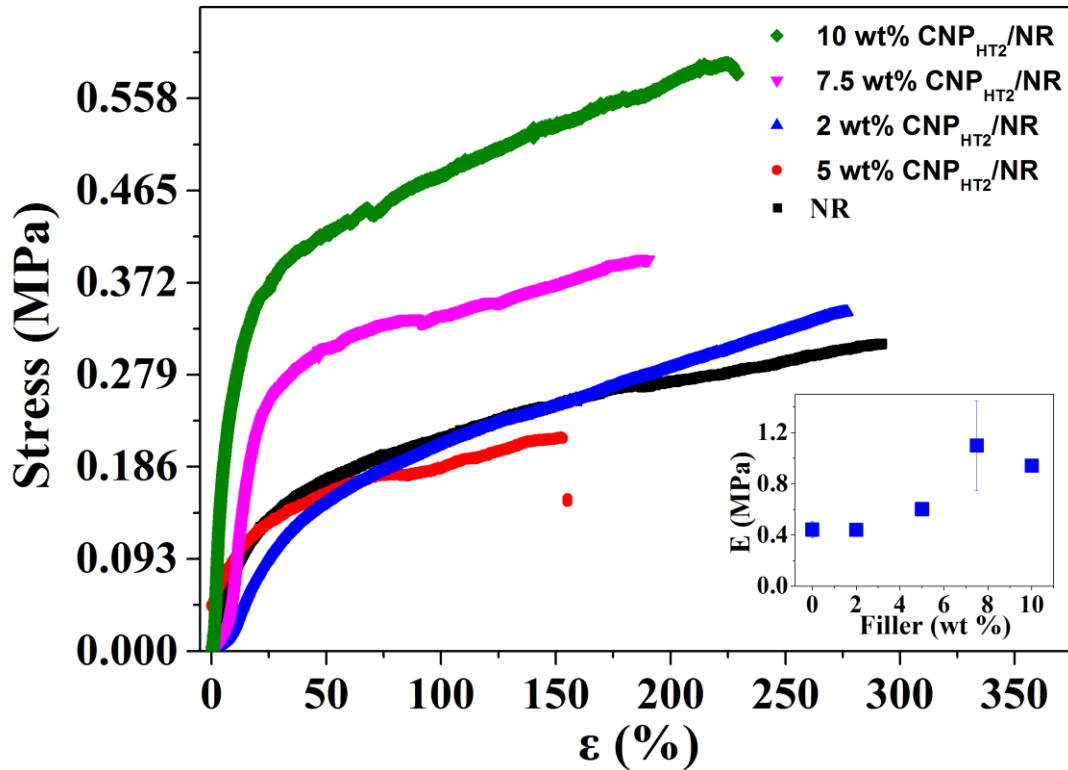


Figure 4.18: Stress-strain curves of CNP_{HT2} and CNP_{HT2}/NR composites Inset: Young's modulus as a function of CNP_{HT2} concentration.

The stress-strain curve of the composites with a low particle concentration follows similar behavior as pure NR. An enhancement in the tensile strength is observed upon the addition of CNP_{HT2} , with the highest breaking stress being 0.6 MPa (twice as much as NR) when 10 wt% filler was used. Moreover, the elastic properties of the polymer are also increased. The Young's moduli of the composites, extracted from the initial slope of the stress-strain graphs, are higher than the Young's modulus of the pure polymer (**fig. 4.18 inset**). For the composite with the 10 wt% filler, the elastic modulus is double than that of the pure rubber. **Table 4.6** discloses all of the mechanical properties observed for the CNP_{HT2}/NR composites.

Table 4.6: Mechanical properties of the CNP_{HT2}/NR composites (the values in brackets represent the errors)

CNP _{HT2} /NR composites: x wt% (x vol%)	E (MPa)	Tensile Strength (Mpa)	Strain at break (%)
NR	0.44 (6)	0.31 (3)	292 (10)
2 (0.83)	0.442 (2)	0.22 (5)	153 (7)
5 (2.1)	0.60 (2)	0.34 (2)	277 (6)
7.5 (3.2)	1.1 (4)	0.41 (3)	191 (10)
10 (4.34)	0.94 (4)	0.59 (5)	299 (7)

The addition of particles in the composites enhances the hardness of the polymer. This is due to a hydrodynamic effect arising from the inclusion of rigid particles into the soft rubber matrix. Since more force is needed for the samples with CNP_{HT2} filler to be elongated, the tensile strength is higher.²⁸ The contact of the particles becomes higher by increasing their concentration in the composite. This could be due to the surfactant (brij s 100) as not a strong stabilizer or from processes during the drying of the composite, allowing the formation of networks within the polymer matrix.

Regarding, the theoretical prediction of the influence of particulate reinforcement on the mechanical responses, it could be considered as relatively simple, even though in practice only the two limits could be calculated, rather than the actual values. In the case of uniform strain, the rule of mixtures can be used to predict the Young's modulus of a particulate composite for optimum reinforcement (upper limit) (**equation 4.5**):²⁹

$$E_c = V_p \cdot E_p + V_m \cdot E_m \quad (4.5)$$

Where E_p is the Young's modulus of the particles (by making the hypothesis that the Young's modulus is the same as of RGO, 250 MPa)^{17,30}, E_m is the Young's modulus of the matrix, V_p is the volume fraction of the particles, V_m is the volume fraction of the matrix. By considering the **equation 4.6**:

$$V_p + V_m = 1 \quad (4.6)$$

In the case of uniform stress (lower limit) the Young's modulus can be determined from the **equation 4.7 (or 4.8)**:

$$E_c^{-1} = V_p \cdot E_p^{-1} + V_m \cdot E_m^{-1} \quad (4.7)$$

Or

$$E_c \cdot E_m^{-1} = E_p \cdot (V_m \cdot E_p + V_p \cdot E_m)^{-1} \quad (4.8)$$

These results are shown in **fig. 19**. The Young's moduli obtained from the experimental data are between the upper and lower calculated limits. In order to properly model the reinforcement induced by the addition of CNP_{HT2}, we adapted the hydrodynamical model of Einstein-Smallwood-Guth as most suitable in our system (**equation 4.9**).¹⁶

$$E = E_m \cdot (1 + 0.67 \cdot f \cdot \varphi + 1.62 \cdot (f \cdot \varphi)^2) \quad (4.9)$$

Where f is the shape factor: 16.7 (50 nm lateral size and 3 nm width – considering individualized particles) and φ is the volume fraction of the filler. The weight fraction was transformed into the volume fraction by using the densities of NR and graphite (for NR; $d = 0.93$ and for CNP_{HT2} the density was considered the same as of the graphite; $d = 2.28$). The theoretical values are in good agreement with the experimental ones and are summarized in **table 4.7**.

Table 4.7: *Theoretical predictions of the Young's moduli of the CNP_{HT2}/NR composites.*

CNP _{HT2} /NR composites: x wt% (x vol%)	E (MPa) f: 16.7 Guth equation (eq. 4.9)	E (Mpa) Rule of mixtures (for uniform stress) (eq. 4.8)
NR	0.44	0.44
2 (0.83)	0.49	0.44
5 (2.1)	0.53	0.45
7.5 (3.2)	0.80	0.46
10 (4.34)	1.03	0.46

Noteworthy is that most of the published works used vulcanized NR as matrix because it has a better mechanical performance compared to unvulcanized NR due to the increased cross-link density. The important thing to note here is that the measurable effect that the CNP_{HT2} filler has on the mechanical properties of the composite is comparable between this study and previous studies that used carbon black as filler.^{13,15} The theoretical values for the lower limit and the experimental ones of E_c/E_m as a function of vol% filler are plotted in the **fig. 4.19**. We used a variety of density values of nanocarbon, from 1.7 to 2.3, to calculate the theoretical values of the Young's modulus of a particulate composite and we found very similar results with the ones shown in **fig. 4.19**.

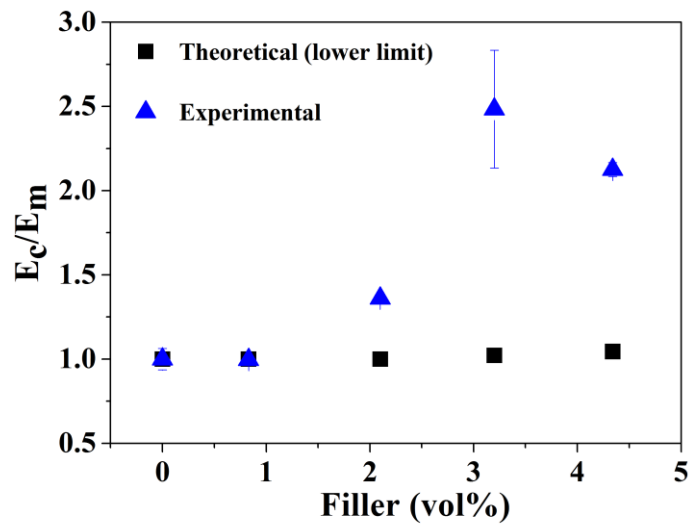


Figure 4.19: E_c/E_m as a function of CNP_{HT2} volume fraction from experimental data and from theoretical calculations from the lower bound of rule of mixtures.

Piezoresistive properties

The dependence of the electrical properties with mechanical deformation was determined by measuring the change of resistance as the samples were elongated by applying force in a tensile deformation. The influence of the sample dimensions was estimated from the resistivity measurements. **Fig. 4.20** to **4.23** show the two trends of the composites.

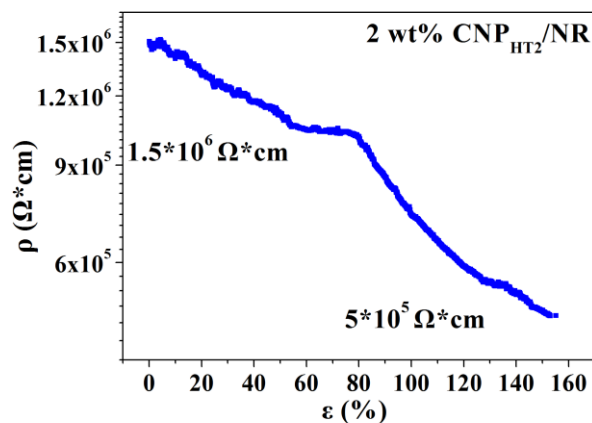


Figure 4.20: Resistivity as a function of strain for 2 wt % CNP_{HT2} /NR composites.

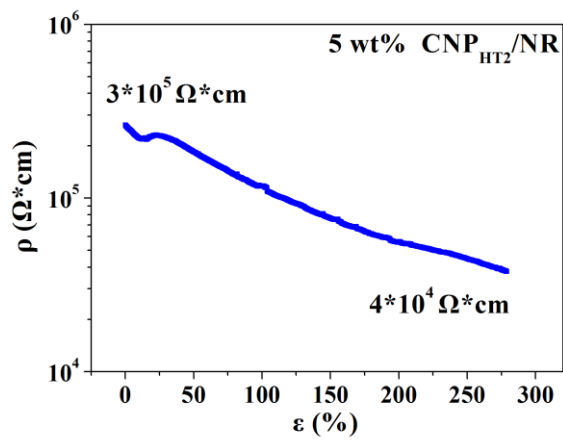


Figure 4.21: Resistivity as a function of strain for 5 wt % CNP_{HT2}/NR composites.

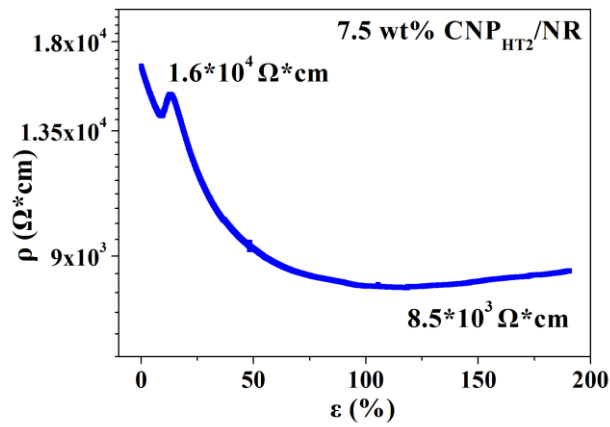


Figure 4.22: Resistivity as a function of strain for 7.5 wt % CNP_{HT2}/NR composites.

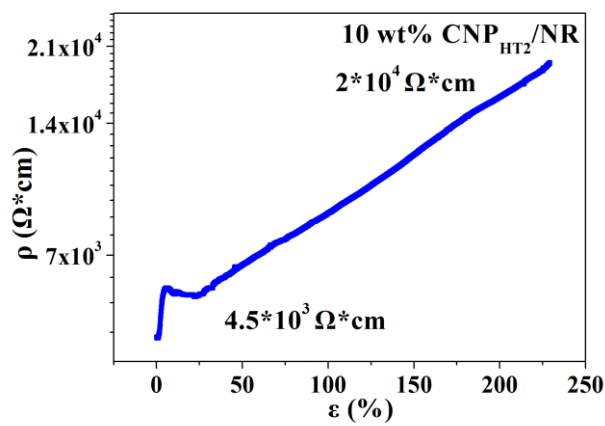


Figure 4.23: Resistivity as a function of strain for 10 wt % CNP_{HT2}/NR composites.

For the composites with a CNP_{HT2} content less than 10 wt% (4.34 vol%) (**fig. 4.20** to **fig. 4.22**), a decrease in resistivity was observed. However, the material with the highest filler concentration shows the opposite behavior. The geometry of the composites reduces the resistivity of the samples with 2, 5 and 7.5 wt% CNP_{HT2} , while for the sample with 10 wt%, it acts synergistically. A hypothesis to explain this phenomenon could be the following: for almost all of the composites undergoing stretching, the probability of contact between the particles decreases in the x axis (the axis where the stretching occurs), while the probability of contact in the y and z axes may be higher (**fig. 4.24**) resulting in the formation of more networks and eventually higher conductivity.

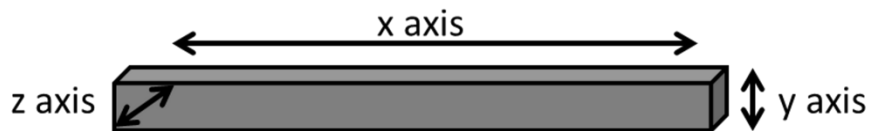


Figure 4.24: Schematic representation of $\text{CNP}_{\text{HT2}}/\text{NR}$ composite. The tensile test occurs at the x axis.

For the composite with the highest CNP_{HT2} amount, however, the contact probability is maximal in all axes due to a higher concentration of particles. When this sample is elongated, the particle distance increases in all the axes, causing lower conductivity values. Moreover, the ratio of the change in resistance and the initial resistance was plotted as a function of the strain on the $\text{CNP}_{\text{HT2}}/\text{NR}$ composites, as shown in **fig. 4.25** to **4.28**.

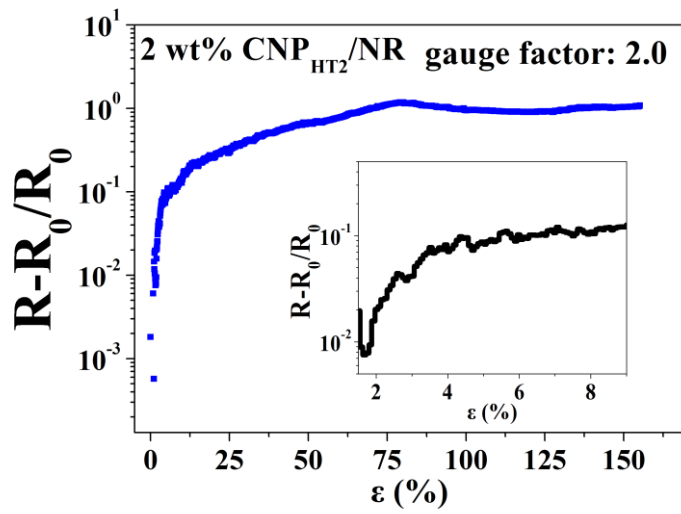


Figure 4.25: Normalized resistance change as a function of strain for the 2 wt% CNP_{HT2}/NR composite. Inset: Initial normalized resistance as a function of strain.

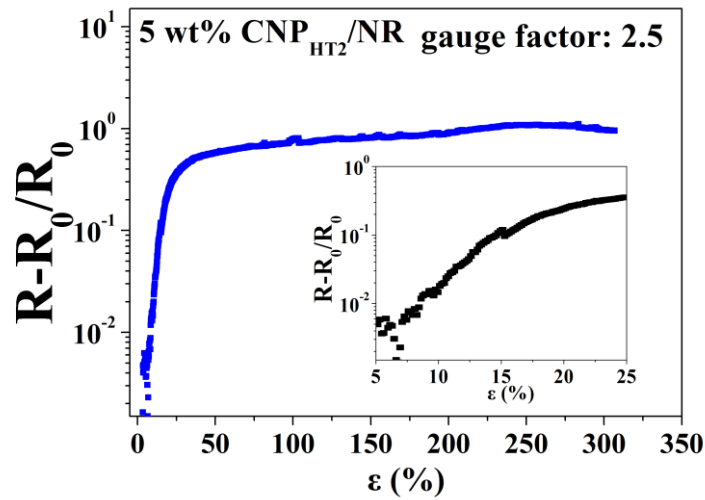


Figure 4.26: Normalized resistance change as a function of strain for the 5 wt% CNP_{HT2}/NR composite. Inset: Initial normalized resistance as a function of strain.

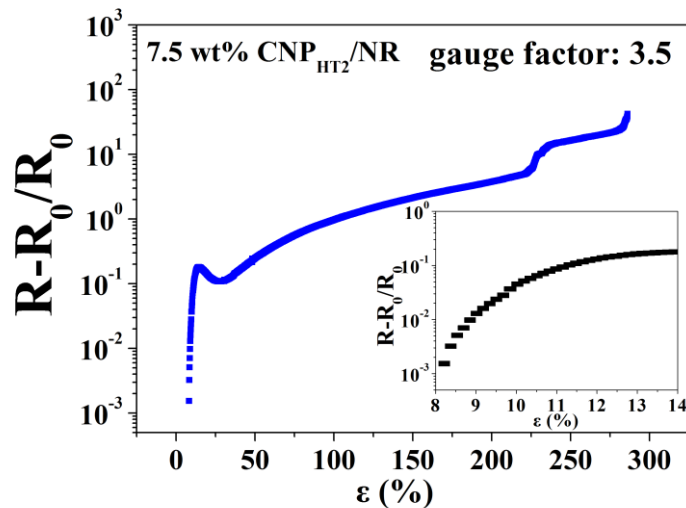


Figure 4.27: Normalized resistance change as a function of strain for the 5 wt% $\text{CNP}_{\text{HT2}}/\text{NR}$ composite. Inset: Initial normalized resistance as a function of strain.

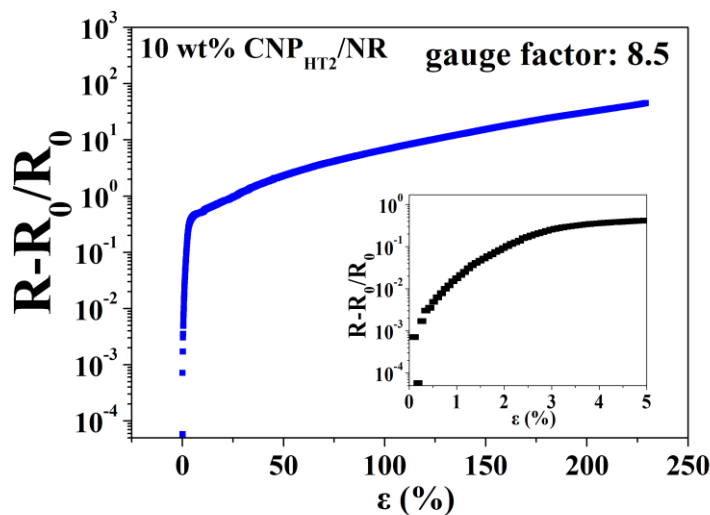


Figure 4.28: Normalized resistance change as a function of strain for the 10 wt% $\text{CNP}_{\text{HT2}}/\text{NR}$ composite. Inset: Initial normalized resistance as a function of strain.

In all samples, an increase is observed. Furthermore, in order to define the sensitivity of the composites, so they can be used as sensors of deformation, the gauge factor (extracted from the slope of the curve at low strain) has been calculated (inset of **fig. 4.25** to **4.28**). For the samples with CNP_{HT2} concentration up to 5 wt%, a relatively low gauge factor is observed. However, an electrical sensitivity almost two times higher is observed for 10 wt% $\text{CNP}_{\text{HT2}}/\text{NR}$ composite (gauge factor of 8.5). These results could also be used to interpret the gauge factor values of the composites. For composites up to 7.5

wt% CNP_{HT2} filler, due to their dimensions, the resistance is increased, but the resistivity is decreased, resulting in a relatively low value (maximum 3.5). For the sample with the highest CNP_{HT2} concentration, the dimensions do not alter the trend of the resistance, imparting a much higher gauge factor.

Conclusion

Two sets of cost-effective, multifunctional and environmentally friendly CNP/NR composites have been successfully prepared from “green” precursors (biogas) by a “green” procedure (latex technology) since no toxic solvents were used. Two different carbon sources and surfactants have been used, each yielding different optimum properties.

For the CNP₅/NR composites, well dispersed particles were obtained with increased mechanical properties. For the CNP_{HT2} composites, the formation of a network of particles was observed in the polymer matrix. This CNP_{HT2} network induces superior electrical properties, which are comparable to NR/carbon allotropes composites with some of the highest conductivity values observed. Furthermore, these systems show significant piezoresistive characteristics (for 10 wt% CNP_{HT2}/NR composite the gauge factor is 8.5).

Overall, the CNP/NR composites exhibit thermal, mechanical, electrical and piezoresistive properties superior to the pure NR, and by altering the carbon source and surfactant, could transform the NR from an insulating to conductive rubber.

References

1. PlasCarb. Available at: <http://www.plascarb.eu/>.
2. Hof, F. *et al.* Conductive inks of graphitic nanoparticles from a sustainable carbon feedstock. *Carbon N. Y.* **111**, 142–149 (2017).
3. Matos, C. F., Galembeck, F. & Zarbin, A. J. G. Multifunctional materials based on iron / iron oxide-filled carbon nanotubes / natural rubber composites. *Carbon N. Y.* **50**, 4685–4695 (2012).
4. Matos, C. F., Galembeck, F. & Zarbin, A. J. G. Multifunctional and environmentally friendly nanocomposites between natural rubber and graphene or graphene oxide. *Carbon N. Y.* **78**, 469–479 (2014).
5. Thomas, S., Chan, C. H., Pothen, L. A., K.R., R. & Maria, H. J. *Natural Rubber Materials Volume 1: Blends and IPNs.* **2**, (Royal Society of Chemistry, 2013).
6. Hosler, D.; Burkett, S. L. . T. Prehistoric Polymers: Rubber Processing in Ancient Mesoamerica. *Science (80-.)*. **284**, 1988–1991 (1999).
7. Goodyear, C. Improvement in India-rubber fabrics. (1844).
8. Ravve, A. *Principles of Polymer Chemistry*. (Springer Science and Business Media, LCC, 1995).
9. Nallasamy, P. & Mohan, S. VIBRATIONAL SPECTRA OF CIS-1,4-POLYISOPRENE. *Arab. J. Sci. Eng.* **29**, (2004).
10. *Rubber Nanocomposites: Preparation, Properties, and Applications*. (John Wiley & Sons, Ltd, 2010).
11. Rippel, M. M. & Galembeck, F. Nanostructures and adhesion in natural rubber: new era for a classic. *J. Braz. Chem. Soc.* **20**, 1024–1030 (2009).
12. Rahimi, A. & Mashak, A. Review on rubbers in medicine: natural, silicone and polyurethane rubbers. (2013).
13. Oliveira, F. A. *et al.* Study of the thermomechanical and electrical properties of conducting composites containing natural rubber and carbon black. *J. Appl. Polym. Sci.* (2007).
14. Bokobza, L., Rahmani, M., Belin, C., Bruneel, J. L. & El Bounia, N. E. Blends of carbon blacks and multiwall carbon nanotubes as reinforcing fillers for hydrocarbon rubbers. *J. Polym. Sci. Part B Polym. Phys.* **46**, 1939–1951 (2008).
15. Sae-Oui, P., Thepsuwan, U., Thaptong, P. & Sirisinha, C. Comparison of reinforcing efficiency of carbon black, conductive carbon black, and carbon nanotube in natural rubber. *Adv. Polym. Technol.* **33**, 1–7 (2014).
16. Bhattacharyya, S. *et al.* Improving reinforcement of natural rubber by networking of activated carbon nanotubes. *Carbon N. Y.* **46**, 1037–1045 (2008).
17. Potts, R., Shankar, O., Du, L., Ruo, R. S. & St, E. D. K. Processing – Morphology – Property Relationships and Composite Theory Analysis of Reduced Graphene Oxide / Natural Rubber Nanocomposites. *Macromolecules* **45**, (2012).
18. Araby, S. *et al.* Electrically and thermally conductive elastomer/graphene nanocomposites by solution mixing. *Polym. (United Kingdom)* **55**, 201–210 (2014).

19. Sun, Y., Wang, J., Qi, S., Tian, G. & Wu, D. Permittivity transition from highly positive to negative: Polyimide/carbon nanotube composite's dielectric behavior around percolation threshold. *Appl. Phys. Lett.* **107**, 12905 (2015).
20. Song, J. *et al.* Modified graphite filled natural rubber composites with good thermal conductivity. *Chinese J. Chem. Eng.* **23**, 853–859 (2015).
21. Vigolo, B. *et al.* Macroscopic fibers and ribbons of oriented carbon nanotubes. *Science* **290**, 1331–4 (2000).
22. Ciesielski, A. & Samorì, P. Graphene via sonication assisted liquid-phase exfoliation. *Chem. Soc. Rev.* **43**, 381–98 (2014).
23. Song, Y. *et al.* Enhancing the thermal, electrical, and mechanical properties of silicone rubber by addition of graphene nanoplatelets. *Mater. Des.* **88**, 950–957 (2015).
24. Zhang, C., Zhai, T., Dan, Y. & Turng, L.-S. Reinforced natural rubber nanocomposites using graphene oxide as a reinforcing agent and their in situ reduction into highly conductive materials. *Polym. Compos.* (2016).
25. Shtein, M., Nadiv, R., Buzaglo, M., Kahil, K. & Regev, O. Thermally conductive graphene-polymer composites: Size, percolation, and synergy effects. *Chem. Mater.* **27**, 2100–2106 (2015).
26. Hernández, M., Bernal, M. del M., Verdejo, R., Ezquerra, T. A. & López-Manchado, M. A. Overall performance of natural rubber/graphene nanocomposites. *Compos. Sci. Technol.* **73**, 40–46 (2012).
27. Boland, C. S. *et al.* Sensitive, high-strain, high-rate bodily motion sensors based on graphene-rubber composites. *ACS Nano* **8**, 8819–8830 (2014).
28. Othman, A. bin & Gregory, M. J. Stiffening effect of carbon black: Its interpretation by a modified Guth-Gold equation. *J Nat Rubb Res* **3**, 7–20 (1988).
29. Young, R. J., Kinloch, I. A., Gong, L. & Novoselov, K. S. The mechanics of graphene nanocomposites: A review. *Compos. Sci. Technol.* **72**, 1459–1476 (2012).
30. Suk, J. W., Piner, R. D., An, J. & Ruoff, R. S. Mechanical Properties of Monolayer Graphene Oxide. *ACS Nano* **4**, 6557–6564 (2010).

Chapter 5

Carbon nanopuck photoluminescence

Table of contents

Chapter 5.....	167
Carbon nanopuck photoluminescence.....	167
Introduction.....	169
1. State of the art	170
2. Experimental section.....	173
a. Solution/dispersion preparation procedures.....	173
Preparation of CNPa.....	174
Preparation of CNPb.....	175
Preparation of CNPc	176
Preparation of CNPd.....	177
b. Characterization techniques	178
3. Results and discussion.....	178
a. CNPa	178
b. CNPb.....	182
c. CNPc	185
d. CNPd.....	188
Conclusion	192
References.....	193

Introduction

In this chapter preliminary tests of the photoluminescence (PL) of carbon nanopucks (CNPs), dispersed and/or dissolved in liquid media are presented.¹⁻⁶ In part 1, a report of the relevant literature on the PL of graphitic materials is given. Part 2 comprises the experimental section which involves the description of four processes allowing the dissolution or the dispersion of CNP in liquid media. Afterwards, the “results and discussions” are presented where the CNPs images for the different preparation procedures are given through atomic force microscopy (AFM). Then, the absorption and emission spectra, as well as possible PL mechanisms, are discussed.

1. State of the art

The number of studies which focus on the photoluminescence of graphitic materials with size in the nanometer scale, progressively increases. Blue to near infrared PL of nanocarbon materials from different precursors, of different sizes, shapes and surface/edges states have been recorded.^{1-4,7} Consequently, a variety of possible PL mechanisms has been proposed. In 2010, Chhowalla's group has performed an interesting study on the PL of graphene oxide (GO) films. When excited in the UV, these films emit a broad blue emission. In this study they investigated the dependence of this emission on reduction of GO films.² The suggested mechanism is shown in **fig. 5.1**.

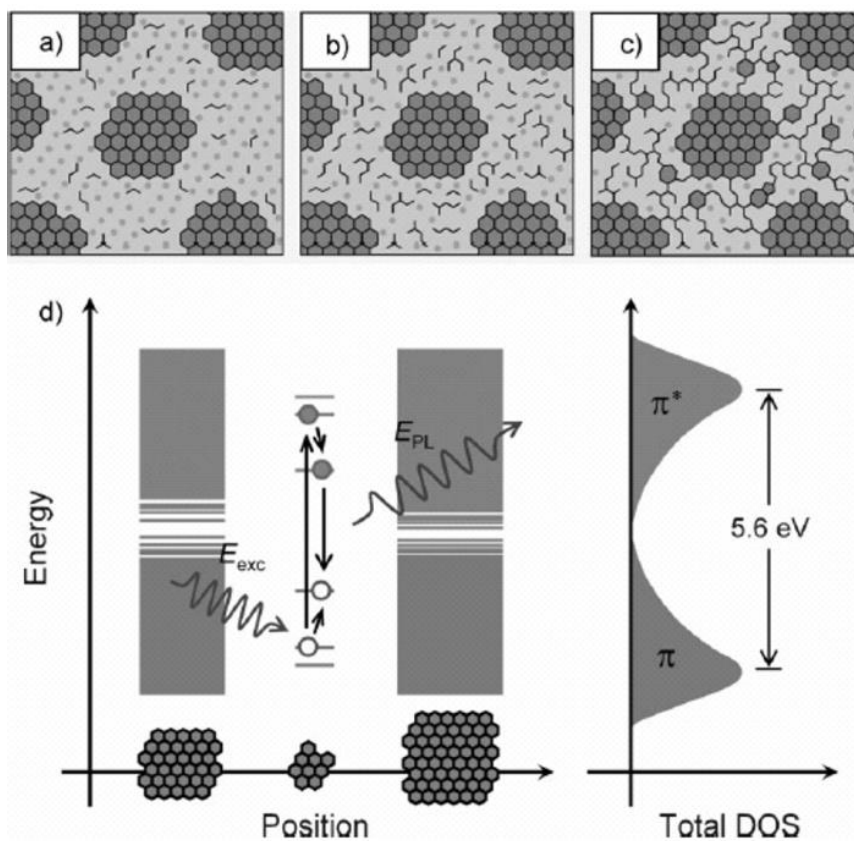


Figure 5.1: a–c) Structural models of graphene oxide at different stages of reduction. The localized sp² domains act as the luminescence centers. d) Band structure of GO.²

The images in **fig. 5.1 a)** to **fig. 5.1 c)** show the structural models of GO at different reduction stages, where GO contains 3 nm sp² clusters and smaller sp² domains (zigzag lines) are all around the insulating sp³ matrix. The grey dots represent the oxygen atoms that a large fraction of carbon is bonded with. **Fig. 5.1 d)** shows the band structure of GO where, due to confinement, for the small sp² configurations, the energy levels are

quantized with a large energy gap. An electron-hole pair radiative recombination is also shown. In Chhowalla's group study, the PL was found to be relatively weak for GO (**fig. 5.1 a**) but increased under reduction (**fig. 5.1 b**). This increase of the blue PL was assigned to the formation of additional small sp^2 fragments between the larger sp^3 clusters due to the reduction of oxygen (**fig. 5.1 b**). Therefore, the PL was attributed to the recombination of confined electron-hole pairs in sp^2 domains because the π and π^* electronic levels lie within the σ and σ^* states of the sp^3 matrix and thus, are strongly localized. However, after extensive reduction, the PL intensity was gradually decreasing. The PL quench was attributed to the fact that the sp^2 domains after a certain reduction level, created percolating pathways among the larger clusters. Therefore, the hopping of excitons to non-radiative recombination centers was facilitated (**fig. 5.1 c**).

In 2011, Galande *et al.* in their study of the pH-dependent photoluminescence of GO, they attributed the observed emission directly to the functionalized groups.⁸ They have shown that the emission spectra were different in acidic and basic media. They proposed that the visible PL derives from quasi-molecular fluorophores similar to polycyclic aromatic compounds. The PL shift was attributed to the fact that the excited state of the fluorophore species was protonated in acidic solution. They suggested that the quasi-molecular fluorophore was due to the electronic couple of carboxylic acid groups with the surrounding carbon atoms of the graphene sheets.

Shang *et al.* proposed that this kind of quasi-molecular fluorophore is caused by the non-oxidized carbon atom regions and the boundary of oxidized carbon atoms.⁴ The latter could be CO, carbonyl and carboxyl functionalized groups. The PL origin was assigned to the recombination of the electron-hole pair from the bottom of the conduction band and neighboring localized states to the valence band. They also observed that the PL features of GO vary with different proportions of oxidized groups.

Another PL mechanism could derive from the edge states which is more prominent when the size of nanocarbon materials is smaller since there is a higher concentration of edges.¹ Radovic and Bockrath reported that the armchair edges are carbyne-like (the singlet ground state being the most common) while the zigzag sites are carbene-like, with the most common to be the triplet ground state.⁹ Carbenes have two electronic configurations in ground states: triplet and singlet. For the s^2 singlet state, there is a pair of two non-bonding electrons in the s orbital and the p orbital is vacant. In the triplet state s^1p^1 , each of the two orbitals s and p are occupied with an electron with an energy difference to be below 1.5 eV.¹

In 2010, Pan *et al.* observed blue PL from graphitic nanoparticles of 9.6 nm, namely graphene quantum dots (GQDs), produced by the hydrothermal deoxidation of pre-oxidized graphene sheets into graphitic nanoparticles.¹ They proposed that the PL may originate from free zigzag sites with a carbene-like triplet ground state, as shown in **fig. 5.2**.

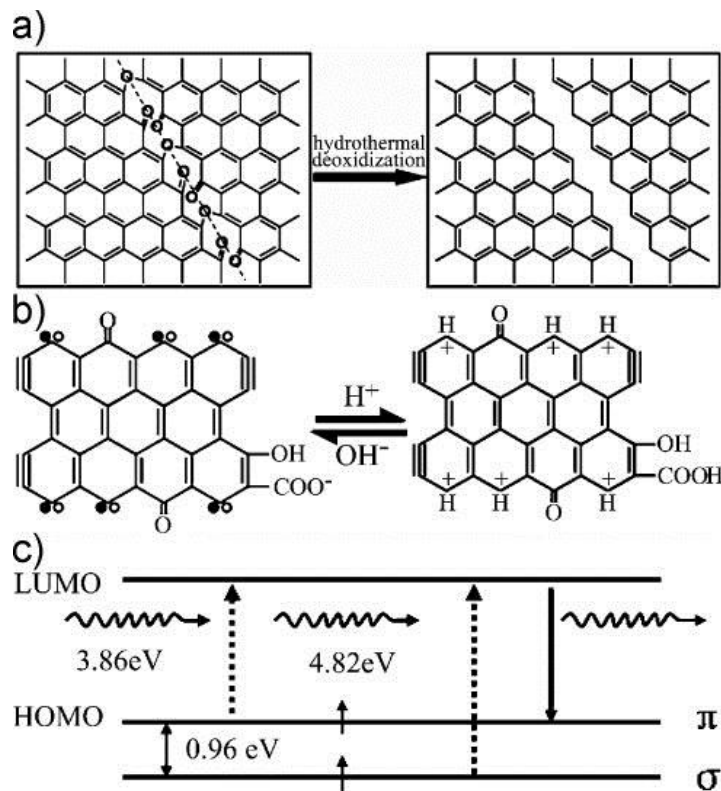


Figure 5.2: a) Mechanism for the hydrothermal deoxidation of oxidized graphene sheets into GQDs. b) Models of the GQDs under alkaline (left) and acidic (right) conditions. c) Typical electronic transitions of triple carbene state at zigzag sites observed in the optical spectra.¹

Fig 5.2 a) shows the chain which consists of epoxy and carbonyl pair groups (left) is being cut under hydrothermal treatment. **Fig. 5.2 b) right** shows that under acidic conditions, the free zigzag sites of the GQDs are protonated, leading to PL quenching due to the breaking of the emissive triple carbene-like state. However, the free zigzag sites are restored under alkaline conditions and the PL is recovered (**fig. 5.2 b) left**). The same group observed in the optical spectra two electronic transitions of 320 nm (3.86 eV) and 257 nm (4.82 eV) as shown in **fig. 5.2 c)**. These transitions were regarded as transitions from the s and p orbitals (energy difference 0.96 eV smaller) and the blue emission was attributed to the irradiation decay of the electrons. In 2010, Lin *et al.* produced GQDs of 20 nm size from carbon nanotubes. The AFM and bright field high resolution TEM (HRTEM) characterizations confirm the single layer objects and the

zigzag edges.¹⁰ On the whole, Pan *et al.* and Lin *et al.* prepared GQDs with sizes of 9.6 nm and 20 nm, respectively with similar absorption and emission behaviors, evidence that the PL mechanism was driven by the triple carbene site at the zigzag edges and not by quantum confinement.

Recently, Huang *et al.* prepared solutions of negatively charged calibrated nano graphene sheets (graphenides) in N-Methyl-2-pyrrolidone (NMP) from graphite nanofibers.¹¹ The size of the dissolved objects were of 1 to 2 nm thickness and 10 nm lateral size. After exposure to air these solutions exhibited strong PL. They also plotted the maximum emission intensity as a function of time and they observed an increase in PL that was followed by PL saturation. This saturation curve was well-fitted with a pseudo-first order kinetic reaction. In particular, they considered the following chemical reaction (**equation (5.1)**), that exhibit PL:



Where $[\text{G}]_{\text{red}}$ is the concentration of graphenides, $[\text{O}_2]$ is the concentration of oxygen and $[\text{G}]_{\text{edge}}$ is the edge states concentration. Since the oxygen amount is infinite, the reaction could be characterized as pseudo-monomolecular and could satisfy the **equation (5.2)**:

$$d[\text{G}]_{\text{edge}}/dt = k'[\text{G}]_{\text{red}} \quad (5.2)$$

Where k' is the monomolecular velocity constant. Thus, the concentration of edge states had the exponential increase as shown in **equation (5.3)**:¹¹

$$1 - \exp(-k't) \quad (5.3)$$

2. Experimental section

a. Solution/dispersion preparation procedures

Carbon nanopucks (CNPs) have been dissolved and dispersed in organic and aqueous media. Through graphite intercalation compounds (GICs) the CNPs have been dissolved a) in organic solvent and dispersed b) in water, following well-established studies from our group.¹²⁻¹⁴ CNPs have been also dispersed in aqueous media c) by a strong oxidation using the so-called modified Hummers method¹⁵⁻¹⁷ and d) by a milder oxidation than the previous using a mixture of nitric and sulfuric acids¹. The CNP₂ grade was used for the

investigation of PL before and after the heat treatment, depending on the preparation process.

In order to distinguish the samples, designations were given. Based on the preparation procedure the CNP solution and/or dispersions were named as CNPa to CNPd as shown in **table 5.1**.

Table 5.1: CNPs designations based on the preparation procedure.

Products designations	Synthetic route
CNP _a	Purified CNP ₂ dissolved in NMP via GIC
CNP _b	Purified CNP ₂ dispersed in H ₂ O via GIC
CNP _c	CNP ₂ dispersed in H ₂ O via oxidation using modified Hummers method
CNP _d	CNP ₂ dispersed in H ₂ O via oxidation using a mixture of H ₂ SO ₄ and HNO ₃ acids

Preparation of CNPa

All procedures that are air sensitive (preparation of KC₈ and its solutions, handling of the solutions, deposition on surfaces) were performed in an Innovative Technology Inc. glove box with less than one ppm O₂ and moisture contents. NMP (anhydrous, Aldrich) was distilled under reduced pressure before entering the glove box.

Preparation of carbon nanopucks intercalation compound (CNPIC)

In a sealed tube, CNP powder was mixed with the potassium metal with a molar ratio of C/K = 8. The reaction took place at 250 °C under vacuum. After a day of reaction, brownish CNPIC (KC₈ has golden/copper color) was collected.

Preparation of CNPIC solution

CNPICs 20 mg were dissolved in 10 mL of distilled anhydrous NMP under inert atmosphere, at room temperature, using a vortex stirrer (800 rpm). After three days of stirring, centrifugation was performed in order to remove the non-soluble material from the solution. The solution in NMP was centrifuged at 6000 rpm for 20 minutes. After centrifugation, the graphenide solution in NMP was recovered. The solution of CNPIC in NMP, namely CNPa, was stored under inert atmosphere. **Fig. 5.3** shows a schematic representation of the preparation of CNPa preparation in NMP and the corresponding

emission spectra were recorded after dilution with distilled NMP (dilution factor, DF=100).

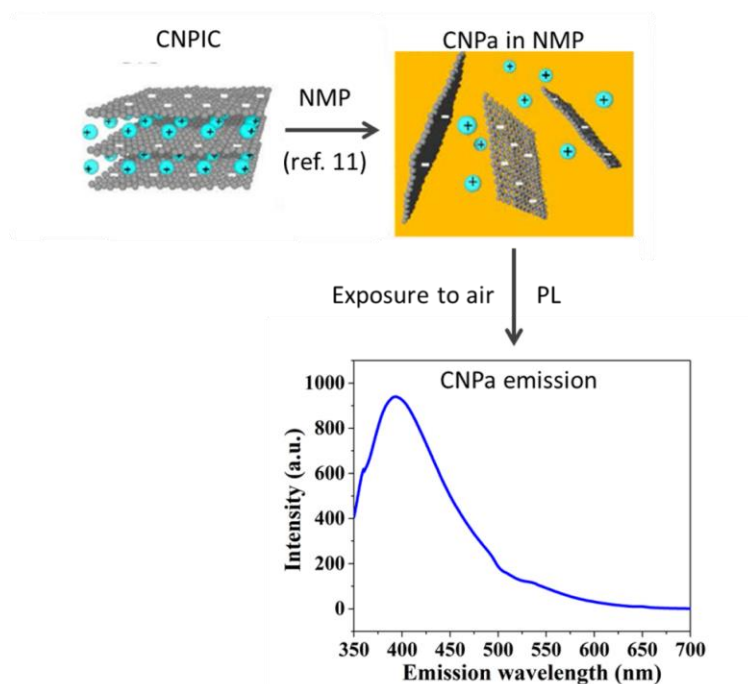


Figure 5.3: Schematics of the preparation of CNPa solution and a representative emission spectrum at λ_{exc} . 220 nm.

Preparation of CNPb

For the CNPb preparation, nearly the same procedures have been followed as for CNPa. CNPa just changing the solvent NMP by THF. Dry THF (contains no stabilizers, Aldrich) was dried on an alumina Pure-Solv purifier column (Innovative Technologies) and then distilled in the glove box.

CNPICs 10 mg were dissolved in 10 mL of distilled THF under inert atmosphere, at room temperature, using a vortex stirrer (800 rpm). After three days stirring, the solution in THF was centrifuged for 30 min/3000 rpm. After centrifugation, the graphenide solution in THF was recovered. The main change by comparison with CNPIC preparation was air exposed and oxidized in air (loss of electrons) which induce a return to neutral graphene. Then, it was directly transferred into degassed water. The CNP dispersion in H₂O with this method will be referred as CNPb (**table 5.1**). The PL for the dispersion in H₂O was recorded for the initial concentration and for dispersion with different DFs. Due to the low initial concentration. A schematic representation of the preparation of CNPb preparation and a representative emission spectrum are shown in **fig. 5.4**.

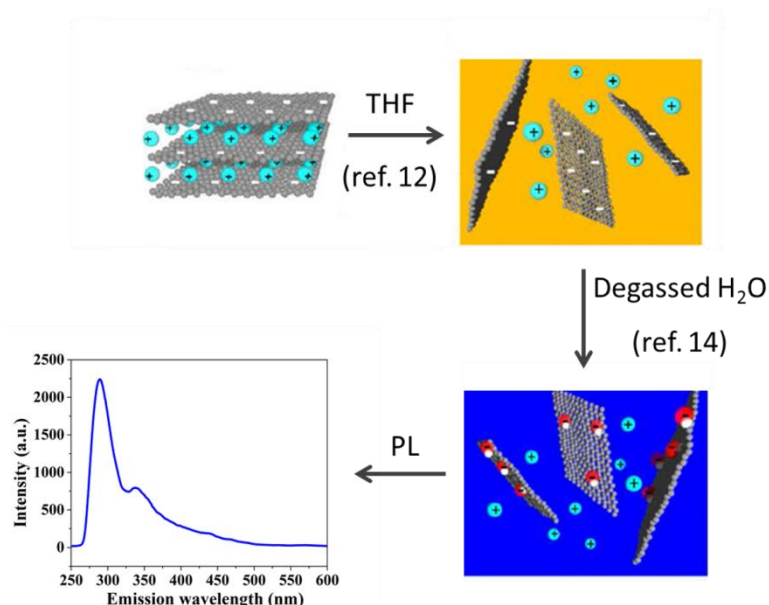


Figure 5.4: Schematics of the preparation of CNPb and a representative emission spectrum at $\lambda_{exc.}$ 325 nm.

Preparation of CNPc

H₂SO₄ (95-97%), HCl and H₂O₂ 30 wt% were purchased from Sigma Aldrich, KMnO₄ was supplied by Merck, Darmstadt, and P₂O₅ and K₂S₂O₈ were purchased from Prolabo. Raw CNP₂ powder was oxidized following the so-called modified Hummers method which involves two oxidation stages.

First oxidation

About 1100 mg of CNP₂ was placed in a 1000 mL boiling flask. 20 g of K₂S₂O₈, 20 g of P₂O₅ and 400 mL of H₂SO₄ (95-97%) were added in the flask. The mixture was heated at 195 °C under reflux for 6 h and then was let at rest overnight at room temperature. Oxidized CNP₂ was filtered with polyvinylidene fluoride (PVDF) membrane (one day duration) and rinsed with abundant distilled water until neutral pH (duration two days). At the end, a wet cake-like material was recovered.

Second oxidation

The previously collected wet cake was placed in a boiling flask. 69 mL H₂SO₄ (95-97%) was added and the mixture was left stirring for 10 min to obtain homogeneous mixture. The flask was kept in an ice bath and 9 g KMnO₄ was added (dark green color). The temperature was adjusted to 35 °C and the mixture was left stirring for 2 h. In another flask which was kept in an ice bath, 560 mL of H₂O was placed and the mixture was added gradually while stirring (until the color of the mixture passed from pink-red to dark brown). 15 mL H₂O₂ (30 wt%) was added (always the flask in an ice bath). Finally,

the mixture was filtered to remove metallic ions with a PVDF membrane under vacuum for three to four days) and rinsed with a 1:10 HCl aqueous solution. The collected material was rinsed with deionized water until neutral. After dispersion in water, tip sonication of 20 min (total energy 9.6 kJ) was performed, using a Branson Digital Sonifier tip sonicator, to improve the stabilization of CNPc dispersion. The final weight of the product was obtained after lyophilization (freeze drying). **Fig. 5.5** shows schematically the preparation of CNPc and a representative emission spectrum.

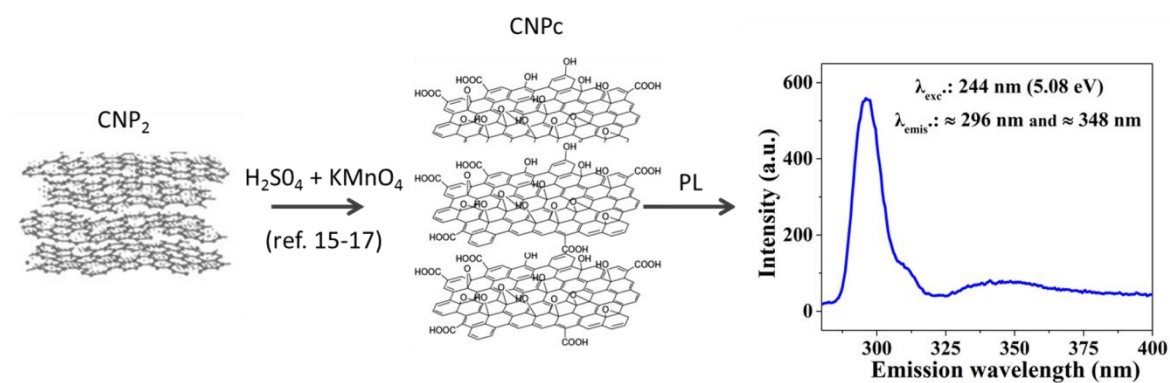


Figure 5.5: Schematics of the preparation of CNPc and a representative emission spectrum at λ_{exc} 244 nm.

Preparation of CNPd

HNO₃ (65 %) and H₂SO₄ (95-97 %) were purchased from Carlo Erba reagents and Sigma Aldrich respectively.

The CNP were oxidized with a mixture of nitric and sulfuric acids.

About 400 mg of raw CNP₂ was placed in a 100 mL boiling flask. Then, 12 mL of HNO₃ (65%) and 38 mL of H₂SO₄ (95-97%) were added in the flask. The mixture was sonicated (bath sonicator Elmasonic X-tra) during 2 h at 80 °C. Then, oxidized CNP was rinsed with abundant distilled water until neutral pH using centrifugation (30 min/4000 rpm)/redispersion cycles. **Fig. 5.6** shows a schematic representation of the CNPd preparation and a representative emission spectrum.

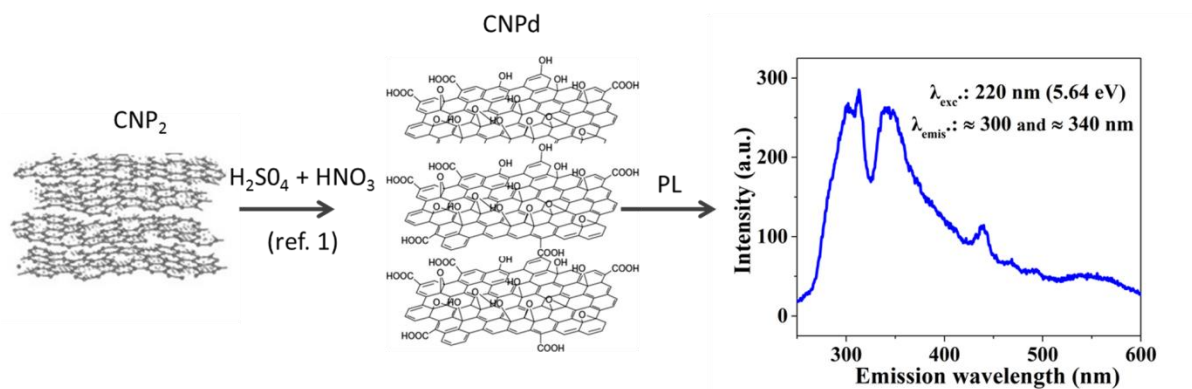


Figure 5.6: Schematics of the preparation of CNPd and a representative emission spectrum at $\lambda_{exc.}$ 220 nm with noisy poor emission.

b. Characterization techniques

Absorption spectroscopy and atomic force microscopy (AFM) imaging were performed as described in Chapter 2. For AFM, regarding the CNPa (CNP solution in NMP) which was stored in inert atmosphere, the deposit was performed in the glove box. In particular, deposit of 30 μ L of CNPa was prepared onto \sim 1 cm² mica substrate (freshly cleaved) by drop-casting inside the glove box. The coated surface was dried under vacuum at room temperature and then taken out of the glove box and washed carefully using deionized water, isopropanol and washed again with deionized water (to get rid of potassium). Finally, the mica substrate was dried at 200 °C overnight. PL mapping and spectra were acquired using JASCO FP-8300 fluorescence spectrometer.

3. Results and discussion

a. CNPa

When CNPa came in contact with air, re-oxidation occurred (charged graphene layers returning mostly to neutral graphene).^{11,12} Oxygen got reduced to superoxide that led to KOH in the presence of moisture. The CNP particles were adsorbed on the mica surface to explore their size and height through AFM topography imaging (**fig. 5.7**).

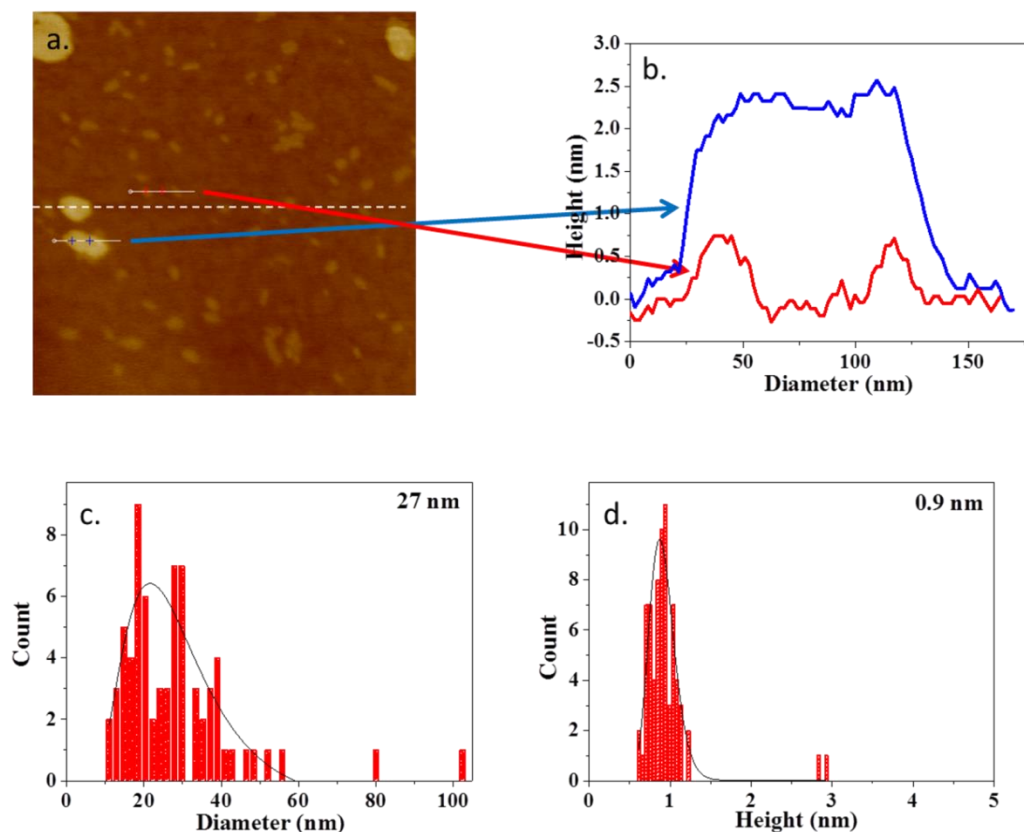


Figure 5.7: *a.* From CNPa AFM topography image of CNP solution drop casted onto a freshly cleaved mica surface. *b.* Cross sections of the topography images are plotted. *c.* Statistical analysis of the diameter of the CNP particles. *d.* Statistical analysis of height of the CNP particles.

The image in **fig. 5.7 a** reveals a flat surface, with homogenous nano objects. Single objects can be clearly observed with heights around 0.6–1.2 nm as well as a few thicker objects, as seen in **fig. 5.7 b**. CNP particles with a mean lateral size of 27 nm (**fig. 5.7 c**) and height of ca. 1 nm (2 to 3 layers) (**fig. 5.7 d**) were acquired as seen in statistical analysis. The next step of this analysis is to record the absorption spectra of CNPa. Mapping of the excitation as a function of the emission wavelength was recorded for the range 200 to 800 nm for the CNPa after 3 days of air exposure. **Fig. 5.8** shows the PL mapping of the wavelength range of interest. The lighter green color represents higher PL intensity.

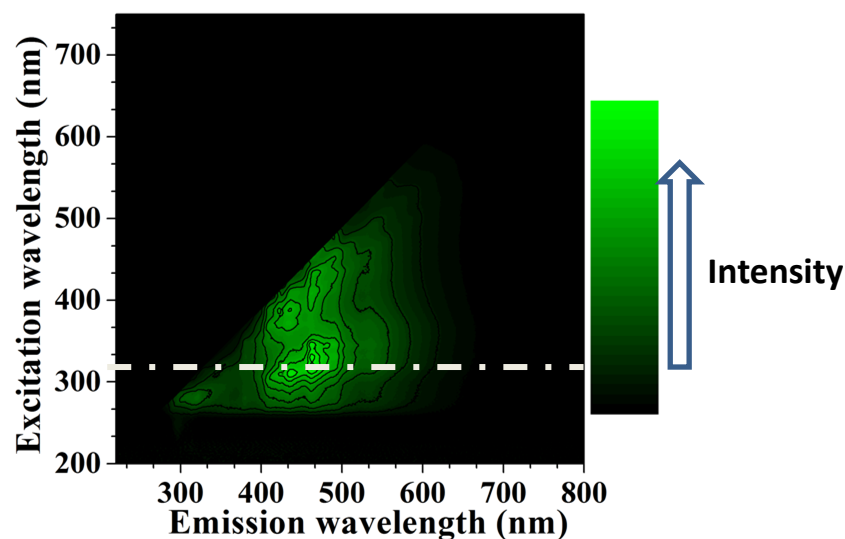


Figure 5.8: PL mapping of excitation wavelength as a function of emission wavelength of CNPa. The intensity numbers correspond to absolute values.

CNP_a exhibits more intense PL in emission wavelength range from 300 to 600 nm at excitation wavelengths between 260 to 500 nm. After taking emission spectra in different wavelengths, λ_{exc} of 325 nm was chosen since it provides the most intense PL. **Fig. 5.9** shows the emission spectra of CNPa upon air exposure from $t = 0$ (before opening) to $t \sim 5$ days at excitation wavelength of 325 nm.

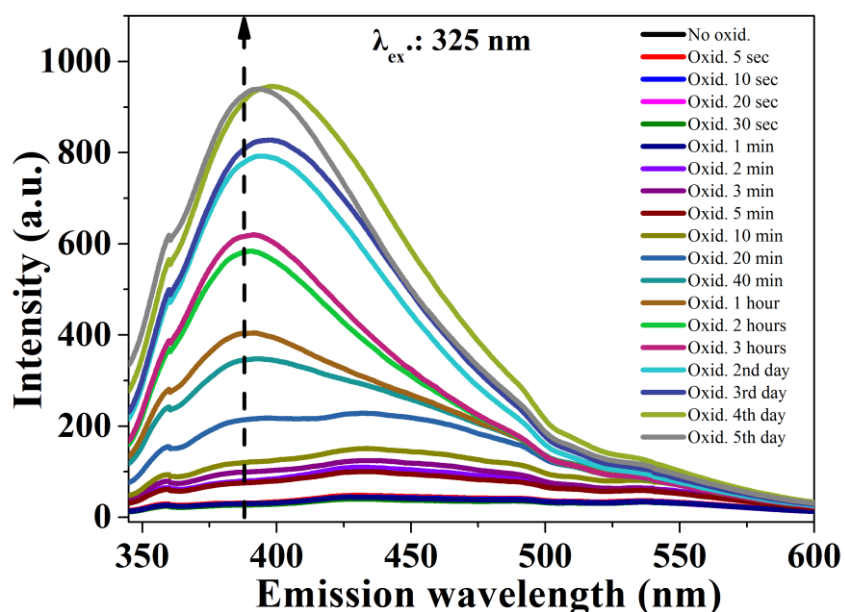


Figure 5.9: Photoluminescence spectra of the CNPa from $t = 0$ (fresh solution in NMP) to 5 days at an excitation wavelength of 325 nm. The intensity numbers correspond to absolute values.

Before air exposure, no PL is evident. After contact with air, a broad blue PL line that continuously increases over time is clearly observed. Moreover, as oxidation continues, a slight red shift (~ 13 nm) of the maximum emission wavelength occurs. **Fig. 5.10** shows the maximum PL intensity as a function of time.

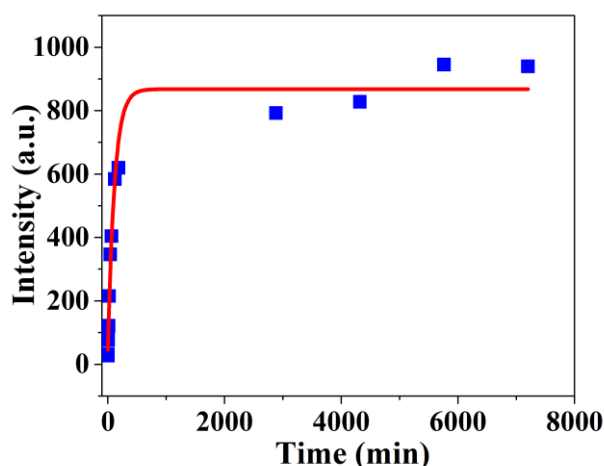


Figure 5.10: Maximum emission as a function of time for the CNPa upon air exposure from $t = 0$ (before opening) to 5 days at excitation wavelength of 325 nm.

A PL increase as a function of time can be seen which is eventually saturated. Based on the study of Huang *et al.* the curve was fitted when considering a pseudo-first order kinetic reaction (**equations 5.1 to 5.3**).¹¹

b. CNPb

Fig. 5.11 shows the absorption spectrum of CNPb (CNP dispersion in water).

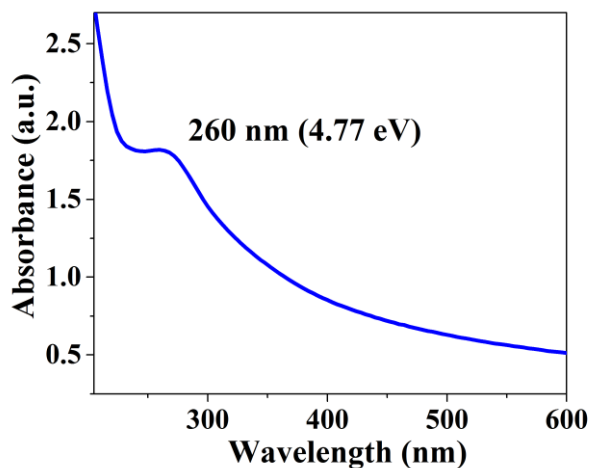


Figure 5.11: Absorption spectrum of CNPb.

The absorption spectrum shows a peak at 260 nm which could be assigned to the π - π^* transition of C=C bonds.^{1,2,4} As for the CNPa, mapping of the excitation as a function of the emission wavelength was recorded for wavelength 200 to 800 nm, in order to determine the excitation and emission range where more intense PL is observed. **Fig. 5.12** shows the CNPb PL excitation-emission map of the wavelength range of interest. As the PL intensity increases, the color becomes lighter.

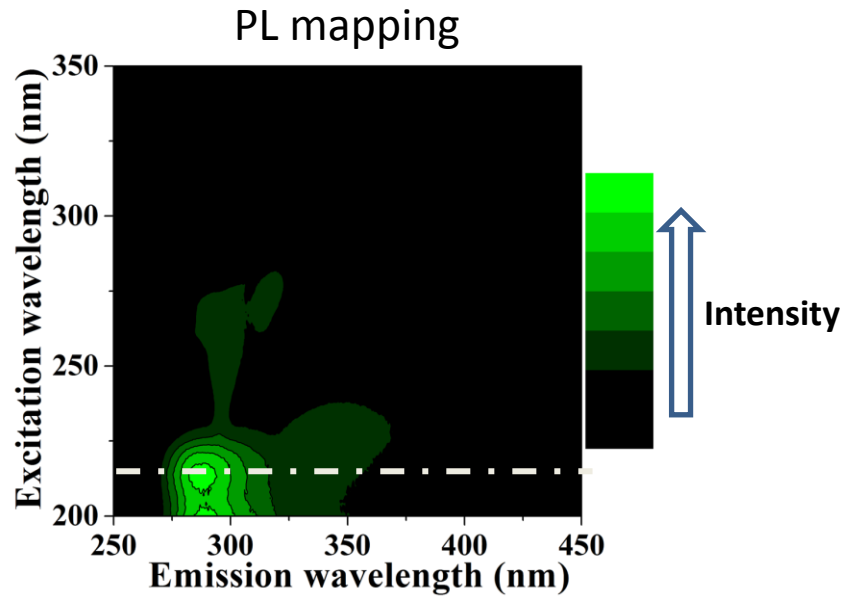


Figure 5.12: PL mapping of excitation wavelength as a function of emission wavelength of CNPb. The intensity numbers correspond to absolute values.

The peak of PL is found at an emission wavelength ($\lambda_{\text{emis.}}$) of ca. 290 nm with another maxima of weaker intensity at ca. 340 nm. CNPb d exhibits this PL maximum at excitation wavelength of about 225 nm. **Fig. 5.13** shows the CNPb emission spectra with $\lambda_{\text{exc.}}$ at 220 nm of different concentrations after dilution (DF from 1.5 to 9).

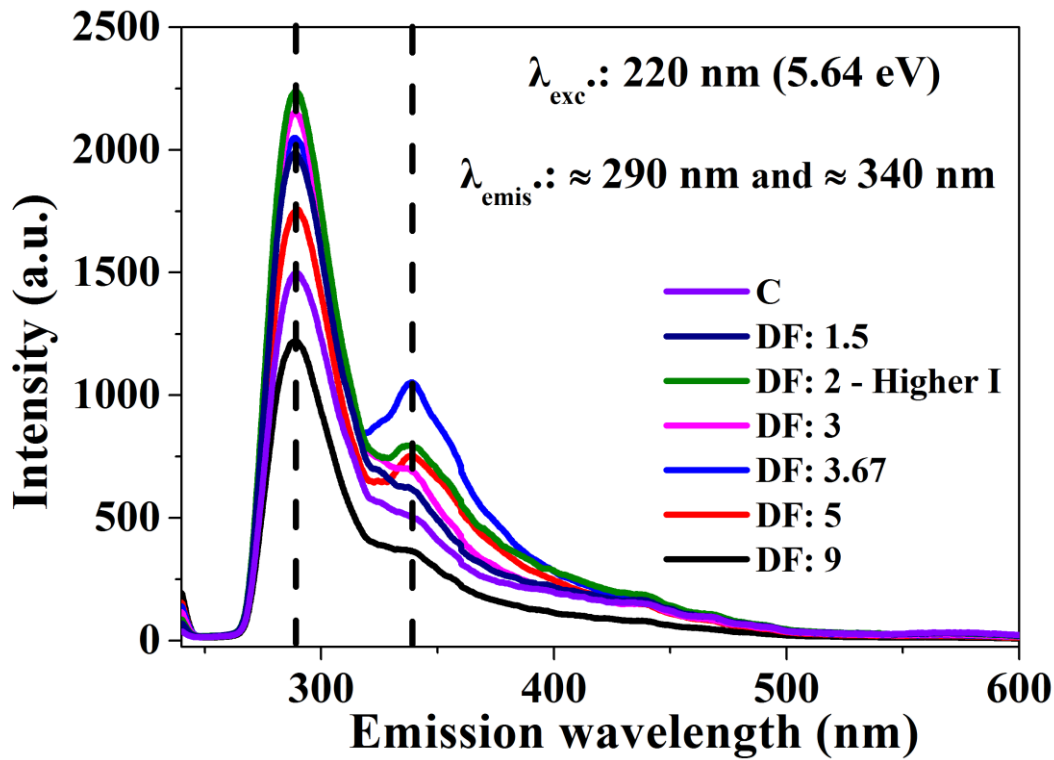


Figure 5.13: PL spectra of CNPb with different dilution factors, λ_{exc} : 220 nm. The intensity numbers correspond to absolute values.

CNPb exhibit strong UV photoluminescence λ_{emis} of ca. 290 and ca. 300 nm as it has been seen for the PL mapping (**fig. 5.12**). Moreover, the maximum emission intensity is not observed for the most concentrated sample but for the sample which was diluted with DF 2. Therefore, its emission spectra in different λ_{exc} were recorded, as shown in **fig. 5.14**.

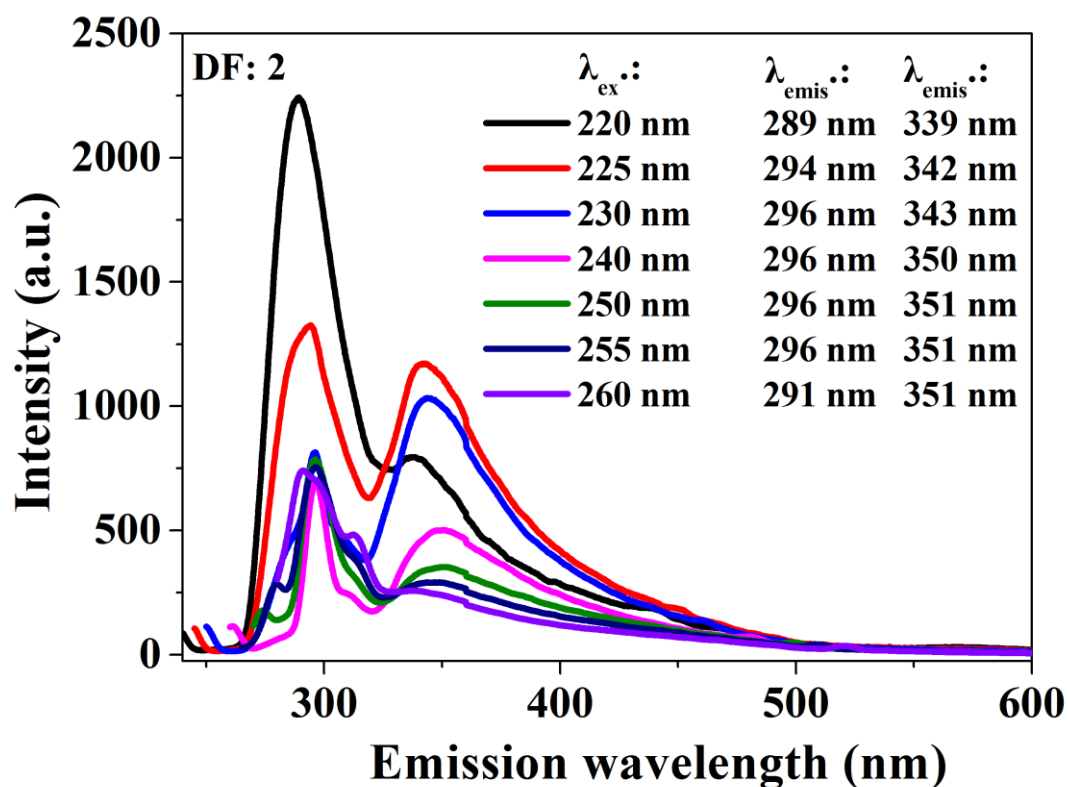


Figure 5.14: PL spectra of CNPb with DF: 2 at different λ_{exc} . The intensity numbers correspond to absolute values.

It can be clearly seen that PL maximum at λ_{emis} of about 290 nm is obtained with λ_{exc} 220 nm and the PL maximum at λ_{emis} of about 340 nm is obtained with λ_{exc} 225 nm.

c. CNPc

Fig. 5.15 shows the absorption spectra of CNPc for given CNP concentrations determined after freeze drying.

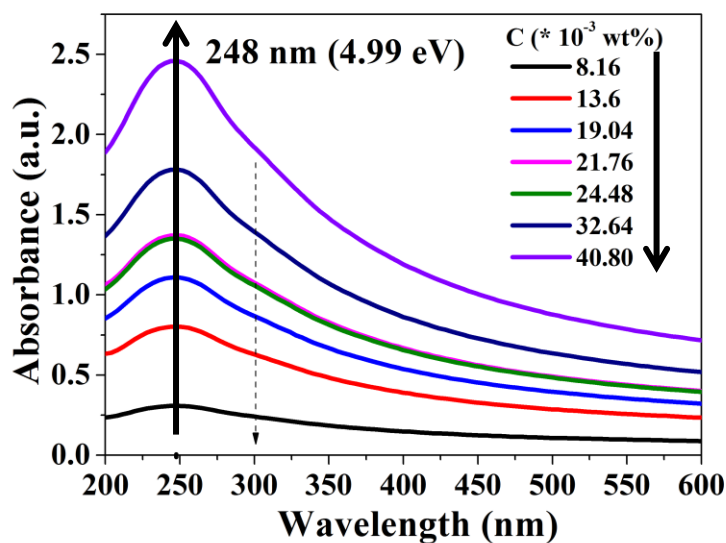


Figure 5.15: Absorption spectra of CNPc for different CNP concentrations.

One main peak at 248 nm originated from the π - π^* transition of C=C bonds in sp^2 hybrid regions is clearly observed. A shoulder at ~ 300 nm could also be seen due to the n - π^* transition of the C=O bond in sp^3 regions although the absorbance is typically weak.^{1,2,4} The graphene oxide (GO) exhibits absorption peak of ca. 230 nm. However, if the carbon is less oxidized, a red-shift of the wavelength is observed.^{3,4,8}

Another important parameter that could be extracted from the absorption spectra, is the absorption coefficient, α . This parameter is important for the characterization of dispersions. The absorption coefficient is related to the absorbance, A , through the Lambert-Beer law ($A = \alpha \cdot C \cdot l$, where C is the concentration and l is the path length). It's an indication of how strongly the chemical species absorb light at a given wavelength. It is an intrinsic property of the species. In order to determine α , the absorbance at 248 nm of the CNPc samples was plotted as a function of the CNP concentration, as shown in **fig. 5.16**. The absorbance is directly plotted, since the path length is 1 cm.

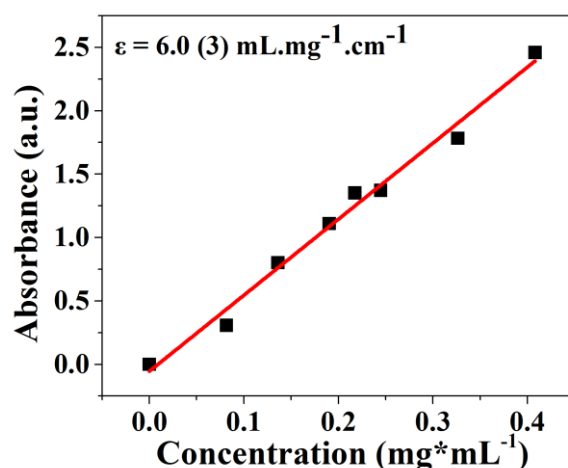


Figure 5.16: Absorbance, at wavelength 248 nm, as a function of the different CNP concentrations for CNPc. From the slope, the absorbance coefficient, a , has been determined.

The absorbance increases linearly with the increasing concentration, indicating that CNPc follows the Lambert–Beer law. A straight line fit through these points gives the absorption coefficient at 248 nm of $\epsilon = 6.0 (3) \text{ mL.mg}^{-1}.\text{cm}^{-1}$ in reasonable agreement with literature and corresponds to good and stable dispersion.^{18,19}

The PL mapping of the excitation as a function of the emission wavelength is shown in **Fig. 5.17** (the wavelength range of interest is illustrated).

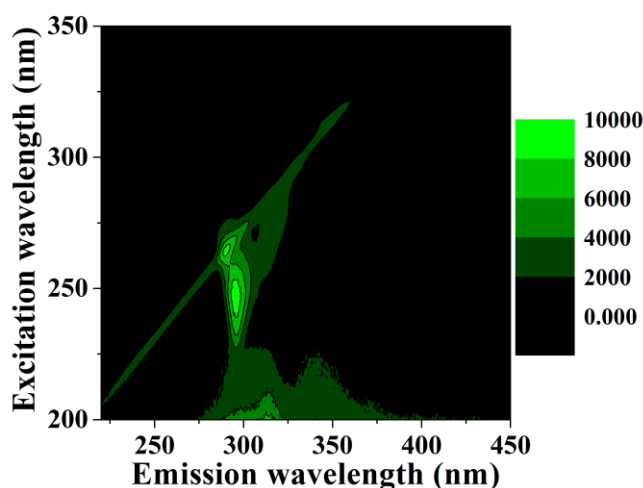


Figure 5.17: PL mapping of excitation wavelength as a function of emission wavelength of CNPc. The intensity numbers do not correspond to absolute values.

The maximum PL is found at λ_{emis} of ca. 300 nm with a weaker emission at about 350 nm when the dispersion is excited with wavelength of ca. 200 to 270 nm. Based on the

mapping results, the emission spectrum of CNPc at $\lambda_{exc.}$ 244 nm was recorded, as shown in **fig 5.18**.

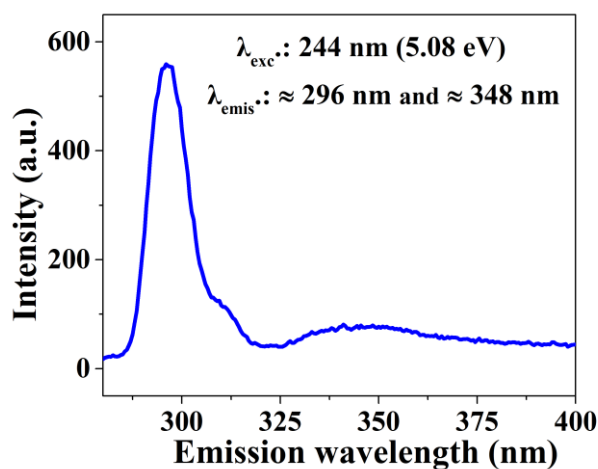


Figure 5.18: Emission spectrum of CNPc at $\lambda_{exc.}$: 244 nm. The intensity numbers correspond to absolute values.

Two PL maxima could be seen at wavelengths ca. 300 and 350 nm. In contrary to CNPa and CNPb, CNPc exhibits a weaker PL intensity.

d. CNPd

The CNP morphology was determined through AFM topography imaging, as shown in **fig. 5.19**.

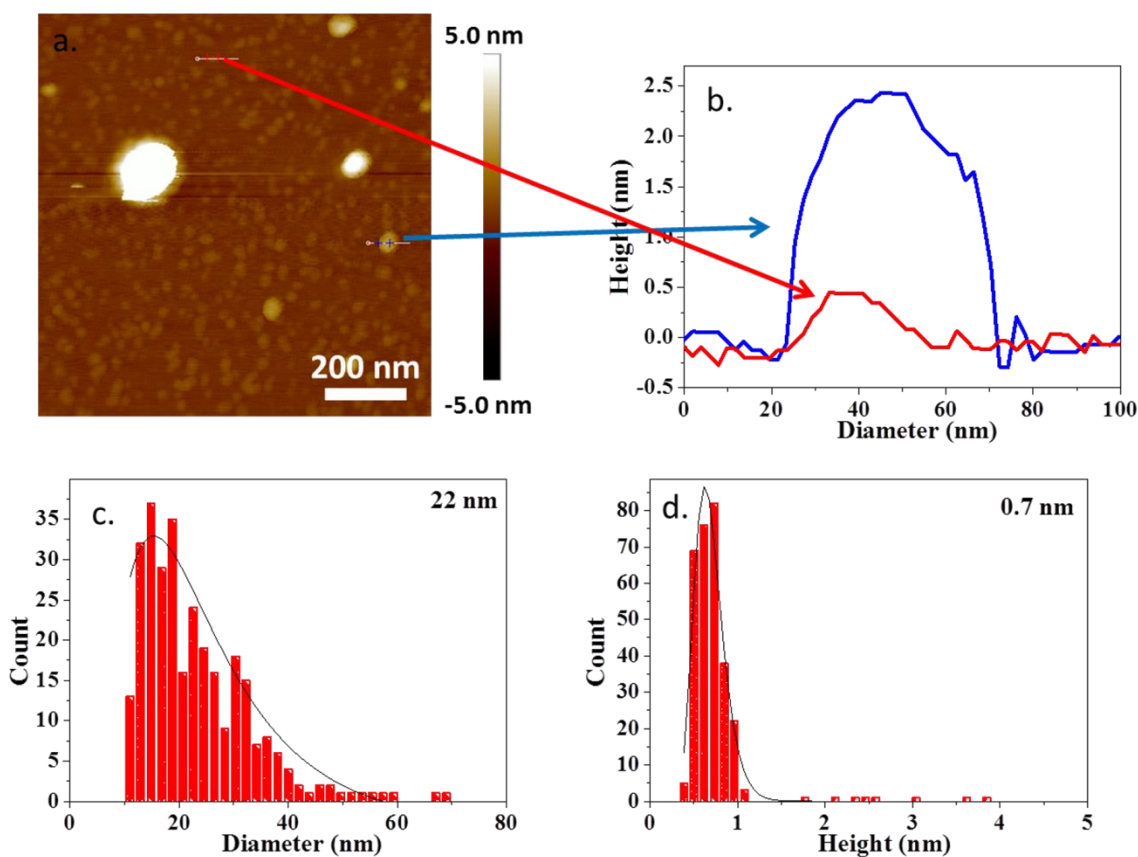


Figure 5.19: a. From CNPd, AFM topography image of CNP dispersion. b. Cross sections of the topography images are plotted. c. Statistical analysis of diameter of CNP particles. d. Statistical analysis of height of CNP particles.

The AFM image in **fig. 5.19 a** reveals a flat surface, having homogenous nano objects. Particles can be clearly observed with different heights, as seen in **fig. 5.19 b**. CNP particles with mean lateral sizes of 22 nm (**fig. 5.19 c**) and height of ca. 0.7 nm (mono and bilayer objects) (**fig. 5.19 d**) were acquired as seen from the statistical analysis.

Fig. 5.20 shows the absorption spectra of CNPc for given CNP concentration determined after freeze drying.

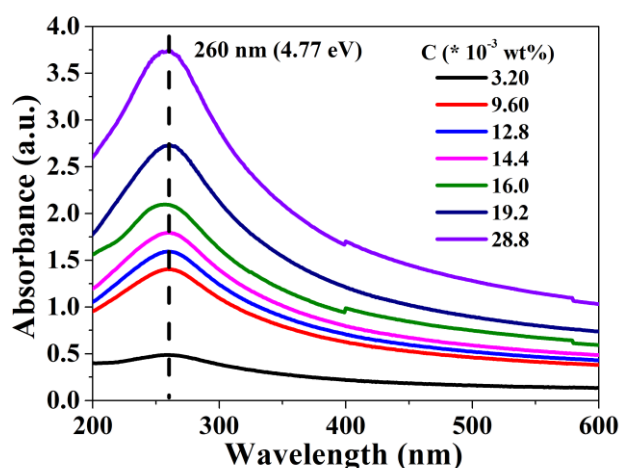


Figure 5.20: Absorption spectra of CNPd with different CNP concentrations.

An absorption peak is clearly observed due to the π - π^* transition of C=C at 260 nm. A typical red shift of the peak located at higher wavelengths is observed related to CNPc where a stronger oxidation occurred (absorbance peak for CNPc = 248 nm). This observation reflects less disruption of the electronic conjugation in CNPd compared to CNPc.¹⁷

Moreover, for CNPd from the plot of the absorbance (at 260 nm) as a function of CNP concentration, the absorption coefficient, α , has been determined, as shown in **fig. 5.21**.

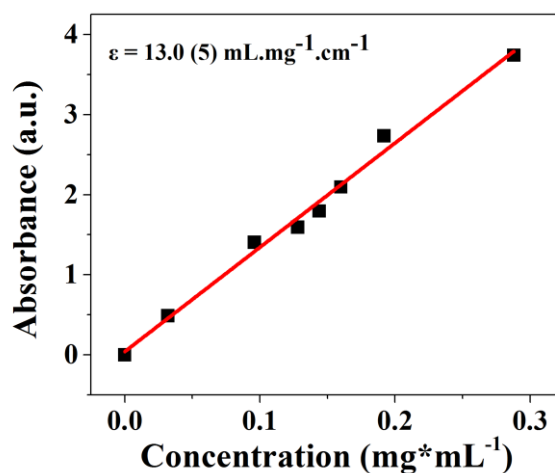


Figure 5.21: Absorbance, at wavelength 260 nm, as a function of different CNP concentrations for CNPd. From the slope, the absorbance coefficient, α , has been determined.

As for the CNPc dispersion, the absorbance increases linearly with increasing CNPd concentration, indicating that the dispersion follows the Lambert–Beer law. The absorption coefficient at 260 nm that was found from the line fit is $\epsilon = 13.0$ (7) $\text{mL.mg}^{-1}.\text{cm}^{-1}$, very close to literature values of graphene dispersed in water with surfactant

where a value of $13.9 \text{ mL.mg}^{-1}.\text{cm}^{-1}$ was reported.¹⁸ The excitation-emission map of the CNPd is seen in **fig. 5.22**.

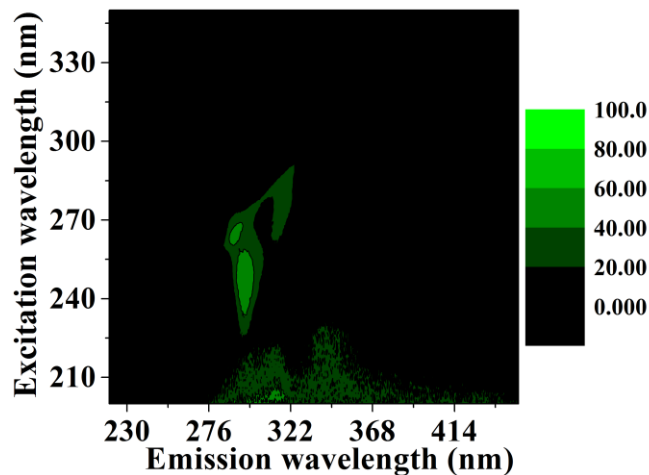


Figure 5.22: PL mapping of excitation wavelength as a function of emission wavelength of CNPd. The intensity numbers do not correspond to absolute values.

.Highest emission is found for $\lambda_{\text{emis.}}$ at ca. 300 nm for λ_{exc} of ca. 200 to 270 nm. Based on the mapping results, the PL spectrum of CNPd at $\lambda_{\text{exc.}}$ 220 nm was recorded, as shown in **fig 5.23**.

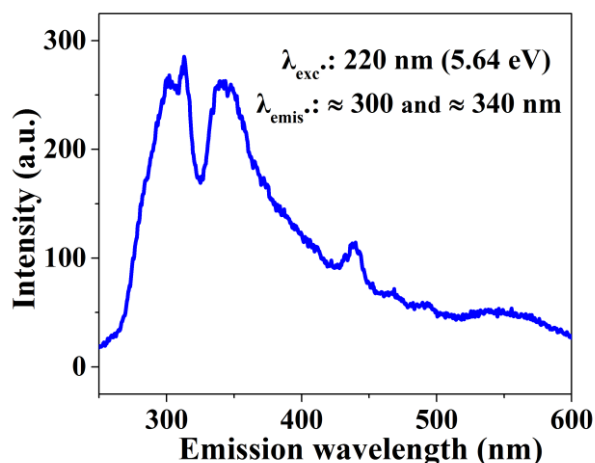


Figure 5.23: Emission spectrum of CNPd at $\lambda_{\text{exc.}}$: 220 nm. The intensity numbers correspond to absolute values.

Two PL maxima could be seen at wavelengths ca. 300 and 340 nm. However, as for CNPc, the PL intensity of CNPd is very weak. Therefore, optimization of the preparation procedure of CNPd deems necessary in order to increase the emission intensity.

Conclusion

Four different solution and/or dispersions have been performed using GIC or oxidative treatments.

CNP_a exhibits a strong PL in organic solvent. The CNP_b, CNP_c and CNP_d (dispersions in water) exhibit the same PL signature with CNP_b showing a strong emission. Moreover, the CNP_c and CNP_d that were achieved through oxidation treatments, show very similar PL behavior with weak intensity.

The PL of CNP_a was monitored as a function of time after air exposure and the curve of maximum emission over time was well-fitted considering a pseudo-first order kinetic reaction based on the study of Huang *et al.*¹¹ Thus, its PL could be attributed to the oxidation of the zigzag edge sites with carbene-like triplet ground states.

Despite possible differences in the size, in the number of layers of particles from one sample to another, all the CNPs in water (CNP_b, CNP_c and CNP_d) exhibit similar PL signature. This could suggest that the PL of these dispersions is an intrinsic characteristic. A possible PL source could be assigned to the zig-zag edge states. Furthermore, since the PL intensity of CNP_b dispersion is much higher, it could be assumed that it has more and better defined sp² fragments that exhibit PL than the oxidized samples (CNP_c and CNP_d) which could even possess sp² domains of bigger sizes and/or higher defect levels that could limit the recombination of radiative electron-hole pairs. This assumption needs further proves to be established

Overall, it could be concluded that CNP in liquid media exhibit strong PL which could be used in applications such as optoelectronics and biological labeling.¹ However, further characterizations are necessary. The next step that will be followed, is by using atomic force microscopy, X-ray photoelectron spectroscopy and Raman mapping to assess the size of particles in the liquid media and the amount of sp³ carbon and/or oxygen. The ultimate aim is to determine the PL yield, to comprehend the PL mechanisms and eventually to explore these systems in appropriate applications.

References

1. Pan, D., Zhang, J., Li, Z. & Wu, M. Hydrothermal route for cutting graphene sheets into blue-luminescent graphene quantum dots. *Adv. Mater.* **22**, 734–738 (2010).
2. Eda, G. *et al.* Blue photoluminescence from chemically derived graphene oxide. *Adv. Mater.* **22**, 505–509 (2010).
3. Kim, S. *et al.* Anomalous behaviors of visible luminescence from graphene quantum dots: Interplay between size and shape. *ACS Nano* **6**, 8203–8208 (2012).
4. Shang, J. *et al.* The Origin of Fluorescence from Graphene Oxide. *Sci. Rep.* **2**, 197–200 (2012).
5. Liu, F. *et al.* Facile Synthetic Method for Pristine Graphene Quantum Dots and Graphene Oxide Quantum Dots: Origin of Blue and Green Luminescence. *Adv. Mater.* **25**, 3657–3662 (2013).
6. Zhu, S. *et al.* The photoluminescence mechanism in carbon dots (graphene quantum dots, carbon nanodots, and polymer dots): current state and future perspective. *Nano Res.* **8**, 355–381 (2015).
7. Dekaliuk, M. O. *et al.* Fluorescent carbon nanomaterials: ‘quantum dots’ or nanoclusters? *Phys. Chem. Chem. Phys.* **16**, 16075 (2014).
8. Galande, C. *et al.* Quasi-Molecular Fluorescence from Graphene Oxide. *Sci. Rep.* **1**, 666–669 (2011).
9. Ljubisa R. Radovic*, † and & Bockrath‡, B. On the Chemical Nature of Graphene Edges: Origin of Stability and Potential for Magnetism in Carbon Materials. (2005). doi:10.1021/JA050124H
10. Lin, L. & Zhang, S. Creating high yield water soluble luminescent graphene quantum dots via exfoliating and disintegrating carbon nanotubes and graphite flakes. *Chem. Commun.* **48**, 10177 (2012).
11. Huang, K. *et al.* Single layer nano graphene platelets derived from graphite nanofibres. *Nanoscale* **8**, 8810–8818 (2016).
12. Catheline, A. *et al.* Graphene solutions. *Chem. Commun.* **47**, 5470 (2011).
13. Pénicaud, A. & Drummond, C. Deconstructing Graphite: Graphenide Solutions. *Acc. Chem. Res.* **46**, 129–137 (2013).
14. Bepete, G. *et al.* Surfactant-Free Single Layer Graphene in Water. *Nat. Chem.* (2016).
15. Hummers, W. S. & Offeman, R. E. Preparation of Graphitic Oxide. *J. Am. Chem. Soc.* **80**, 1339–1339 (1958).
16. Marcano, D. C. *et al.* Improved Synthesis of Graphene Oxide. *ACS Nano* **4**, 4806–4814 (2010).
17. Zamora-Ledezma, C. *et al.* Liquid Crystallinity and Dimensions of Surfactant-Stabilized Sheets of Reduced Graphene Oxide. *J. Phys. Chem. Lett.* **3**, 2425–2430 (2012).
18. Lotya, M. *et al.* Liquid phase production of graphene by exfoliation of graphite in

- surfactant/water solutions. *J. Am. Chem. Soc.* **131**, 3611–20 (2009).
19. Hernandez, Y. *et al.* High-yield production of graphene by liquid-phase exfoliation of graphite. *Nat. Nanotechnol.* **3**, 563–568 (2008).

General conclusion

Crystalline carbon nanopucks (CNPs) of turbostratically packed layers of graphene have been generated via microwave plasma process from the splitting of methane/carbon dioxide mix within the framework of the European project PlasCarb. CNP is the material which this PhD thesis focuses on. It could be placed between two carbon forms, graphene and carbon black due to its structure and characteristics. Graphene is one of the most promising materials and has attracted much attention in the scientific and industrial community due to its unique structure and properties. On the other side, CB is an industrial product, commonly produced via incomplete combustion of crude oil (petroleum). However, both of these carbon materials have some drawbacks; graphene production is still highly costly while carbon black is not an environmentally friendly product. Therefore, CNP could be a promising alternative solution. The objective of this thesis has been to optimize, characterize and utilize this carbon material to different applications.

CNP grades have been initially characterized by Raman spectroscopy and thermogravimetric analysis (TGA). From these techniques the amount of amorphous material within the sample has been determined. Likewise, they have been improved by purification. By applying heat treatment, amorphous carbon content of ca. 12% has been successfully removed. Further characterization of the samples has been performed by using a variety of techniques such as the aforementioned as well as X-ray diffractograms (XRD), atomic force microscope (AFM), scanning tunneling microscopy (STM), X-ray photoelectron spectroscopy (XPS), infrared (IR) spectroscopy, UV/vis absorption spectroscopy, static light scattering (SLS), transmission electron microscopy (TEM) and scanning electron microscopy (SEM).

Afterwards, in order to harness their properties, dispersion of CNPs has been performed. Their dispersion in aqueous media was feasible by optimizing several parameters; choice of surfactant, sonication time-energy and type, surfactant concentration, centrifugation time and ultimately the maximum CNP concentration that could be successfully dispersed. Well-defined high concentrated (6 wt% and 2.2 wt%) CNP dispersions of two and one size populations have been acquired. Monodispersed samples (yield of ca. 50%) have been produced with lateral size of ca 30 to 80 nm and thickness of ca. 20 to 40 nm, results acquired from their analysis with techniques such as optical microscopy, static light scattering, atomic force microscopy and high resolution transmission electron microscopy. The conductivity of these dispersions has been

determined after the formulation of their films using filtration under vacuum. Resistivity of ca. 1 $\Omega\cdot\text{cm}$ could place CNP in the range of high quality CB grades (10^0 - 10^{-1} $\Omega\cdot\text{cm}$). By compression of the films, sheet resistance of 220 $\Omega\cdot\text{sq}^{-1}$ can be obtained, which makes CNPs suitable for conductivity related applications including conductive coatings and as fillers for conductive composites.

Based on the above results, CNPs have been used as additives in natural rubber (NR) composites so as to reinforce their properties. Two sets of CNP/NR composites have been successfully prepared. They differ in terms of surfactant used in CNP dispersion as well as CNP precursor. Carbon deriving from biogas, NR extracted directly from the tree *Hevea Braziliensis* and the use of latex technology (no toxic solvents) contribute to the production of environmentally friendly CNP/NR composites. The two set of composites yield different optimum properties; one system significantly increases the mechanical properties while the other exhibits superior electrical properties (σ : 7.5 $\text{S}\cdot\text{m}^{-1}$) that can be compared to systems with the highest conductivity values observed. Moreover, these composites show interesting piezoresistive characteristics (gauge factor with the best value of 8.5). Overall, the composites have thermal, mechanical, electrical and piezoresistive properties superior to the pure polymer.

The last property of CNP materials that has been tested and has been described in this manuscript is their photoluminescence (PL) profile. CNP has been dissolved and dispersed in water and organic solvent using four different preparation procedures (through graphite intercalation compounds (GIC) and by the use of oxidative agents). The PL of these systems has been measured. The CNP samples dispersed in water have been found to exhibit the same blue PL signature with strongest emission the one prepared via GIC. Regarding the CNP solution in organic solvent, it shows high PL but red-shifted emission wavelength related to the PL of the dispersions in water. From these PL preliminary tests, it could be concluded that CNP could be used in applications such as optoelectronics and biological labeling.

Acronyms

AFM	Atomic Force Microscopy
ASTM	American Society for Testing and Materials
CAGR	Compound annual growth rate
CB	Carbon Black
CMC	Critical Micelle Concentration
c-MWCNT	carboxylated- Multi-Walled Carbon NanoTubes
CNP	Carbon NanoPuck
CNP _{HT}	Heat Treated Carbon NanoPuck
CNPIC	Carbon Nanopuck Intercalation Compound
CNT	Carbon NanoTube
CVD	Chemical Vapor Deposition
CTAB	CetylTrimethyl AmmoniumBromide
DF	Dilution Factor
DMA	Dynamic Mechanical Analysis
DMF	DiMethylFormamide
EMI	Electromagnetic Interference
FGS	Functionalized Graphene Sheet
FLG	Few Layer Graphene
FWHM	Full Width at the Half Maximum
GIC	Graphite Intercalation Compound
GnP	Graphene Platelet
GO	Graphene Oxide
GQD	Graphene Quantum Dot
HOPG	Highly Oriented Pyrolytic Graphite
HRTEM	High Resolution Transmission Electron Microscopy
IL	Ionic Liquid
IR	Infrared
LCA	Life Cycle Analysis
MWCNT	Multi-Walled Carbon NanoTube
NC	NanoCarbon
NMP	N-Methyl-2-Pyrrolidone
NR	Natural Rubber
oDCB	ortho DiChloroBenzene

PAH	Polycyclic Aromatic Hydrocarbon
PE-PEG	PolyEthylene-block-Poly(Ethylene Glycol)
PET	PolyEthylene Terephthalate
phr	parts per hundred parts
PL	PhotoLuminescence
PVDF	PolyVinylidene Fluoride
PVP	PolyVinylPyrrolidone
P123	Poly(ethylene glycol)-block-poly(propylene glycol)- block-poly(ethylene glycol)
rGO	reduced Graphene Oxide
RH ₂	Renewable Hydrogen
RPC	Renewable PlasCarbon
SBR	Styrene-Butadiene Rubber
SDBS	Sodium Dodecyl Benzene Sulfonate
SDS	Sodium DodecylSulfate
SEM	Scanning Electron Microscopy
SLS	Static Light Scattering
STM	Scanning Tunneling Microscopy
SWCNT	Single-Walled Carbon NanoTube
TEM	Transmission Electron Microscopy
THF	TetraHydroFuran
TGA	ThermoGravimetric Analysis
UV	UltraViolet
XPS	X-ray Photoelectron Spectroscopy
XRD	X-ray Diffraction

Nanocarbone à partir de déchets alimentaires: dispersions et applications

Cette thèse se concentre sur la caractérisation, la dispersion, ainsi que les différentes applications d'un nouveau type de matériaux dérivé de la dégradation de biométhane dans le cadre d'un projet Européen, le projet PlasCarb. Nous appelons ces matériaux les nanopalets de carbone (CNP). Notre étude commence avec la caractérisation des CNP, puis nous poursuivons avec l'obtention de dispersions aqueuses bien définies et hautement concentrées de CNP. Ces dispersions ont été utilisées pour la préparation de films conducteurs et de composites conducteurs avec du caoutchouc naturel. Enfin, la photoluminescence des CNP dispersés et solubilisés dans un milieu liquide a été évaluée. Des tests préliminaires montrent une photoluminescence dans le bleu très prometteuse.

Mots clés: nanopalets de carbone, dispersions, caoutchouc naturel, composites, conductivité, photoluminescence

Nanocarbon from food waste: dispersions and applications

This PhD thesis is focused on the characterization, dispersion and applications of graphitic material (in this manuscript referred as carbon nanopuck (CNP)) that derives from the splitting of biogas and obtained within the framework of the European project "PlasCarb". This study starts with CNP characterization. Afterwards, well-defined, high concentrated CNP dispersions in water, calibrated in size have been obtained. These dispersions have been used to prepare conductive films and as components of conductive composites with natural rubber. Ultimately, the photoluminescence of CNP dispersed and dissolved in liquid media has been tested. Preliminary tests of these systems exhibit promising blue PL.

Keywords: carbon nanopucks, dispersions, natural rubber, composites, conductivity, photoluminescence

Unité de recherche

Centre de recherche Paul Pascal, UPR 8641, 115 Av. Schweitzer, 33600 Pessac